Electronic properties of diffusive three-terminal Josephson junctions and non-local quartet mechanism

Andreas H Pfeffer

Electronic properties of diffusive three-terminal Josephson junctions and non-local quartet mechanism

Andreas H. Pfeffer

UNIVERSITÉ DE GRENOBLE

THÈSE

Pour obtenir le grade de

DOCTEUR DE L'UNIVERSITÉ DE GRENOBLE

Spécialité : **Physique/Nanophysique**

Arrêté ministériel : 7 août 2006

Présentée par

Andreas Helmut PFEFFER

Thèse dirigée par **François LEFLOCH**

préparée au sein **Laboratoire de Transport Electronique Quantique et Supraconductivité, CEA Grenoble**
et de **l'école doctorale de physique de Grenoble**

Electronic properties of diffusive three- terminal Josephson junctions and non-local quartet mechanism

Thèse soutenue publiquement le **18 décembre 2013**,
devant le jury composé de :

Marco APRILI
Laboratoire du physique des solides, Orsay, Rapporteur
Detlef BECKMANN
Karlsruhe Institute of Technology, Karlsruhe, Rapporteur
Vincent BOUCHIAT
Institut Néel/ CNRS & Université de Grenoble, Président
Denis FEINBERG
Institut Néel/ CNRS Grenoble, Examinateur
François LEFLOCH
SPSMS/ CEA Grenoble, Directeur de thèse
Christian SCHÖNENBERGER
Universität Basel, Examinateur

Contents

Abstract

0.1 Summary (english)

During this PhD, I have first finished the development of a unique experimental set-up, dedicated for studies of electronic transport of low impedance multi-terminal nanostructures. This set-up allows conductance and noise measurements at very low temperature ($30\,mK$), with a resolution of a few pico-ampere by using SQUIDs as current amplifiers. In chapter 5, I give some explanation of the measurement working principle. Furthermore, I explain the calibration of the experimental set-up as well as how to extract physical quantities from the measurements.

In chapter 6, I explain transport measurements on diffusive tri-terminal junctions (tri-junction). In a T-shape called geometry, the superconducting Al-electrodes are connected via a common metallic, non-superconducting part of Copper. For these nanostructures, we observe features in the conductance at low voltage, which have been never observed yet experimentally. These features in conductance/resistance have a striking resemblance with a dc-Josephson effect, appearing when two applied potentials on the tri-junction compensate exactly each other. In literature, two mechanisms are proposed to explain this effect. The first mechanism, called "mode-locking", corresponds to a dynamic locking of ac-Josephson currents, which is induced by the experimental environment (circuit). This situation has been extensively studied in the 60's on coupled microstructures, based on weak links. In order to test this explanation, we have measured a junction, which is composed of two spatially separated Josephson junctions. The anomalies does not show up in such a geometry, even not with strongly reduced amplitude. This indicates, that synchronization via the experimental environment can't be the origin of the observed features.

The second theoretical mechanism is named "quartet-mode" and has been recently proposed by Freyn and Co-workers. In this process, one superconducting electrode emits doublets of Cooper-pairs. Each of the two pairs splits into two quasi particles propagating toward different superconducting contacts. In such a mechanism, two quasi-particles originating of two different Cooper-pairs, arrive each in the two superconducting contacts. If the applied voltage between the emitting superconducting contact and the two other contacts is exactly opposite, the phase of the electronic wave functions of the arriving quasi-particles on the same superconducting contact are such, that these two quasi-particles can recombine by forming a Cooper-pair. Due to this mechanism, the emitted doublet of Cooper-pairs is coherently distributed as two Cooper-pairs, each of them in a different superconducting contact. This mechanism is favored, since it is robust with respect to disorder and can hence also exist over a large range of voltage. During this PhD, I have shown

that these anomalies are indeed present for applied voltage corresponding to energies well above the Thouless energy. Argumentum a contrario, the coherent effects responsible for the ac Josephson-effect have to be strongly attenuated over the same range of energy, which makes low probable the effect of mode-locking. The observed dependency with applied magnetic field and the temperature are further indications for the quartet-mode. Unfortunately, for the moment, no microscopic complete theory of such a trijunction exists in order to provide an inevitable argumentation. Nevertheless, a phenomenological approach has been developed based on a extended RSJ model. This allows an estimation of the influence of the particularities of the experimental set-up (voltage-/current-bias). The first part of the manuscript (chapter 1-4) consists of an introduction, followed by a quite detailed description of mesoscopic physics, on which the further manuscript is based as well as a state-of the art about the studies of coupled Josephson junctions. Chapter 5-7 describes the performed experimental work. In chapter 8, I give a conclusion about the effected work and propose complementary experiments as well as long term perspectives.

0.2   Résumée de Thèse (français)

Pendant ce travail de thèse, j'ai tout d'abord finalisé le développement d'un système expérimental unique dédié aux études de transport électronique de nanostructures multi-terminaux de faible impédance. Ce dispositif permet des mesures de conductance et de bruit à très basse température (30 mK), avec une résolution du pico-ampère en utilisant des SQUIDs comme amplificateurs de courant. Dans le chapitre 5, je fournis une description du fonctionnement de la mesure. De plus, je décris la calibration du dispositif et la manière de déduire des quantités physiques à partir des mesures. Au Chapitre 6, je décris des mesures de transport avec des jonctions diffusives à trois terminaux (tri-jonctions). Dans une géométrie, que l'on appelle T-shape, des électrodes supraconductrices d'Aluminium sont connectées entre-elles par une partie centrale métallique non-supraconductrice de Cuivre. Pour ces nanostructures, on observe des anomalies de conductance à basse tension qui n'ont jamais été observées expérimentalement. Ces anomalies de résistance/conductance ressemblant fortement à l'effet Josephson apparaissant lorsque deux des potentiels appliqués à la trijonction ont une somme nulle. Les anomalies sont présentes sur une large échelle de tension sans perte d'amplitude. De-même, elles montrent une grande robustesse en température. Des expériences sous champ magnétique appliqué montrent une forte suppression des anomalies pour un champ magnétique correspondant à flux magnétique dans la partie normale de l'ordre d'un quantum de flux. Ceci indique qu'un mécanisme cohérent de phase doit être à l'origine des anomalies. Dans la littérature, deux mécanismes sont proposés pour expliquer ces effets. Le premier, nommé "mode-locking", est un accrochage dynamique des courants Josephson ac, qui est induit par l'environnement expérimental (circuit). Cette situation a été étudiée dans les années soixante sur des microstructures Josephson couplées à base de liens faibles. Pour tester cette explication, nous avons mesuré un échantillon composé de deux jonctions Josephson spatialement séparées. Les anomalies n'apparaissent pas dans une telle géométrie, pas même avec une amplitude réduite. Ceci indique qu'une synchronisation par l'environnement expérimental ne peut pas être à l'origine des anomalies observées. Le deuxième mécanisme théorique évoqué est nommé "mode de quartet" et a été proposé récemment par Freyn et collaborateurs. L'une des électrodes supraconductrices distribue alors des doublets de paires de Cooper. Chacune de ces deux paires se scindent alors en deux quasiparticles se propageant chacune vers deux contacts supraconducteurs différents. Dans un tel mécanisme deux quasiparticules, issues de deux paires de Cooper différentes, arrivent sur chacun des deux contacts supraconducteurs. Lorsque les tensions appliquées entre le contact supraconducteurs émetteur et les deux autres contacts sont exactement opposés, les phases des fonctions d'ondes électroniques des quasiparticules arrivant sur un même contact supraconducteur sont telles que ces deux quasiparticules peuvent se recombiner pour former une paire de Cooper. Par ce mécanisme le doublet de paires de Copper émis se distribue de manière cohérente en deux paires de Cooper chacune dans un contact supraconducteur différent. Ce mécanisme est favorable, car il est robuste envers le désordre et peut ainsi exister sur une large échelle de tensions. Au cours de cette thèse, j'ai montré que ces anomalies sont effectivement présentes pour des tensions appliquées correspondant à des énergies bien supérieures à l'énergie de Thouless. A contrario, les effets cohérents responsables de l'effet Josephson ac doivent être fortement atténués sur cette même échelle d'énergie, ce qui rend peu probable le mécanisme de mode-locking.

La dépendance observée avec le champ magnétique et la température sont d'autres indications de l'existence du mode de quartet. Malheureusement, il n'existe pour l'instant, pas de théorie microscopique complète d'une telle trijonction pour fournir une argumentation incontournable. Néanmoins, une approche phénoménologique a été développée sur la base d'un modèle RSJ élargi. Celui-ci permet une estimation de l'influence des particularités du dispositif expérimental (voltage-/current-bias). La première partie de mon manuscrit (chapitre 1, 2, 3 et 4) présente une introduction, une description assez détaillée des concepts de supraconductivité mésoscopique utiles au reste du manuscrit ainsi qu'un état de l'art dans l'étude des jonctions Josephson couplées. Dans le Chapitre 8, je donne une conclusion du travail effectué et je propose des expériences complémentaires et des perspectives à long terme.

Chapter 1

Introduction

Quantum physics, is without doubt one of the supreme achievements of the 20th century and has definitively changed the understanding of physics up to our days. Especially because of the concept of particle-wave duality and the superposition-mechanism, quantum physics was for a long time considered as an incomplete theory. One of the most astonishing consequences of quantum mechanics is the existence of entangled states. This is the starting-point of the famous work of Einstein, Podolsky and Rosen [1]. Their reasoning, now known as EPR-paradox, can be summarized as follows: When the quantum states of two particles are entangled, the measurement of one of these particles reveals instantaneously the state of the second particle. This remains true even if the two particles have propagated on both ends of the universe. Since the result of the first measurement occurs with a certain probability, Einstein and co-workers came to the conclusion: "Can the quantum-mechanical description of physical reality be considered complete?"

Until the sixties, a common opinion was that a mechanism, which is not considered within the theory yet, would govern the outcome of each measurement and resolve the EPR-paradox. This unconsidered mechanism is called hidden variable. In 1965 however, J.S. Bell [2] achieved to reformulate this paradox in a mathematical form and showed, that quantum mechanics is not consistent with any hidden-variable theory. Furthermore, he pointed out, that this incompatibility can be tested experimentally. Up to our days, thousands of experiments have confirmed the concept of quantum physics.

Over the last decades, several systems have been found, where quantum properties can be observed at a macroscopic scale. Among them the so-called Josephson junctions are the most extensively studied over the last 50 years.

In 1962, B. D. Josephson predicted, that a supercurrent could flow at zero applied voltage between two superconducting reservoirs only separated by an insulating layer. Furthermore, he predicted that for finite voltage across such a junction, an ac-current can be generated. These effects were confirmed experimentally few years later [3–7] and were named Josephson-effects named after their discoverer. Further studies have shown [8], that Josephson effects can be observed generally in all structures, where two superconductors are connected by a "weak link" (tunnel barrier, normal metal, semiconductor, geometrical constriction etc.). Therefore, Josephson junctions developed into a highly active field of fundamental and industrial research [9].

As a result of the progress in fabrication techniques, more and more complex structures have been studied. First experiments on coupled Josephson junctions were performed

in the late sixties. Depending on device-geometry and performed experiments, different mechanism have been revealed both in experiment and theory, for instance phase-/voltage-locking (for more detailed review, please refer for instance to [10, 11]). Due to deeper understanding of the underlying physics and permanent progress in fabrication techniques, more and more sophisticated devices get available during the last decade, such as Josephson transistors [12] or so-called Josephson mixers, which allow signal amplification near the quantum limit [13, 14].

At the end of the 90's, theory predicted that after Andreev reflection, incident and the retro-reflected particles can be spatially separated by choosing an appropriate geometry [15, 16]. This process arises for instance in three-terminal structures, where two metallic contacts, situated within a distance of the superconducting coherence length ξ_s, are connected to a superconductor. In this kind of structures, there is a non-zero probability, that an incident electron from contact 1 is retro-reflected as a hole into contact 2. This process, is called Crossed Andreev reflection (CAR). It did not take long time, before people realized that CAR could be use-full for application in solid-state quantum computers and future electronics. Cooper-pairs are naturally entangled electrons, a controllable CAR-process would help to generate entangled electrons on demand. A so-called electronic "EPR-source" offers promising perspectives for application and research (quantum cryptography, quantum computing, spintronics, etc.). For that reason, the community working on experiments toward the realization of such an electronic EPR-source has grown continuously over the last years. However, before this milestone in solid-state physics, a few major steps have to be accomplished.

In a first step, the theoretical prediction of CAR has to be confirmed experimentally. The first experimental proof of CAR has been given by Beckmann et al. [17] with the help of ferromagnetic materials. Within the last few years, CAR has equally been observed in various other materials and geometries [18–22] and it turned out that even splitting-efficiencies of nearly 100 % can be achieved in appropriate device geometries [23].

Another approach to study the entanglement is to investigate devices involving three superconducting electrodes. Within these devices, superconducting correlations are expected to be strongly enhanced, allowing to study noise properties and transport involving Cooper-pairs in more detail. Furthermore, recent theoretical predictions announce new transport mechanisms for multi-terminal structures with all superconducting electrodes, which have not been reported yet experimentally, such as 3-terminal MAR [24] or the coherent transport in dynamic regime via quartet-modes [25, 26].

Within the framework of this PhD, I finished the development of a unique experimental set-up which allows detailed studies of such all-superconducting multi-terminal devices for low impedance samples. The measurements are performed with SQUIDs acting as current amplifiers, which allow conductance- and noise measurements with a resolution in the pico-ampere range. Furthermore, we report of conductance measurements in three-terminal diffusive Josephson junctions, where features occur in the low-voltage range, which are consistent with the recent theoretical prediction of non-local quartets. These non-local quartets, once established, can be seen as a further and final proof of the CAR, since CAR is an unavoidable ingredient of this transport-mechanism.

Chapter 2

Hybrid Nanostructures

The interplay of a superconductor with normal metals is an active field of fundamental research for already more than 30 years ([9, 10, 19, 27–30]; for an historical overview, see for instance [31]). The underlying mechanism providing electronic transport below the superconducting gap Δ through hybrid structures composed of a superconductor and a normal metal is called Andreev reflection. Within this process, an incoming electron from the normal metal side is retro-reflected as a hole, which leads to the creation of a Cooper-pair in the superconductor. Electron and hole (named "Andreev-pairs" in the following) stay coherent over a coherence length L_ϵ which can be limited by various parameters, such as temperature, applied voltage or material properties. Depending on the interface transparency, normal metal and superconductor exchange their properties at the interface, which is known as (inverse) proximity effect. This interplay of macroscopic coherence due to superconductivity and microscopic coherence in normal metals provides rich phenomena in hybrid nanostructures.

In the following chapter, I will first introduce some basic principles of superconductivity. Then, a short overview of phenomena, arising in more complex devices, will be given.

2.1   S/N: Andreev reflection and Coherence

Let's consider an interface between a superconductor and a normal metal. Due to the gap in the superconducting density of states around the Fermi-energy E_F, excited quasiparticles from normal metal-side cannot enter if their energy ϵ is smaller than the superconducting gap Δ, $\epsilon = |E - E_F| < \Delta$. However, Andreev reflection (AR) provides a coherent mechanism, which converts the dissipative transport via excited electrons (quasi-particles) in a normal metal into dissipation-less supercurrent via Cooper pairs (for a visualisation of the Andreev reflection process, see Fig. 2.1 and 2.2).

Within this process, an incoming electron from normal metal side with energy $E_e = \epsilon + E_F$, momentum $k_e = k_F + \delta k$ and spin $S = \sigma$ is retro-reflected as a hole with opposite spin and momentum ($S = -\sigma, k_h = k_F - \delta k$) at an energy $E_h = -\epsilon + E_F$, where $\delta k \approx \epsilon/\hbar v_F$, v_F is the Fermi velocity. Furthermore, a Cooper-pair is generated in the superconductor [32, 33] [1]. During the AR-process, the retro-reflected hole wave

---

1. Off course, also the inverse process is possible, where an incoming hole gets retro-reflected as an electron by removing a Cooper pair from the superconductor.
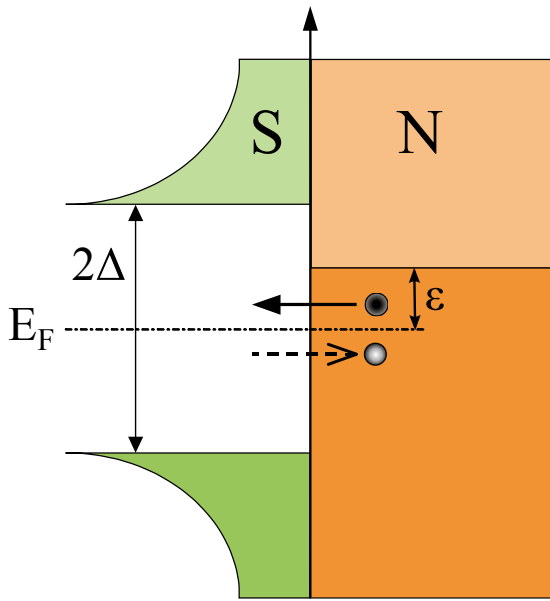
Figure 2.1: Andreev-reflection in energy space: an incoming electron is retro-reflected as a hole; this leads to the creation of a Cooper-pair in the superconductor (Figures reproduced from Thesis C. Hoffmann [34]
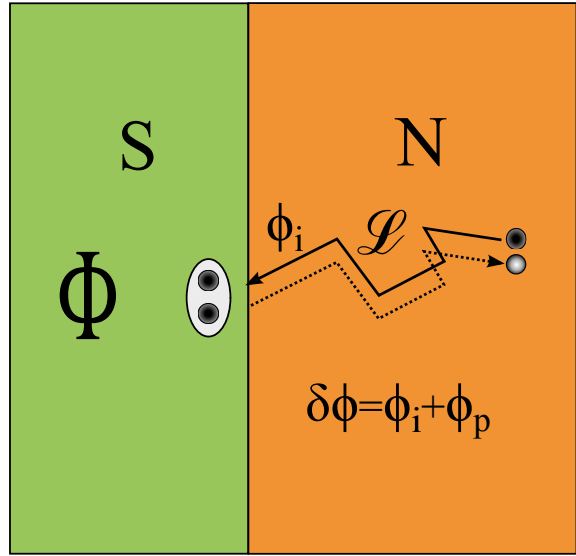
Figure 2.2: In Andreev reflection, the total phase-shift between electron and hole consists of a phase-relative de-phasing at the interface Φ_i and a propagation-induced contribution Φ_p

function picks up the macroscopic superconducting phase as well as an additional, energy-dependent relative phase ϕ_i:

$$\phi_i = \Phi - \arccos\left(\frac{\epsilon}{\Delta}\right) \tag{2.1}$$

where Φ is the macroscopic superconducting phase, ϵ the energy of the incoming electron with respect to the Fermi-level (see Fig. 2.1). Away from the S/N interface, the electron and hole wave functions de-phase due to the mismatch of their wave vectors

$$k_e - k_h = 2\delta k \approx 2\frac{\epsilon}{\hbar v_F}. \tag{2.2}$$

As can be seen easily, perfect retro-reflection is just possible for $\epsilon = 0$. This means, that the hole follows exactly the same path as the incident electron and propagation does not lead to additional de-phasing. In that case, the coherence of the Andreev-pair is limited by the individual phase coherence of a quasi-particle, L_Φ.

If $\epsilon \neq 0$, a propagation-induced phase-shift Φ_p between electron and hole takes place. After a diffusion path $\mathcal{L}$ or equivalently a time $\tau = \mathcal{L}/v_F$, one gets

$$\phi_p = 2\delta k \, \mathcal{L} = \frac{2\epsilon\mathcal{L}}{\hbar v_F}. \tag{2.3}$$

Hence, for $\epsilon \neq 0$, the phase-shift $\Delta\phi = \phi_i + \phi_p$ is composed by two contributions: the obligatory part due to AR as well as a propagation-induced phase-shift which strongly depends on the material properties (ballistic or diffusive).
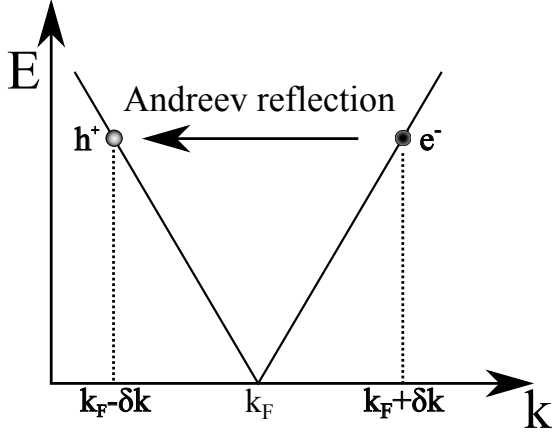
Figure 2.3: Andreev reflection, expressed in k-space [31]
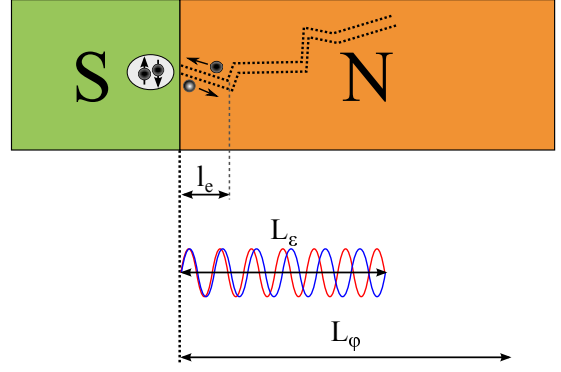
Figure 2.4: Sketch of some important length scales in S/N nanostructures: l_e: mean free path; L_ϵ coherence length of an Andreev pair; L_Φ: quasi-particle coherence length; reproduced from [35]

Following equation Eq. 2.3, one can define an energy-dependent length-scale (respectively time-scale), above which electron and hole phase-differences are randomized. This length scale (respectively time scale) defines the coherence of the Andreev pairs:

$$\mathcal{L}_\epsilon = \frac{\hbar v_F}{\epsilon} \quad \text{or} \quad \tau_\epsilon = \frac{\hbar}{\epsilon}$$

In the diffusive limit, one prefers to deal with the actual distance L_ϵ from the interface:

$$L_\epsilon = \sqrt{D\tau_\epsilon} = \sqrt{\frac{\hbar D}{\epsilon}} \tag{2.4}$$

where D is the diffusive constant of the normal metal[2]. The limiting parameters for this coherence length can have various origin, for example applied voltage eV or temperature $(2\pi k_B T)$. The expression of L_ϵ allows to define the so-called Thouless energy E_{Th}

$$E_{Th} = \frac{\hbar D}{L^2}. \tag{2.5}$$

Therefore, the Thouless energy E_{Th} specifies the energy window within which an Andreev-pair remains coherent at a given distance L. Finally, the ultimate length scale is given by the single particle phase coherence length L_Φ: experiments in diffusive metal nanostructures revealed phase coherence lengths L_Φ up to $10\,\mu m$, strongly dependent on the material purity [36–38].

---

2. In the ballistic limit, $\mathcal{L}_\epsilon$ corresponds to L_ϵ

2.1.1 Proximity effect

So far, the material properties of superconductor (S) and normal metal (N) have been considered as homogeneous, even near the interface (ideal N-S boundary) - and Andreev reflection was considered to take place exactly at the interface. In reality, this is not necessarily the case. A good electrical contact between a superconductor and a normal metal leads to important modifications in the local density of states (DOS) as well as the transport properties (see Fig. 2.5). As seen in section 2.1, Andreev reflection forms an electron-hole pair, staying coherent over a length L_ϵ in N. This coherence induces superconducting properties into the normal metal, which is called *proximity effect*. Cooper-pairs can be formed even in the normal metal within the range $\xi_N = \sqrt{\hbar D_n/\Delta}$, because the pair amplitude is still present there (BCS-theory).

The first theory, taking into account this energy-dependent superconducting coherence, was given by the Bogoliubov-de Gennes equations [39]. Within the Bogoliubov-de Gennes equations, the superconducting excitation spectrum is described by a set of coupled differential equations, where $u(\mathbf{x})$ describes the electron-component of the wave-functions (respectively hole-component $v(\mathbf{r})$). They read

Figure 2.5: Proximity effect at S/N interface

$$\begin{pmatrix} H_0 & \Delta(x) \\ \Delta(x) & -H_0^* \end{pmatrix} \begin{pmatrix} u(x) \\ v(x) \end{pmatrix} = \epsilon \begin{pmatrix} u(x) \\ v(x) \end{pmatrix} \tag{2.6}$$

H_0 is the one-electron-Hamiltonian, $\Delta(x)$ is the so-called pair potential, providing the coupling between electron- and hole-wave function $u(x), v(x)$. For $\Delta(x) = 0$, the equation decouple and describe electrons and holes in a normal metal. If $\Delta(x) \neq 0$, the equations allow to describe electron-hole excitations at sub-gap energies around the S/N interface.

Within this theory, the induced superconductivity is described by a superconducting pair amplitude $F(x) = \langle \Psi_\uparrow(x)\Psi_\downarrow^*(x)\rangle$, which is related to the Ginzburg-Landau order parameter. This pair amplitude decays exponentially as $\Delta(x,\epsilon) \propto \exp(-kx)$ with $k = \sqrt{\epsilon/\hbar D}$, where x indicates the spatial distance to the superconductor. Thus, the pair amplitude is zero and d.c. Josephson current vanishes, if $x >> L_\epsilon$ (coherence is lost, hence no supercurrent can flow). The proximity induced superconductivity also strongly depends on the interface quality of the S/N contact.

Of course, also the superconducting properties are changed in proximity of the normal metal N. Over a length $\xi_S = \sqrt{\hbar D_s/\Delta}$, the pair potential gets suppressed at superconductor-side near the interface, which is known as *inverse proximity effect*. In a quasi-classical approximation [40], the consequent suppression of the pair amplitude on S-side can be

given by γ, whereas γ_B quantifies the jump in the pair amplitude directly at the interface

$$\gamma = \frac{\rho_s \xi_s}{\rho_n \xi_n} \tag{2.7}$$

$$\gamma_B = \frac{R_i}{\rho_n \xi_n} \tag{2.8}$$

R_i is the interface resistance, $\rho_{s,n}$ are the normal state resistivity of N and S [9, 40, 41]. An overview of the important length scales and their corresponding energies is given in Fig. 2.6.
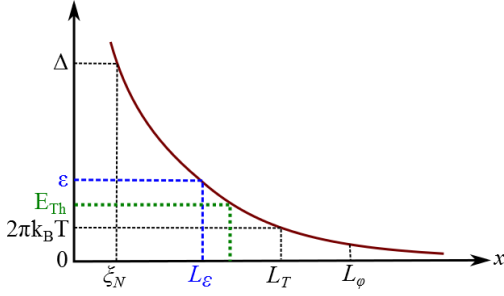
Figure 2.6: Energy-length scale relation: The coherence length $L\epsilon$ of an Andreev-pair is situated between the two limits, given by ξ_n and L_Φ; L_T gives the thermal length for propagating pairs at finite temperature, when $\epsilon = 2\pi k_B T$ (reproduced from [42]).

2.1.2 Interface

Up to now, we discussed electronic transport through an S/N boundary with the assumption of an ideal interface. This means, that each incoming electron with $\epsilon < \Delta$ from the normal-metal-side performs an Andreev reflection. This is a highly simplified model. In reality, Andreev reflection does not provide the only possible process at the S/N interface for incoming quasi-particles. A real junction, always has a finite barrier strength. Depending on interface transparency and energy of the quasi-particle, other mechanisms come into play, such as specular reflection of the incoming electron. This makes electronic transport in hybrid nanostructures rather complex. However, in 1982, Blonder, Tinkham and Klapwijk (BTK) presented a complete, though simplified model (ballistic, single-channel, T=0) which describes the transport through a S/N interface of arbitrary barrier strength Z [43].

Within this model, the barrier is expressed as a repulsive potential, $U\delta(x)$, which enters as parameter $Z = U/\hbar v_F$. The barrier transparency can be also expressed in more convenient units as $T = 1/(1 + Z^2)$. Hence, $Z = 0$ can be associated with a perfectly transparent, barrier-less interface, whereas $Z >> 1$ corresponds to the tunnel limit. According to the BTK-model, an incoming electron from normal-metal side can undergo four processes at the S/N interface [44]:

A. Andreev reflection: retro-reflection of incoming electron as a hole, associated with a probability $A(\epsilon, Z)$

B. specular reflection: reflection of incoming electron as an electron, with a probability $B(\epsilon, Z)$

C. transmission (I): transfer of an electron through the barrier as electron-like quasi-particle, with a probability $C(\epsilon, Z)$

D. transmission, including branch-crossing (II): transfer of an electron into the super-
conductor as a hole-like quasi-particle, with a probability $D(\epsilon, Z)$

The probabilities result of calculations using Bogoliubov-de Gennes equations for a
given barrier strength. Due to probability conservation, $A + B + C + D = 1$. As can
be deduced from Fig. 2.7, reproduced from [43, 45], the contribution of each of these
processes drastically change with the energy of the incident quasi-particle. In general,
one can show that the total current through the structure can be written as

$$I_{NS} = I_{NN} \int\limits_{-\infty}^{\infty} [1 + A(\epsilon, Z) - B(\epsilon, Z)][f(\epsilon - eV) - f(E)]d\epsilon. \qquad (2.9)$$

Naturally, the contribution of ordinary reflection (B) and transmission (C) dominates
at high energies ($\epsilon > \Delta$). With increasing transparency ($Z << 1$), transmission ex-
ceeds the contribution due to specular reflection. However, if the quasi-particle energy is
low ($\epsilon < \Delta$), no quasi-particle transmission is possible, hence $C = D = 0$ and depend-
ing the barrier strength, Andreev reflection (A) or specular reflection (B) represent the
dominating process, with $A + B = 1$.

Andreev reflection (A) dominates especially for large barrier transparencies. For per-
fect transparency (Z=0), below the gap Δ, the conductance was found to be twice the
normal state conductance and represents even the only possible process - this results from
the double charge transfer during each Andreev reflection and has been confirmed for
instance by noise measurements [46, 47]. Branch-crossing transmission (D) however just
gives a significant contribution near the superconducting gap Δ.
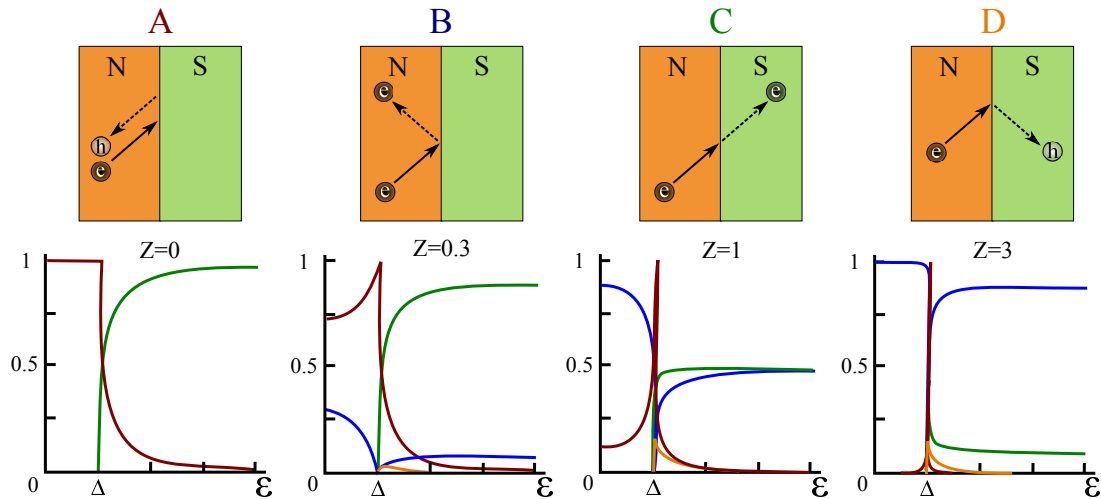
Figure 2.7: Schemes representing the four elementary processes which are taken into
account in the BTK-model. Each of them is associated with a probability which depends
on the barrier strength parameter Z [43, 48].

Even if this model is restricted to 1D case, it nevertheless allows quite accurate results
for both limits - metallic (no-barrier) junctions and tunnel junctions. Furthermore, it even
offers an explanation for the sub-gap structure, observed in weak-links [49, 50]. Different

authors afterwards improved the BTK-model. For instance, Son et al. included the gap-reduction of the superconductor near the interface due to inverse proximity effect [51] or Mortensen et al. extended the model to multi-dimensional case [52].

Chapter 3

Josephson junctions

In 1962, B. D. Josephson[1] predicted a supercurrent between two superconducting reservoirs, only separated by an insulating layer, at zero applied voltage [53]

$$I_s = I_c \sin(\Phi) \tag{3.1}$$

In this context, Φ expresses the phase difference of the Ginzburg-Landau wave functions in the superconducting electrodes [54] and I_c is the critical current of the junction. Furthermore, he predicted a simple relation between phase ϕ and applied voltage across the junction

$$\frac{d\Phi}{dt} = \frac{2eV}{\hbar} \tag{3.2}$$

Few years later, [3,4] the so-called stationary or **dc-Josephson effect** (eq. 3.1) as well as the **ac-Josephson effect**[2] (eq. 3.2) have been confirmed experimentally [5–7]. Ever since, a continuous interest persists in fundamental and industrial research into these phenomena due to their complexity as well as promising perspectives for application [9]. Further studies have shown [8], that Josephson effects can be observed generally in all structures, where two superconductors are connected by a "weak link" (tunnel barrier, normal metal, semiconductor, geometrical constriction etc.).

In a first step, we will show an intuitive deviation of the Josephson effects in the (ideal) case of a tunnel barrier Josephson junction, just starting from fundamental Schroedinger equations. Then we will continue with a more detailed discussion of phenomena arising in diffusive Josephson junctions in stationary and dynamic regime.

---

1. The work of B. D. Josephson was awarded with the Nobel prize in 1973
2. non-stationary

3.1 Josephson junctions with an insulating barrier
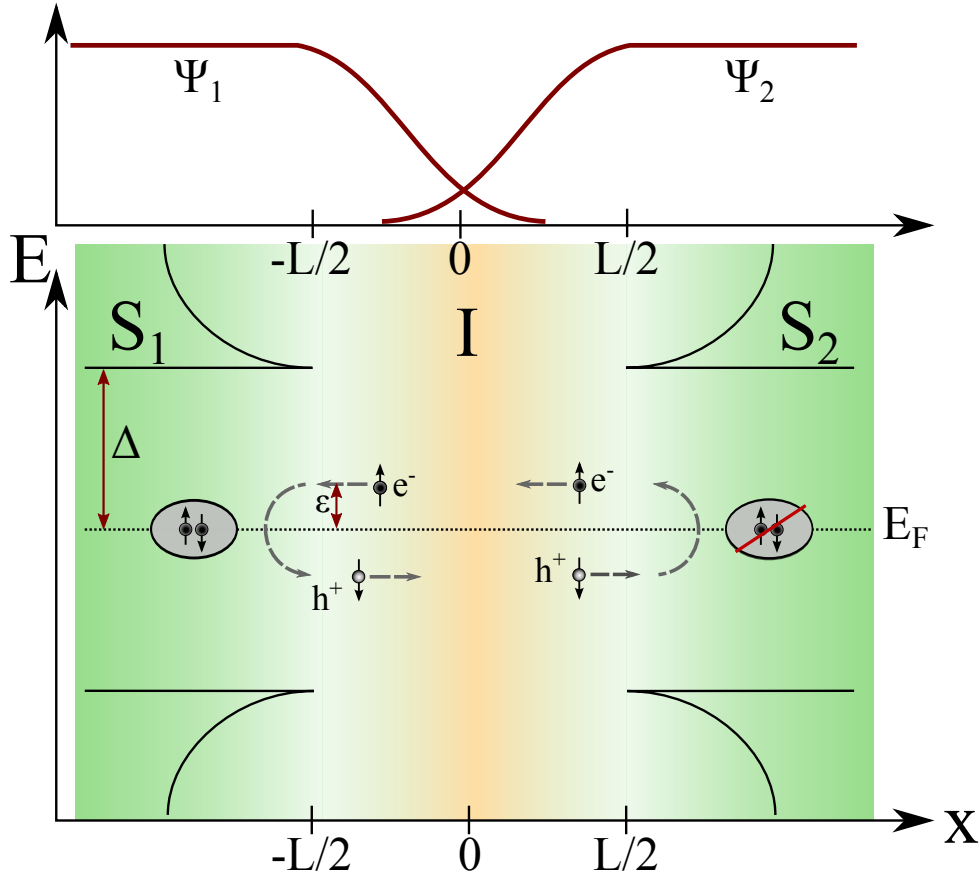
Figure 3.1: Josephson junction: inside the barrier, the wave function of each superconductor decays exponentially (upper sketch); if the superconducting reservoirs are close enough, their pair amplitudes can superpose in the isolating layer and enable supercurrent through the tunnel barrier (see sketch below)

The beauty of the Josephson effect is twofold. First, it provides rich phenomena as consequences of quantum physics in macroscopic scale. Second, it can be directly derived from the basic Schroedinger equations, one of the most fundamental relations of quantum mechanics [55, 56]. Let us consider two superconductors, which are close to each other. Each of them can be described by a macroscopic wave function

$$\Psi_1 = \sqrt{n_1} \exp\left(i\,\Phi_1\right), \Psi_2 = \sqrt{n_2} \exp\left(i\,\Phi_2\right) \tag{3.3}$$

In this context, $\Phi_{1,2}$ describes the macroscopic phase of the respective superconducting electrode, $n_{1,2}$ the superconducting carrier density in superconductor 1 or 2. If the two superconductors are close enough to each other, separated by a tiny insulating barrier, their wave functions can overlap and the total system energy is reduced due to this (weak) coupling. When the coupling exceeds the thermal excitation, the macroscopic phase will lock and a supercurrent can flow. Then, the time evolution of each superconducting wave

function can be described by

$$i\hbar\frac{\partial\Psi_1}{\partial t} = U_1\Psi_1 + K\Psi_2 \tag{3.4}$$

$$i\hbar\frac{\partial\Psi_2}{\partial t} = U_2\Psi_2 + K\Psi_1 \tag{3.5}$$

where U_1, U_2 describes the chemical potential of each reservoir and K stands for the coupling constant between the two reservoirs. For some applied voltage V across the junction, we define $U_1 = qV/2$, $U_2 = -qV/2$, q being the charge carrier [3]. Now, we can solve the equations using the wave functions above, just by separating imaginary and real contributions. From real part, we get the dc Josephson effect

$$J_s(\Phi) = J_c\sin(\Phi) \tag{3.6}$$

where $\Phi = \Phi_2 - \Phi_1$ expresses the phase difference of the Ginzburg-Landau wave functions in the superconducting electrodes, J_c is the critical current density [4] and J_s the circulating supercurrent density with respect to the applied phase difference. From the imaginary part, we get the ac-Josephson effect

$$\dot{\Phi} = \frac{qV}{\hbar} \tag{3.7}$$

Since the charge transport in a superconductor is provided by Cooper pairs, as already explained in 2.1, we can set $q = 2e$. Finally, we can introduce the so-called Josephson energy, which is an indicator for the coupling strength of the system. This coupling of the Ginzburg-Landau wave functions reduces the energy of the total system by a maximal amount of

$$E_J = \frac{I_c\Phi_0}{2\pi} \tag{3.8}$$

3.2 DC Josephson effect - stationary regime

In order to understand the physics of diffusive Josephson junctions, it is helpful to return to the perspective of Andreev reflection. For the moment, we restrict our description to the ballistic limit ($L < l_e$) in 1D case, since it is easier to describe but we consider hybrid systems when a non-superconducting material of length L is connected to two superconducting reservoirs.

In section 2.1, we have seen that the process of Andreev reflection (see Eq.2.1) together with the propagation in the normal metal (see Eq. 2.3), leads to de-phasing between electron and hole of the Andreev-pair. Supposing now an incident electron at S_1, with energy $0 < \epsilon < \Delta$, $k_{e1} = k_F - \delta k_1$ (see Fig. 3.1). An Andreev-reflection leads to the creation of a Cooper-pair in S_1 and a hole $k_{h1} = k_F - \delta k_1$. This hole can propagate to S_2,

---

3. For simplicity, we assume $-\dot{n_1} = \dot{n_2} = \dot{n_s}$, and $n_1 = n_2 = n_s$
4. In this description, the critical current density depends on the coupling parameter K: $J_c = 4eKn_s/\hbar$

performing another Andreev reflection at S_2. Hence, an electron $k_{e2} = k_F - \delta k_2$ is created, accompanied by the absorption of a Cooper-pair in S_2. From a macroscopic point of view, this process has transferred a Cooper-pair from S_1 to S_2 (see Fig. 3.5). If now the total phase accumulated during the total process is an integer multiple of 2π, two resonant standing waves can establish, which form the so-called "Andreev Bound states" (ABS). These ABS are symmetric with respect to the Fermi-surface and carry the supercurrent through the junction.

More generally, an Andreev Bound state can be formed between two superconducting electrodes at any energy $\epsilon_n < \Delta$, if the following condition is fulfilled:

$$\Delta\Phi = \frac{2\epsilon_n L}{\hbar v_F} \pm \Phi + 2\arccos\frac{\epsilon}{\Delta} = 2\pi n \qquad (3.9)$$

where n is an integer. In the limit $E_{Th} < \Delta$, two successive levels are separated by πE_{Th}. For $\Phi = 0$ and perfect transmission, the ABS are energetically degenerated, hence no current is flowing[5]. For $\Phi \neq 0$, the degeneracy is lifted and the ABS are populated according to the thermal distribution function (lower levels are more occupied than higher ones), leading to effective non-zero supercurrent [58]. The spectrum of ABS in the ballistic limit, as presented above, is a sequence of δ-peaks [59]. For long, diffusive Josephson junctions ($L >> l_e$), the level-spacing of ABS is so small, that - combined with the smearing of the energy-distribution function - the Andreev Bound states form a continuum (see Fig. 3.2).
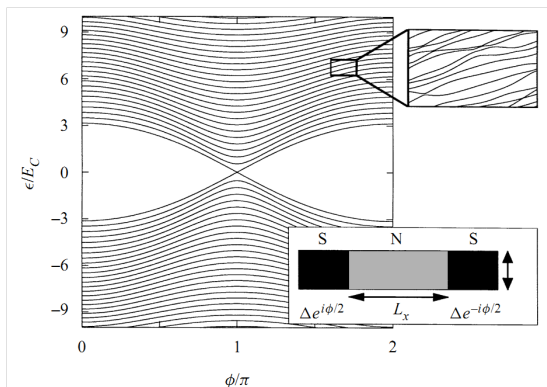
Figure 3.2: Simulation of ABS in a diffusive JJ [60]
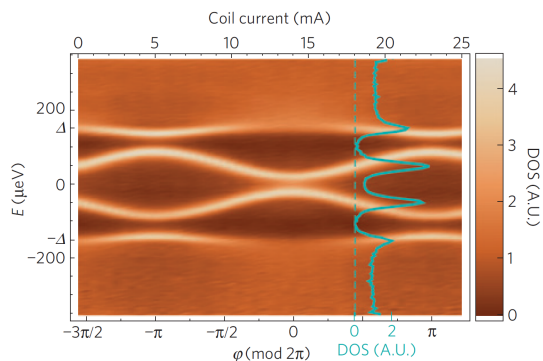
Figure 3.3: Exp. observation of ABS in a CNT-device [61]

Experimentally, the dc Josephson effect has been first revealed by measuring a zero-resistance state up to a critical current I_c [3]. Furthermore, a Josephson junction is sensitive to the number of quantum flux units penetrating its junction area which allows another experimental technique to identify a Josephson junction. The phase-dependence of the critical current (see eq. 3.1) gives rise to a characteristic Fraunhofer-like pattern [4](see for instance Fig. 3.4) for the critical current as a function of applied magnetic field. Recent experiments confirmed the existence of Andreev Bound states in Quantum point contacts [62], Carbon-Nanotube-based devices [61,63] or quantum dots [64], see Fig. 3.3.

---

5. For any ABS carrying current in one direction, there exists another degenerate state carrying current in opposite direction, which cancel each other, giving no net supercurrent [42,57]
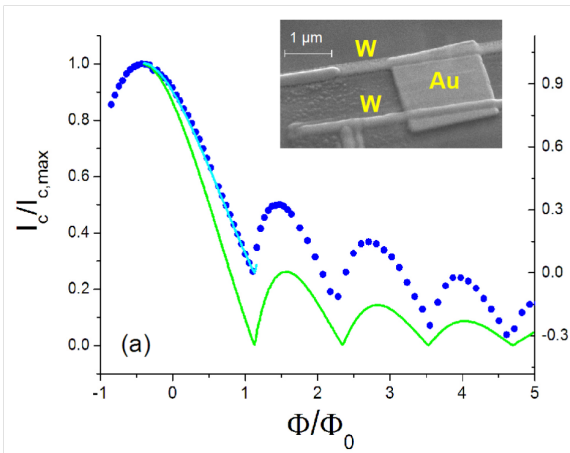
Figure 3.4: Fraunhofer-like pattern, observed in a diffusive SNS-Josephson junction; the green fit follows from the solution of the Usadel-equations [65]
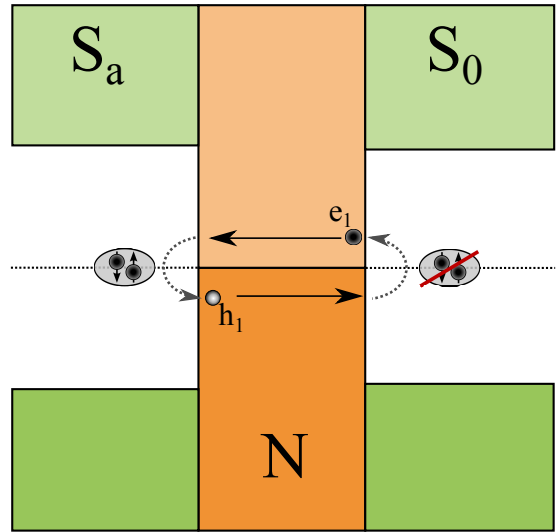
Figure 3.5: Sketch of an Andreev Bound state at zero-voltage

3.3 Dynamic regime

If the current through a Josephson junction exceeds its critical current I_c, the system enters in the so-called dynamic or non-equilibrium regime.

3.3.1 ac Josephson effect

If one considers a constant voltage V, the phase difference changes linearly with time according to equation 3.2. The superconducting current is now oscillating in time (eq. 3.1) and in addition, a normal contribution I_n to the total current develops. The total current through the junction is then

$$I = I_c \sin(\omega_J t + \Phi) + I_n \tag{3.10}$$

with $\omega_J = 2eV/\hbar$ and $< I_n > = \frac{V}{R_n}$, where R_n is the normal state resistance. Hence, the junction generates an ac-current at Josephson-frequency f_J which depends on the applied voltage and is given by

$$\frac{f_J}{V} = \frac{2e}{h} \approx 484\,MHz/\mu V \tag{3.11}$$

The ac-Josephson effect was first directly observed by Yanson et al. [7] by studying the coupling between a Josephson junction and a wave guide (for more details, see for instance [66–68]). They observe a resonance peak in the microwave spectrum, when the emitted ac-signal matches the resonance frequency of their resonator. A more convenient approach was first performed by Shapiro [5,69]: in these experiments, in addition to the dc voltage bias V an external microwave $A\cos(\omega_{rf}t)$ is applied to the Josephson junction[6]. In this

---

6. A: amplitude of the external microwave; $\omega_{rf}/2\pi$: applied microwave frequency

case, visible resonances between the ac-Josephson current and the external microwave appear in the IV-characteristics for well-defined values of voltage (see Fig. 3.6):

$$V = p \frac{\hbar \omega_{rf}}{2e} \tag{3.12}$$

where p is an integer. These resonances are known as "Shapiro-resonances" and are established as a standard technique, in order to prove the existence of an ac Josephson-effect in new materials or geometries [70–72]. When the Current-Phase relation of the Josephson junction is not perfectly sinusoidal, additional resonances occur at

$$qV = p \frac{\hbar \omega_{rf}}{2e} \tag{3.13}$$

leading to non-integer resonances.
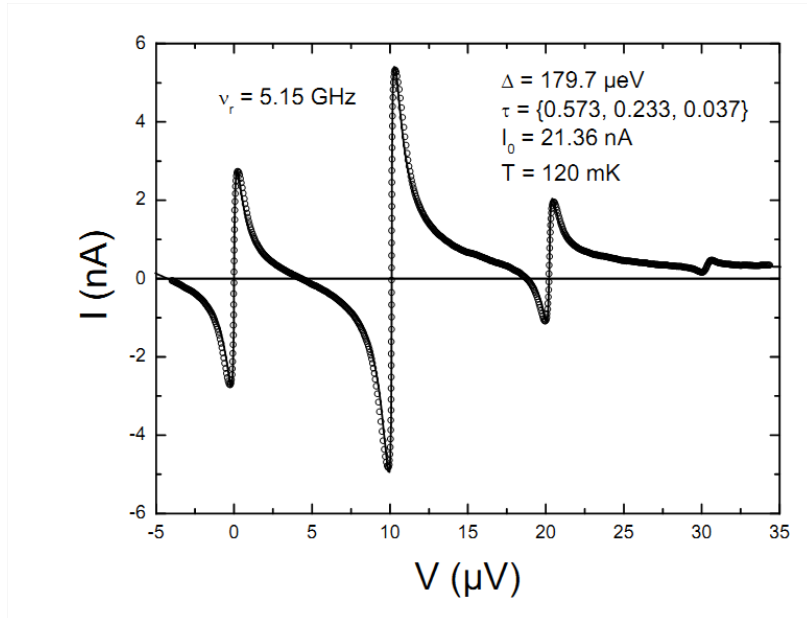
Figure 3.6: Shapiro-resonances, observed by Chauvin et al. in a Quantum Point contact at $T = 20\,mK$ with microwave frequency of $\omega_r = 5.125\,GHz$ [73]

3.3.2 Multiple Andreev Reflections

The sub-gap current in SNS junctions can be described in terms of Andreev reflection. If a voltage is applied across the junction, a quasi-particle gains energy, each time it propagates through the normal part. Supposing a Voltage $V = 2\Delta/3e$ between the two superconductors S_0 and S_a (see Fig. 3.7a).

Let us consider a situation where a voltage $V = 2\Delta/3$ is applied across a two-terminal Josephson-junction. Then an electron e_1 with energy $\epsilon = |-\Delta|$, which passes from the valence band of S_0 into the normal part N, gets accelerated by the applied voltage towards the superconductor S_a. There, it performs an Andreev reflection, creating a hole h_1 with an energy $\epsilon = |-\Delta + eV|$ which travels toward S_0. There, it performs another Andreev reflection which gives rise of en electron e_2 with an energy $\epsilon = |-\Delta + 2\,eV|$ propagating toward S_a. A further Andreev reflection creates the hole h_2 with energy $|-\Delta + 3\,eV|$, traveling back toward S_0. A final Andreev reflection transforms the hole into an electron

e_3 which has finally an energy $\epsilon = |-\Delta + 4\,eV| = \Delta$ and can escape into available states in superconductor S_a. During the whole process, one quasi-particle and 2 Cooper-pairs have been transferred.

If we reduce now slightly the applied voltage $V < 2\Delta/3e$, we can imagine that the electron e_3 which could just reach the conduction band of S_a in the previous situation will no longer be able to pass. Then, a further cycle of Andreev reflection is necessary and *an additional Cooper-pair* is transferred during the whole process. These variations in the number of transferred Cooper-pairs give rise to a step in the current.

More generally, during this process, one quasi-particle and n Cooper-pairs are transferred, where n indicates the number of performed Andreev reflections. These **M**ultiple **A**ndreev **R**eflections (MAR) lead to features in the IV-characteristics, each time the applied voltage is an integer fraction of twice the gap, see Fig. 3.7a.

$$V = \frac{2\Delta}{ne} \tag{3.14}$$

where n is an integer. MARs have been observed in various devices, whose length $L < L_\epsilon$. First studied in micro-bridges [74], tunnel junctions, and QPCs [75], the MAR induced sub-harmonic gap structure has been also proven in diffusive S-Sc-S [76, 77] and S-N-S junctions [78].

(a) MAR-process for $eV = \frac{2\Delta}{3}$ (b) MAR-process for $eV = \frac{2\Delta}{3} - \epsilon$
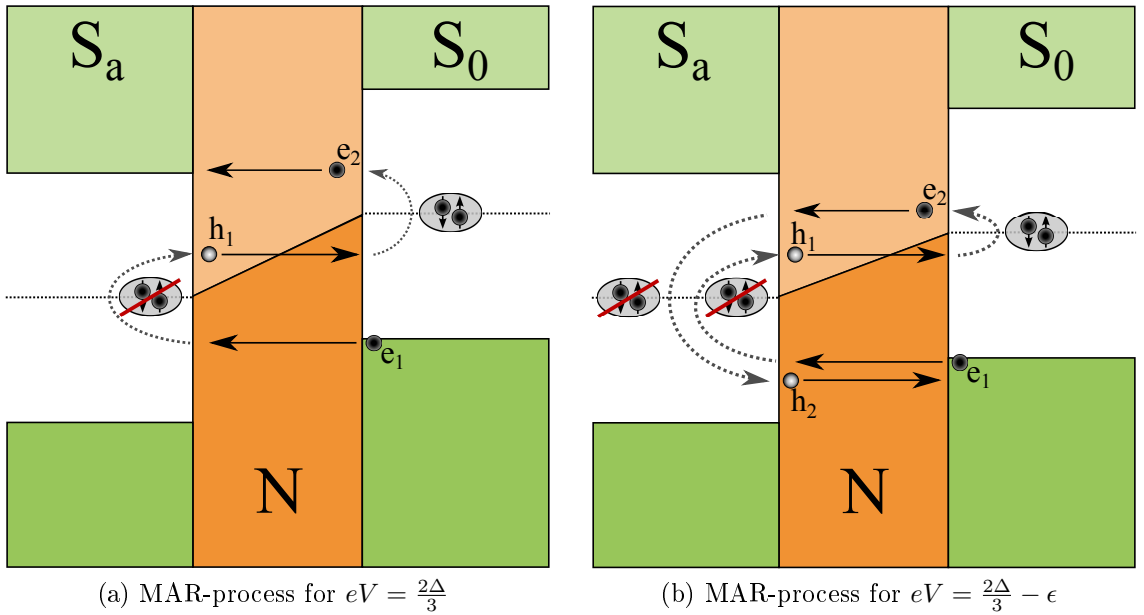
Figure 3.7: Illustration of the Multiple Andreev reflection process: Each time the applied voltage is an integer fraction of twice the gap, the number of transferred particle during one process changes, giving rise to a feature in the conductance through the Josephson junction.

3.4 Special Characteristics of diffusive Josephson junctions

In previous sections about the Josephson effect, we explained the underlying mechanism of Josephson junctions in the most simple case of ballistic junctions. From now, we will focus on long, diffusive Josephson junctions with highly transparent contacts. In these devices, physics gets much more complicated for several reasons:

- **Barrier**: the high transparent barriers lead to a strong impact of (inverse) proximity effect. This means, that also at energies below the superconducting gap ($\epsilon < \Delta$), quasi-particle current through the junction is possible.
- **Coherence**: in diffusive junctions, as already mentioned in section 2.1, coherence is a limiting factor, which has important consequences in the dynamic regime

In the following, we would like to give a short overview about the results and actual knowledge, concerning diffusive Josephson junctions.

3.4.1 dc Josephson effect - Critical current

The current-phase relation (CPR) of diffusive Josephson junctions can show strong deviations of the ideal dc-Josephson effect, as already mentioned in section 3.2 [42,58,79] [7]. In a general form, the CPR can be expressed as

$$I_s = \sum_n I_n \sin(n\chi) + J_n \cos(n\chi) \qquad \textbf{with} \quad n \in \mathbb{N} \tag{3.15}$$

The coefficients J_n vanish if the time reversal symmetry is maintained. A review about possible CPR and their origin in different Josephson junctions is given in [9].

There has been a lot of effort to find a valid formula to describe the temperature dependence of the critical current of diffusive Josephson junctions. Up to now, there exists no formula describing the whole temperature range precisely. In previous work, two formula have been used extensively, respectively for the low-temperature and high temperature limits. For the low temperature limit ($k_B T < 2.5 E_{Th}$), the critical current $I_c(T)$ is given by

$$\frac{e R_n I_c(T)}{E_{Th}} = b \left[1 - 1.3 \exp(-b E_{Th}/(3.2 k_B T))\right] \tag{3.16}$$

where the variable $b = e R_n I_c(T = 0)/E_{Th}$ depends on the ratio Δ/E_{Th}; for very long junctions, it converges toward 10.82. The critical current in diffusive Josephson junctions in high temperature regime ($k_B T > 5 E_{Th}$) usually fits well with the formula found by Wilhelm et al. [30,83]

$$I_c(T) = 64\pi k_B T \sum_n \sqrt{\frac{2\omega_n}{E_{Th}}} \frac{\Delta^2 \exp(-\sqrt{2\omega_n}/E_{Th})}{[\omega_n + \Omega_n + \sqrt{2(\Omega_0^2 + \Omega_n \omega_n)}]^2} \frac{1}{e R_n} \tag{3.17}$$

where $\Omega_n = \sqrt{\Delta^2 + \omega_n^2}$, with ω_n being the Matsubara frequency.

---

7. Up to now, there is an ongoing discussion, if the non-sinusoidal CPR arises due to external perturbations [79] or is a characteristic property of a diffusive Josephson junction [80–82]

3.4.2 Dynamic regime

The dynamic range of diffusive Josephson junctions, is composed of a coherent and an incoherent part. At very low temperature, the coherence length L_ϵ of an Andreev pair is limited by $L_V = \sqrt{\frac{\hbar D}{eV}}$.

3.4.2.1 Coherent dynamic regime: ac-Josephson effect

If the applied voltage is below the Thouless energy, $eV < E_{Th}$, phase coherence is preserved between successive Andreev reflections, and hence, ac-Josephson effect can be observed. This range is called coherent regime.

If the applied voltage V exceeds the Thouless energy, $eV >> E_{Th}$ the phase coherence between successive Andreev reflections is lost and as a consequence, the ac-Josephson effect vanishes. However, the decrease of the ac-Josephson effect is found to be quite smooth. Shapiro-steps, which are a signature for the presence of ac-Josephson effect, have been observed in previous work up to the mini-gap at $E_g = 3.12E_{Th}$ (see for instance [30,80]. More recent experiments by Chiodi et al. [65,84], even report (integer) Shapiro-steps up to $\omega_{rf} = 2E_g$ (see Fig. 3.8). Unfortunately, just qualitative studies to the appearance of Shapiro-steps have been reported for diffusive Josephson junctions. To our knowledge, detailed studies of the decreasing of the ac-Josephson current amplitude with increasing applied voltage have not been reported yet.

In practice, the power of the rf-source is ramped such that Shapiro-steps appear, but the actual rf-current, flowing through the junction is unknown. As the amplitude of the steps depends on the ratio between this rf-current and the ac-Josephson current (see section 3.5, eq. 3.28), it is difficult to extract the true amplitude of this ac-Josephson current.

(a) Shapiro-resonances, measured in a diffusive SNS junction by Chiodi [65]

(b) Observed Shapiro-resonances as a function of applied voltage eV, reproduced from [65]
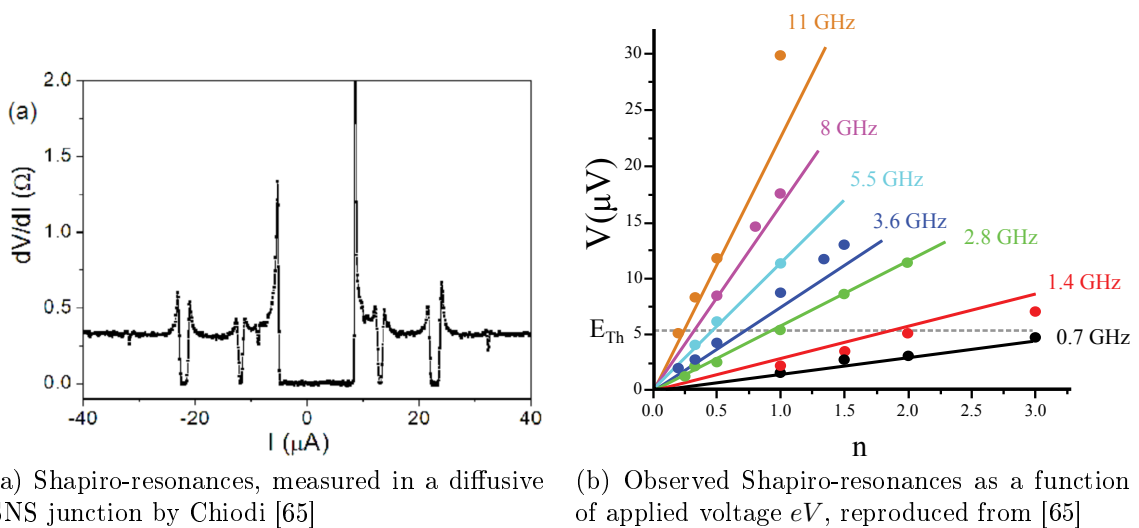
Figure 3.8: Shapiro-resonances in a diffusive SNS-junction

3.4.2.2   Incoherent dynamic regime

Independently of the Thouless energy E_{Th}, for $eV < \Delta$, successive Multiple Andreev reflections are the mechanism which is responsible for the sub-gap conductance. It gives rise to a Subharmonic Gap structure (SGS) for $eV < 2\Delta/n$, where n is an integer. In diffusive Josephson junctions however, they can usually only be observed up to $n = 4$. The reason for this can be found in the necessary time scale in order to perform MARs with $n > 4$. For a MAR-cycle, ending with a quasi-particle, which escapes into available states above the superconducting gap, a total time $\tau_{total} = N_{AR}\tau_D \leq \tau_{in}$ is needed, where N_{AR} is the number of performed Andreev reflections.
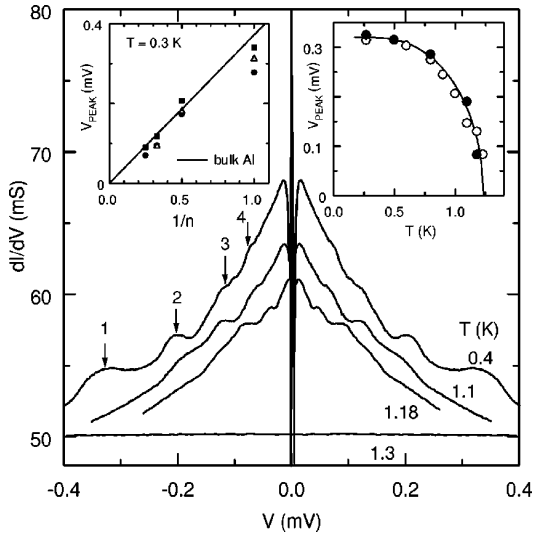
Figure 3.9: MAR-structure in the differential Conductance of a diffusive SNS-junction [78]. Features occur in the conductance, each time the applied voltage is an integer fraction of twice the gap.

If the total time for the MAR-cycle τ exceeds the inelastic scattering time τ_{in}, $\tau_{total} \gg \tau_{in}$, we get incomplete or interrupted MAR. Then, since the process does not end up above the gap, no appropriate feature in the SGS can be found. The experimental limit to observe SGS can be determined by $\tau_{total} \approx \tau_{in}$, which gives in the diffusive limit about $N_{AR} = 4$ (see Fig. 3.9).

3.4.2.3   Role of inelastic interaction

The transition from the coherent into the incoherent regime manifests itself when one studies the spectral noise density as a function of polarization voltage V. This transition gives rise to a pronounced dip in the noise density, situated at the Thouless energy E_{Th} (see Fig. 3.10a).

In the incoherent regime, when the total time of a process $N_{AR}\tau_D$ exceeds the inelastic scattering time τ_{in}, successive multiple Andreev reflections are in general interrupted

(a) The presented data have been obtained by Hoffmann et al. [34, 85], in a two-terminal SNS-device with a length $L = 0.85 \, \mu m$, giving a Thouless energy $E_{Th} \approx 10 \, \mu eV$.

(b) Schematic of the thermal model of the device; reproduced from [86]
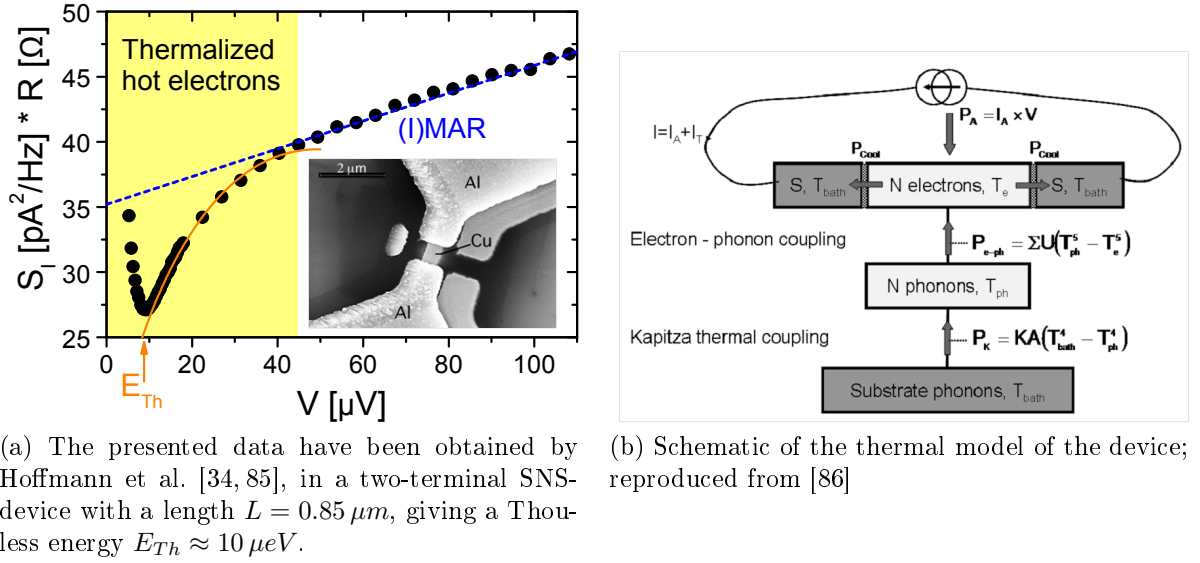
Figure 3.10

before a quasi-particle can escape the superconducting gap Δ.

If one considers that inelastic processes are dominated by electron-electron interaction, the electrons can exchange energy, leading to an effective temperature T_e. Since the effective quasi-particle temperature T_e exceeds the base temperature, this regime is called the "hot electron regime". The electronic temperature T_e is determined as the equilibrium between the injected power in the resistive normal part R_e and its dissipation. For the dissipation, several mechanism exist: first, electron-phonon interaction is a possible cooling mechanism. Dissipated heat into the phonons of the metal part can be evacuated by a cooling chain, passing through the substrate onto the sample-holder (for a schematic sketch of the cooling cycle, see Fig. 3.10b). The second possibility is interaction with quasiparticles of higher energy, which evacuate some heat by passing through the S/N interface. Of course, this process is quite improbable for low energies.

The cross-over from IMAR, with incomplete MAR, to the hot electron regime explains the disappearance of the sub gap anomalies in the IV-characteristics and shows up in the shot noise of a diffusive SNS junction (Fig. 3.10a).

3.5 R(C)SJ model

The Resistively and Capacitively Shunted Junction (RCSJ) model represents the simplest model for the description of static and dynamic properties of Josephson Junctions. Within this model, the real Josephson junction is modeled by three circuit elements in parallel: a shunt capacitance C, an ohmic resistance R_N and a pure (ideal) Josephson junction (see Fig. 3.11a). The capacitance takes into account the geometrical capacitance of the two superconducting electrodes that form the weak link. It is especially important in SIS junctions where two parallel superconducting electrodes are separated by a thin insulating barrier. In diffusive SNS-junctions, as studied in this PhD thesis, this capacitance is small and the RCSJ model reduces to the RSJ model. For that reason, we will detail here only the RSJ-model without any capacitance implied. The Josephson

junction can then be described by its energy $E(\phi) = -E_J \cos \phi$, where E_J is the Josephson energy $E_J = \hbar I_c / 2e$, ϕ describes the phase difference between the two superconductors. Within this model, the total current writes

$$I = I_s + I_n = I_c \sin(\Phi) + \frac{V}{R_n}. \tag{3.18}$$

We also recall the voltage-phase-relationship, given by

$$\dot{\Phi} = \frac{2eV}{\hbar}. \tag{3.19}$$

If zero voltage is applied ($V = 0$), following eq. 3.19, we get $\dot{\Phi} = 0$. This means that the phase Φ is a constant, and eq. 3.18 reduces to

$$I = I_s + I_n = I_c \sin(\Phi).$$

If there is a finite voltage across the junction, $V \neq 0$, the phase Φ is time-dependent. In voltage-bias configuration, meaning that $V = constant = V_0$, the phase Φ between the two superconducting electrodes drifts linearly and can be written as

$$\Phi = \frac{2eV_0 t}{\hbar} + \Phi(t = 0). \tag{3.20}$$

The total current then can be written as

$$I = I_c \sin \left(\frac{2eV_0 t}{\hbar} + \Phi(t = 0) \right) + \frac{V}{R_n} \tag{3.21}$$

The ac-component of the current is known as ac-Josephson current. The mean current however is simply $< I > = V_0 / R_n$. Hence, the IV-characteristic is linear as depicted in Fig. 3.11b (black dotted line).

In the case of current bias ($I = constant$), we get

$$\frac{\hbar}{2eR_n} \frac{d\phi}{dt} = I - I_c \sin \phi. \tag{3.22}$$

In this case, the voltage evolution in time gives (for $T = 0$)

$$< V > = R_n \sqrt{I^2 - I_c^2} \tag{3.23}$$

In this model, no hysteresis occurs, meaning that the transition of the Josephson junction from the normal in the zero-resistance state (re-trapping current I_r) is equal to the critical current I_c, where the junction switches from the zero-resistance state into the normal state, $I_c = I_r$. The transition of the zero-resistance state gives a characteristic feature in the differential resistance, depicted in Fig. 3.11b.

A typical IV-characteristics of a Josephson junction is presented in Fig. 3.11b. By taking into account the effect of temperature, the transition at the critical current gets rounded.

In a second step, we want now to illustrate the appearance of Shapiro-steps within the RSJ-model in the voltage-bias configuration. The microwave excitation with amplitude ν can be considered as an oscillating contribution to the voltage V. This gives
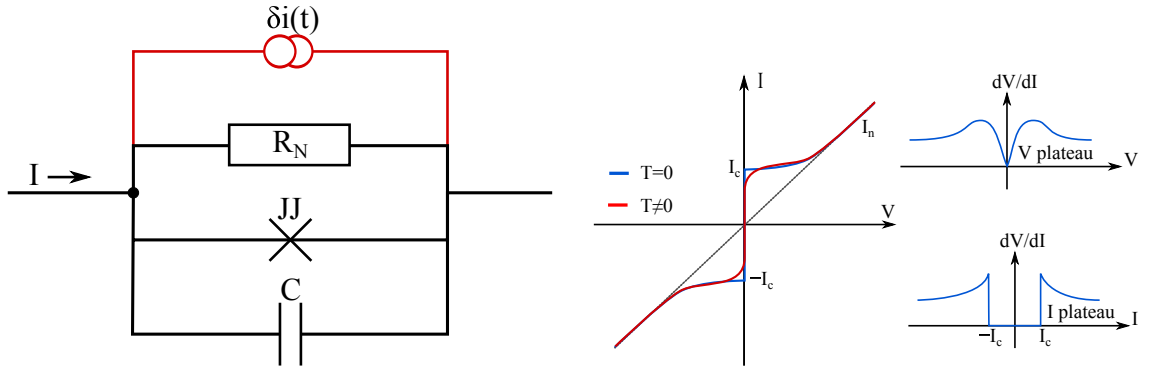
(a) Sketch of the RCSJ-model; the real Josephson junction is modeled as a Resistance, a Capacitor and a pure Josephson junction, which only carries the supercurrent through the junction

(b) Typical IV-characteristic for a Josephson contact; below the critical current I_c, the junction is in a zero-resistance state (dc Josephson effect). At I_c, a transition into normal state takes place, which is rounded for $T \neq 0$ (blue graph); The characteristic response at current- and voltage-bias in the differential resistance for the transition of the Josephson contact is given aside.

Figure 3.11: Illustration of the RCSJ-model

$$V = V_0 + \nu \sin(\omega_{rf}t) \tag{3.24}$$

The time-dependent phase-evolution then gives

$$\Phi = \Phi_0 + \frac{2eV_0t}{\hbar} - \frac{2e\nu}{\hbar\omega_{rf}}\cos\omega_{rf}t. \tag{3.25}$$

The total current through the junction then writes

$$I = I_c \sin\left[\frac{2eV_0}{\hbar}t - \frac{2e\nu}{\hbar\omega_{rf}}\cos((\omega_{rf}t) + \Phi(t=0))\right] + \frac{V_0}{R_n} \tag{3.26}$$

where $\frac{2eV_0}{\hbar} = \omega_J$ is the ac-Josephson frequency at the applied Voltage V_0. Now, the current-phase relation does no longer drifts linear in time. When the ac-Josephson-current with frequency ω_J is in resonance with the applied microwave frequency ω_{rf}, resonances can develop, which lead to additional dc-current. They get visible, for instance as steps in the IV-characteristic and are called Shapiro-steps. The condition for Shapiro-steps is given by $p\omega_J = q\omega_{rf}$, where p, q are integers and occur for a voltage

$$V_0 = \frac{p}{q}\frac{\hbar\omega_{rf}}{2e} \tag{3.27}$$

The maximum amplitude of the nth Shapiro-step I_n is found to scale with the nth Bessel-function J_n [87]

$$|I_n(V_{rf})| = I_c\left|J_n\left(\frac{nV_{rf}}{V_n}\right)\right| \tag{3.28}$$

where I_c is the critical current of the junction, V_{rf} the applied microwave voltage and V_n is the applied voltage across the junction.

This work is about multi-terminal Josephson-junctions. In the frame of this work, an extended RSJ-model for multi-terminal devices has been developed in cooperation with Denis Feinberg and Régis Mélin of the Institut Néel Grenoble. This model will be explained in the experimental part of this work, see section 6.4.1.

Chapter 4

Multi-terminal weak-link junctions

Already since the late sixties, first experiments were performed using coupled Josephson junctions. Depending on device-geometry and performed experiments, different mechanism have been revealed both in experiment and theory, for instance phase-/voltage-locking (for more detailed review, please refer for instance to [10, 11]). Due to deeper understanding of the underlying physics and permanent progress in fabrication techniques, more and more sophisticated devices get available in our days, such as Josephson transistors [12] or so-called Josephson mixer, which allow signal amplification near the quantum limit [13, 14].

End of the 90's, theory predicted that after Andreev reflection, incident and the retro-reflected particle can be spatially separated by choosing an appropriate geometry [15, 16]. This process arises for instance in three-terminal structures, where two metallic contacts N_1 and N_2, situated within a distance of the superconducting coherence length ξ_s, are connected to a superconductor S. In these kind of structures, there is a non-zero probability, that an incident electron from contact N_1 is retro-reflected as a hole into contact N_2 (see Fig. 4.1a)). This process, called Crossed Andreev reflection (CAR), once proven and sufficiently controlled, opens a lot of new perspectives for application and research, for instance:

- A controllable, efficient source of coherent electrons would allow key experiments of quantum physics in solid state physics, i.e. concerning the EPR-paradox
- Spintronics: controllable CAR-processes involving ferromagnetic contacts
- Quantum computing: error correction code

Within the last few years, CAR has been proven in various materials and geometries [17–22] and it turned out that even efficiencies of nearly 100 % can be achieved in appropriate device geometries [23].

Finally, recent theoretical predictions predict new transport mechanism for multi-terminal structures with all superconducting electrodes, which have not been reported yet experimentally, such as 3-terminal MAR [24] or the coherent transport in dynamic regime via quartet-modes [25, 26]. In this chapter, we will give a short overview about historical experiments with as well as recent theoretical predictions.

4.1 Multi-terminal structures - superconducting and normal electrodes

Devices with several normal electrodes, connected by a superconductor with lateral dimensions shorter than the superconducting coherence length ξ_s have given first experimental evidence for the process of Crossed Andreev Reflection (CAR). In this process, an incoming electron with spin $\uparrow$ (respectively electron with spin $\downarrow$) at lead N_1 is retro-reflected as a hole with spin $\downarrow$ (respectively hole with spin $\uparrow$) into a lead N_2 and creates a Cooper-pair in S (see Fig. 4.1a)). According to theoretical predictions, this process is equivalent to the spatial separation of entangled electrons of a Cooper pair. CAR is one of the key ingredients towards the realization of a source of EPR (Einstein-Podolsky-Rosen) pairs of quantum-entangled objects in solid state physics. Although generation of such EPR-pairs has been already realized in optics long time ago in various systems and experiments [88–91], analogous experiments in solid state-physics stay an un-reached ambitious goal up to now. Nevertheless, due to the promising perspectives, on ce realized, various research groups work on the realization of an electronic EPR-source: for instance, it is hoped, that solid-state quantum computers or other new technologies would benefit of such an available electronic EPR-source [92]. However, there is still a long way to go toward solid-state EPR-experiments: In a first step, the existence of CAR has to be proven. Furthermore, an appropriate control has to be found in order to favour the process of CAR and to isolate it from other occurring effects. This is the actual state of research, which is briefly presented below.
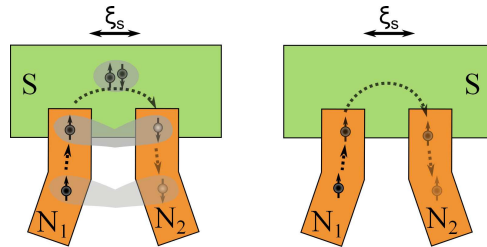
Figure 4.1: Illustration of CAR and EC-process in a device with two normal-metal contacts within a distance $L < \xi_s$ in contact to a superconductor. **left:** CAR or Non-local Andreev reflection involves an electron entering the superconductor through the normal contact N_1; by performing an Andreev reflection, a Cooper-pair is generated in the superconductor. The retro-reflected hole travels back in the second normal contact N_2. Electron and hole form an (virtual) Andreev-pair, which is coherent over a certain length (illustrated by the transparent cloud). This process is equivalent to a Cooper-pair, which splits its electron into the contacts N_1 and N_2. **right:** Elastic co-tunneling (EC), is a process in which an electron tunnels directly between metallic contacts N_1 and N_2 through an intermediate excited states above the gap in the superconductor. This process is in permanent competition with the CAR-process.

4.1.1 CAR vs EC

Unfortunately, CAR is not the only possible process in experiments involving one superconductor and two normal leads. Another process, called Elastic Co-tunneling (EC), is in permanent competition with Crossed Andreev-reflection (CAR). During this process, an incoming electron of lead N_1 with spin $\uparrow$ (with spin $\downarrow$) is reflected into lead N_2 via a virtual state in S (see Fig. 4.1b)). We insist on the fact, that for the EC-process the spin-orientation of the initial electron is maintained. According to standard BCS theory, CAR and EC cancel each other to lower order of tunneling rates in normal metal/insulator/superconductor (NIS) systems for low transparency T and bias [93,94]. Due to these two competing mechanism, first an appropriate experimental condition has to be found to favour CAR with respect to EC (for some realized experimental geometries, see Fig. 4.3). From theory-side, several possibilities have been proposed to lift this cancellation, such as higher transmissions [95], spin-active interfaces [96] and ferromagnetic contacts [97].

First evidence for CAR was performed by Beckmann et al. [17] in spin-valve structures consisting of several Ferromagnetic Fe-tunnel probes connected to a superconducting Aluminium (Al) wire (see Fig. 4.2). In their experiments, they inject a current I_A and measure non-local resistance between the Al wire and different Fe-probes. Due to the spin-orientations of the processes, as explained above, parallel magnetization alignment of the Fe-contacts are expected to favour the EC-process. On the contrary, anti-parallel magnetization of the Fe-contacts are expected to favour CAR-processes. Indeed, they observe a small difference ΔR, for parallel and anti-parallel configurations below T_c of the Al-wire. As expected for CAR- and EC-processes, the observed feature decays on a shorter length scale than the spin-valve signal which is observed, when the Al-wire is in its normal state ($T \gg T_c$). Unfortunately, this slightly small effect turned out to be superposed to a dominating effect, induced by charge imbalance.
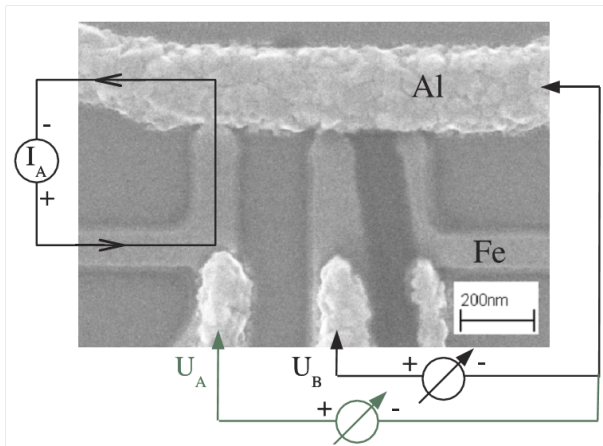
Figure 4.2: Exp. scheme of the experiment of Beckmann et al. [17]: Three vertical iron wires are connected by point contacts to a horizontal aluminium bar. The outer two iron wires have additional voltage probes. An example of the current injection (I_A) and both local (U_A) and non-local (U_B) voltage detection scheme for one pair of contacts is also shown.

Another promising candidate for future entanglement experiments are for instance diffusive NSN-structures: especially the reproducibility of devices and a high control of the fabrication process allow extremely reliable experiments. In such multi-terminal diffusive NSN structures with low transparent tunnel contacts, various experiments report a bias-dependent sign-inversion of the non-local resistance. In spite of general agreement, that this energy-related cross-over is due to EC-dominated to CAR-dominated transport [18,98,99], the physical origin of domination of one process with respect to the other is

not clear yet. As explanation, quantum-mechanical interaction [18] as well as Coulomb-interaction [93,99] have been proposed.

So far, several groups report of successful Cooper-pair splitting experiments [20–22, 100, 101] in metallic nanostructures as well as in CNT [1]- and Nanowire-based devices. Over the last years, several parameters have been identified which help to favour CAR-process, such as contact resistance, applied voltage or Coulomb-interaction [18, 19, 93, 98, 99]. Actually, it seems that Nanowires and CNT-devices are more suitable for coming EPR-sources: for instance, Schindele et al. [23] report even a CAR-probability of nearly 100% in appropriate experimental conditions.
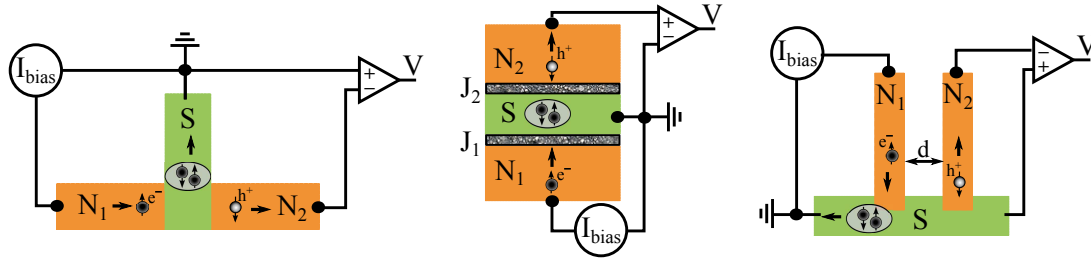
Figure 4.3: Sketch of three sample geometries for CAR-experiments. **left** "classical" beam-splitter set-up (topview) used by [20, 21]; **middle:** device developed by Russo et al. [18](cross-section); device of Beckmann et al. [17] (topview). reproduced from [102]

4.2 Multi-terminal structures - all superconducting electrodes

Multi-terminal structures with all superconducting electrodes are the centre of interest of this PhD work. They bring a wealth of new phenomena into play, among several have not been studied experimentally yet. First experiments on such kind of structures where performed in arrays of Josephson junctions [66, 103]. At the beginning, studies of interacting Josephson junctions was driven by the technical interest on applications and a better understanding of its dynamic properties in the non-equilibrium state [11]. Early experiments by Giaever [66] showed that these high-frequent behaviour can be most sensitively monitored using another weak link as detector. Furthermore, arrays of Josephson junctions were studied in order to increase the amplitude of effects appearing in each junction to a detectable level. One extensively studied effect was the so-called phase- or voltage-locking, where interactions between micro-bridge junctions, connected

---

1. CNT=Carbon-Nanotube

in series or parallel give rise of features in the IV-characteristic and conductance, when the junctions are common- or opposite-biased [11, 104].

Concerning application, the perspective of a high-frequency controlled oscillator with high tuning-agility excited a high effort in research and yield to the development of a high variety of detectors, mixers and parametric amplifiers, based on the properties of Josephson junctions. However, a real breakthrough for this technology has not been achieved yet, since the use for applications is limited due to several factors

- Josephson junctions have to be cooled down to low temperatures, below T_c of the superconductors, which is well below room temperature, even for exotic superconducting compounds
- low voltage ($V \cong 1mV$) and power-level of the junctions

That is why application of Josephson-mixers and -detectors are up to now quite restrictively used, for instance as quantum-limit amplifiers in fundamental research [14] or in astronomy.

The last few years, an arising interest in Multi-terminal Josephson junction has been observed, due to new theoretical predictions and the technical progress in fabrication technology, which opens perspectives towards more and more sophisticated device geometries. For instance, MAR-features are expected to be much richer than in "conventional" 2-terminal SNS structures [24]. Furthermore, these geometries are exciting, because - for instance - shot noise and correlations [105, 106] are expected to be largely enhanced. Finally, a new transport mechanism, called quartet-mode has been proposed [26, 107], which has not been reported experimentally, yet.

4.2.1 Induced Shapiro-steps - voltage-locking

In the 70's, first experiments were performed toward coherent coupling of Josephson junctions [103, 109, 110]. The observation of observed interaction-mechanism leaded to active research in the field. Individual biased coupled superconducting weak links were first considered in the 80's with the theoretical work of Nerenberg et al. [111]. They studied two Josephson junctions shunted by an external resistance and proposed to extend the known RSJ-model to a three-terminal geometry (Fig. 4.4). In their model, they suppose that each Josephson junction has a perfectly sinusoidal CPR and calculated the ac-current at any point of the circuit considering a current biased scheme. In that case, the equations of current read:

$$
\begin{aligned}
\frac{d\Phi_1}{dt} &= \frac{2eR_1^*}{\hbar}(i_1 - i_{c1}\sin(\Phi_1) - \alpha_1(i_2 - i_c2\sin(\Phi_2))) \\
\frac{d\Phi_2}{dt} &= \frac{2eR_2^*}{\hbar}(i_2 - i_{c2}\sin(\Phi_2) - \alpha_2(i_1 - i_c1\sin(\Phi_1)))
\end{aligned}
\tag{4.1}
$$

with $\alpha_1 = R_2/(R_s + R_2)$, $\alpha_2 = R_1/(R_s + R_1) = \alpha/\delta$. In this context, R_1 and R_2 are the junction resistances, R_s is the shunt-resistance and $R_1^* = [R_1(R_2 + R_s)]/(R_1 + R_2 + R_s)$, $R_2^* = [R_2(R_1 + R_s)]/(R_1 + R_2 + R_s)$.

In equation 4.1, the α_1-term gives the amount of current flowing in Josephson junction 2 (respectively 1) originating from Josephson junction 1 (respectively 2). When this term is non-zero, i.e. when the shunt resistance R_s is not too large compared to the normal state resistance of the two Josephson junctions, two ac-currents of frequencies set by the
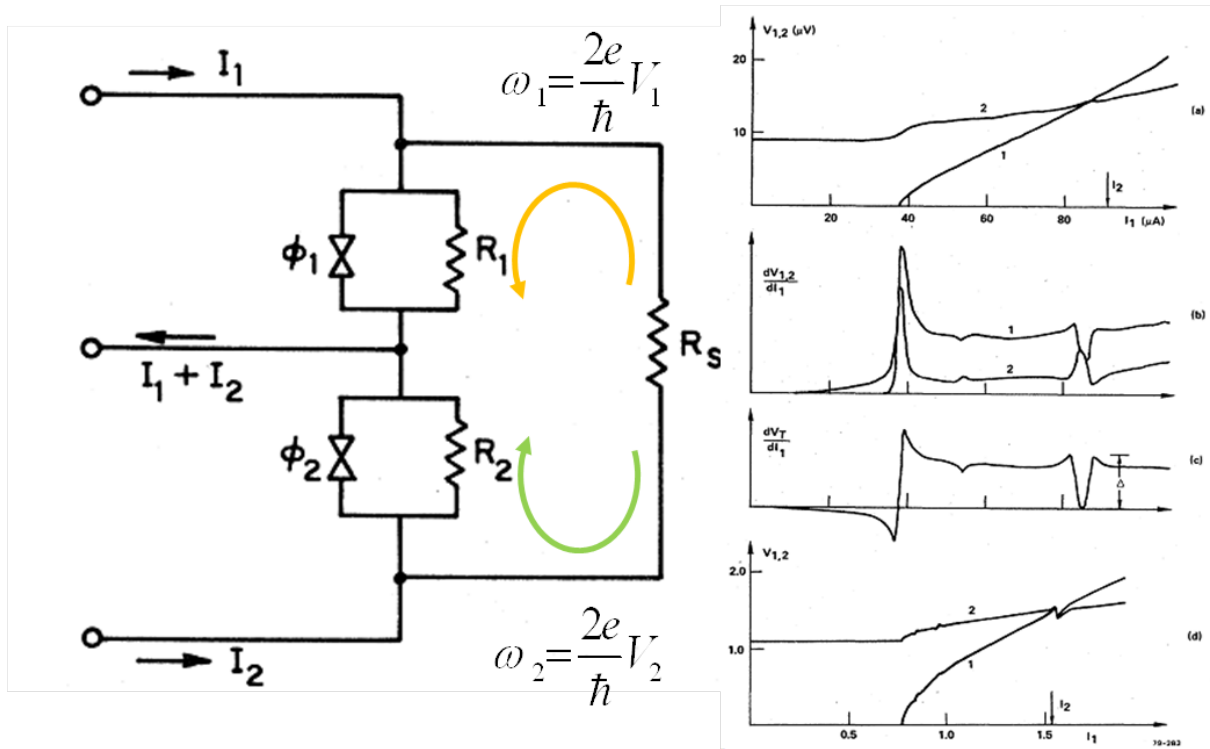
Figure 4.4: left: experimental scheme; right: a-c: experimental results; a) IV-curve as a function of i_1; i_2 is hold constant at 91 μA, whereas i_1 is swept; b) differential resistance as a function of i_1 for each junction; c) total differential resistance as a function of i_1; d) numerical simulation of IV-curve a); [108]
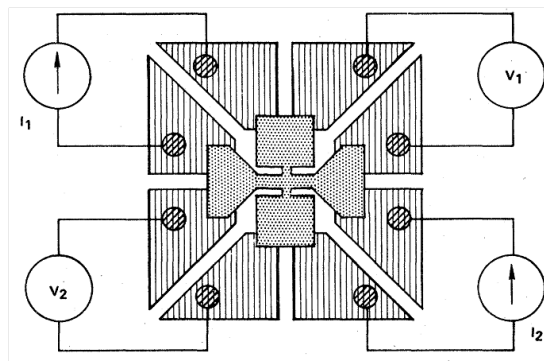
Figure 4.5: Experimental set-up of Jillie et al. [108]: coupled thin-film indium microbridges (dotted region), provided with eight gold contacts for two separate four-terminal measurements

voltages V_1 and V_2 across the junctions are flowing in each Josephson junction. Because of the non-linear response of a Josephson junction, down-mixing occurs, giving rise to d.c. features in the IV-characteristics. The first relevant experiments have been performed by Jillie et al. [108, 112]. Their sample geometry consists of two coupled indium micro-bridges (see Fig. 4.5), where they vary the bridge separation between 1.6 and $3.0\,\mu m$.

In their experiments, they observe features in IV-characteristics and differential resistance, when the two junctions are series- (current flowing in same direction) or opposed biased (current flowing into opposite directions) for all bridge separations up to $3\,\mu m$.

Due to these large scales, they exclude simple heating effects as origin of these features. Furthermore, due to different behaviour of their anomalies, they attribute the observed effects to so-called "voltage-locking interaction". The effect is observed in a experimental window close T_c $(0.98\,T_c < T < T_c)$ and in voltage-range up to $\approx 70\,\mu V$ (however strongly reduced above $35\,\mu V$). Jillie et al. show in their paper, that quasi-particle diffusion currents can play the role of the shunt resistance R_s in the model of Nerenberg et al.

4.2.2   3-terminal IMAR
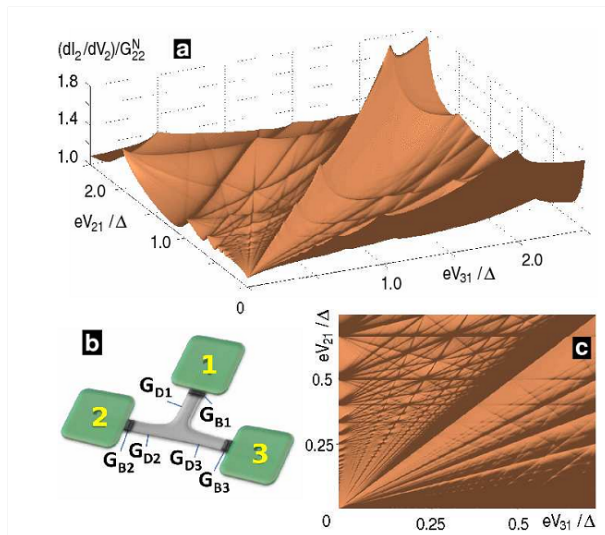
Figure 4.6: Three-terminal MAR as a function of voltage normalized to the gap Δ. All appearing lines are due to MAR processes. whereas horizontal and vertical lines correspond to 2-Terminal MARs, all lines with a finite slope are due to 3-terminal MARs; [24]

As introduced in section 3.3.2, multiple Andreev reflections (MAR) give rise to a sub-harmonic gap structure (SGS) at $eV = 2\Delta/n$ (n being integer) in the current-voltage characteristics of two-terminal structures with two superconducting electrodes. Experimental and theoretical studies concerning MAR were mostly restricted to two-terminal structures. However, in terms of MARs, junctions with multiple superconducting electrodes reveal rich additional phenomena. For instance, phase-dependent MAR-transport has been investigated in a diffusive conductor [76] and strongly enhanced current-cross correlations due to MAR are predicted between superconducting leads as well [105]. However, all this work was done at one bias between the different leads.

M. Houzet and P. Samuelsson [24] propose experiments with all superconducting leads, where the chemical potential of the electrodes can be tuned individually. They propose a device composed of three superconducting leads S_1, S_2 and S_3, which share a common normal part (see Fig. 4.6 (b)). In this description, the voltage difference between S_1 and

S_2 is named V_{12} (respectively, the voltage difference between S_1 and S_3 is named V_{13}). Restricted to the diffusive long junction limit in the incoherent regime ($E_{Th} \equiv 0$), they predict a much richer sub-harmonic gap structure than known from two-terminal devices (see Fig. 4.6). More precisely, they predict SGS, when

$$pV_{12} + qV_{13} = \frac{2\Delta}{e} \qquad \text{or} \qquad (4.2)$$

$$pV_{12} + qV_{13} = 0 \qquad (4.3)$$

where p and q are integers and $V_{12} = V_1 - V_2$ (resp. $V_{13} = V_1 - V_3$). Evidently, direct transmission without necessity of Andreev reflections can take place, when the voltage drop between two terminals exceeds twice the superconducting gap Δ, $\|V_{\alpha\beta}\| > 2\Delta/e$, with $V_{\alpha\beta} = V_\alpha - V_\beta$. This gives rise of three SGS-lines, situated at $V_{21} = \pm 2\Delta/e$, $V_{31} = \pm 2\Delta/e$, and $V_{21} - V_{31} = \pm 2\Delta/e$ For $p = 0$ with $q \neq 0$ (respectively $q = 0$ with $p \neq 0$) or $p = q \neq 0$, eq. 4.2 reduces to that of a two-terminal Josephson junction.

Especially, when $p \neq 0$ and $q \neq 0$, eq. 4.2 gives rise to SGS-features which are specific for this three-terminal device. In this case, MAR do not take place between two superconducting electrodes, but three. Numerous possible processes get possible which rise the quasi-particle's energy till it exceeds the superconducting gap Δ of one of the involved superconductors.

SGS-features, given by eq. 4.3 arise due to an interplay between different MAR-processes. For instance, if $V_{21} = V_{31} > 2\Delta/e$, an electron with energy $\epsilon < -\Delta V_{21}$ has two options: it can escape into lead S_2 *or* S_3 and no Andreev-reflection is necessary. Assuming now, that we reduce the voltage drop V_{21} just enough, so that the energy $\epsilon + eV_{21} < 2\Delta$. Then, the only possible process for the electron in order to escape the normal part is to leave into lead S_3 - otherwise, the process would require an additional Andreev-reflection. The immediate variation of available options would hence lead to a reduced amount of transmitted electrons and hence give rise to a feature. The same reasoning holds, if for instance if $V_{21} = 2V_{31}$ with $\|V_{21}\| > 2\Delta/e$.

These predicted anomalies are expected to be smeared out at temperatures comparable to the energy-scale of the gap $\Delta \approx k_B T$. As experimental conditions, a highly transparent contact between S-leads and their intermediate N-region are recommended, since a high probability of Andreev reflections is necessary to observe a high number of these features.

4.2.3 Voltage-induced Shapiro-steps

Starting-point of this recent article were experiments performed by Pierre et al. [113] on a diffusive SNS-structure. Using a normal tunnel-probe, they reveal steps in the quasi-particle distribution function $f(E)$ in non-equilibrium, which manifest Multiple Andreev Reflections at the S/N interface. These results inspired Cuevas and Pothier [114] to study a similar device, where the normal metal tunnel-probe is replaced by a superconducting one (see Fig. 4.7a). On the contrary, the interfaces $N - S_{l,r}$ are assumed to be fully transparent and eventual phase-breaking phenomena are neglected.

In their simulations, based on time-dependent Usadel-equations, features appear for $V = mU/2$, where m is an odd integer (see Fig. 4.7b). They explain these features by interference-effects between the two ac-Josephson currents, arising between S_l and S_p
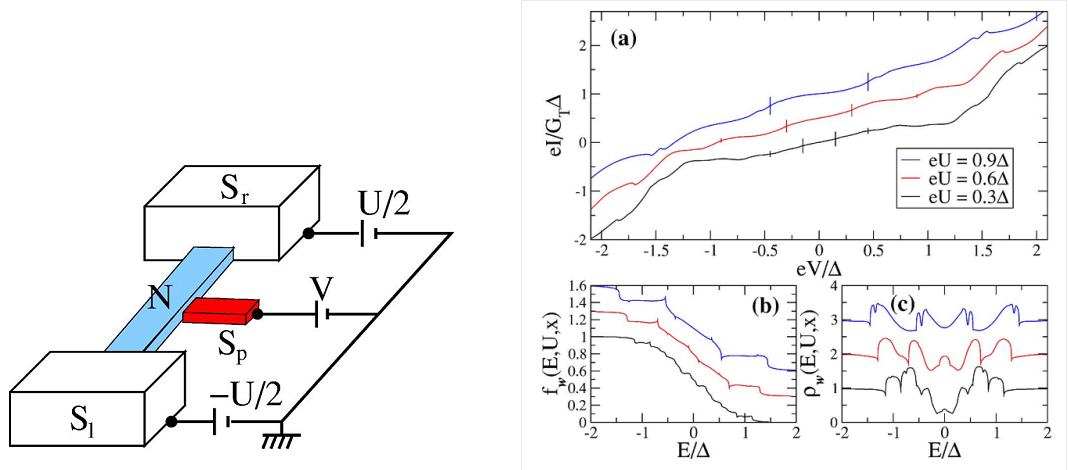
(a) Voltage-induced Shapiro-steps in a diffusive wire with superconducting contacts: the proposed sample geometry consists of two superconducting electrodes S_l and S_r, biased at $\pm U/2$ which are connected by a metallic wire N; the central superconducting contact S_p is supposed to be a tunnel probe, situated at potential V [114]

(b) (a) IV-characteristics (at $T = 0$), measured by tunnel probe S_p, situated at $x = L/2$ for $L = 2\xi$ for three values of voltage U: from bottom to top $eU/\Delta = 0.3, 0.60.9$; (b) corresponding d.c.-contribution in f(E); (c) corresponding spectral density f(E) [114]

on one side, and S_r and S_p on the other. For an applied potential difference U across the wire, ac-Josephson effect generates an ac-current with frequency $2e(V \pm U/2)/h$. Interference between these ac-currents then leads to an additional contribution in the dc-current through the superconducting tunnel probe S_p, which get visible as "Voltage-induced Shapiro-steps" for discrete voltage. The expression "Voltage-induced Shapiro-steps" has been chosen in order to underline the analogy to Shapiro-steps, where an external microwave-signal interferes with the ac-Josephson current of the junction. The current from S_l to S_r can be expressed in the form

$$I(V,T) = \sum_{m=-\infty}^{\infty} \sum_{n=-1}^{1} I_n^m(V) \exp i(n\Phi + 2n\,eVt/\hbar + m\,eUt/\hbar) \qquad (4.4)$$

where Φ is the dc-part of the phase difference. Eq. 4.4 contains two contributions, among a background current, which is present over all voltage V. The other contribution is responsible for the Voltage-induced Shapiro-steps. It just contributes to the transport at discrete voltages $V_m = m\,U/2$ with m odd, producing Shapiro-like peaks.

In their calculation, they also study the height of these induced features as a function of position of the tunnel-probe S_p and different wire lengths. It turns out, that the features decrease for $L >> \xi_s$. The maximal height of the voltage-induced Shapiro-steps is expected to be smaller than the critical current at $U = 0$. Another crucial parameter for the size of the features is the applied voltage U. A feature at $V = m\,U/2$ (m odd), indicates a coherent transfer of $n = m + (|m| + 1)/2$ Cooper pairs, requiring hence at least n coherent MARs. This limits - especially in long, diffusive junctions ($L >> \xi_s$), as seen in section 3.4 - the number of appearing features. Finally, an important decrease of the anomaly-amplitude with increasing voltage U appears (see Fig. 4.7b).

4.2.4 Non-local quartets

Recent theoretical calculations by Freyn and Co-workers predict a new transport mechanism in multi-terminal nanostructures, which propose coherent transport over a large range of voltage, even above the mini-gap [25]. They study a structure, where a central superconducting electrode S_0 builds two spatially separated Josephson junctions with the electrodes S_a, and S_b via two normal parts N_a and N_b (see Fig. 4.7a)). They assume that the distance L between the two Josephson junctions is small compared to the superconducting coherence length, $L << \xi_s$ and suppose an arbitrary S/N contact-transparency.

As they are especially interested in coupling-mechanism between the two junctions, they choose a generalization of Andreev-Kulik-Saint-James states as starting point of their calculations. For each of the two-terminal Josephson junctions, Andreev-Bound states are formed, if the chemical potential μ between the superconducting electrodes is zero: $\mu_s - \mu_a = V_a = 0$ and $\mu_s - \mu_b = V_b = 0$. Since the length L of the central superconductor is smaller than the superconducting coherence length ξ_s, one can imagine as well that - instead of successive Andreev reflections on both S_0-interfaces - higher order processes, such as crossed-Andreev reflection (CAR) or elastic co-tunneling (EC) appear. This allows now the appearance of new coherent transport-mechanism, which interlink Andreev-reflections in both junctions, $S_0 N_a S_a$ and $S_0 N_b S_b$. They call these new mechanism, in analogy to the two-terminal mechanism, double-elastic Co-tunneling (dEC) and doubled Crossed Andreev-reflection (dCAR).

In the process of dEC, an electron e_1 originating from S_a with energy ϵ propagates toward S_0 and acquires the energy eV_a set by the potential V_a (see Fig. 4.7 b)). But, instead of undergoing an Andreev reflection at S_0, e_1 tunnels through the central superconductor S_0 into the second junction, $S_0 N_b S_b$ and propagates towards S_b acquiring the energy eV_b. Arrived at the $N_b - S_b$-interface, the electron e_1 has accumulated an energy $\epsilon + V_a - V_b$. Then, it performs an Andreev reflection, which creates a Cooper pair in S_b and retro-reflects a hole h_1 with energy $-\epsilon + V_a - V_b$. If this hole h_1 tunnels through S_0 as well, it can perform another Andreev reflection at S_a which destroys a Cooper pair in S_b and a retro-reflected electron e_2 with energy $\epsilon + V_a - V_b$ appears. If the de-phasing during the whole process is sufficiently small and $V_a = V_b$, electron e_1 and e_2 have the same energy and are coherent. During the whole process, a Cooper-pair has been created in S_a and another has been removed from S_b. Hence, the described process leads to the formation of Andreev-Bound-States and causes a d.c.-Josephson effect between S_a and S_b. For simplicity, this mechanism will be called d.c.-Josephson effect J_{ab} in the following. In Fig. 4.8 a), the process is illustrated in Band-scheme-representation.

The process of dCAR represents an even more interesting transport mechanism, which appears, when the two junctions are opposite biased, $V_a = -V_b$. Supposing a Cooper-pair in S_0 which is split into two electrons with energy ϵ due to crossed Andreev reflection. The left electron e_1 with an energy ϵ propagates toward S_a and gains an energy $\epsilon + V$, whereas the right electron e_2 moves toward S_b, accumulating an energy $\epsilon - eV$. Both electrodes undergo an Andreev-reflection at S_a (respectively S_b) which create a Cooper-pair in S_a and another in S_b. Afterwards, a hole h_1 with energy $-\epsilon + eV$ and a hole h_2 with energy $-\epsilon - eV$ return toward S_0 where they can recombine by absorbing a Cooper-pair of S_0. If we consider now the complete process, two Cooper-pairs have been removed from central superconductor S_0 and distributed into S_a and S_b. This process shows a

striking resemblance with an Andreev-Bound-state, but at non-zero Voltage. The process of dCAR is also called mechanism of Non-local Quartets due to its distribution of two pairs of electrons. In the following, we will call this mechanism *Quartet-mode*. For a scheme of the described process, see Fig. 4.7c), the corresponding Band-scheme is given in Fig. 4.8 b). In Fig. 4.8 c), we illustrate, that already a small variation of ϵ destroys the quartet-resonance and the energy ϵ has accumulated after a complete cycle.

Experimentally, especially the quartet-mode is expected to be preserved over a large range of voltage: First, as shown in section 4.1, applying opposite voltage favours the dCAR-process. Second, the Andreev-reflections at S_a and S_b are performed in a much lower felt potential that helps to keep the de-phasing in the junctions themselves relatively low. On the other hand, the Josephson effect J_{ab} is especially favoured for low voltage, as it is the case, when $V_a = V_b$.

The current, for instance in junction a composes as follows

$$I_a(t) = I_a^0 \sin\left(\delta\Phi_a(t)\right) + I^{dCAR} \sin\left(\delta\Phi_a(t) + \delta\Phi_b(t)\right) + I^{dEC} \sin\left(\delta\Phi_a(t) - \delta\Phi_b(t)\right) \quad (4.5)$$

where the first term indicates the d.c.-Josephson effect between S_a and S_0, the second is the quartet-mode contribution and the third is due to the d.c.-Josephson effect J_{ab}. All contributions - since they originate from coherent effects - depend on the phase differences between the superconducting electrodes, $\delta\Phi_a = \Phi_a - \Phi_s$, respectively $\delta\Phi_b = \Phi_b - \Phi_s$. Generally, the intensity of each current is due to the phase-synchronization of the ac-oscillation of the Josephson junctions. The quartet-mode results in a dc-current contribution, which develops when the phase-relation $\delta\phi_a(t) + \delta\phi_b(t) = e(V_a + V_b)t/\hbar + \delta\Phi_a + \delta\Phi_b$ gets time independent.

The dCAR and dEC-mode are not the only anomalies appearing in their calculations, but also higher order processes (sextet, octet etc.). More generally, their calculation reveal features whenever

$$pV_a + qV_b = 0 \tag{4.6}$$

where p and q are integers.
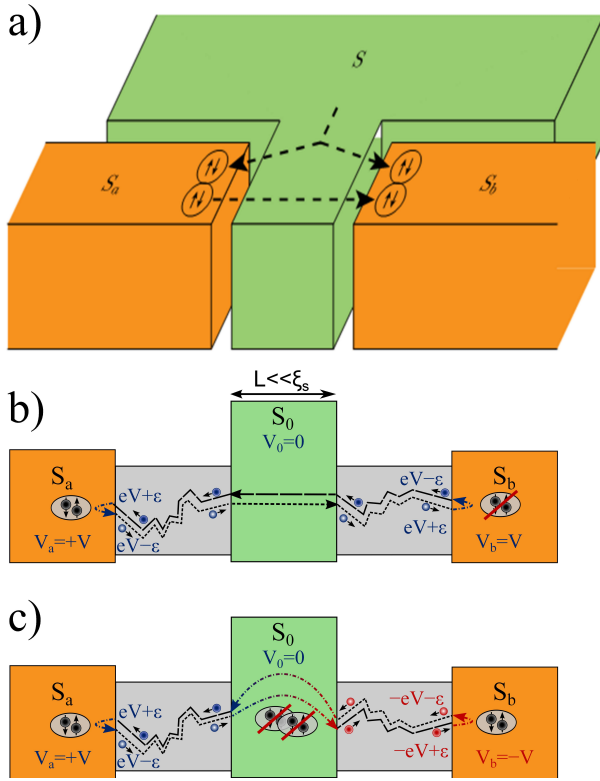
Figure 4.7: (a) $S_a S S_b$ structure, normal parts are not presented for clarity;
(b) Mechanism of dEC: when $V_a = V_b$, a dc Josephson effect J_{ab} can develop between the electrodes S_a and S_b; e_1 and h_1 pass through the central superconductor S_0 by elastic co-tunneling, EC
(c) Scheme of the quartet-mode: This phase-sensitive transport mechanism appears, when the two junctions are opposite biased, $V_a = -V_b$. In this process, a Cooper-pair of electrode S_0 is split and its electrons travel individually, one toward S_a, the other toward S_b. Each of them performs an AR, leading to two holes traveling back to S_0. There, they recombine, now by absorbing a Cooper-pair. In total, one can show that this process leads to a coherent transfer of two Cooper-pairs of S_0 into S_a and S_b.
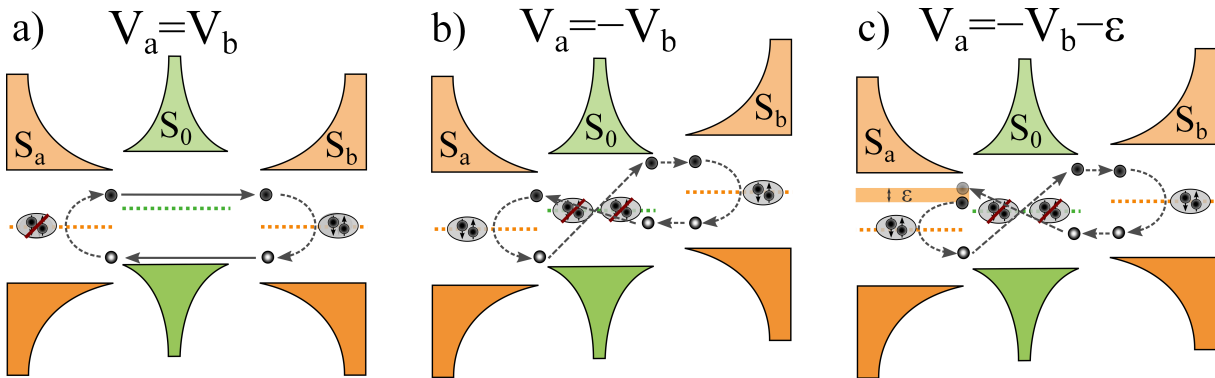
Figure 4.8: Band-scheme illustration of Fig. 4.7
a) $V_a = V_b$: double-elastic Co-tunneling or dc-Josephson-effect J_{ab}
b) $V_a = -V_b$: In the quartet-mode, the coherence over the whole process gets preserved; an electron e_1 can interfere with the electron finishing the process
c) $V_a = -V_b - \epsilon$: Near the Quartet-mode, the whole process does not stay coherent over the complete mechanism, a mismatch of ϵ accumulates over the whole trajectory and the coherence of the process is lost quite fast

Chapter 5

Experimental set-up

In this chapter, we will present the working principle of our measurement set-up. Then, we will proceed with the performed calibration measurements, which have been performed during this thesis and have been summarized in [115].

5.1 Dilution fridge

In the here presented work, we use a standard ^3He-^4He dilution fridge which has been developed in the laboratory during the PhD thesis of Olivier Coupiac [116]. It offers a base temperature of 30 mK with a cooling power of $35\,\mu W$ at 100 mK and is equipped with 3 commercial SQUIDs acting as current amplifiers, which are situated at the 4 K stage. For temperature regulation, we are using an ABB TRMC2 temperature controller.

Clamped outside of the lower part of the VTI, a magnetic coil (superconducting wire, $\varnothing 0.4$ mm) has been mounted during my thesis, which allows measurements with a maximal magnetic field of $200\,mT$.

5.2 SQUIDs as Pico-ampere meter

A SQUID consist of a superconducting loop, which is interrupted by one or more Josephson junctions. There exist two types of SQUIDs: direct current (DC) and radio frequency (RF) SQUIDs (for a review, see for instance [117]). Due to their better performance in noise, we use DC SQUIDs for our experiment. For that reason, we will just refer in the following to the working principle of a DC SQUID.

For functioning, a d.c. SQUID is biased with a polarization current I_{pol}, and the voltage across it is recorded (see Fig. 5.1). If the polarization current I_{pol} is kept slightly above the critical current I_c of the two Josephson junctions, we expect a working point in the IV-characteristics, with a high differential resistance and any small variation in the applied current leads to a large response. The working principle of the SQUID relies on the fundamental property of a superconductor that the flux threading a loop is quantized. Any deviation from this quantization induces a screening current I_{screen} in the superconductor. In the SQUID-loop, this screening current adds to the applied polarization current I_{pol}, and hence leads to variations of the critical current I_c (see Fig. 5.2).
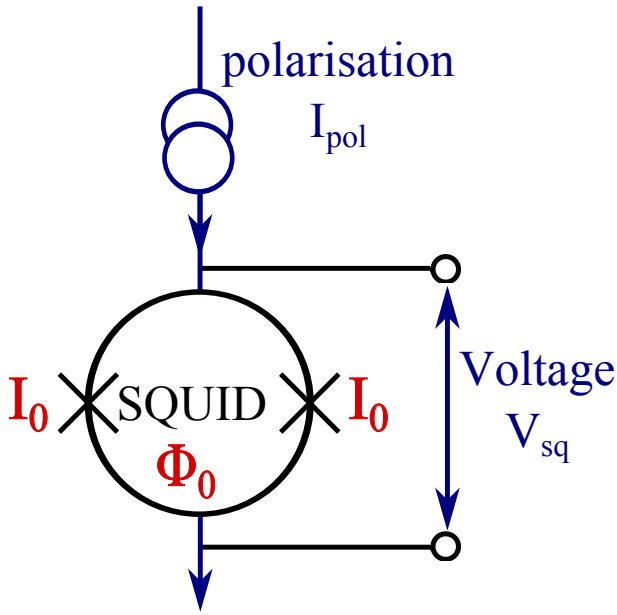
Figure 5.1: Basic working scheme of a SQUID device: A current $I_{pol} > I_c$ polarizes the SQUID near the critical current of the two junctions I_O; any change in flux Φ leads to a variation of the detected Voltage V

Each time the flux Φ exceeds an integer multiple of the quantum flux $\Phi_0 = h/2e \approx 2\,10^{-15} Tm^2$, a vortex is created in the ring. For an integer number of flux quanta inside the superconducting loop, $\Phi = n\Phi_0$, the screening current I_{screen} has a minimum, and consequently a maximum in the critical current of the SQUID can be observed, $I_c = 2I_0$, where I_0 is the critical current of one Josephson junction. On the contrary, a decrease of the critical current can be observed, if $\Phi = (n+1/2)\Phi_0$. In this case, the screening current I_{screen} exhibits a maximum. When properly current-biased, this periodicity in integers of Φ_0 of the SQUID-response also appears in the measured voltage, leading to the typical Voltage-flux characteristics of a SQUID-device (see Fig. 5.2).

A SQUID can also act as high-performance current-amplifier. For that purpose, the SQUID has to be coupled to the measurement line via an inductance (input coil). Then, any current flowing through this input-coil varies the magnetic flux in the superconducting ring. That is how our SQUID current-amplifiers work - in our SQUIDs, an input coil with an inductance of $\approx 2\,\mu H$ is used. For operation, the SQUIDs are working in "flux-locked loop" mode (see section 5.2.1).

5.2.1 Flux-locked Loop

In flux-locked loop technique (for a scheme, see Fig. 5.3), an additional coil (modulation or feed-back coil) is added on the SQUID chip, in which a modulation current I_{mod} with a frequency $f_M = 500kHz$ is applied. The amplitude of this current I_{mod} is such that it generates an ac-flux in the SQUID that is much smaller than Φ_0. This leads to an oscillation of the SQUID response which depends on the actual position in the flux-voltage characteristics $V(\Phi)$. Indeed, at $\Phi = n\Phi_0$, the SQUID-response δV_{sq}^{ac} is doubled with respect to the modulation-frequency, $f = 2f_m$ (see Fig. 5.2, right). Away from this working point, a linear term at $f = f_m$ shows up in the voltage response.

In a first step, this signal δV_{sq}^{ac} gets 5 times amplified at 4K by a transformer (Fig. 5.1). All further amplification is performed by an amplification chain, situated at room temperature. Finally, the resulting signal enters in a Lock-in amplifier centred at the
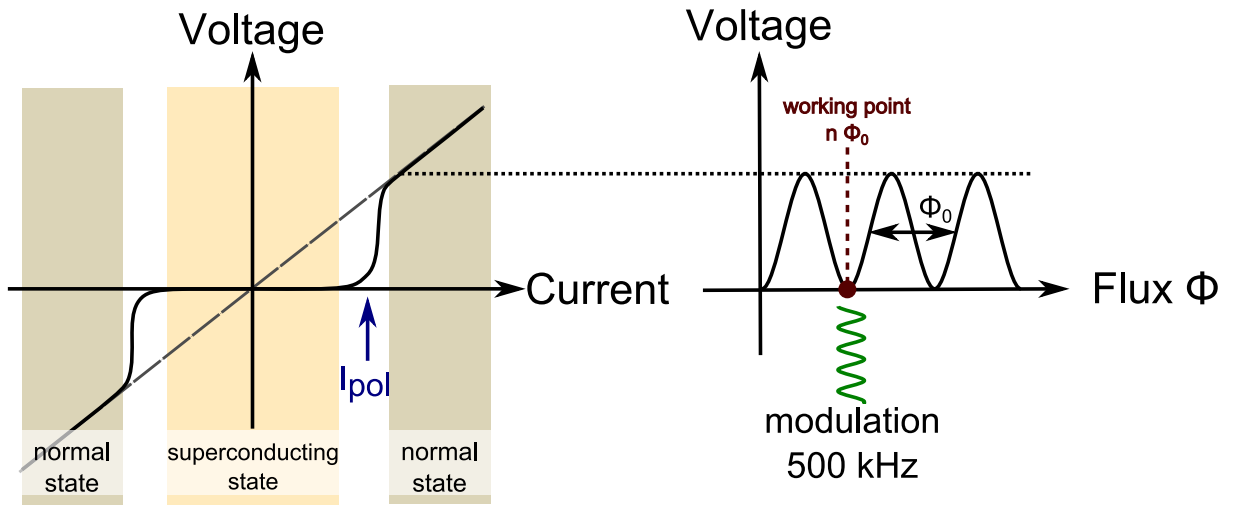
Figure 5.2: Working principle of a SQUID: a) Typical IV-characteristics of a current-biased SQUID-device; the critical current I_c is the sum of its two Josephson tunnel junctions; if the SQUID gets polarized with a current I_{pol}, slightly above the critical current, due to the non-linearity in the IV-curve, high sensitivity to any variation of the injected current can be achieved. Any induced screening current leads to an increase or decrease of the critical current I_c. By keeping the polarization current I_{pol} fix, this screening current shifts the working point into the superconducting or normal state. b) Flux-voltage characteristics $V(\Phi)$ of a SQUID-device: depending on the penetrating flux Φ, the critical current of the SQUID gets modulated and also the measured voltage across. For $\Phi = n\Phi_0$, the critical current has a maximum $I_c = 2I_0$ and hence also the voltage is minimum; If $\Phi = (n + 1/2)\Phi_0$, the measured voltage has a maximum. From that follows a Φ_0-periodicity of $V(\Phi)$, where a working point of the SQUID can be chosen.
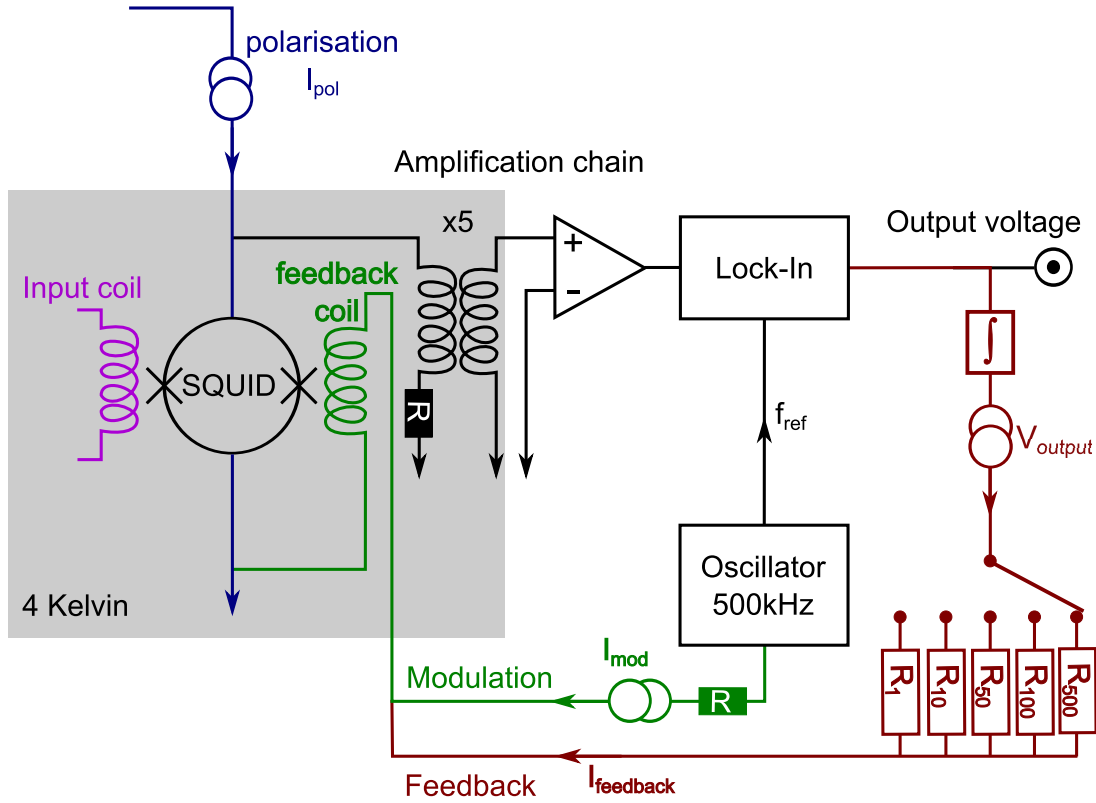
Figure 5.3: Working principle of flux-locked loop of our SQUID electronics

modulation frequency f_m. The voltage-readout of the Lock-In gives a voltage V_{out} which is proportional to the linear part in the SQUID response δV_{sq}^{ac} at the reference frequency f_m. It is therefore sensitive to the change in the SQUID flux.

The idea of a flux locked loop is now to compensate this flux variation and to maintain the chosen working point of the SQUID at $\Phi = n \, \Phi_0$. For that purpose, a d.c. current $I_{feedback}^{dc}$ is sent to the feedback coil and generates the flux which is necessary to return to the initial working point. The overall gain can be changed simply by changing simply the Feedback resistor that converts the read-out voltage V_{output} into the feedback current $I_{feedback}^{dc}$.

For all variations of the detected flux, which exceeds $\Delta\Phi_{max} = \Phi_0/4$, the feedback must be sufficiently fast to keep the signal at the working point. This "reactivity" of the set-up is given by the so-called "slew-rate". In our set-up, the slew-rate is given by a frequency $f_{slewrate} = 50 \, kHz$.

High-frequency perturbations or variations exceeding the slew-rate lead to an uncontrolled shift of the working point and hence also in the recorded voltage-response. For that reasons, strong efforts have to be made to protect the SQUID from external perturbations, such as vibrations or external magnetic fields. In general, such unexpected jumps in the SQUID response appear rarely, but as long as these jump correspond to multiples of Φ_0, they can be corrected easily in final curves.

Our SQUIDs are delivered by TRISTAN TECHNOLOGIES (for the detailed properties, provided by the manufacturer, see Table 5.1) and their control is assured by commercial electronics, delivered from TRISTAN electronics. It performs the read-out of all our

		Squid 1	Squid 2	Squid 3
Bias Current	$[\mu A]$	24	25.03	25.65
SQUID gain	$[mV/\Phi_0]$	1.084	0.948	0.653
Signal Magnification	$[mV]$	0.25	0.256	0.181
Modulation coil coupling M_{SQUID}	$[\mu A/\Phi_0]$	1.51	1.50	1.61
Input coil coupling	$[\mu A/\Phi_0]$	0.194	0.186	0.189
Input coil Inductance	$[\mu H]$	1.96	1.89	1.85
Current limit	$[\mu A]$	> 16	> 22	> 22
1/f Noise corner Frequency	$[Hz]$	< 0.325	< 0.3	< 0.2
No load	$[\mu\Phi_0/\sqrt{Hz}]$	3.15	2.85	2.54
Load	$[\mu\Phi_0/\sqrt{Hz}]$	3.62	3.67	2.32

Table 5.1: Experimental properties of the three SQUIDs,used in our experiment, provided by the manufacturer TRISTAN electronics

three SQUID-channels. The measured voltage $V_{TRISTAN}$ is proportional to the current I_{input}, provided by the inductive coupling M_{SQUID} of the input coil to each SQUID (in nA/Φ_0).

Depending on the chosen amplification gain of the electronics $G_{TRISTAN}$ (in V/Φ_0), we get

$$I_{measure} = V_{TRISTAN} \frac{M_{SQUID}}{G_{TRISTAN}}. \tag{5.1}$$

The SQUID gain[1] can be varied between 1 and 500. With the inductive coupling of $200\,nA/\Phi_0$, the SQUIDs provide at maximum gain an amplification of about $50\,nA/V$. The maximal resolution of our set-up is then, assuming a accuracy of the Lock-In read-out of $100\,\mu V$, easily in the order of one pico-ampere.

5.3   3-SQUID Measurements: Working principle

As already explained above, SQUID can act as highly sensitive amplifiers for small variations of current through the input coil. Due to its high accuracy, SQUIDs are promising devices to measure current fluctuations (noise) and current cross correlations. Already beginning of the 20th century, Schottky [118] realized, that noise spectra can give complementary information to electronic transport experiments. Based on this knowledge and encouraged by more recent theoretical predictions [119–123], experiments have been made to explore current and noise correlations in multi-terminal devices. Measurement of positive correlations in N-S-N geometries have been supposed to proof the existence of Crossed Andreev reflection as one key element toward EPR-experiments in solid-state devices.

In this context, our experimental set-up, equipped with 3 commercial dc SQUIDs, acting as current amplifiers has been developed. Its high sensitivity as pico-ampere meter provide unique properties in order to test conductance and noise in low impedance multi-terminal devices. Furthermore, SQUID-amplifiers and electronics are available as

---

1. The available gains are in total (1, 2, 5, 10, 20, 50, 100, 200 and 500)

commercial products and no exhaustive development has to be done. Figure 5.4 shows a schematic of the experimental set-up, including an image of a typical three-terminal device. It consists of three superconducting electrodes S_0, S_a and S_b, connected through some normal part, which can be modeled as two non-linear resistors R_1 and R_2. Each of these superconducting electrodes is connected to a SQUID amplifier.

Since we also want to measure current fluctuations, our sample needs to be voltage-biased. This can be achieved by choosing macroscopic resistors r_1, r_2 and R_{ref} (referred here after as biasing resistors), whose resistances are much lower than the device resistance in normal state.

The approach of voltage-biasing at low temperatures has the advantage to reduce the unavoidable thermal noise of the biasing resistors. Then, a low noise current source I_{dc1} injecting current between device and R_{Ref} is used to voltage-bias the system. If desired, a second current source I_{dc2} connected near r_1 and r_2 can be used to control individually the voltage drop V_a and V_b. V_a and V_b are systematically measured with two differential amplifiers situated at room temperature as well.

5.3.1 Calibration of experimental set-up

Before proceeding with measurements on more complex samples, we tested the performance of our instrument.

5.4 Measurements

In order to properly control the experimental environment of the sample, it is necessary to know exactly the resistances of all resistors in the measurement circuit. Those include not only the biasing resistors r_1, r_2 and R_{ref}, but also all kind of parasitic resistance, that could appear due to bonding, soldering or oxidation. Especially the parasitic resistors, named r_{p1}, r_{p2}, r_p, which are situated between sample and SQUID, have to be taken into account in the experiment. Therefore, once a new sample is mounted, some systematic measurements need to be done. For a scheme of the experimental set-up, including the position of the various resistors, see Fig. 5.4. All wires between the circuit elements are superconducting and hence, do not add any additional resistance into the measurement scheme. The SQUID-sensors are located at the 4K-flange of the dilution fridge, all other elements, especially sample and biasing resistors (r_1, r_2 and R_{ref}) are anchored at the mixing chamber. The location of the parasitic resistors can be either located on the soldering points near the sample holder, situated on the mixing chamber or on the contacts toward the input coil of each SQUID (4K).

5.4.1 Conductance measurements with the 3-SQUID set-up: Calibration

As already explained in section 5.3, our experimental set-up is suited for low-impedance samples. Here, we will detail the systematic procedure, which is performed for each measurement run, before starting serious experiments.
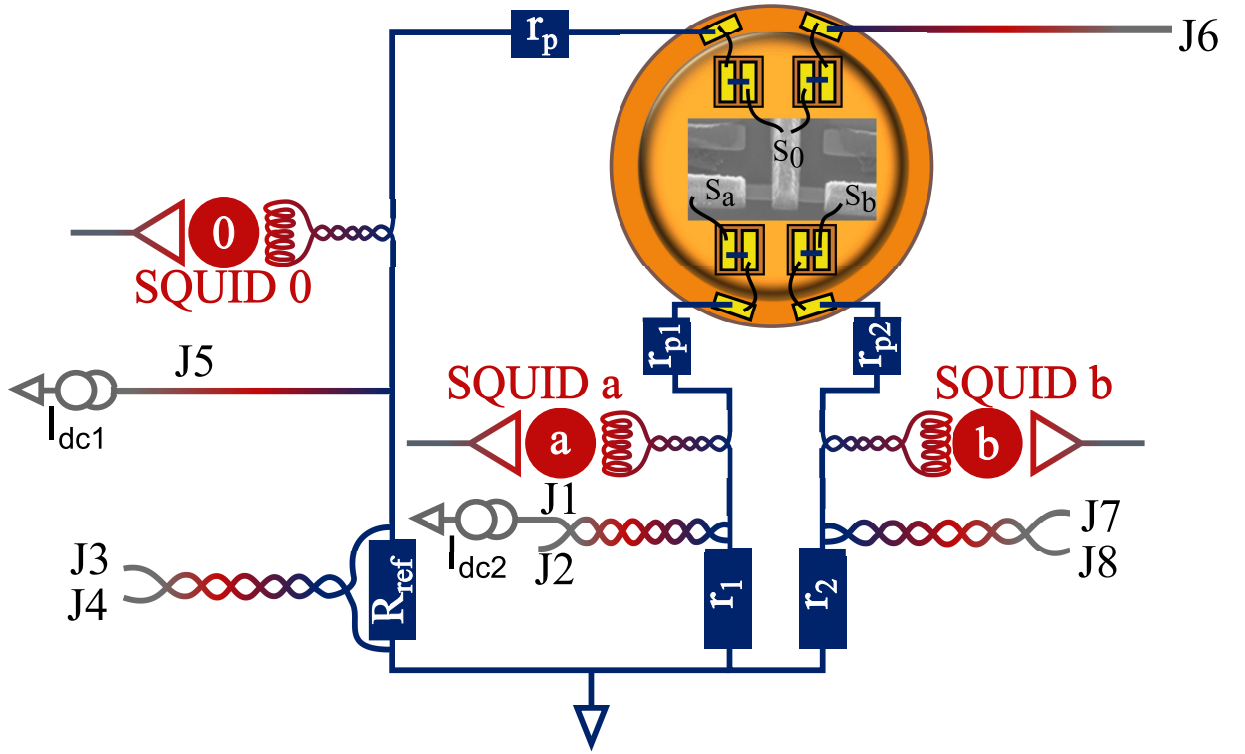
Figure 5.4: Complete scheme of experimental set-up: blue parts represent parts of the measurement circuit at base temperature of the dilution fridge, red parts are at 4K, wires at room temperature are coloured in grey. The orange part represents the sample holder. The inner disc can be removed in order to change the sample chip. Black lines indicate connections to be established before each run.

First, we check at room temperature that the sample is "alive" by sending an ac-current ($\approx 1\,\mu A$) on connection J6 and measuring the voltage drop at the same connector. At room temperature, all compounds in the measurement circuit, including the SQUID-amplifiers are resistive. In resistive state, the input coil exhibits a resistance of about $22\,k\Omega$. In order to minimize risks to damage the SQUIDs during the preparation of experiments, each SQUID is shunted by a resistance of $1k\Omega$ which is placed in parallel to the input coil of each SQUID. The initial test is then that the overall impedance of the circuit is $\approx 333\,\Omega^{\,2}$. At 4 K, the SQUID's are now superconducting and can be used for more precise calibration. In a first step, all implemented resistances must be determined.

As described in section 5.4.1, we have identified three parasitic resistors r_p, r_{p1} and r_{p2}, see Fig. 5.4. Other occurring resistors can be included into the bias resistors. Here, we detail the procedure to extract r_p at $T = 4K$. First, a d.c. current is sent through connection J6 and the current in each SQUID is recorded. According to Kirchhoff's laws, applied to each node, the current passing towards the sample reads:

$$I_{sq1}^{J6} + I_{sq2}^{J6} = \frac{R_{ref} + r_p}{R_{eq} + r_p + R_{ref}} I_{J6} \tag{5.2}$$

where R_{eq} is the equivalent resistance, considering the simplified scheme, see Fig. 5.5a.

---

2. When a value of $500\,\Omega$ is found instead, it means that one arm is broken

Similarly, the current flowing towards the sample when a d.c. current is sent through the J5 connection is:

$$I_{sq1}^{J5} + I_{sq2}^{J5} = \frac{R_{ref}}{R_{eq} + r_p + R_{ref}} I_{J5} \tag{5.3}$$

Figure 5.5b shows the behaviour of the two measurements as a function of the applied d.c. current. Knowing the resistance of the R_{ref} resistor, the value of r_p is then obtained from the ratio α of the two slopes

$$r_p = (\alpha - 1)R_{ref}. \tag{5.4}$$

With a typical value of $R_{ref} = 90\,m\Omega$, we find $r_p = 30\,m\Omega$. Similar measurements allow measuring the two other parasitic resistances, r_{p1} and r_{p2}. The resistance of the macroscopic resistors r_1, r_2, R_{ref} can be measured directly with the help of our differential amplifiers. In a typical measurement, we find following values, with small deviations ($\pm 5\,m\Omega$) between different measurement runs: $r_1 = 0.090\,\Omega$, $r_1 = 0.091\,\Omega$, $R_{ref} = 0.0885\,\Omega$, $r_{p1} = 0.0565\,\Omega$, $r_{p2} = 0.065\,\Omega$, $r_p = 0.107\,\Omega$. In the following, these resistances will be taken into account in the formulas, but no longer mentioned explicitly.
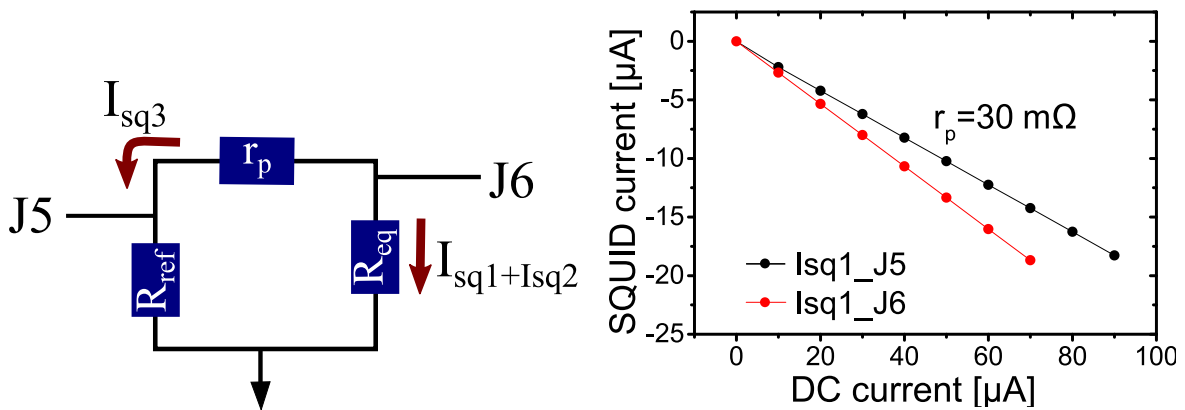
(a) Simplified measurement scheme: By injecting current at connections $J5$ and $J6$, the resistance r_p can be extracted easily. R_{eq} represents all resistances which are on the sample side.

(b) Device T-shape No.2: Squid-current (squid 2) as a function of sweeped d.c.-current at J5 and J6. The insert shows the deviated parasitic resistance r_p, using equation 5.4

For the measurement of differential resistance, an ac-current is sent, usually at connection J5 and the output of each SQUID is measured by a SR 830 Lock-In amplifier. The differential resistances are defined as follows

$$R_{diff_{a,(b)}} = \frac{dV_{a,(b)}}{dI_{a,(b)}} = \frac{R_{ref}(\delta I_{ac} - \delta I_{ac,0}) - r_p\,\delta I_{ac,0}}{\delta I_{ac,1(2)}} - (r_{1,(2)} + r_{p1,p2}). \tag{5.5}$$

We define $\delta I_{ac,0}$ as the ac-current, measured by SQUID 3, $\delta I_{ac,a}$ the ac-current in SQUID 1 (respectively, $\delta I_{ac,b}$ the ac-current in SQUID 2)

In order to control individually the voltage across each sample branch, we usually send a current $I_{dc,1}$ in the Reference side and $I_{dc,2}$ at r_1.
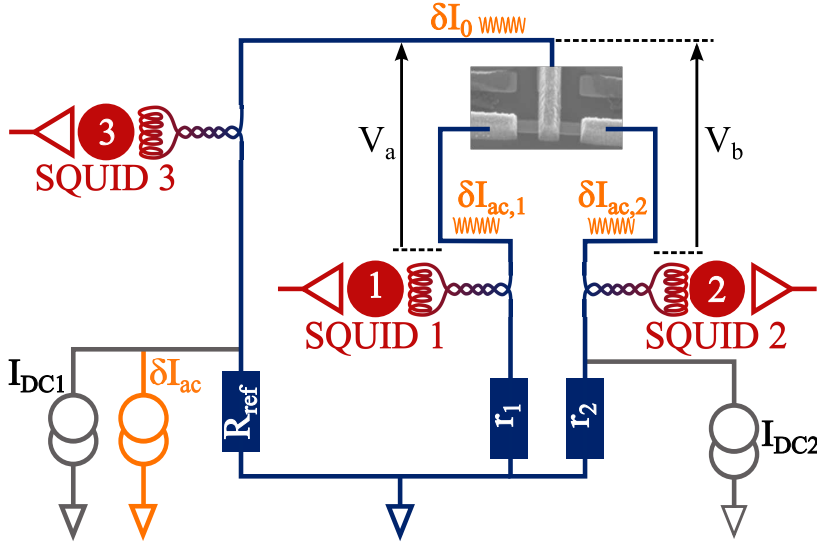
Figure 5.5: Experimental set-up for conductance measurements; using two current sources I_{dc1}, I_{dc2} the voltage drop across the two junctions, V_a and V_b can be controlled individually. The SQUIDs are used to measure the contribution of the ac-modulated probe current (in this example, injected at the reference-branch). The SQUID-current in SQUID S is called $\delta I_{ac,0}$, the ac-current in SQUID 1 $\delta I_{ac,1}$ and the ac-current in SQUID 2 $\delta I_{ac,2}$

5.4.2   3-SQUIDs for Noise and Correlation measurements

A full scheme of our experimental set-up has been given in Fig. 5.4. For noise measurements however, it must be considered, that each resistive element R_i in the circuit generates current fluctuations in the circuit. In accordance with the Nyquist representation, we can model these fluctuations by a current δI_i emitted by a current source which is situated in parallel of the respective resistor R_i. For the complete experimental, noise-adapted scheme, see Fig. 5.6. Each of these sources is characterized by its spectral density of noise[3] $S_i = \langle \delta I_i^2 / \Delta f \rangle$. In the case of pure thermal noise, this spectral density of noise corresponds to $S_i = 4 k_B T / R_i$. The current $I_{sq,i}$, flowing through Squid i, is then given by

$$\delta I_{sq,i} = \left(\frac{\widehat{R_i}}{\widehat{R_i} + \widehat{R_{jk}}} \right) \widehat{\delta I_i} - \left(\frac{\widehat{R_{jk}}}{\widehat{R_i} + \widehat{R_{jk}}} \right) \left(\widehat{\delta I_j} + \widehat{\delta I_k} \right) \tag{5.6}$$

where $\widehat{R_i}$ is the sum of the resistances in branch i, $\widehat{\delta I_i}$ the weighted current contribution of all the elements in branch i and $\widehat{R_{jk}}$ the equivalent resistance of $\widehat{R_j}$ in parallel with $\widehat{R_k}$. For instance,

$$\widehat{R_1} = R_1 + r_1 + r_{p1} \qquad \widehat{R_3} = R_{ref} + r_p$$
$$\widehat{\delta I_1} = \frac{R_1}{\widehat{R_1}} \delta I_1 + \frac{r_1}{\widehat{R_1}} \delta I_{r1} + \frac{r_{p1}}{\widehat{R_1}} \delta I_{rp1} \qquad \widehat{\delta I_3} = \delta I_{ref} + \delta I_{rp}. \tag{5.7}$$

From these three SQUID-measurements $\delta I_{sq,i}$, we can perform six non-independent measurements: three auto-correlations $AC_i \equiv \delta I_{sq,i} \delta I_{sq,i}$ and three cross-correlations $XC_{ij} \equiv \delta I_{sq,i} \delta I_{sq,j}$, which are defined by:

---

3. for simplicity, we will use the expression "noise" in the sense of "spectral density of noise"
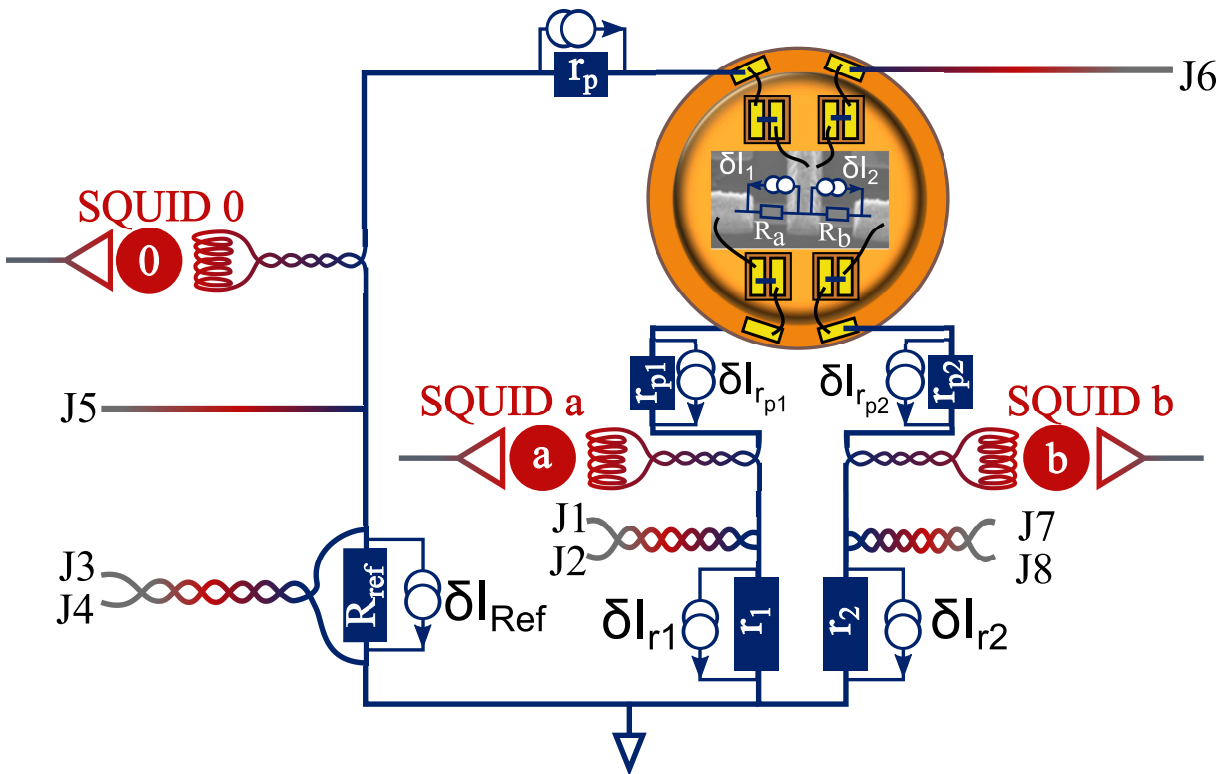
Figure 5.6: Schematic description of the experimental set-up. The red circuit's elements are at 4.2 K and the blue ones are thermalized with the mixing chamber of the dilution fridge. For calibration measurements, the sample has been replaced by two macroscopic resistors of $\sim 1\,\Omega$ resistance whereas the others macroscopic resistors in the circuit have a resistance of $\sim 0.1\,\Omega$. All the wiring is made from superconducting leads.

$$AC_i = \frac{\overline{\delta I_{sq,i}}^2}{\Delta f} = \frac{1}{(\widehat{R_i} + \widehat{R_{jk}})^2}\left[\widehat{R_i}^2\widehat{S_i} + \widehat{R_{jk}}^2\left(\widehat{S_j} + \widehat{S_k} + 2\widehat{S_{jk}}\right) - 2\widehat{R_i}R_{jk}\left(\widehat{S_{ij}} + \widehat{S_{ik}}\right)\right]$$

$$XC_{ij} = \frac{\overline{\delta I_{sq,i}\delta I_{sq,j}}}{\Delta f} = \frac{1}{(\widehat{R_i} + \widehat{R_{jk}})(\widehat{R_j} + \widehat{R_{ik}})}[-\widehat{R_i}\widehat{R_{ik}}\widehat{S_i} - \widehat{R_j}\widehat{R_{jk}}\widehat{S_j} + \widehat{R_{jk}}\widehat{R_{ik}}\widehat{S_k}$$

$$+(\widehat{R_i R_j} + \widehat{R_{jk}R_{ik}})\widehat{S_{ij}} + (\widehat{R_{jk}R_{ik}} - \widehat{R_j R_{jk}})\widehat{S_{jk}} + (\widehat{R_{jk}R_{ik}} - \widehat{R_i R_{ik}})\widehat{S_{ik}}]$$

(5.8)

where $\widehat{S_i}$ is the spectral density of noise of the noise source $\widehat{\delta I_i}$ and $\widehat{S_{ij}}$ the correlation between the sources $\widehat{\delta I_i}$ and $\widehat{\delta I_j}$.

In principle, the six measurements are related to the noise and cross-correlations of each element of the circuit. This can be very much simplified since cross-correlations between macroscopic resistors are zero. That means, that cross correlation-fluctuations including at least one of these macroscopic resistors are decorrelated and can be set to zero. Therefore, the system of equations reduces to

$$\begin{bmatrix} AC_1 \\ AC_2 \\ AC_3 \\ XC_{12} \\ XC_{13} \\ XC_{23} \end{bmatrix} = M_{red}\begin{bmatrix} S_1 \\ S_2 \\ S_{12} \end{bmatrix} + N_{tot}\begin{bmatrix} S_{r1} \\ S_{r2} \\ S_{ref} \end{bmatrix} + O_{tot}\begin{bmatrix} S_{rp1} \\ S_{rp2} \\ S_{rp} \end{bmatrix} + \begin{bmatrix} AC_1^0 \\ AC_2^0 \\ AC_3^0 \\ XC_{12}^0 \\ XC_{13}^0 \\ XC_{23}^0 \end{bmatrix}$$

(5.9)

where S_{ref}, S_{r1} and S_{r2} are the thermal noise of the three macroscopic resistors R_{ref}, r_1 and r_2. Here S_{rp1}, S_{rp2} and S_{rp} is the noise generated by the parasitic resistors. Furthermore, all connected instruments, such as amplifiers or voltage sources lead to a constant offset in the measurements, which will be taken into account by the constants AC_1^0, AC_2^0, AC_3^0, XC_{12}^0, XC_{13}^0 and XC_{23}^0. The three quantities of interest are the noise in each part of the device i. e. $S_1 \equiv \delta I_1 \delta I_1$ and $S_2 \equiv \delta I_2 \delta I_2$ and the cross-correlated noise $S_{12} \equiv \delta I_1\delta I_2$. Therefore, only three measurements are necessary and we usually choose AC_1, AC_2 and XC_{12} that are related to the physical quantities in the following way:

$$\begin{bmatrix} AC_1 \\ AC_2 \\ XC_{12} \end{bmatrix} = M\begin{bmatrix} S_1 \\ S_2 \\ S_{12} \end{bmatrix} + N\begin{bmatrix} S_{r1} \\ S_{r2} \\ S_{ref} \end{bmatrix} + O\begin{bmatrix} S_{rp1} \\ S_{rp2} \\ S_{rp} \end{bmatrix} + \begin{bmatrix} AC_1^0 \\ AC_2^0 \\ XC_{12}^0 \end{bmatrix}.$$

(5.10)

Following equation 5.6, the matrix elements are given by the values of various resistances. It must be stressed out, that in the case of "real" samples, the sample resistances R_1 and R_2 can show non-linear characteristics. Then, R_1 and R_2 are differential resistances. By putting numbers as an example, the three 3x3 matrices M, N and O, for $R_1 = R_2 = 1.0\,\Omega$, $R_{ref} = r_1 = r_2 = 0.1\,\Omega$, and $r_p = r_{p1} = r_{p2} = 0.01\,\Omega$, are:

$$M = \begin{bmatrix} 0.7072 & 0.0049 & -0.1179 \\ 0.0049 & 0.7072 & -0.1179 \\ -0.0589 & -0.0589 & 0.7105 \end{bmatrix}$$

$$N = \begin{bmatrix} 0.007072 & 0.000049 & 0.0059 \\ 0.000049 & 0.007072 & 0.0059 \\ -0.000589 & -0.000589 & 0.0059 \end{bmatrix} \qquad (5.11)$$

$$O = \begin{bmatrix} 0.0007072 & 0.0000049 & 0.00059 \\ 0.0000049 & 0.0007072 & 0.00059 \\ -0.0000589 & -0.0000589 & 0.00059 \end{bmatrix} .$$

From this example, we see that the AC_1 (AC_2) is mostly due to the noise S_1 (S_2). Especially the parasitic contributions in matrix O are almost negligible and will just give small corrections even though their thermal noise can be large due to their small resistance. Focusing on XC_{12}, it reads:

$$\begin{aligned} XC_{12} = & - \mid M_{31} \mid S_1 - \mid M_{32} \mid S_2 + \mid M_{33} \mid S_{12} \\ & - \mid N_{31} \mid S_{r1} - \mid N_{32} \mid S_{r2} + \mid N_{33} \mid S_{ref} \\ & - \mid O_{31} \mid S_{p1} - \mid O_{32} \mid S_{p2} + \mid O_{33} \mid S_p \end{aligned} \qquad (5.12)$$

where $\mid M_{ij} \mid$ refers to the absolute value of the matrix element M_{ij}. This notation shows that the sign of XC_{12} is not necessary that of the crossed correlated noise S_{12} and that the contribution S_{ref} is always positive. There are different ways to extract S_{12} from XC_{12}. First, if all the contributions other than S_{12} are known, the crossed correlated noise of a sample is known simply by removing those contributions from XC_{12} and divide by M_{33}. Usually, S_1 and S_2 are not known. In that case, the matrix M in equation 5.10 can be inverted and both the spectral densities of noise S_1 and S_2, and the cross-correlations S_{12} can be obtained from measurements.

5.4.3   Calibration for noise measurements

For the following test runs, the macroscopic resistors R_1 and R_2, are mounted in place of a typical sample, in order to simulate future experiments. Since just macroscopic resistors are included in this configuration, we expect that the detected current noise will be given by the thermal noise $S_i = 4k_BT/R_i$ of each resistive element R_i in the circuit (all intrinsic cross-correlations should be zero, since all elements are macroscopic). That's why, in a first step, we determine precise by the resistance of each resistor in the circuit. We find $R_1 = R_2 = 0.88\,\Omega$ and $r_1 = r_2 = R_{ref} = 0.088\,\Omega$ [4]. In the presented data, we get $r_p = r_{p1} = r_{p2} = 0$. For the procedure, how to measure the respective resistors, please infer to 5.4.1.

Fig. 5.7 shows the variation of the six possible measurements as a function of temperature. In order to simulate the real-experiment configuration, one DC current source is connected with zero output, in order to take into account its associated noise which will

---

4. We have performed several runs, always obtaining about the same resistance
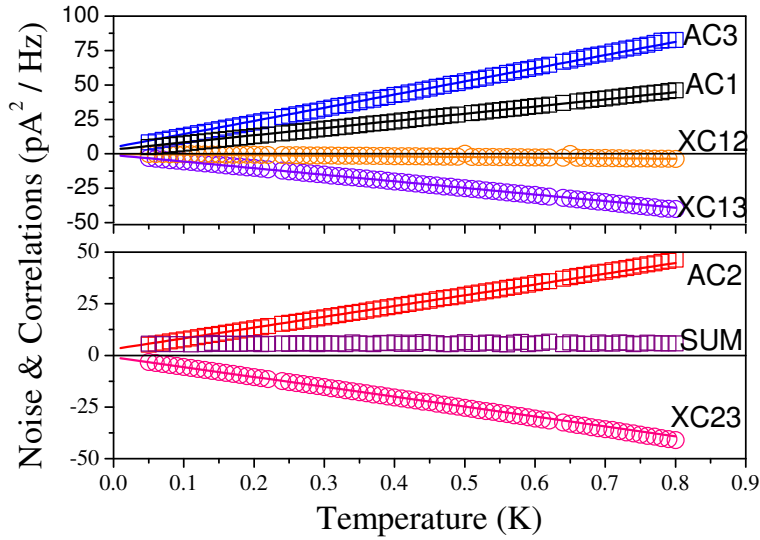
Figure 5.7: Noise AC_i and correlations $XCij$ of the three SQUIDs as a function of the mixing chamber temperature for zero DC current; "SUM" has been calculated in order to verify the current conservation in the circuit (see text); for the measurement scheme, see Fig. 5.6

be present to any future experiments. Furthermore, in order to verify current conservation in the measurement circuit, the sum of all circulating current contributions has been calculated and added to the graph, $"SUM" = (\sum \delta I_{sq_i})^2 = \sum AC_i + 2 \sum XC_{ij}$:

Since in this calibration run all resistors in the measurement circuit are macroscopic, all the correlation terms S_{ij} are zero. Knowing the values of the macroscopic resistors, we can compare the data of Fig. 5.7 with eq. 5.9. The only unknown quantities are the contributions of the set-up noise, which can be found by extrapolating the data to zero temperature. We find a set-up noise level of the order of $2 - 3\,pA^2/Hz$, which is close to the noise level given by manufacturer, see Table 5.1. Concerning the cross-correlations XC_{ij}, the solid lines in Fig. 5.7 assume no intrinsic cross-correlation, i. e. $XC_{ij}^0 = 0$.

The fair agreement confirms that there exist no measurable correlations between the 3 SQUID output signals. If we focus now on each measurement in detail, we find that there is a deviation of about 8 % between the slope of the measured signals and their fits. This has been observed systematically in all measurements and does not match neither with additional parasitic resistors nor with deviations in the amplification gain. However, if we assume that the temperature T^* of the resistors is different from the temperature T of the mixing chamber, we obtain a perfect fit with

$$T^* = 0.92\,T \qquad (5.13)$$

The origin of the temperature mismatch is unclear. We have also checked by sweeping the temperature up and down, that this difference is not due to some thermalization delay. Because of lack of time, we decided to accept the error of 8 %, which is remarkable enough for such complex measurements.

In a second test, we measure noise and correlation as a function of a DC current at fixed temperature. For these measurements, the current source I_{dc1} is used. We sweep the current up to 1.5 mA at fixed temperatures of 100, 300 and 500 mK. A typical result is shown in Figure 5.8, at a temperature of 100 mK. Because of the macroscopic nature of our resistive elements, the detected noise should be given by the thermal noise of the
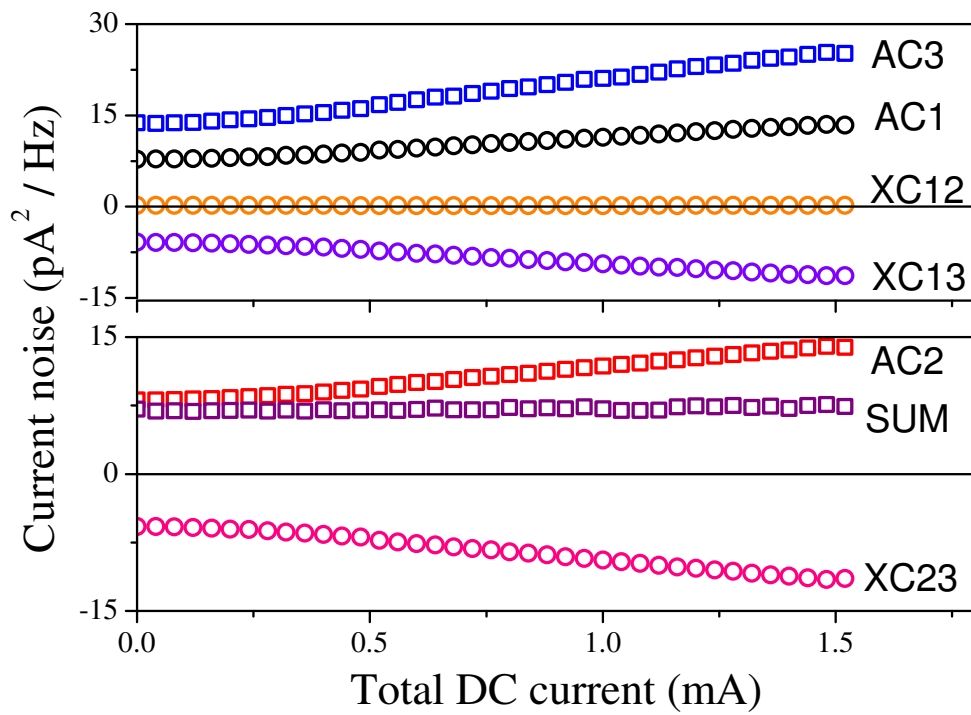
Figure 5.8: Noise AC_i and correlations $XCij$ of the three SQUIDs as a function of the total DC current I_{dc1} applied on reference resistor side at 100 mK.
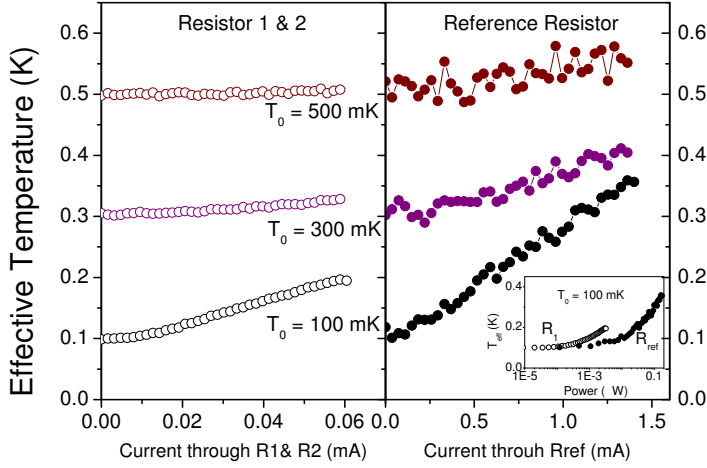
Figure 5.9: Electronic temperature of the reference resistor R_{ref} and of the sample resistors R_1 and R_2 as a function of the dc current flowing through each of them for three different regulated temperatures. The inset shows the effective temperatures at a base temperature of 100 mK as a function of the dissipated power.

resistors. However, a clear increase of noise and correlation can be seen with increasing the total current, which is due to the rise of the electronic temperature of the resistors in the circuit due to Joule heating, even if the mixing chamber temperature was kept regulated at 100 mK. As we will show, we can now extract the effective temperature of each resistive element in the measurement circuit, but for that we have to make some assumptions:

First, since the biasing resistors R_{ref}, r_1 and r_2 are anchored directly on the mixing chamber, their thermal coupling to the bath is better than that of R_1, R_2, which are used to simulate future samples. Furthermore, as $R_{ref} << R_1, R_2$, the amount of current flowing in R_{ref} is much larger than that flowing through R_1 and R_2. Finally, the symmetry of our circuit helps us to simplify by considering $T_{R_1}=T_{R_2}=T_R$ and $T_{r_1}=T_{r_2}=T_r$ where T_R is the effective temperature of a resistor R - both temperatures being different from T_{Ref}. In order to estimate the effective temperature, we use AC_1 and AC_3. By considering purely thermal noise, we get:

$$AC_1 = \alpha_1 T_R + \alpha_2 T_r + \alpha_3 T_{ref} + AC_1^0$$
$$AC_3 = \beta_1 T_R + \beta_2 T_r + \beta_3 T_{ref} + AC_3^0$$

$$(5.14)$$

where for instance $\alpha_1 = 4k_B(M_{tot_{11}}/R_1 M_{tot_{12}}/R_2)$ and AC_1^0, AC_3^0 the respective set-up noise of each SQUID (obtained from 5.7). A further simplification of the equations can be achieved by neglecting the current noise contribution of resistors r_1 and r_2, which is justified regarding their weight of contribution: on one hand, $\alpha_1 \approx 10\,\alpha_2$ (same for β_1); on the other hand, the current in r_1 and r_2 is much smaller than through R_{ref} [5]. Finally, the results of the effective temperature, obtained from Equation 5.14 are depicted in Figure 5.9.

As we can see, the temperature increase gets weaker as the base temperature is raised, and for temperatures above 500 mK, the temperature increase almost disappears. This behaviour can be explained by the increase of the electron-phonon coupling as the temperature is raised. Furthermore, we see a more pronounced temperature increase in the reference resistor as in the sample resistors. This effect is strongest for the lowest investi-

---

5. More detailed calculations, taking into account all contribution confirmed the result.

gated temperature ($T_{base} = 100\,mK$). The maximal temperature-difference ΔT between base-temperature T_{base} and resistor for the reference resistor is $\Delta T_{ref} = 250\,mK$, whereas for the sample resistors, we find $\Delta T_R = 100\,mK$. As an inset, we show the effective temperature as a function of dissipated power $P = RI^2$ in each resistor - the different traces for T_{ref} and T_R reflect their different coupling to the mixing chamber. Even if we have found an increase of the effective temperature, its contribution for future experiments stays moderate but should be taken into account especially for cross-correlation measurements.

5.5 Technical measurement details

For the moment, the noise measurements have been presented somehow as a "black box". But how do we proceed to measure the spectral noise density?

As mentioned in section 5.3, the SQUID electronics gives us a voltage-value, which is proportional to the current-induced flux in the SQUID-loop. With the help of a spectrum analyzer, the voltage fluctuations $\delta V(t)$ can be decomposed in a frequency spectrum by Fourier transformation. Usually, we use the options "Power spectrum" and "Cross-Spectrum", both in units V^2/Hz. Then the amplitude at a given frequency gets normalized with respect to the band width of the system. This quantity is equivalent to the spectral noise density, $S_v(f)$.

5.5.1 Cut-off frequency of the set-up and separation of noise contributions

In Fig. 5.10, we present the noise spectrum over the whole accessible measurement range, obtained for a fake-sample or different temperatures. At very low frequency, we observe an strong increase in the response, which can be attributed to the 1/f noise. We can also identify the 50 Hz-peaks and its harmonics due to the power line. Between 800 Hz and 7 kHz, we observe a rather flat plateau which will be used to estimate the noise level. At frequencies above 10 kHz, a significant decrease of the noise signal gets visible because of the frequency cut-off of our experimental set-up. Taking into account SQUID input coil inductance and the implemented reference resistors r_1, r_2 and R_{ref}, leads to an expected cut-off frequency $f \approx R_{ref}/2\pi L \approx 10\,kHz$. Experimentally, for all temperature, the noise spectra can be fitted by

$$AC_i(f) = AC_i^0 / \left[1 + (f/f_{cutoff})^2 \right] \tag{5.15}$$

Using this formula, we find a cut-off frequency f_{cutoff} of 27 kHz, in agreement with the estimates.

5.5.2 Data acquisition

To extract the spectral noise density level, we choose a frequency range between 800 Hz and 4.2 kHz. In this range, the noise spectra are rather flat (see Fig. 5.10) and only a few peaks appear due to 50 Hz-harmonics. Fig. 5.11a shows a histogram of a typical
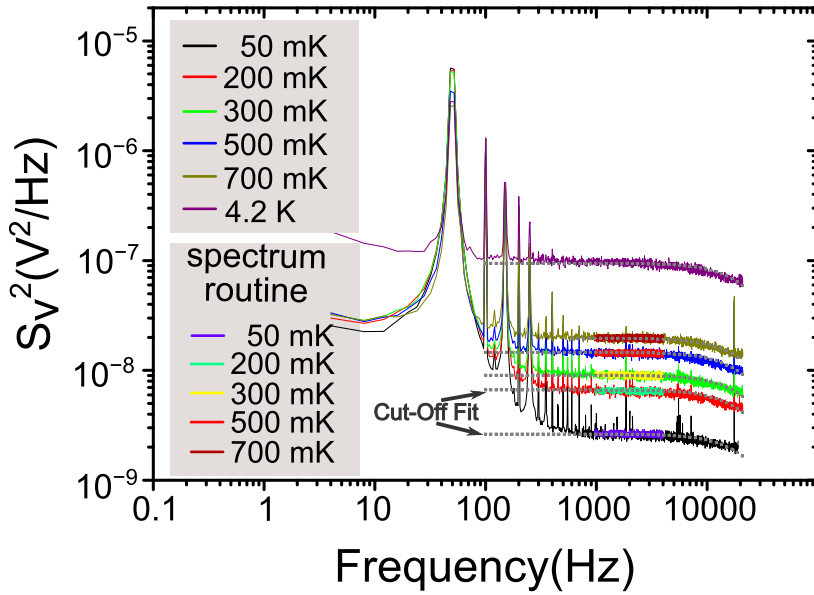
Figure 5.10: Typical noise spectra for different temperatures, provided by our spectrum analyzer (in this example, AC_1); between 50 Hz and 800 Hz, 50 Hz-harmonics appear; we also determine a noise increasing at low frequency due to 1/f noise; From a simple fit, we extract a cut-off frequency of 27 kHz.

spectrum. This curve can be fitted with a Gaussian distribution (see Fig. 5.11a, obtained for AC_1 at 500 mK). The resulting mean value gives the noise level (see red dashed line).

For routine experiments, this procedure is a bit too complicated and takes to much time. We use instead the following measurement routine, created by Olivier Coupiac, which has been approved over years in the Laboratory. The procedure is to remove the first 30 and the last 20 points as well as the 20 highest peaks of a spectrum. Fig. 5.11b shows some spectra obtained for different temperatures. The noise level is then obtained by taking the mean value of each spectrum. The dashed line shows this noise level at 500 mK. A general comparison of the two techniques, is shown in Fig. 5.11c. Even if there is a small discrepancy between the two techniques, it shows that the mean-value technique extracts with sufficient accuracy the noise level.
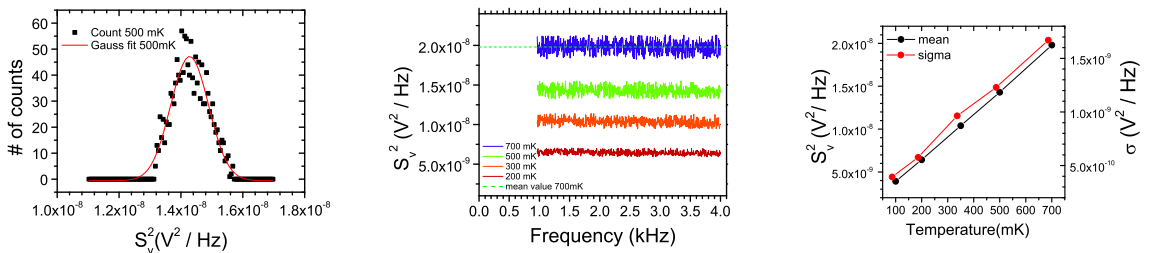
(a) Histogram of the spectrum at 500mK: the red curves shows a Gaussian fit

(b) noise density spectrum for different temperatures: the dashed line indicates the extracted mean value

(c) The Comparison of mean-value with Coupiac-methode to that obtained by Gaussian distribution

Figure 5.11: Noise-measurement: Data acquisition

5.5.3   Magnetic field: ultimate challenge for a SQUID set-up

During this thesis, we added the option to apply magnetic field to our SQUID-set-up. This needs some effort, because -as already mentioned in chapter 5 - SQUIDs are powerful sensors for magnetic flux and hence extremely sensitive to all type of external perturbations. For that reason, we tried to keep the magnetic field as local as possible, that its influence on the SQUIDs is negligible. This can be achieved by mounting a magnetic coil directly on lowest 13 cm of the VTI[6]. The magnetic coil consists of a superconducting NbTi[7] wiring, which gives $390\,Gauss/Ampere$. As reference for our tests, we use an exemplary differential resistance line-trace (see Fig. 5.13).
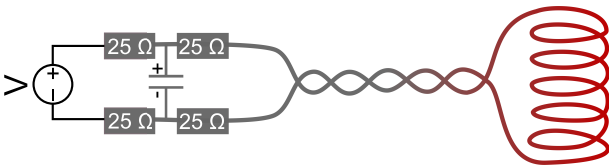
Figure 5.12: Experimental sketch: Magnetic coil, mounted around the VTI is connected to a low noise voltage source; two pairs of $25\,\Omega$ resistances and a $800\,\mu F$ capacitor are connected on each line. This allows to reduce the fluctuations of the voltage source which are sent into the fridge.

In order to generate a magnetic field, we use a low-noise voltage source and connect it with a biasing resistors to the ends of the magnetic coil. Since our low noise sources are limited to a maximal output of $30\,V$ and $110\,mA$, we need low resistive resistors to achieve the maximal available magnetic field. First attempts have been realized using standard $1/4\,W$ resistors, which gives another limit for the magnetic field due to the maximal dissipated power in the resistors. A first working configuration for measurements without perturbing the SQUIDs achieved, when putting two pairs of $25\,\Omega$ resistors and a chemical bi-polar capacitor of $800\,\mu F$ (see Fig. 5.12). Within this configuration, we see that the measurement does not differ significantly with respect to the reference line-trace.

However, within this configuration, the maximal magnetic field is limited to only 50 Gauss. This corresponds maximal to a few flux quantum Φ_0 in the junction area and detailed studies of field dependence is not really possible. In the second configuration, we use $10\,\Omega$ WELWYN aluminium housed resistors, type WH5, which can work up to $10\,W$. Together with the Voltage source Agilent E3633A, we can measure up to $500\,Gauss$, which should be even enough to exceed the critical field B_c of Al. We tried various arrangements, all showed that only a few available voltage sources are stable enough to allow unperturbed SQUID-measurements with magnetic field: Yokogawa 7651, ADRET 104A and Agilent E3633A.

---

6. Variable temperature insert
7. Niobium Titan
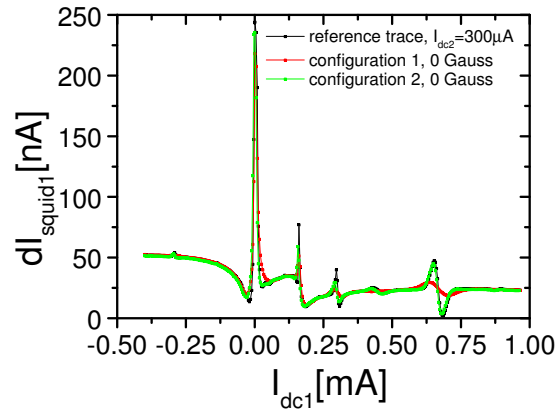
Figure 5.13: Sample T-shape No.2: line-traces within different configurations for magnetic field; reference trace, no power supply connected to magnetic coil; configuration 1 (red): low-noise voltage source as power supply for the magnetic field, with two biasing resistors of $50\,\Omega$ in each line; configuration 2: two biasing resistors in each line, and a bi-polar resistor situated in-between, shunting the Voltage output + and -.

Chapter 6

Electronic transport in diffusive TRI-junctions

In this chapter, we will give first a short overview about the sample fabrication, followed by a general characterization of the junction. We will show, that the general properties such as critical current reproduce the behaviour of 2-terminal SNS junction. Experimentally, we extract the Thouless energy from the temperature dependence of the critical current, in good agreement to the junction area and material constants, which have been found in previous work. Our analysis shows, that a too low de-pairing current and strong excess current restrict our voltage range to low energies ($eV << \Delta$). The features are rather robust in temperature and their amplitude stays constant over a large voltage range which largely exceeds the Thouless-energy.

6.1   Sample fabrication-small overview

For the main part of this thesis, the samples have been fabricated by Hervé Courtois at the Nanofab in the Institut Néel using shadow mask evaporation. All our TRI-junctions consist of aluminium as superconductor and Copper with a purity of 99.9999 % was used as normal metal. The phase coherence length L_Φ in copper is known of previous work to be around $1 - 2\,\mu m$ at 100 mK. We used two different sample designs which we will call in the following "T-shape" and "separated" geometry. In T-shape geometry, the superconducting electrodes share a common normal part (see Fig. 6.1 a)), whereas in separated geometry, the central superconductor is arranged in a way that two spatially separated Josephson junction are formed (see Fig. 6.1 b)). The length of the normal metal varies between 1.0 and 1.3 μm, which exceeds the superconducting coherence length $\xi_s^N = \sqrt{\hbar D/\Delta} \approx 200\,nm$. The diffusion constant in the normal wire is estimated to $D \approx 10^{-2}\,m^2/s$. In Fig. 6.2, the involved steps during the sample fabrication process are illustrated.

In a first step of the sample fabrication, a bilayer of PMMA/MAA resist is spinned on top of a standard Si-substrate (see Fig. 6.2a). In a second step, the mask geometry is designed by e-beam lithography (EBL), see Fig. 6.2b. Since the bottom layer is more sensitive than the top layer, an undercut is assured. After development of the resist, the exposed resist can be removed. If exposure dose and design are well adjusted, regions can be defined, which are only covered by the suspended top layer resist (see Fig. 6.2c). Now,

the sample can be fabricated by evaporation of the normal metal and the superconducting electrodes. Using different angles, allows to evaporate the two materials [1] *in situ*, without breaking the vacuum (see Fig. 6.2d). This allows on one hand highly transparent and reproducible interfaces between the materials, but imposes on the other hand restrictions in the geometry (for instance size and thickness of electrodes).
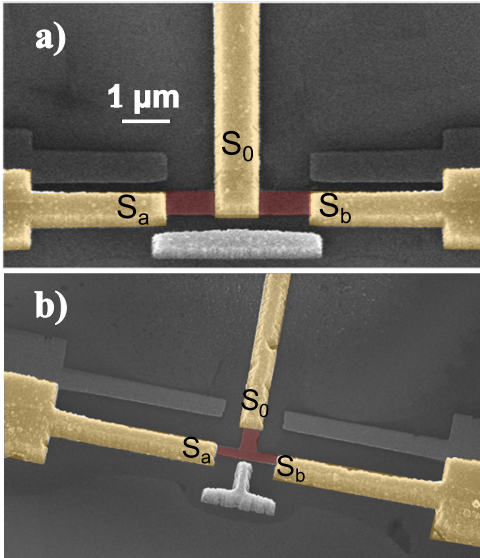
Figure 6.1: measured sample designs: a) separated geometry; b) T-shape geometry; the red coloured part correspond to normal metal parts, whereas the orange coloured parts correspond to the superconducting electrodes S_0, S_a, S_b.

For our samples, 50 nm of Copper is evaporated first (Fig. 6.2e). After changing the angle, 500 nm of Aluminium are evaporated (Fig. 6.2f). After a final lift-off, the last residual of the resist mask can be removed. Finally, we fabricated TiAu contact pads which allow an easier bonding to the chip-holder. These contacts are designed by optical lithography. Usually, the normal resistance of the resulting junctions is quite symmetric $(R_n = R_a \approx R_b)$ and varies between 1.3 and 1.7 Ω between batches of different fabrication runs.

---

1. for our structures: Copper, Aluminium
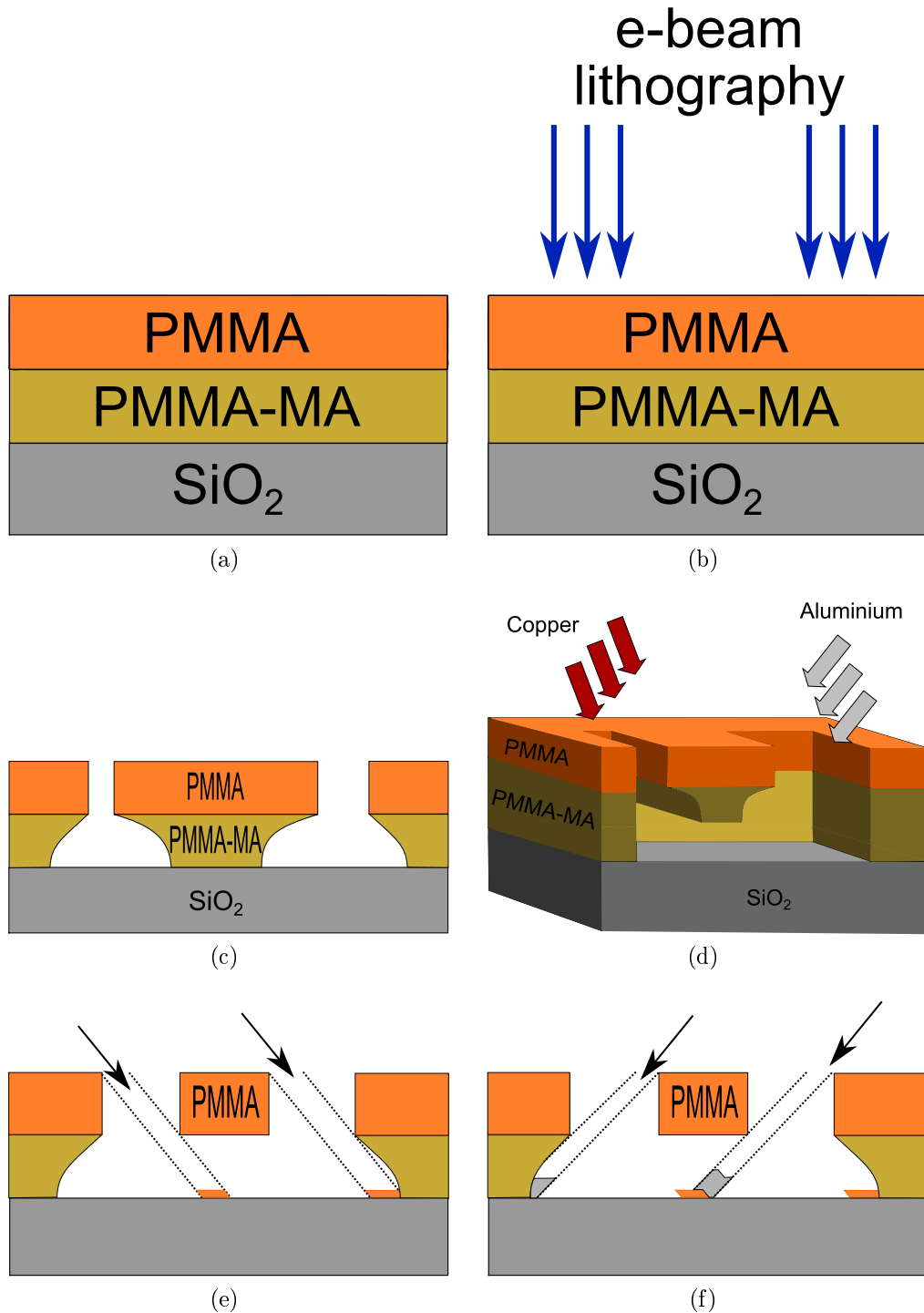
Figure 6.2: Sample fabrication: complete fabrication cycle; a) Covering chip with a double-layer of PMMA-MA/PMMA resist; b) with e-beam lithography, the resist is partly developed; c)-d) the remaining resist builds now some kind of a mask, because the lower resist-layer is more sensitive as the top layer; e) angle-evaporation of Cu; f) angle-evaporation of Al; superposition of Al and Cu at specific regions form the desired geometry

6.2 General characterization

The routine of general characterization before starting serious measurements will be described below. In a first step, sample-intrinsic parameters are measured carefully, such as critical current as a function of temperature. Furthermore, the depairing current of the aluminium electrodes will be determined.

6.2.1 Set-up calibration for DC-measurements

As already explained in chapter 5, our experimental set-up is suited for low-impedance samples. In order to properly control the voltage across the sample, it is necessary to know exactly the resistances of the external resistors. Those include the biasing resistors r_1, r_2 and R_{ref}, but also all kind of parasitic resistance, that could appear due to bonding, soldering or oxidation. Therefore, once a new sample is mounted, some systematic measurement need to be done. As described in section 5.4.1, we have identified three parasitic resistors r_p, r_{p1} and r_{p2}, see Fig. 5.4. As a reminder, we usually obtain the following values, with small deviations ($\pm 5\,m\Omega$) between different measurement runs: $r_1 = 0.090\,\Omega$, $r_2 = 0.091\,\Omega$, $R_{ref} = 0.0885\,\Omega$, $r_{p1} = 0.0565\,\Omega$, $r_{p2} = 0.065\,\Omega$, $r_p = 0.107\,\Omega$.

6.2.2 Critical current: temperature dependence

Below $T \lesssim 800\,mK$, the sample goes into zero resistance state and exhibits a critical current that depends on temperature. Fig. 6.3 shows this behaviour for the T-shape sample No.1. The critical current I_c corresponds to the total current injected into the junction from connection J5. Both junctions have about the same critical current, hence $I_{c,a} = I_{c,b} = 1/2 I_c$. The decay of the critical current I_c with temperatures fits very well with the formula found by Wilhelm et al. [83], see equation 3.4.1.

Interestingly, we obtain the best fit assuming a Thouless energy E_{Th} of $5.25\,\mu eV$, which corresponds exactly to the junction length of $L = 1.2\,\mu m$, obtained from SEM images[2]. Only for temperatures below $150\,mK$, the experimental points deviate from the theory and also other known formulas for the low temperature regime do not reproduce this feature (for instance eq. 3.4.1). At this temper-

Figure 6.3: Critical current as a function of temperature: the red dashed line indicates the fit; below 150 mK, theory and experiment deviate.

ature, small hysteresis appears in the IV-characteristics. Hence, the experimental points below this temperature correspond no longer to the critical current I_c but represent a so-called switching current I_{switch} which is much more sensitive to fluctuations. Indeed, whenever the actual set current value exceeds the critical current due to its fluctuations, the sample jumps into the normal state.
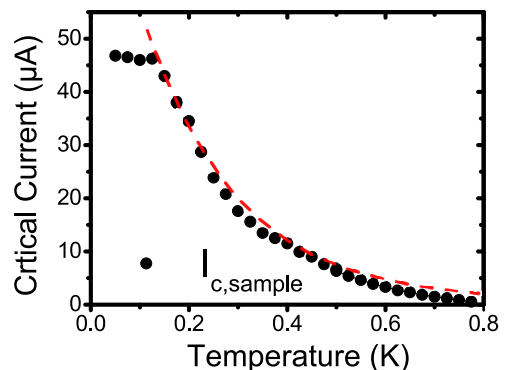
---

2. Scanning Electron Microscope

6.2.3 DC transport: Temperature and voltage dependence

In a next step, we measure the differential resistance of the sample as a function of voltage by sweeping the DC current I_{dc1}. Fig. 6.4 shows the response $R_{diff,a}$ of sample T-shape No.1 for various temperature between 100 and $800\,mK$. The differential resistance shows strong non-linearities above $\approx 100\,\mu V$. We attribute this behaviour to the depairing current of the superconducting electrode that decreases with increasing temperature. Because of this rather low depairing current, sub-gap features that could appear in a voltage range above $50\,\mu V$ are difficult to detect. For that reason, we focused our investigations in the low voltage range below $50\,\mu V$.
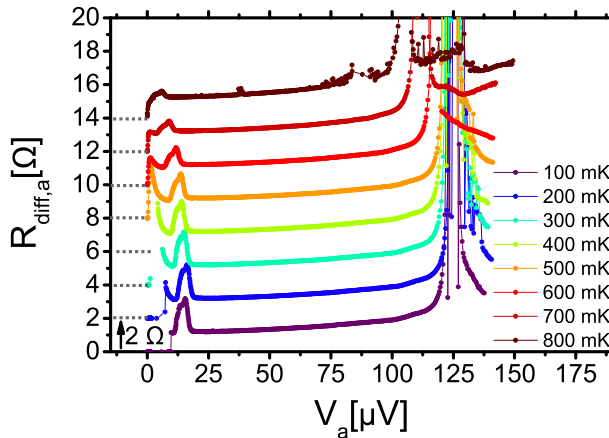

Figure 6.4: Differential resistance $R_{diff,a}$ as a function of voltage V_a for different temperatures. The curves have been shifted for clarity by 2Ω.

6.3 T-shape: hunting for quartets

6.3.1 Measurement procedure

After the general characterization as described above, we proceed to more elaborated experiments. We use two external d.c. current sources to investigate the response of the sample in the entire (V_a, V_b)-plane. The first current source I_{dc1} is usually connected to the J5 connection and the second one to the J1 connection. Since the biasing resistors R_{ref}, r_1 and r_2 have resistances much lower than the normal resistance of a typical sample, the current source I_{dc1} allows varying the voltage V_a and V_b equally i.e. along the first diagonal of the (V_a, V_b)-plane and the second source mainly changes V_a.

Each line within the (V_a, V_b)-plane is recorded using the following procedure: First, an I_{dc2} current is fixed, which sets a certain value V_a by keeping $V_b \approx 0$. Then, the current I_{dc1} at the first source is varied in order to keep V_a and V_b in the $[-50\,\mu V, 50\,\mu V]$ range (see red arrow, Fig. 6.5). For each point along this diagonal line, the ac-currents $\delta I_{sq1}, \delta I_{sq2}$ flowing through SQUID 1 and SQUID 2 are recorded in response to an ac-current $\delta I_{ac} \approx 1\,\mu A$ applied to the J5 connection. Once the line-trace is finished, we increase the current source I_{dc2}, which shifts the following line-trace in V_a (green arrow). The overall procedure is repeated for different values of I_{dc2}, until the (V_a, V_b)-plane is entirely investigated.

Some raw data δI_{sq1} and δI_{sq2} are plotted in Fig. 6.6a as a function of I_{dc1} for different values of I_{dc2}. From these raw data, the differential resistances $R_{diff,a}$ and $R_{diff,b}$ can
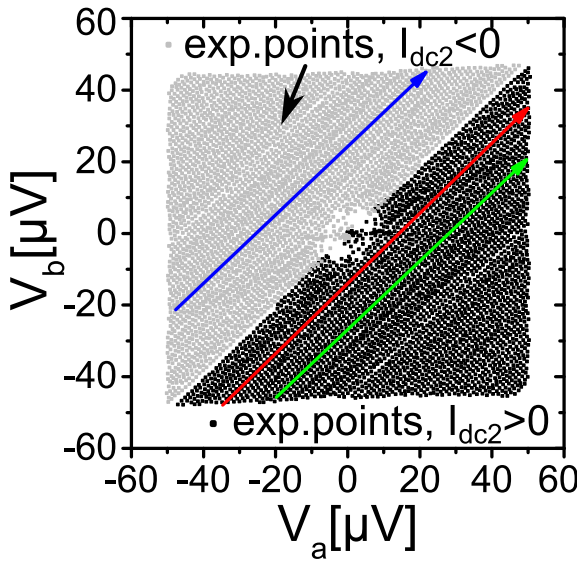
Figure 6.5: black data points: Measurement in the (V_a, V_b) plane for $\pm 50\,\mu V$. For a fixed dc current I_{dc2}, we sweep I_{dc1} which leads to a line-trace, indicated by the red arrow. Variation of I_{dc2} shifts the line-trace, as illustrated by the green arrow ($I_{dc2} = 300\,\mu A$). The grey data are obtained for negative values of I_{dc2}. The blue arrow corresponds to a measurement with $I_{dc2} = -300\,\mu A$. For a comparison of the line-traces $I_{dc2} = \pm 300\,\mu A$, see Fig. 6.7b
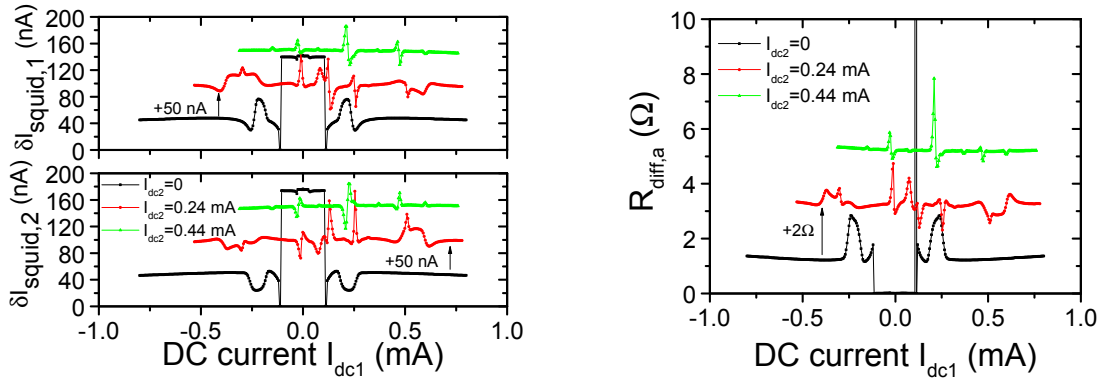
(a) Raw-data δI_{sq1}, δI_{sq2} as a function of dc-current I_{dc1}; the line-traces have been shifted in y-axis for clarity

(b) $R_{diff,a}$ as a function of dc-current I_{dc1}; the line-traces have been shifted in y-axis for clarity

Figure 6.6: Typical line-traces (I), sample T-shape No.1

be calculated following equation 5.5, given in section 5.4.1. The resulting differential resistance $R_{diff,a}$ as a function of I_{dc1} for different values of I_{dc2} is shown in Fig. 6.6b. We see that many features appear, as well in the raw data as in the differential resistance. The discussion of the origin of these features is the main scope of this thesis.

If we focus on the voltage V_a as a function of I_{dc1}, we observe that the overall slope does not change for different I_{dc2} (see Fig. 6.7a). This indicates, that - apart the regions, where V_a or V_b are close to zero - our sample is voltage-biased.

The parameters for this experimental procedure has been chosen in a way, that the overall measurement time is not too large but accurate enough not to miss any features. The increment in I_{dc1} is usually set to $2\,\mu A$, whereas that in I_{dc2} is usually ten times larger. With this conditions, the 2D scan of the (V_a, V_b)-plane can be achieved within ≈ 7 days. In order to reduce the measurement time even more, only half of the (V_a, V_b)-plane is measured as the response of the sample shows a centre point symmetry. Nevertheless, we have checked, that this is indeed the case, by measuring the full (V_a, V_b)-plane for
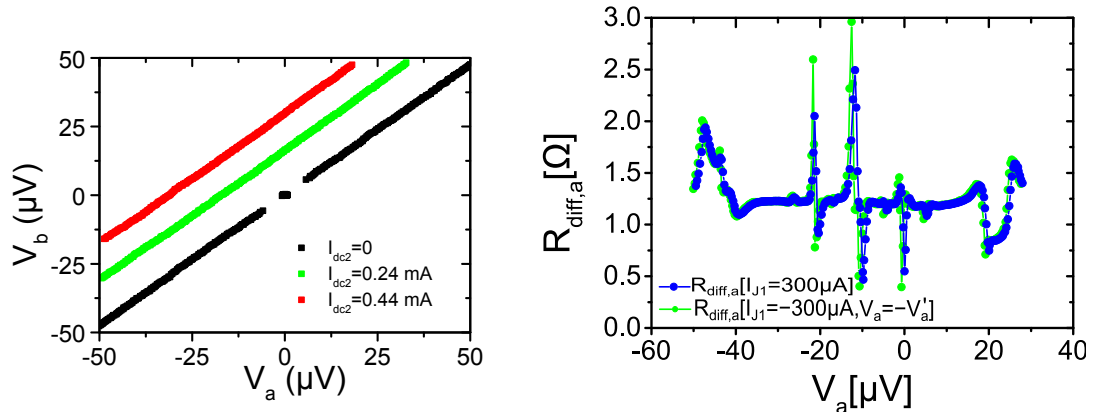
(a) Typical line-traces in the (V_a, V_b)-plane: their overall slope stays roughly the same, except where V_a or V_b are close to zero: this confirms that our experimental set-up is voltage-biased, except around the strong non-linearities due to dc-Josephson-effect

(b) T-shape No1, T=200 mK: comparison of a measured line-trace $R_{diff,a}(I_{dc2} = \pm 300\,\mu A)$

Figure 6.7: Typical line-traces (II), T-shape No.1

sample T-shape No.1 at 200 mK (see Fig. 6.8). For a comparison of a point-inverted line-trace and a real measured one, see Fig. 6.7b.

Because the incremental values of I_{dc1} and I_{dc2} are not equal, the density of points in the 2D-plot is not constant. Moreover, as the X and Y-axis are measured data, the distance between two consecutive points is not constant as well. Therefore, the $R_{diff,a}$-matrix that is used to create the 2D-plot is obtained using an interpolation algorithm. We have checked that this interpolation procedure does not generate any features. However, white dots in Fig. 6.8 appear along the two lines at $V_b = 2V_a$ and blue dots along $V_b = 1/2V_a$. They can be attributed due to the experimental procedure. In Fig. 6.9a, we show a zoom into Fig. 6.8 around $V_b = 1/2\,V_a$, together with the traces, where the differential resistance has been measured. Each green dot corresponds to a measurement point. We can see, that the blue (respectively white) sparkles correspond to the place in the (V_a, V_b)-plane, where measurements cross the feature at $V_b = 1/2\,V_a$ ($V_b = 2\,V_a$). The width of the dots is due to the interpolation procedure and it is limited in the (V_a, V_b)-plane. Since between two white dots (blue dots), there is no true measurement, the interpolation gives the average response of nearest points around, which corresponds to the blue (white) colour level. Fig. 6.9b shows two examples of line-traces, which contain measurement points within the feature $V_b = 1/2\,V_a$.

In Fig. 6.8, obtained at T=200 mK, various features appear, among which several have been never reported experimentally. For $V_a = 0$ or $V_b = 0$, d.c. Josephson effect[3] is expected in junction a, respectively b. Indeed, for $V_a = 0$ or $V_b = 0$, one branch goes into a zero-resistance state like in a conventional two-terminal junction.

---

3. In following discussions, we will use the convention: J stands for DC Josephson effect, the indices 0a indicate the involved electrodes, so Josephson effect between S_0 and S_a ($V_a = 0$) will be named as J_{0a}, dc Josephson effect between S_0 and S_b ($V_b = 0$) will be named as J_{0b}
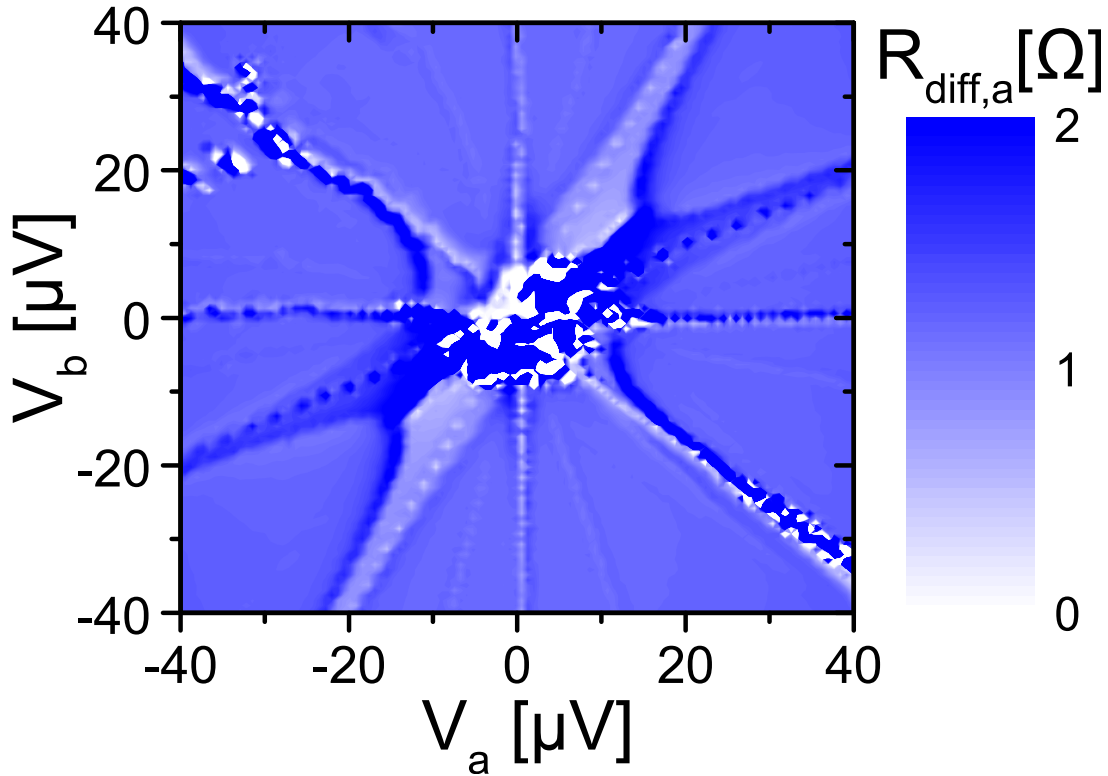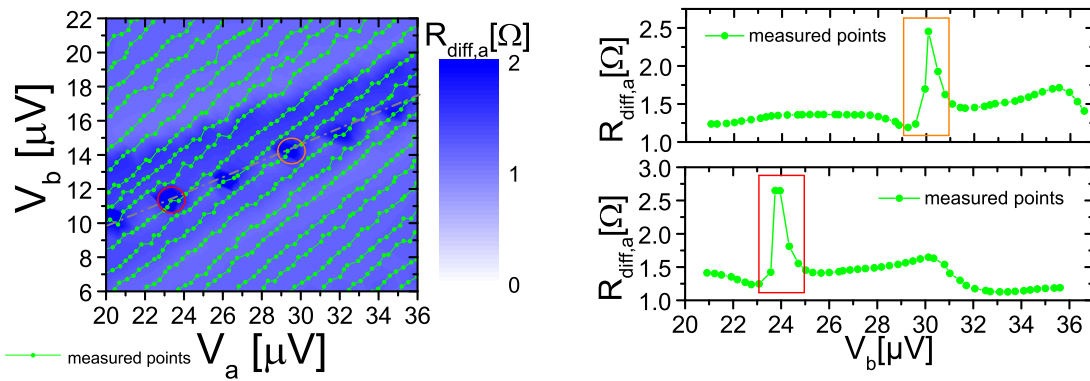
Figure 6.8: Sample T-shape No.1: differential resistance $R_{diff,a}$ as a function of Voltage V_a and V_b at 200 mK.

(a) Zoom in Fig. 6.8 around $V_a = 2\,V_b$; the green dots represent measurement points

(b) extracted linetraces; the marked peaks correspond to the circles in Fig. 6.9a
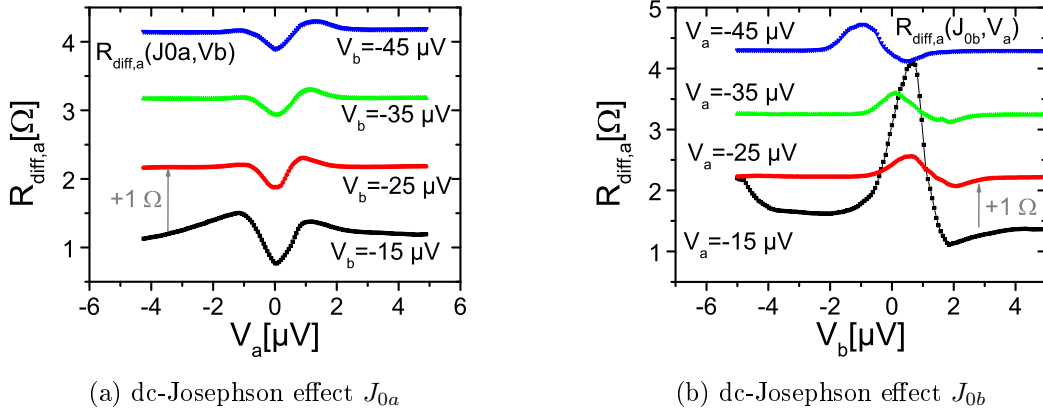
Figure 6.9: Typical line-traces, sample T-shape No.1

(a) dc-Josephson effect J_{0a}

(b) dc-Josephson effect J_{0b}

Figure 6.11: Sample T-shape No.1, $R_{diff,a}$, $T = 200mK$: line-traces for across the dc-Josephson resonances J_{0a} and J_{0b}.

By focusing on the dc-Josephson effect J_{0a}, we see, that the differential resistance $R_{diff,a}$ is not perfectly zero, when $V_a = 0$ and $V_b \neq 0$ but shows a pronounced minimum (see Fig. 6.11a). The reason for this feature is unclear yet, but most probably, non-equilibrium effects, introduced by the fact that $V_b \neq 0$ lead to an important suppression of the critical current $I_{c,a}$. Correspondingly, we observe in Fig. 6.10, that $R_{diff,b}$ shows a pronounced maximum. If we consider the ac-current δI_0 that flows through S_0 (which can be measured by SQUID 3), we find that it is almost constant over the J_{0a}-resonance. Since the ac-current is injected initially at the J5 connection, it indicates, that the overall resis-

Figure 6.10: Typical line-traces of differential resistance $R_{diff,b}$ crossing the feature J_{0a}, as a function of voltage V_b

tance does not vary much. Therefore, if the differential resistance $R_{diff,a}$ decreases, the current in branch a increases. Consequently, as the total ac-current δI_0 is almost constant, the ac-current δI_b on branch b is must decrease leading to a maximum on $R_{diff,b}$.

The same arguments apply for the dc-Josephson effect J_{0b} at $V_b = 0$: it appears as an increase of the differential resistance $R_{diff,a}$ and as a decrease in the differential resistance $R_{diff,b}$.

For symmetry reasons of the sample design, also the dc-Josephson effect J_{ab} - between left and right electrode - would be expected when $V_a = V_b$. There exist several reasons, why we do not observe dc-Josephson effect J_{ab} in these measurements. A first reason of this missing line is, that we are probing with an ac-excitation, situated at J5. This leads to high sensitivity of all processes, that include electrode S_0. However, J_{ab} is a process, that leads to a reduction of the differential resistance between S_a and S_b, and does not

(a) excitation at J1 connection   (b) excitation at J5 connection   (c) excitation at J7 connection
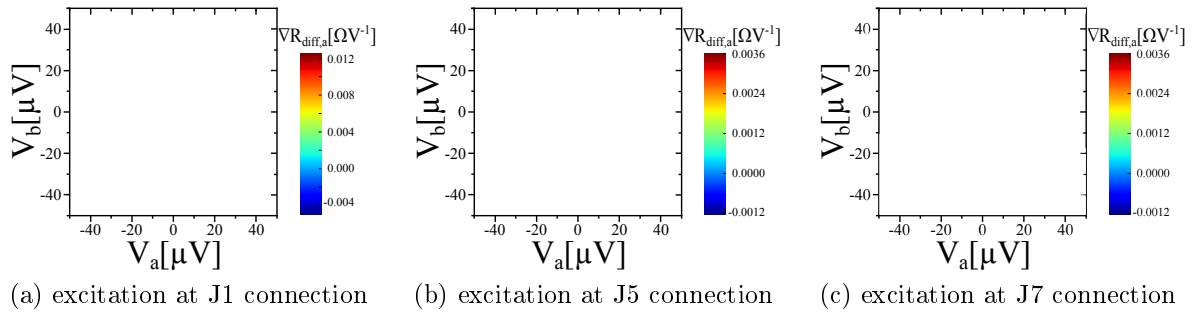
Figure 6.12: T-shape No.2: $R_{diff,a}$ as a function of voltage V_a, V_b for different ways of injecting the ac probe current. In order to improve the resolution of the striking features, a background signal has been subtracted.

affect the way the ac-current is distributed when injected at the S_0-electrode. Therefore, J_{ab} is not seen in plot of Fig. 6.8. Furthermore, as explained in 6.3.1, the measurement-procedure consists to measure line-traces, where the current I_{dc2} is fix and I_{dc1} is varied. This leads to line-traces which are parallel to the expected line at $V_a = V_b$.

We have checked with further experiments in other devices, that J_{ab} can be revealed by putting the ac-excitation on either J1 or J7 (see Fig. 6.12). The presented data originate from T-shape sample No. 2 [4]. Indeed, depending on the place of the ac-excitation, the intensity of the anomalies changes.

For an ac-excitation, situated at connection J5 (see Fig. 6.12b), the same lines appear as already observed for sample T-shape No.1. At $V_a = 0$, a clear line appears due to dc-Josephson effect J_{0a}. Furthermore, lines appear at $V_a = -V_b$, $V_a = 2 V_b$ and $V_a = 1/2 V_b$, as already observed above. Their origin will be discussed below. The dc Josephson effect J_{0b} at $V_b = 0$ is barely visible, since in this experiment, measurements have been performed along V_a-direction: In this sample, line-traces have been taken, keeping I_{dc1} fix and varying I_{dc2}. This leads to line-traces rather oriented along the V_a-axis. Conform to the results of sample T-shape No.1, the dc Josephson effect at $V_a = V_b$ is not visible.

For an ac-excitation situated on J1 (see Fig. 6.12a), a clear visible line appears at $V_a = V_b$, indicating the dc Josephson effect J_{ab}. Off course, also the dc Josephson effect J_{0a} is marked by a clear feature at $V_a = 0$. Again two further lines appear at $V_a = -V_b$ and $V_a = 1/2 V_b$. However, the feature at $V_a = 2 V_b$ is no longer visible.

For an ac-excitation situated on J7 (see Fig. 6.12c), dc Josephson effect J_{ab} shows up as a clear visible line at $V_a = V_b$. Now, the most emphasized line is situated at $V_b = 0$, indicating the dc Josephson effect J_{0b}. Furthermore, two lines appear at $V_a = -V_b$ and $V_a = 2 V_b$. In this configuration however, the feature at $V_a = 1/2 V_b$ is no longer visible.

The most prominent line in the 2D-plot is found at $V_a = -V_b$. This feature corresponds in the picture of quartet-modes [5] to the splitting of two Cooper-pairs of the central electrode S_0, which create two spatially separated Cooper-pairs in S_a and S_b and will be

---

4. Since the features are much weaker than in previous measurements, an algorithm has been applied, which removes the background. The resulting data are derived. Data treatment: Jean-Eudes Duvauchelle

5. For the following discussion, these features will be named for simplicity quartet-modes. The author is aware that no final evidence can be given yet. Nevertheless, various arguments will be detailed in the following, which favour quartet-mechanism as origin of these features.
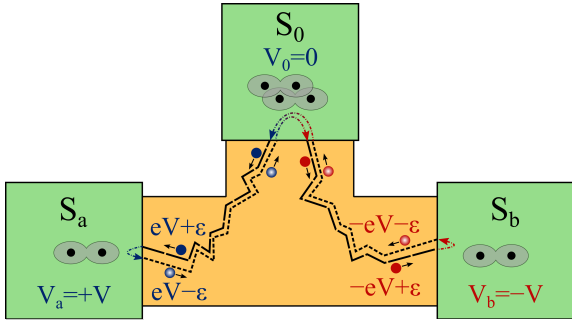
Figure 6.13: When the two junctions are opposite biased, $V_a = -V_b$, splitting of a Cooper-pair in S_0 is favoured into two electrons with energy ϵ due to crossed Andreev reflection. The left electron e_1 with an energy ϵ propagates toward S_a and gains an energy $+eV$, whereas the right electron e_2 moves toward S_b, accumulating an energy $\epsilon - eV$. Both electrodes undergo an Andreev-reflection at S_a (respectively S_b) which create a Cooper-pair in S_a and another in S_b. Afterwards, a hole h_1 with energy $-\epsilon + eV$ and a h_2 with energy $-\epsilon - eV$ return toward S_0 where they can recombine by absorbing a Cooper-pair of S_0. If we consider now the complete process, two Cooper-pairs have been removed from central superconductor S_0 and distributed in S_a and S_b. This process is in striking resemblance with an Andreev-Bound-state, but at Non-zero Voltage. The process of dCAR is also called mechanism of Non-local Quartets due to its distribution of two pairs of electrons [25]

named in the following as quartet-mode Q_0. The Quartet-mode has been introduced in section 4.2.4. For illustration of the Quartet-mode, see as a reminder Fig. 6.13. In the differential resistance $R_{diff,a}$, the Quartet-mode Q_0 gives rise to a large increase of the differential resistance, followed by a slight decrease (see Fig. 6.15a). The strength of the feature shows a maximum in the amplitude at the line-trace obtained with $V_b = 25\,\mu V$. The width of the structure remains rather constant over the investigated range.
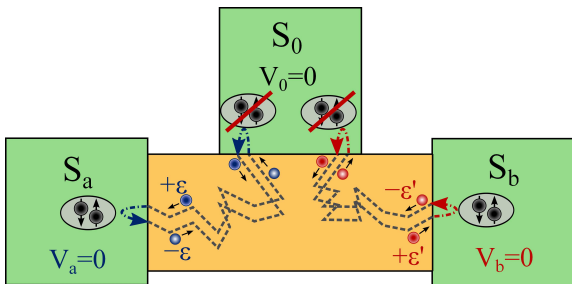
Figure 6.14: Model of the down-mixing process: Whenever $p\,V_a + q\,V_b = 0$ (p, q integer), the ac-Josephson currents in both junctions can interfere. Then, each junction can be associated with an intrinsic microwave source.

For symmetry reasons, two other quartet-modes can exist. First, a quartet-mode, called Q_a, which originates from Cooper pairs emitted from S_a into S_0 and S_b, when $V_b = 2\,V_a$. The second quartet-mode Q_b appears, when $V_b = 1/2\,V_a$, which corresponds to the emission of Cooper-pairs from S_b into S_0 and S_b. At Q_a, a reduced differential resistance is observed and Q_b gives an increased differential resistance in $R_{diff,a}$, see Fig. 6.15. If we consider the structures in $R_{diff,b}$, we observe inverted behaviour. Q_a, a

increased differential resistance is observed and Q_b gives an reduced differential resistance. This change in resistance can be explained in terms of three-terminal mechanism and is consistent with the quartet mechanism. Since the quartet resonance is similar to a Josephson resonance, it leads to an increase in the conductance (respectively decrease of the resistance) towards the reference electrode because of additionally flowing current. Therefore, for a quartet Q_a centred in S_a, the a.c. current sent at S_0 will increase towards the a-branch. As seen in Fig. 6.8, $R_{diff,a}$ shows a decrease at the Q_a resonance. For the Q_b-resonance, the same argument applies and the current towards S_b increases. However, since the a.c. current sent to S_0 is almost constant, as the current towards S_a decreases, an increase of $R_{diff,a}$ can be observed.

Finally, barely visible, small features can be observed on both sides of J_{0a} and J_{0b}. Their origin is not clear yet. They are assumed to be higher-order effects.

(a) Quartet-mode Q_0 (b) Quartet-mode Q_a (c) Quartet-mode Q_b
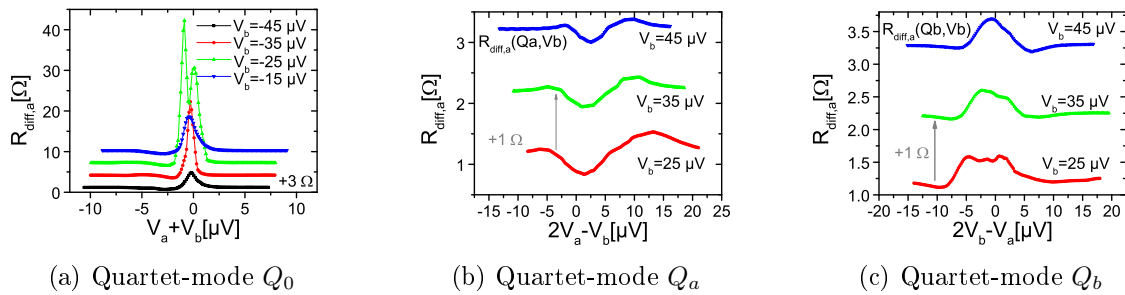
Figure 6.15: T-shape sample No.1: $R_{diff,a}$ as a function of voltage V_a, V_b; line-traces have been taken perpendicular to each of the anomalies, in order to extract its form. The form of resonances is expected to be symmetric to both sides.

In Fig. 6.15, some line-traces have been extracted of Fig. 6.8, perpendicular to the features Q_0, Q_a and Q_b. The line-traces are taken in regular spaces of $10\,\mu V$. The x-axis has been chosen in a way to centre the anomalies at zero. The general form of the Q_0-feature shows a strong asymmetry. For data with $V_a > 0, V_b < 0$, a smooth dip is followed by a huge peak (for $V_a < 0, V_b > 0$, this behaviour is just inverted), the maximum amplitude of the peak is observed in the line-trace at $25\,\mu V$. Concerning the anomaly Q_a, we observe a rather asymmetric dip[6]. The feature Q_b shows a asymmetric, smooth peak in all line-traces. Both, amplitude and width of the anomalies in voltage are rather constant over the whole observed range for the three features Q_0, Q_a and Q_b.

6.3.2 Form of the quartet-anomalies

Even if the general appearance of the features at $V_b = -V_a$, $V_b = V_a/2$ and $V_b = 2\,V_a$ fits to theoretical predictions, their un-symmetric form with respect to the centre of the anomaly is somewhat surprising: since their origin is due to Josephson-like resonances, it would be expected, that their form resembles, too. Obviously, this is not the case. However, since the Quartet-mode is a three-terminal related mechanism, we should consider the sample in its complete geometry. Then, a more suitable measure is given by the

---

6. the line-trace of Q_a and Q_b for $V_a, V_b = 15\,\mu V$ are not shown, since they are situated in the centre of Fig. 6.8, where several features are merged together

differential resistance of the overall sample, $R_{diff,ab}$, where we consider the two junction arms $R_{diff,a}$ and $R_{diff,b}$ in parallel:

$$R_{diff,ab} = \frac{R_{diff,a}R_{diff,b}}{R_{diff,a} + R_{diff,b}} \tag{6.1}$$

Indeed, the total differential resistance $R_{diff,ab}$ shows the same anomalies as described above (see Fig. 6.17). Now however, the Quartet-modes Q_a and Q_b give both a reduction in the differential resistance, as well as the Josephson anomalies J_{0a} and J_{0b} (see Fig. 6.17). Furthermore, the form of the anomaly Q_0 at $V_a = -V_b$, shows the symmetric form as expected for a Josephson-like resonance (see Fig. 6.16).
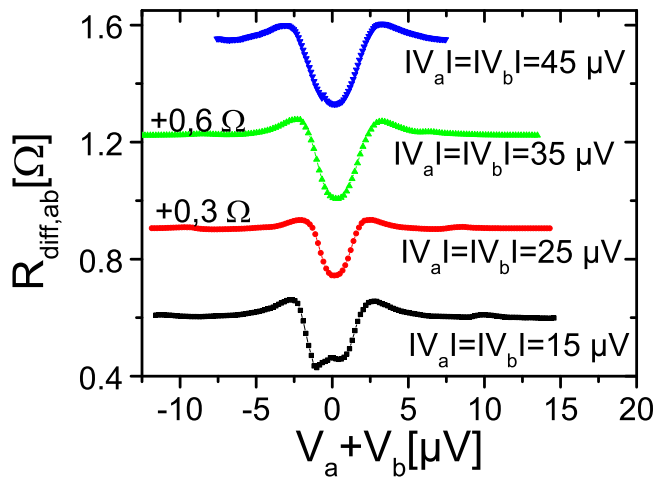
Figure 6.16: T-shape sample No.1, line-traces of $R_{diff,ab}$ for different voltage V_a, V_b, taken perpendicular to the Q_0-feature

6.4   Discussion: Quartets vs down-mixing: how to discriminate?

As already introduced in section 4.2, there exist several models, which predict features, appearing at $pV_a + qV_b = 0$ (with p,q being integers). First, we discuss the model proposed by Houzet and Samuelsson [24] (see also section 4.2.2). Even though their predictions apply very well to our geometry, the underlying mechanism to explain the sub-gap features in the three-terminal Josephson junction is related to trajectories that bring a quasi-particle above the gap. We know that, at low voltage, those are interrupted by inelastic collision and therefore, these sub-gap features does not show up in the differential resistance at low voltage. Therefore, we can exclude this model, as the features we observe are visible down to very low voltage.

Another possible mechanism would be the so-called voltage-locking or down-mixing (section 4.2.1). Within this mechanism, the ac-Josephson currents of two junctions - in our case junction a and b - interfere and produce features in the IV-characteristics of the device, whenever $pV_a + qV_b = 0$ (with p,q being integers). This process can be understood as well as Shapiro-steps, caused by an on-chip microwave-source, which corresponds to the second junction.
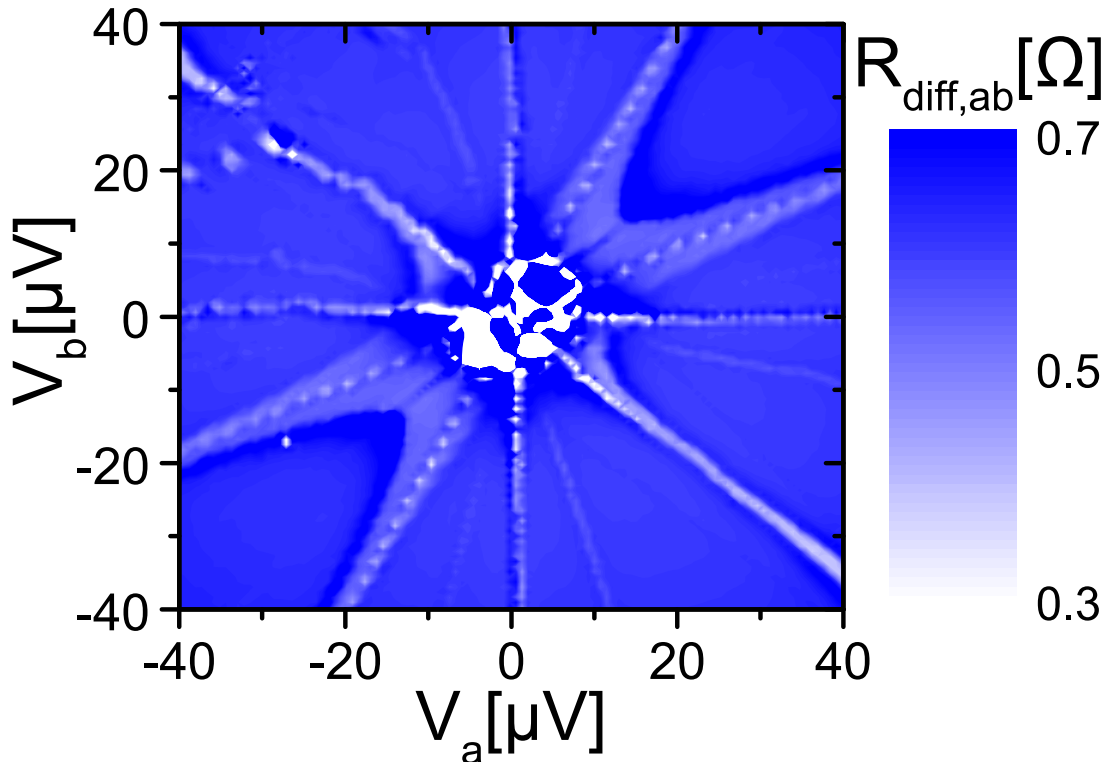
Figure 6.17: T-shape No.1: differential resistance $R_{diff,ab}(V_a, V_b)$ as a function of voltage V_a and V_b at $T = 200\,mK$

What are the ingredients for the existence of the voltage-locking or down-mixing mechanism?

First, we need a non-linear behaviour of the junctions. The non-linearity is a core property of hybrid nanostructures and has been extensively in two-terminal devices [30,65, 70,80]. Since we are dealing with hybrid nanostructures, this condition is full-filled. The observation of the dc-Josephson effect J_{0a}, J_{0b} in our junctions over the whole measurement range is a clear proof.

Second, we need two ac-Josephson currents, which can interfere. As explained in section 3.3, the ac-Josephson effect can be revealed in form of Shapiro-steps, when the junction is irradiated by a microwave signal. Indeed, Shapiro-steps have been observed in Two-terminal Josephson junctions with comparable dimensions of our junctions (see Fig. 6.18). The presence of ac-Josephson effect has been even verified in such two-terminal superconducting hybrid nanostructures up to $eV > 3\,E_{Th}$. Chiodi even reports Shapiro-steps up to six times the Thouless energy E_{Th}. Nevertheless, the ac-Josephson is a coherent process. That means, that the amplitude of the ac-Josephson current should decrease when increasing the voltage above the Thouless energy E_{Th}/e.

Even if though this decrease may not be sharp, we expect the ac-Josephson current of a long Josephson junction to decrease significantly as the voltage gets larger than E_{Th}/e. Therefore, if down-mixing would be the mechanism explaining our features, those should decrease in amplitude as V_a and V_b increase. As shown before, the observed resonance does not change neither in amplitude nor in width as the voltage V_a and V_b are raised.

For that reason, it is very unlikely, that synchronization of two ac-Josephson-currents can explain our observation.
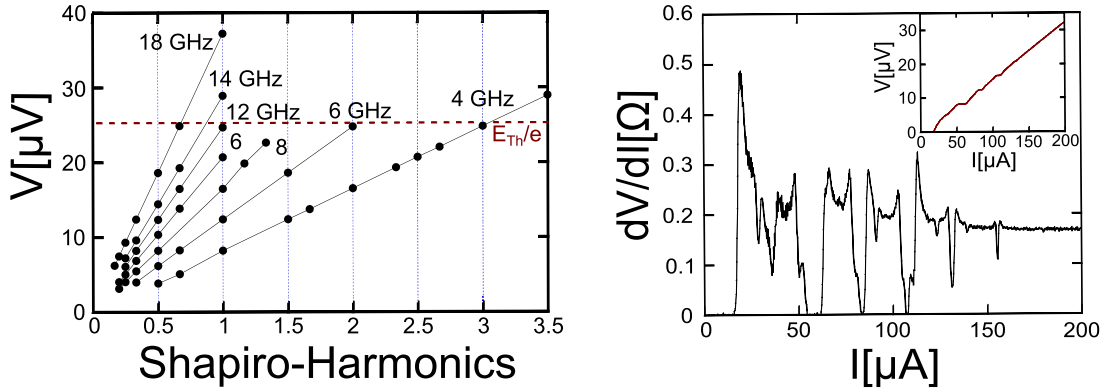
Figure 6.18: Shapiro-measurements by Dubos et al.; left: observed Shapiro-harmonics for different voltage and the applied microwave frequency.
right: typical differential resistance spectrum as a function of current; the observed peaks correspond to Shapiro-steps, in the upper insert, the corresponding IV-characteristics is given [80]

Finally, we can state: Two theories persist, which are in general consistent with our experimental observations in the coherent regime: Voltage-locking and the Quartet-mechanism. Even if the arguments presented above favour the quartet-mode as an explanation of the experimentally observed features, no final proof can be given, unless there is no full mesoscopic theory, which takes into account all possible mechanism. However, as a first approach, we can generalize the RSJ-model (introduced in section 3.5) into an appropriate model for our three-terminal junctions. We hope that this rather simplified model can deliver eventual hints how to distinguish features, which arise from the two theories. This work has been performed in cooperation with Régis Mélin and Denis Feinberg (Institut Néel, Grenoble) (see section 6.4.1).

From experimental side, there exist a few parameter which can be explored, such as temperature and magnetic field. These results will be discussed below as well.

6.4.1 Extended RSJ-model for Tri-junction

We have developed a simple model based on the RSJ-approach applied to our geometry (Fig. 6.19). It consists of three resistors connected by a common central node and three pure Josephson couplings. The model has an uni-axial symmetry. This means that only the junctions $S_0 - N - S_a$ and $S_0 - N - S_b$ have the same length. For the normal branch, this asymmetry is taken into account by the parameter γ. We define $R_a = R_b = R$ and $R_0 = \gamma R$. In the same way, we parametrize the coupling of the Josephson junction between S_a and S_b by the parameter β.

The total current in each node writes $i_{0,a,b} = i^S_{0,a,b} + i^N_{0,a,b}$, where $i^N_{0,a,b}$ describes the current through the resistive branch and $i^S_{0,a,b}$ corresponds to the Josephson current. This

gives two equations for the current

$$i_a = i_a^n + i_a^s = i_a^n + i_c \sin(\phi_{0a}) - \beta i_c \sin(\phi_{ab}) \tag{6.2}$$

$$i_b = i_b^n + i_b^s = i_b^n + i_c \sin(\phi_{0b}) + \beta i_c \sin(\phi_a - \phi_b) \tag{6.3}$$

where $\phi_{0a} = \phi_0 - \phi_a$, $\phi_{0b} = \phi_0 - \phi_b$ and $\phi_{ab} = \phi_a - \phi_b$.

In this model, the voltage across the junctions is just described by the current through the resistive element of the junctions R, hence

$$V_a = \frac{\hbar \dot{\Phi}_a}{2e} = -R(\gamma + 1)i_a^n - \gamma R i_b^n = -R(\gamma + 1)(i_a - i_a^s) - \gamma R(i_b - i_b^s) \tag{6.4}$$

$$V_b = \frac{\hbar \dot{\Phi}_b}{2e} = -R(\gamma + 1)i_b^n - \gamma R i_a^n = -R(\gamma + 1)(i_b - i_b^s) - \gamma R(i_a - i_a^s) \tag{6.5}$$

From eq. 6.4, we already notice that the feature due to dc Josephson effect, centred at $V_a = 0$, will appear when

$$R(\gamma + 1)i_a^n = -\gamma R(i_b^n) \tag{6.6}$$

Therefore, plotted in the (I_a, I_b)-plane rather than in the (V_a, V_b)-plane, the $J_{0a}-$ and J_{0b}-features should appear along tilted lines. This will allow us to extract the quantity γ directly from our experimental data.

Using eq. 6.2, eq. 6.4 can be written as

$$V_a = -R(1 + \gamma)i_a - \gamma R i_b + R(1 + \gamma)i_c \sin(\phi_{0a}) + \gamma R i_c \sin(\phi_{0b}) + (1 + 2\gamma)\beta i_c \sin(\phi_{ab}) \tag{6.7}$$

$$V_b = -R(1 + \gamma)i_b - \gamma R i_a + R(1 + \gamma)i_c \sin(\phi_{0b}) + \gamma R i_c \sin(\phi_{0a}) + (1 + 2\gamma)\beta i_c \sin(\phi_{ab}) \tag{6.8}$$

As in the two-terminal case, equation 6.7 can be solved easily, if the system is in a current-bias configuration ($di/dt = 0$) or in a voltage-bias configuration ($dV/dt = 0$) Our experimental set-up however is neither purely voltage- nor purely current-biased. For $i < i_c$, it is current-biased, whereas for $i > i_c$, it is in a voltage-bias situation, even if not perfect, since $r_1 = r_2 = R_{ref} \approx 1/10 \, R_s$.

In a second step, we will now include the experimental environment in the model. Experimentally, the voltage V_a and V_b are controlled by two external current sources, I_{dc1} and I_{dc2}. This gives

$$\begin{aligned} V_a &= R_{ref}(I_{dc1} + i_a + i_b) - r_1(I_{dc2} - i_a) \\ V_b &= R_{ref}(I_{dc1} + i_a + i_b) + r_2(i_b) \end{aligned} \tag{6.9}$$

The SQUID-inductance will be neglected within this model. For convenience, we will assume, that the biasing resistors have the same resistance $r_1 = r_1 = R_{ref} = r$. We introduce now a parameter ρ, defined as $r = \rho R$ allowing to switch easily between current- and voltage-bias. For $\rho << 1$, the system is voltage-biased, since then $r << R$. On the contrary, for $\rho >> 1$, the system is current-biased, since $r >> R$. With $V_\alpha = R_r I_{dc1} - r_1 Idc2$ and V_β, we get

$$V_a = V_\alpha + 2\rho R i_a + \rho R i_b \tag{6.10}$$

$$V_b = V_\beta + 2\rho R i_b + \rho R i_a \tag{6.11}$$

Combining eq. 6.2 and 6.10

$$V_a = V_\alpha + 2\rho R i_a^s + \rho R i_b^s - \frac{2\rho}{1 + 2\gamma}[(1 + \gamma)V_a - \gamma V_b] - \frac{2\rho}{1 + 2\gamma}[(1 + \gamma)V_a - \gamma V_b] \tag{6.12}$$
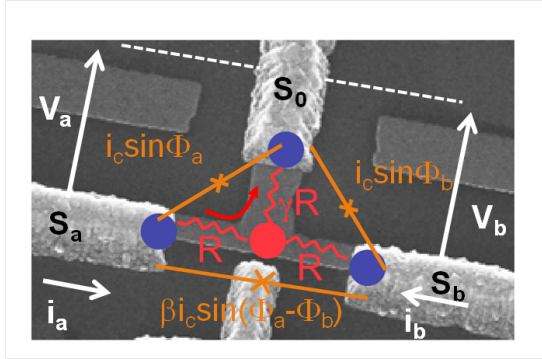
(a) Sketch of the RSJ-model adapted to our device geometry: in red, the resistive circuit is denoted, whereas orange indicates the Josephson coupling of the three junctions.
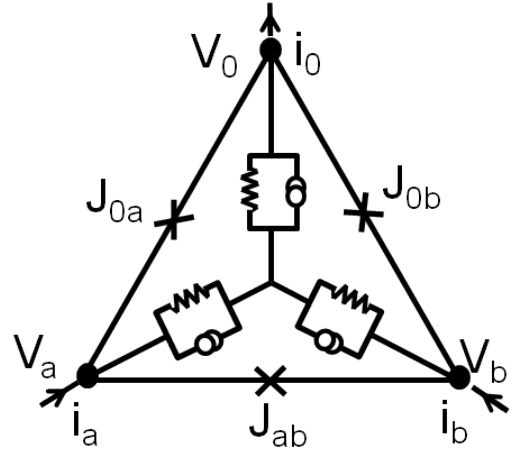
(b) Sketch of the Three- terminal RSJ-model: the resistive branch of Josephson junction is composed of a resistive element R and a noise source in parallel, emitting thermal noise; furthermore, the superconducting channel adds, denoted J_{0a}, J_{0b} and J_{ab}

Figure 6.19: Extended RSJ-model for Three-terminal geometry: the current, coming from S_a is denoted i_a, current from S_b as i_b; the currents i_a and i_b are composed of a normal contribution, i_n and a superconducting current i_s; γ describes the asymmetry in the resistive branch, whereas β takes into account the asymmetry in the Josephson coupling.

$$V_b = V_\beta + (2\rho R)i_b^s + ri_a^s - \frac{2\rho}{1+2\gamma}[(1+\gamma)V_b - \gamma V_a] - \frac{\rho}{1+2\gamma}[(1+\gamma)V_a - \gamma V_b] \quad (6.13)$$

This can be written as

$$M_{aa}V_a + M_{ab}V_b = W_\alpha \quad (6.14)$$
$$M_{ba}V_a + M_{bb}V_b = W_\beta \quad (6.15)$$

where

$$M_{aa} = 1 + \frac{\rho + (1+\gamma)\rho}{1+2\gamma} \quad (6.16)$$

$$M_{ab} = 1 + \frac{\rho(1-\gamma)}{1+2\gamma} \quad (6.17)$$

$$M_{ba} = 1 + \frac{\rho(1-\gamma)}{1+2\gamma} \quad (6.18)$$

$$M_{bb} = 1 + \frac{\rho + (2+\gamma)\rho}{1+2\gamma} \quad (6.19)$$

and

$$W_\alpha = V_\alpha + 2\rho R \sin(\Phi_a) + \rho R \sin(\Phi_b) - \beta \rho R \sin(\Phi_a - \Phi_b) \quad (6.20)$$
$$W_\beta = V_\beta + \rho R \sin(\Phi_a) + 2\rho R \sin(\Phi_b) + \beta \rho R \sin(\Phi_a - \Phi_b) \quad (6.21)$$

Now we include as well the thermal noise of the resistive elements in the circuit, $\delta i(t)$. This leads to

$$W_\alpha = V_\alpha + 2\rho R \sin(\Phi_a) + \rho R \sin(\Phi_b) - \beta \rho R \sin(\Phi_a - \Phi_b) + \delta I(t) \qquad (6.22)$$

$$W_\beta = V_\beta + \rho R \sin(\Phi_a) + 2\rho R \sin(\Phi_b) + \beta \rho R \sin(\Phi_a - \Phi_b) + \delta I(t) \qquad (6.23)$$

The second Josephson relation then reads

$$\begin{bmatrix} \dot{\Phi}_a \\ \dot{\Phi}_b \end{bmatrix} = \frac{2e}{\hbar} M^{-1} \begin{bmatrix} W_\alpha \\ W_\beta \end{bmatrix} \qquad (6.24)$$

Furthermore, terms corresponding to the Quartet-modes can be added. The quartet-contribution adds to the superconducting current $i^S_{0,a,b}$, which gives

$$i^S_{a,full} = i^s_a + q i_c \sin(\Phi_a + \Phi_b) - 2q\beta' i_c \sin(\Phi_b - 2\Phi_a) + q\beta' i_c \sin(\Phi_a - 2\Phi_b) \qquad (6.25)$$

$$i^S_{b,full} = i^s_b + q i_c \sin(\Phi_a + \Phi_b) + q\beta' i_c \sin(\Phi_b - 2\Phi_a) - 2q\beta' i_c \sin(\Phi_a - 2\Phi_b) \qquad (6.26)$$

where q gives the amplitude of the quartet-current compared to the dc-Josephson current, and β' takes into account the asymmetry in the quartet-modes Q_a and Q_b (see Fig. 6.20).
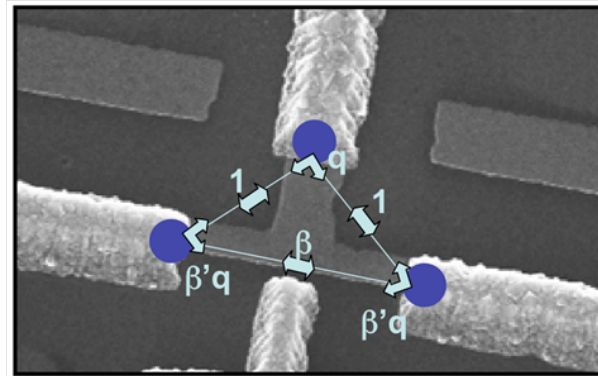

Figure 6.20: Illustration of quartets within the RSJ-model; they add to the couplings of Fig. 6.19a

6.5 Comparison of simulations with the experiment

In section 6.3.1, we have presented experimental results, obtained with sample T-shape No.1. These measurements had been performed in voltage-bias. It arises the question, whether the measurement-configuration (current- or voltage bias) favour one or another mechanism. The effect of temperature will be studied as well.

6.5.1 T-shape: Current-/Voltage bias

By knowing the dc-voltage V_a, V_b, we can calculate the currents i_a^n, i_b^n using eq. 6.9.

The resulting plot of $R_{diff,a}$ in the (I_a, I_b)-plane for sample T-shape No.1 at 200 mK is shown in 6.21a. We can see, that the position of the features has turned with respect to Fig. 6.8. Only the quartet-mode Q_0 is still situated at $V_a = -V_b$. From the position of the features, we can extract the parameter γ, which will be needed for the theoretical simulations, introduced in section 6.4.1. With eq. 6.6, we obtain $\gamma = 0.65$. This is in good agreement with the dimensions, which we can from the SEM-images (Fig. 6.21).
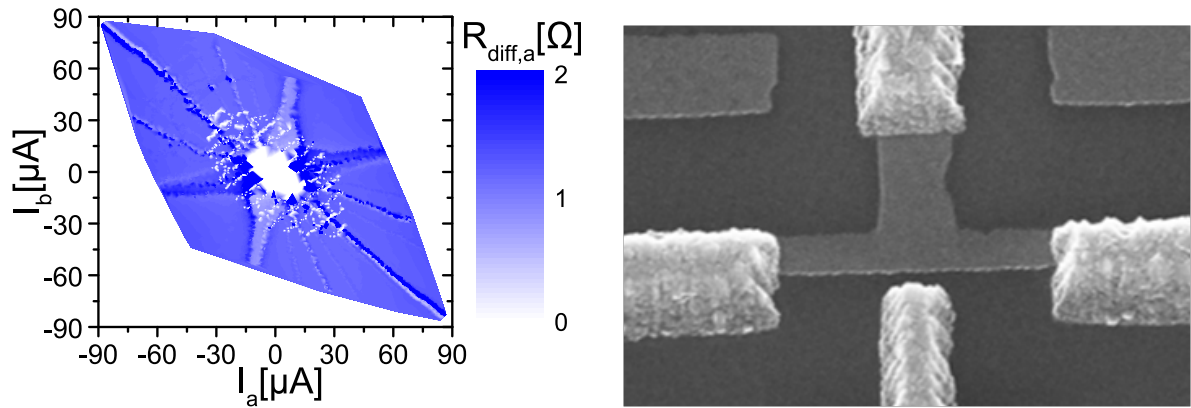
(a) $R_{diff,a}(I_a, I_b)$: T-shape No.1, T=200 mK; voltage-bias configuration

(b) $R_{diff,a}(V_a, V_b)$: T-shape No.1, SEM image

Figure 6.21: Sample T-shape No.1; from the calculated dc-currents I_a, I_b, we can extract the parameter $\gamma = 0.65$ which is in good agreement with the dimensions obtained from the Fig. 6.21a: Plot of $R_{diff,a}$ in the (I_a, I_b)-plane showing the tilting of some features. This allows to extract the γ-parameter $\gamma = 0.65$ in good agreement with the dimensions seen at the SEM image 6.21b.

Furthermore, we tried also measurements in current-bias configuration. In a first attempt, we just removed the ground connections at low temperature.

Unfortunately, this configuration did not allow proper measurements. Fig. 6.22 shows exemplary recorded oscilloscope-signals for SQUID 1. The junctions are biased by $I_{dc1} = 21.2\,\mu A$, situated at J1 and $I_{dc1} = 20\,\mu A$, situated at J7.

Already without any applied ac-excitation, just with a ground connection at J5, oscillations can be observed with $50\,Hz$-periodicity (Fig. 6.22a). The red dashed line gives as 50Hz-signal as a reference. Its amplitude is about $100\,nA$, which is in the order of the expected resolution of our measurements. The origin of this $50\,Hz$-signal is related to ground loops in the experiment. Fig. 6.22b shows, that the $50\,Hz$ Signal is indeed so

strong that it hides completely the response to the ac-excitation, sent at $777\,Hz$. In the case of a $50\,\Omega$ ground plug instead of a direct ground connection at J5, the ac-signal gets visible, but the $50\,Hz$ signal is still dominating (Fig. 6.22c). The only proper measurement of the excitation is possible, if no ground connection is in the measurement circuit. But then, no experiments are possible in a non-equilibrium of the sample.

(a) no ac-excitation, ground at J5

(b) $I_{ac}^{J1} = 100nA$, ground at J5

(c) $I_{ac}^{J1} = 100nA$, 50Ω ground at J5
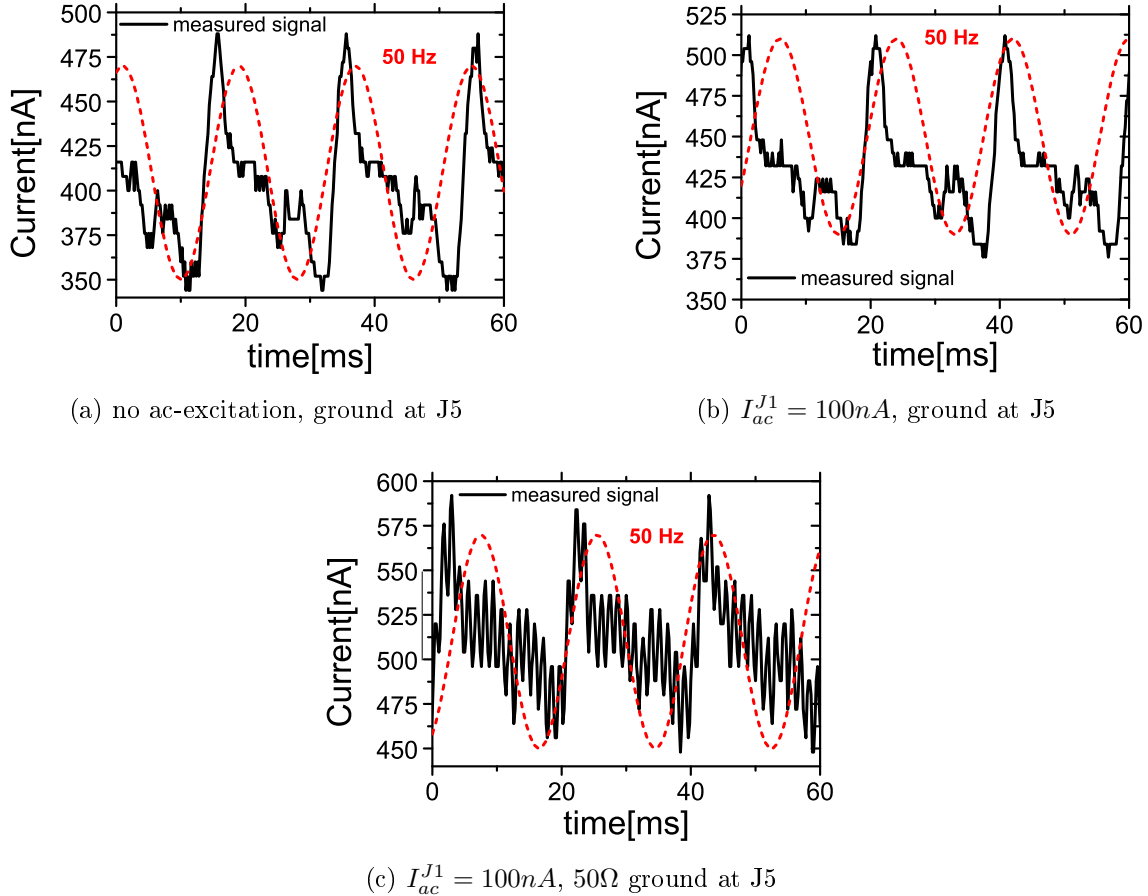
Figure 6.22: sample T-shape No. 5: 50 Hz-noise, due to Ground at room temperature

In a second attempt, we choose a configuration, where a the ground connection close to R_{ref} is kept at low temperature. In this way, we avoid the ground loop of the previous experiment, but are less flexible in the experiment, since biasing is now only possible with the J1 and J7 connection. Fig. 6.23a shows the differential resistance $R_{diff,a}$ in the (I_a, I_b)-plane of sample T-shape No. 3 in current-bias configuration at 100 mK. We observe two features, situated at $I_b = -4.5\,I_a$ (due to J_{0a}), respectively $I_b = -0.28\,I_a$ (due to J_{0b}). With eq. 6.6, we get for sample T-shape No.3 $\gamma = 0.18$. This is in rather good agreement with the dimensions in the SEM-image (Fig. 6.23b). Apart from the features due to dc-Josephson effect J_{0a} and J_{0b}, no features can be determined in sample T-shape No.3.

The extracted experimental parameter γ can be inserted into our extended RSJ-model.

(a) T-shape No. 3: $R_{diff,a}(I_a, I_b)$, T=100 mK

(b) T-shape No.3, SEM-image
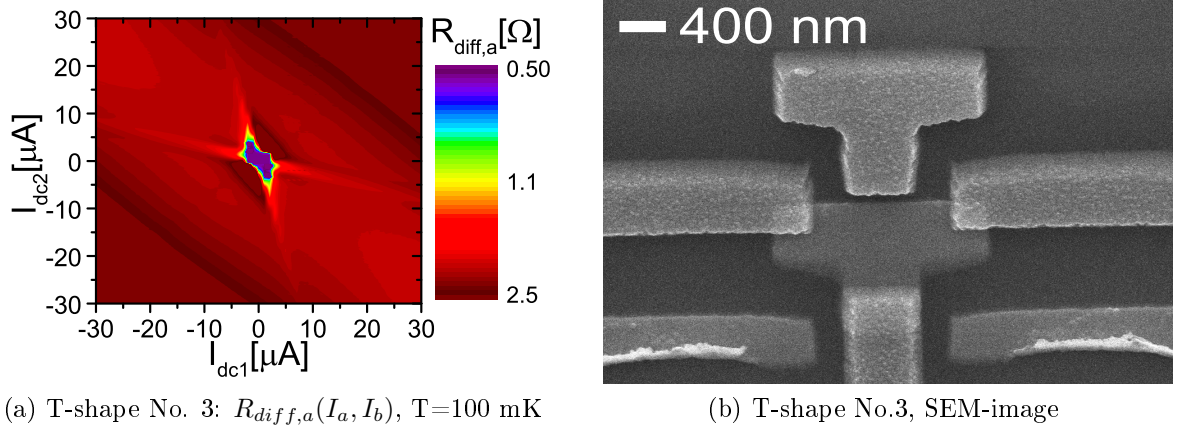
Figure 6.23: T-shape No. 3; Current-bias configuration

6.5.2   Separated geometry $(\gamma = 0)$

The simplest situation for comparing experiment and simulation is for $\gamma = \beta = 0$. In this limit, the geometry simplifies to a Bi-junction, where two spatially separated Josephson junctions share a common superconducting electrode (in our case, S_0). A possible synchronization of the junction then must be mainly mediated by the experimental environment. This mechanism of synchronization corresponds to that, reported by Jillie et al. as Voltage-locking [108] (see also section 4.2.1).

The simulation confirm this expectation: Indeed, just the dc-Josephson resonances J_{0a} and J_{0b} are clearly visible are for both configurations, voltage- and current-bias. However, for voltage-bias configuration (Fig. 6.24a), just barely visible, features appear for $V_a = V_b$, $V_a = 1/2V_b$ and $V_a = 2V_b$. Even less visible, a still smaller feature appears for $V_a = -V_b$.

In the current-bias configuration (Fig. 6.24b), no features appear because the resistance of the biasing resistor is now assumed to be $100\,\Omega$. Therefore, current via the external circuit is almost negligible compared to the voltage-bias configuration.

(a) voltage-bias configuration:
$\gamma = \beta = q = 0;\ R = 1\Omega;\ r = \rho R = 0.1\,\Omega$

(b) current-bias configuration:
$\gamma = \beta = q = 0;\ R = 1\Omega;\ r = \rho R = 100\,\Omega$
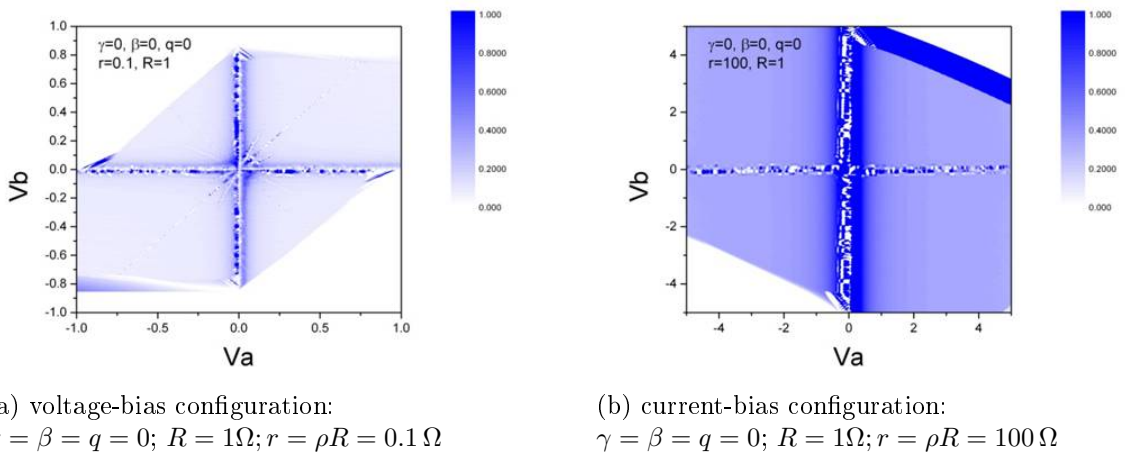
Figure 6.24: Simulations in voltage- and current-bias configuration using our extended RSJ-model, in bijunction configuration $(\gamma = 0)$

In our experimental realization, the normal part N is continuous between the left electrode S_a and the right electrode S_b, but a common superconducting electrode S_0 of a size $L_0 = 600\,nm \approx 3\,\xi_s$ is deposited in-between (see Fig. 6.25a). The proximity effect onto the normal metal just below the S_0 electrode is however strong enough to induce a superconducting gap which corresponds to the superconducting gap of the Aluminium electrodes Δ. Indeed, the thickness of the Copper part underneath this central electrode is 50 nm which is smaller than the coherence length ξ_s of Aluminium.

The length L of each Josephson junction is $1.1\,\mu m$, which is comparable to the length-scale of the studied junctions in the T-shape geometry.

(a) SEM image of the measured sample in separated geometry

(b) $R_{diff,a}(V_a, V_b)$ at T= 100 mK
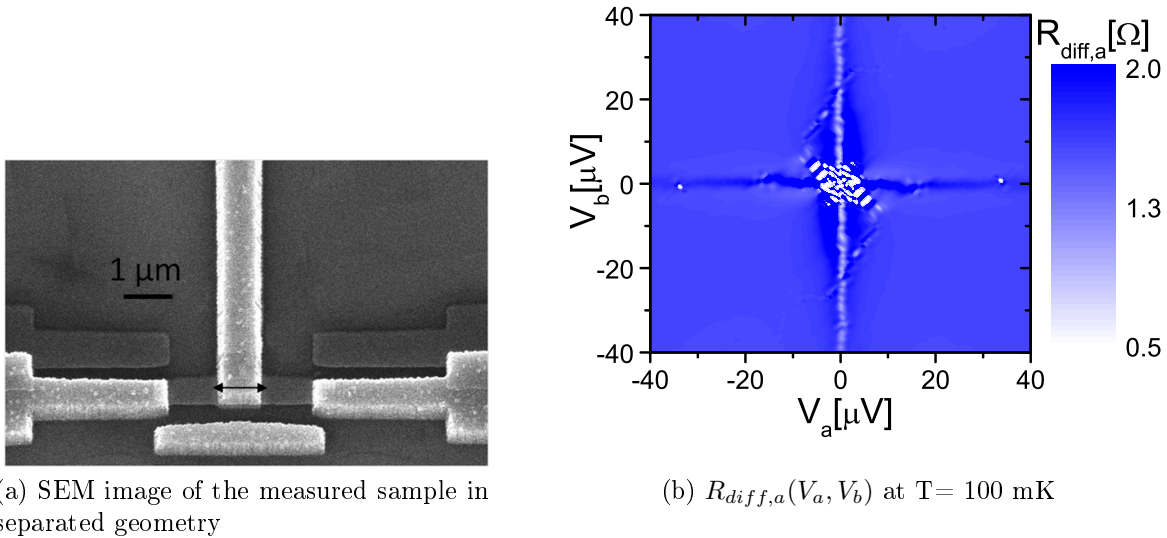
Figure 6.25: Separated Sample No.1 at T= 100 mK: differential resistance $R_{diff,a}$ as a function of voltage V_a and V_b.

In device "separated No.1", we find a critical current I_c of about $5\,\mu A$ in each junction (T=100 mK), with roughly the same normal resistance for both junctions ($R_{n,a} = 1.313\,\Omega, R_{n,b} = 1.317\,\Omega$). In Fig. 6.25b, the differential resistance $R_{diff,a}$ as a function of voltage V_a and V_b is presented for sample separated No.1 (obtained at $T = 100\,mK$). For $V_a = 0$, a minimum in the differential resistance $R_{diff,a}$ is observed, indicating d.c.-Josephson effect. Similar to the T-shape-sample which has been discussed in section 6.3.1, d.c.-Josephson effect in junction a leads to a simultaneous increase of the junction b. Accordingly, as d.c.-Josephson effect arises in junction b at $V_b = 0$, a simultaneous increase of $R_{diff,a}$ is detected in junction a (inverse behaviour in $R_{diff,b}$).

Apart from these described lines, no further features show up in the plot. This plot has been obtained with the standard parameters of T-shape sample. In order to check whether the absence of the additional features could be due to experimental conditions, we changed them in order to increase the sensitivity. In that purpose, we have increased the SQUID gain and also changed the ac-modulation amplitude. Fig. 6.26) illustrates such investigations. The left insert illustrates the location of the chosen $R_{diff,a}$ line-trace with respect to the 2D-plot, presented in Fig. 6.25b. The black trace corresponds to a measurement with a SQUID-amplification of 10, where an ac-excitation $I_{ac,J5} = 20\,\mu A$ was chosen. The red curve indicates the line-trace, performed with the same parameters

as Fig. 6.25b, with a SQUID gain 50 and $I_{ac,J5} = 1\,\mu A$. The green line-trace has been performed with a resolution of $I_{ac,J5} = 300\,nA$ and a maximal SQUID-amplification of 500. The overall-behaviour of the measurement is for all three resolutions reproduced.
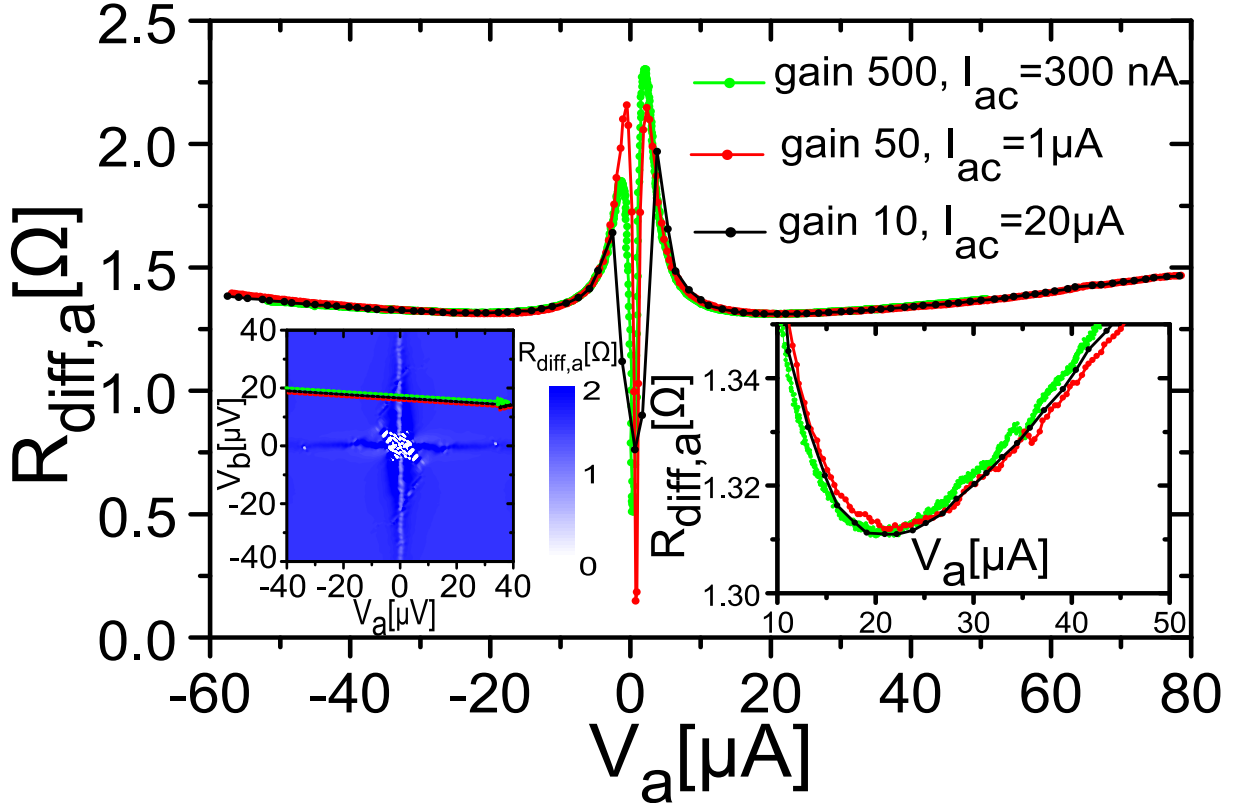
Figure 6.26: **Line-traces, separated geometry, No.1:** line-traces of differential resistance $R_{diff,a}$ for different ac-excitations and SQUID-amplification gains; *left insert:* location of the chosen line-trace in Fig. 6.25b; *right insert:* zoom into the line-traces for $10\,\mu V < V_a < 35\,\mu V$; for an amplification of 50 and 500, a feature around $V_a = 35\,\mu V$ appears, which can be explained by a soldering in measurement-branch a

Certainly, the d.c.-Josephson effect J_{0a} at $V_a = 0$ gets broadened for the line-trace with an ac-current of $20\,\mu A$, since it includes the largest steps between the measurement point. For the other two traces, the d.c.-Josephson effect J_{0a} is reproduced with almost the same accuracy. If we zoom now into the line-trace (see Fig. 6.26, right insert), a small feature is visible in the red and green line-trace at $V_a \approx \pm 35\,\mu V$. Further measurements (line-traces for $V_b > 20\,\mu V$, situated below and above the presented data) with maximal resolution showed, that it systematically appears at $V_a \approx 35\,\mu V$ in all line-traces. The symmetry in voltage, $V_a = \pm 35\,\mu V$ for all traces indicates that the origin of this feature is most probably induced by a transition of a soldering point, situated in junction-branch a.

The results of these detailed studies confirm, that there are no hidden features in the observed voltage-range for the sample separated No.1 like those, which have been observed in the T-shape geometry. Measurements on a second sample in separated geometry confirmed the absence of any features at the observed low-voltage range. For $300\,mK$ and $500\,mK$, only the dc Josephson effect J_{0a} shows up in the differential resistance $R_{diff,a}$

(and J_{0b} is only visible in $R_{diff,b}$). This indicates, that from this temperature on, the two junctions can be really considered as independent.
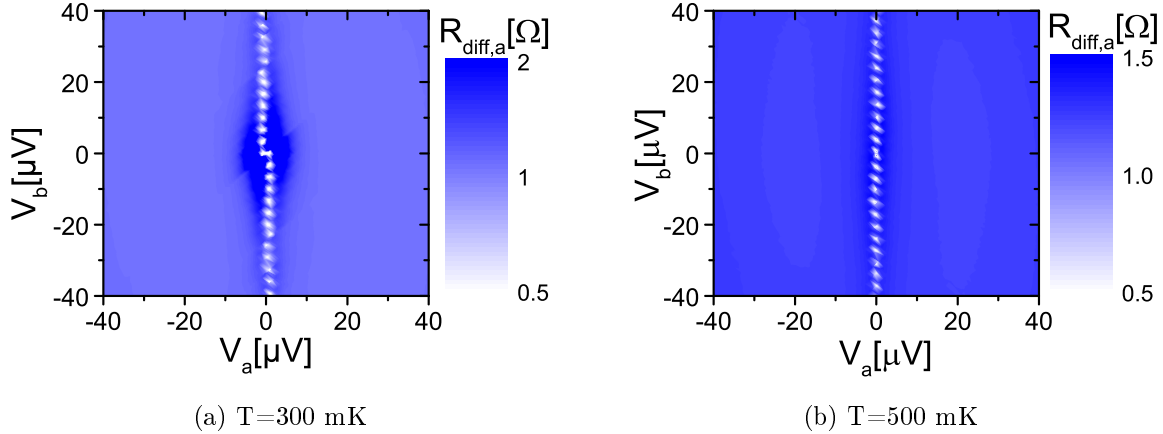

(a) T=300 mK

(b) T=500 mK

Figure 6.27: Separated sample No.2: differential resistance $R_{diff,a}$ in the (V_a, V_b)-plane for 300 and 500 mK. At these temperatures, the two junctions can be considered as independent, since dc-Josephson effect in one junction does not appear in the other.

We also checked, whether some anomalies could be revealed by putting the ac-excitation on other connections. Fig. 6.28 shows the obtained 2D-plots for the device separated No.2. Since the signals are rather weak ($I_c < 3\,\mu A$ at T=100 mK), we plot the raw-data, dI_{sq1} and dI_{sq2}, each in one half of the plot. The blue colour-scale corresponds to dI_{sq1}, the red colour-scale corresponds to dI_{sq2}. The raw-data are more sensitive to any change, because their variations have higher amplitude than the differential resistance $R_{diff,a}$, respectively $R_{diff,b}$. Furthermore, dI_{sq1} is the dominant contribution of $R_{diff,a}$ and dI_{sq2} is the dominant contribution of $R_{diff,b}$. They can be considered as inverse proportional to the respective differential resistance, since now increased current corresponds to a reduced resistance.

For ac-excitation on the J1 connection (Fig. 6.28a), in dI_{sq1}, only an increase shows up for $V_a = 0$, due to the Josephson effect J_{0a}. In dI_{sq2}, we see an increase in the response for the Josephson effect J_{0a} as well as for the dc-Josephson effect J_{0b}, at $V_b = 0$. This can be understood in the sense, that the amount of the ac-current flowing from the J1 connection toward the sample directly depends on the resistance of junction a. For the Josephson effect J_{0a} between the electrodes S_0 and S_a, more ac-current flows into S_0 and distributes according to Kirchhoff law, mainly toward R_{ref} since $R_{ref} << r_1 + R_b$. Nevertheless, the current into junction b increases and hence also the measured current dI_{sq2}[7].

The same arguments apply for the case, where the ac-excitation is connected at connection J7 (Fig. 6.28c). But now, of course, we see the anomalies J_{0a} and J_{0b} showing up in the dI_{sq1}-response, but only J_{0b} is visible in the dI_{sq2}-signal.

Concerning the signal dI_{sq1} for the excitation at connection J5 (Fig. 6.28b), we see an increase at $V_a = 0$ and a decrease for $V_b = 0$. This confirms, that J_{0a} increases the current in junction a, hence giving a reduced (zero-resistance) state. On the contrary, an increase

---

7. Also within these experiments, no signature of anomalies at $V_a = V_b$ or $V_a = -V_b$ has been observed

in resistance is observed, as soon as the feature J_{0b} appears, leading to more current into junction b.

(a) $dI_{sq,1,2}(V_a, V_b)$: ac-excitation at J1

(b) $dI_{sq,1,2}(V_a, V_b)$: ac-excitation at J5

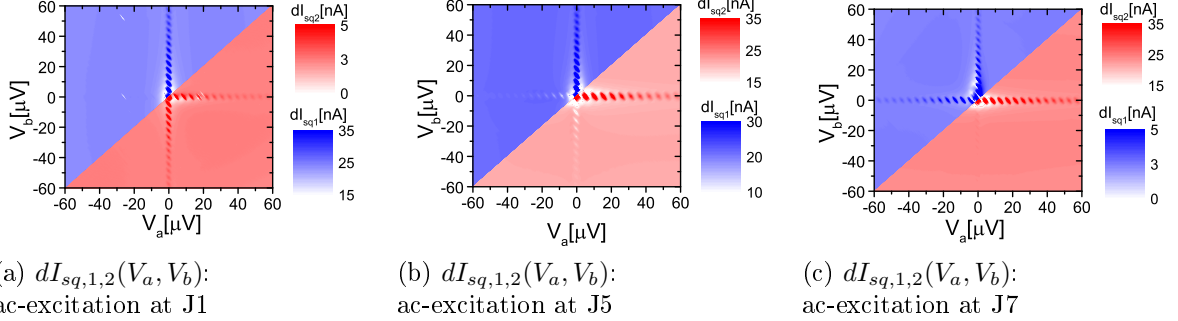(c) $dI_{sq,1,2}(V_a, V_b)$: ac-excitation at J7

Figure 6.28: Separated sample No.2: different configurations for ac-excitation; since the signal is that weak, we present raw data, captured by the SQUIDs, dI_{sq}

These observations indicate, that in separated geometry the two junctions can be indeed treated as independent. The mechanism, responsible for the observed features in T-shape geometry is no longer present or not detectable. This excludes eventual locking-mechanisms through the external measurement circuit.

6.5.3   T-shape geometry ($\gamma = 0.5$ and $\beta = 0.75$)

In a second step, we add the coupling between S_a and S_b. We assume $\beta = 0.75$, which means that the coupling of S_a to S_b is about 25 % weaker than the coupling S_0 to S_a (respectively, S_0 to S_b), which is reasonable with respect to the dimensions, estimated from the SEM-image. The resulting device corresponds now the Tri-junction geometry. The results of the simulations with these parameters are shown in Fig. 6.29a and Fig. 6.29b for both the voltage-bias and current-bias configuration. Clear additional features appear as compared to the previous situation. We remind that we still do not include the quartet-coupling ($q = 0$). Therefore, these features are due to voltage-locking.

In a final step, we include also the quartet-contribution. We assume a maximal contribution of only 20 % with respect to the maximum critical current ($q = 0.2$), which corresponds to the estimate that has been done by Régis Mélin and Denis Feinberg. In their estimate they consider that the quartet current is proportional to the conductance of the CAR mechanism. Now, we observe that the existing features due to voltage-locking are further emphasized by the quartet-mode and a few further features appear (see Fig. 6.29c and 6.29d). Especially in the voltage-bias configuration, the quartet-mode Q_0, situated at $V_a = -V_b$ is strongly pronounced with respect to Fig. 6.29b. The same trend is visible in the current-bias configuration.

6.5.4   Temperature dependence

Fig. 6.30 shows the temperature dependence of T-shape-sample No.1. The reported features of Fig. 6.8 are rather robust in temperature: even up to $700 \, mK$, all features, especially the quartet-modes, stay clearly visible. A full DC-Josephson effect, is present
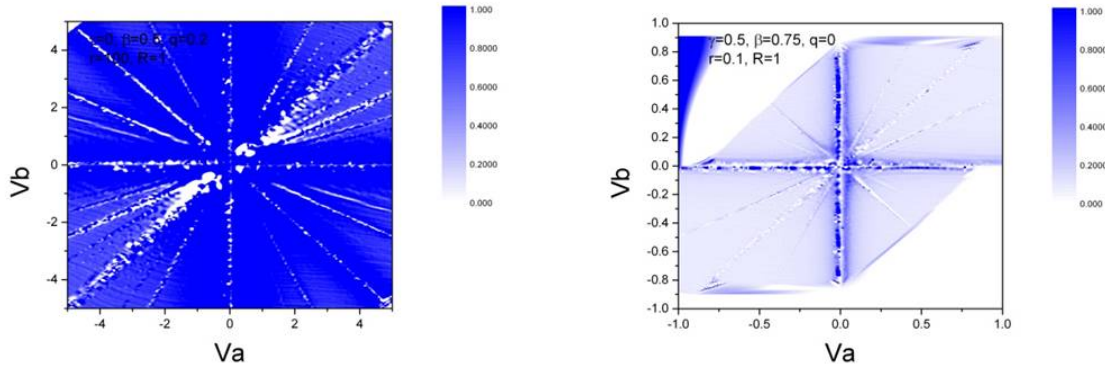
(a) current-bias: $\rho = 100, R = 1$
$\gamma = 0.5, \beta = 0.75, q = 0$

(b) voltage-bias: $\rho = 0.1, R = 1 \gamma = 0.5$
$\beta = 0.75, q = 0$
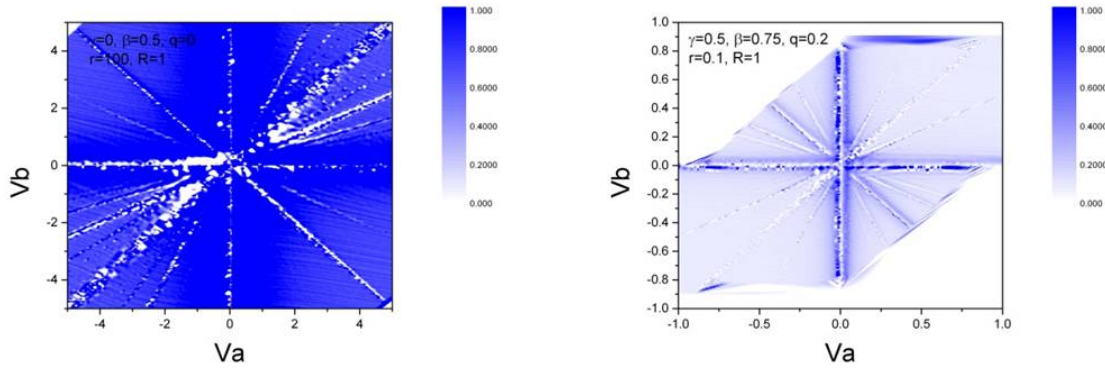
(c) current-bias: $\rho = 100, R = 1$
$\gamma = 0.5, \beta = 0.75, q = 0.2$

(d) [voltage-bias: $\rho = 0.1, R = 1 \gamma = 0.5$
$\beta = 0.75, q = 0.2$

Figure 6.29: RSJ-simulations, provided by Régis Mélin in voltage- and current-bias configuration

up to $500\,mK$ (zero-resistance state) around the origin (0,0) in the (V_a, V_b)-plane. At higher temperatures, the critical current approaches $1\,\mu A$ (Fig. 6.30c) and a decrease of the differential resistance, but no zero-resistance state is measured. The reason can be found in the step-size between the experimental points, which exceeds the critical current. Since the exact detection of the critical current is not essential for all temperatures, we did not reduce the step-size for higher temperatures.

(a) $T = 100\,mK$ (b) $T = 500\,mK$ (c) $T = 700\,mK$
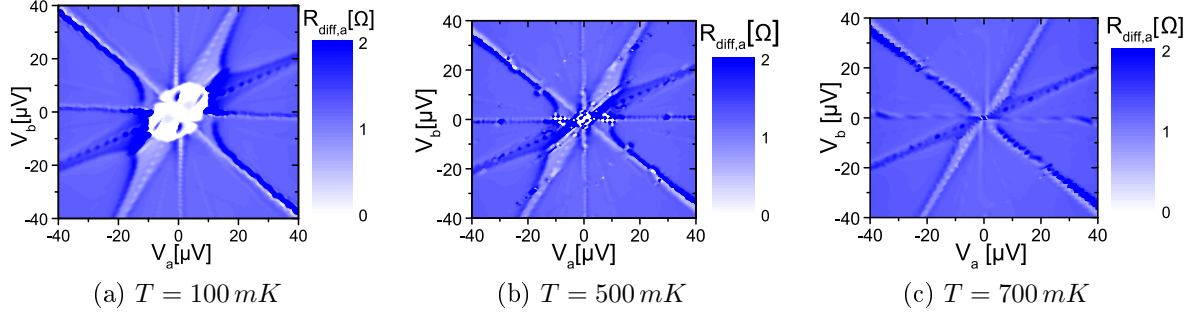
Figure 6.30: T-shape No. 1, differential resistance $R_{diff,a}(V_a, V_b)$ as a function of voltage V_a and V_b for different temperatures

For a more quantitative comparison of the decrease, see Fig. 6.31: these line-traces are extracted from the presented 2D-plots at different temperatures of T-shape No.1 for a fixed voltage V_b: In all chosen line-traces, especially the quartet-modes Q_a and Q_0 is well pronounced up to $700\,mK$. The quartet-mode can be well determined, but is only included in the line-trace for $V_b = 20\,\mu V$ (Fig. 6.31a). The Josephson-effect J_{0a} is barely visible at higher temperatures, as already observed in the 2D-plots. This is a further indication about the robustness of the quartet-features.

(a) $V_b = 20\,\mu V$ (b) $V_b = 30\,\mu V$ (c) $V_b = 40\,\mu V$
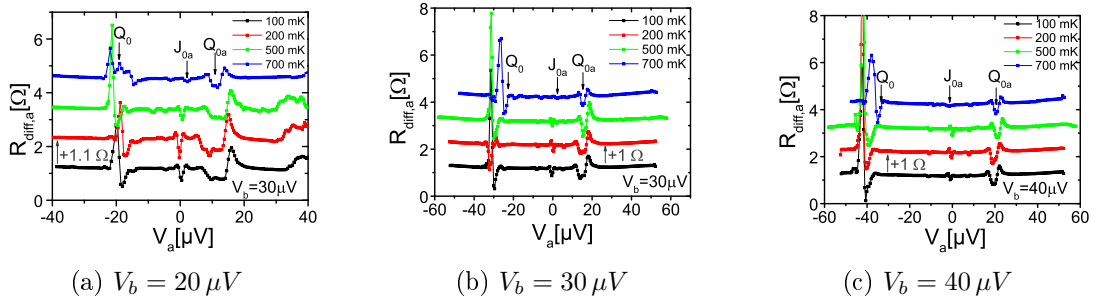
Figure 6.31: line-traces of differential resistance $R_{diff,a}$ for a constant voltage V_b at different temperature.

Within our theoretical model, we tried to estimate the impact of temperature of the two mechanism. The simulations presented present data for temperature $T = 0$ (first column) with and without the quartet-mode Fig. 6.32a, and Fig. 6.32c. Then, simulation with the same parameter are shown now with $T \approx 0.1\,E_J$. Of course, such a temperature is not realist, since this corresponds to a temperature of $T \approx 50\,K$. Nevertheless, it can be interpreted as a general trend. We observe that the features are visible with a better contrast for finite temperature, when the quartet-mode is taken into account (Fig. 6.32d and 6.32b). This is in good agreement with the experimental data.

(a) with Quartets: $T = 0$;
$\gamma = 0.5$, $\beta = \beta' = 0.75$, $q = 0.2$

(b) with Quartets: $T = 0.1 E_J$
$\gamma = 0.5$, $\beta = \beta' = 0.75$, $q = 0.2$

(c) down-mixing: $T = 0$
$\gamma = 0.5$, $\beta = \beta' = 0.75$, $q = 0$

(d) down-mixing: $T = 0.1 E_J$
$\gamma = 0.5$, $\beta = \beta' = 0.75$, $q = 0$
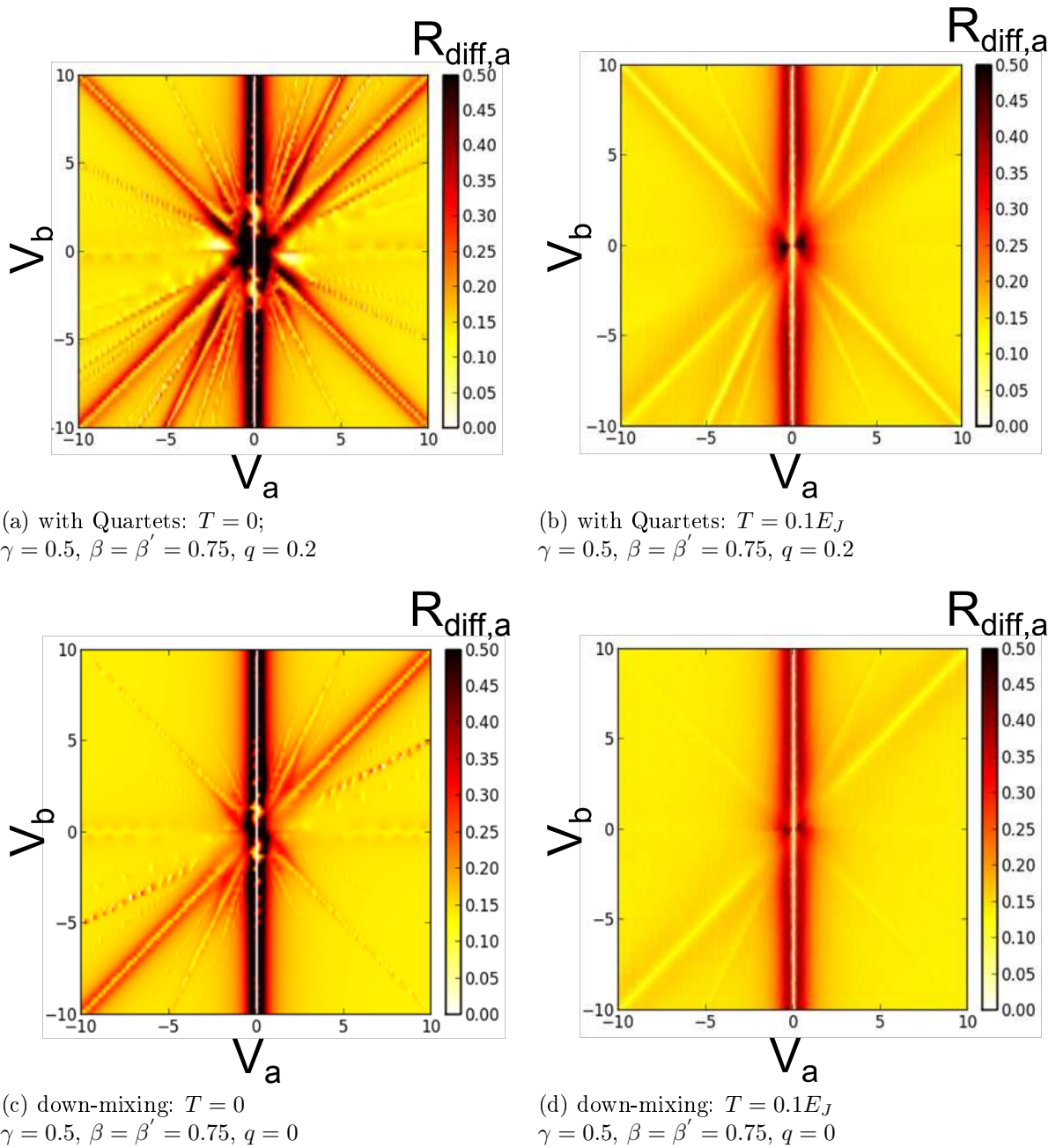
Figure 6.32: Down-mixing vs Quartet-mode; the parameter of the simulation correspond to them, estimated for junction T-shape No.1; An increase of temperature shows, that the quartet-mode is more robust for the parameter of temperature

6.6   T-shape: Magnetic field

Another essential parameter in mesoscopic physics is provided by the magnetic field. Especially for coherent transport-processes like the quartet-mode, one would expect, that magnetic field should lead to a significant decrease of the feature-amplitude. Unfortunately, we could not perform these measurements on a sample with comparable parameters as the device T-shape No.1 because more recent fabricated chips did not achieve

the same quality: First, SEM-images show, that the Al-electrodes do not fully cover the normal part as in the first sample and the geometry is not as well defined as in the first samples (see Fig. 6.33a). Furthermore, their length L seems to be slightly longer. That may also be an explanation, why further samples have shown a strongly reduced critical current. In Fig. 6.33b, we show a comparison of the critical current I_c^{sample} of sample T-shape No.1 as a function of temperature, in comparison with the critical current of device T-shape No.3. We see, that the maximum critical current of T-shape No.3 is only 30% of the first sample. Since the upper limit for the anomaly-amplitudes is given by the critical current, also the amplitude of any other feature will gives a strongly reduced amplitude with respect to previous measurements.
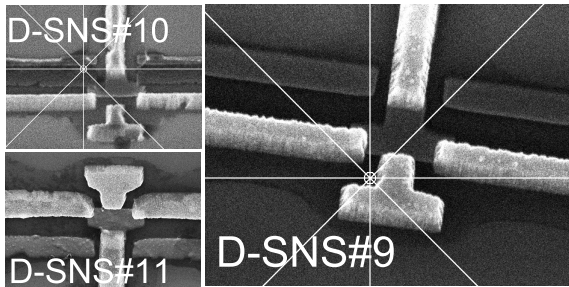
(a) Exemplary SEM-images of different chips which we have measured; $D-SNS\#9$ contains T-shape No.1, T-shape 6 is situated on chip $D-SNS\#10$, T-shape 3-5 are situated on chip $D-SNS\#11$; for an overview about measured samples and their properties, see Annexe B,Tab. B.
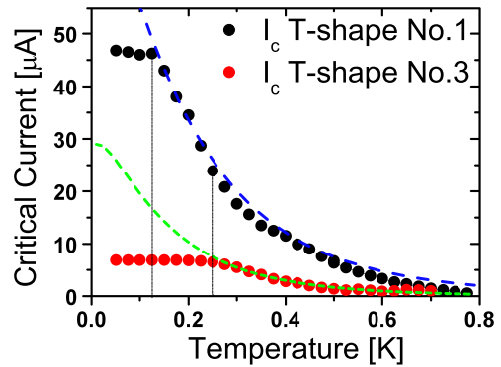
(b) Comparison of the critical current of sample T-shape No.1 and T-shape No.3; the maximum critical current of all fabricated samples after $D-SNS\#9$ is reduced of about 70%

Figure 6.33: Comparison of samples originating from different fabrication runs: Fig. 6.33a illustrates the technical problems in the sample fabrication on the best devices of the respective fabrication run; we observe much better covering of the superconducting electrodes with the copper part in $D-SNS\#9$ than in the other series; furthermore, $D-SNS\#10$ and $D-SNS\#11$ grey shadows are visible around the devices, which indicate problems to remove the resist from the sample after fabrication.

The here presented results are mainly obtained with sample T-shape No.2. Fig. 6.34 shows the comparison of the differential resistance $R_{diff,a}$ in the configuration with excitation on J1 and J5, with and without magnetic field.

Without applied magnetic field, we recognize the dc-Josephson effect J_{0a} as reduced differential resistance at $V_a = 0$, and a increase of the differential resistance at $V_b = 0$. We remind, that this line is just barely visible, since these data are obtained by sweeping the dc-current I_{dc2}, situated at the J1 connection and keeping fix the current I_{dc1} at J5. With an ac-excitation situated at J5 (Fig. 6.34a), we recover the quartet-mode Q_a at $V_a = 2\,V_b$ and Q_b at $V_a = 1/2\,V_b$. The quartet-mode Q_0 at $V_a = -V_b$ shows some deviation at low voltage, recovering however the slope $V_a = -V_b$. The origin of this effect is unclear.

Fig. 6.34c shows the differential resistance $R_{diff,a}$ for an excitation situated at J1 for zero magnetic field [8]. In this configuration, the J_{0b}-feature is not visible. The quartet-mode Q_b results now in a minima, even if much less pronounced as in the J5-case. The Q_0-feature shows the same deviation at low-voltage as observed in Fig. 6.34a, but we recognize a reduced amplitude of the feature. This can be explained by the fact, that the Q_0-feature emits Cooper-pairs into junction a and b and is hence best visible for an excitation situated at the J5 connection. Additionally, a feature appears at $V_a = V_b$, which corresponds to the dc-Josephson effect between S_a and S_b. Above $V_b = 20\,\mu V$, it is just barely visible, which might be an indication of a quite weak Josephson coupling.

If we apply some magnetic field, the quartet-mode Q_0 strongly decreases and is disappears completely for a magnetic field of $55\,Gauss$ in both configurations (see Fig. 6.34b and Fig. 6.34d). The width in voltage and amplitude of the Q_a-feature is also significantly reduced. Now, the quartet-mode Q_a shows a deformation at low voltage, as already observed at zero magnetic field for the quartet-mode Q_0. The width of the Q_b-mode seems to be unchanged, but the maximum, marked by a fine line, which was visible at zero magnetic field, has disappeared. The Josephson-effects J_{0a} and J_{0b} are less visible as well.

For more detailed studies we have extracted line-traces at different magnetic fields for ac-excitation situated at J1 and J5. They are depicted in Fig. 6.35. We can observe, that J_{ab} strongly reduces with increasing magnetic field. Furthermore, the quartet-mode Q_0 is indeed suppressed for high magnetic fields, being generally better visible in the J5-configuration. Interestingly, the Josephson-effect J_{0a} shows up as a small minimum, but neither reaches zero, even for low voltage. Furthermore, J_{0a} is completely disappeared for $20\,Gauss$ within all line-traces and recovers for higher magnetic fields. Interestingly, the magnetic field of $20\,Gauss$ matches with estimated magnetic field corresponding to one flux-quantum Φ_0 in the junction area. This might be an indication, that a Fraunhofer-pattern could be revealed within our structure, within more detailed studies of the magnetic field.

An attempt for a more sophisticated studies of the magnetic field has been tried with sample T-shape No.4 and is depicted in Fig. 6.36. We choose a line-trace where I_{dc1} at J5 connection is kept fix, which gives $V_b \approx 20\,\mu V$. Then, we sweep the current I_{dc2} situated at J1-connection for different magnetic fields ($\pm 40\,Gauss$). Since the features are quite weak in this sample, we remove the overall-background and plot the gradient of the differential resistance $R_{diff,a}$. We can identify the J_{0a}-feature as well as a feature at $V_a = 20\,\mu V$ which corresponds to the J_{ab} dc Josephson effect. J_{ab} shows a decrease for high magnetic fields. At $V_a = 10\,\mu V$, a feature appears, which decreases with increasing magnetic field and disappears above $35\,Gauss$. Further lines appear at $V_a \approx \pm 40\,\mu V$ which might be artefacts due to transition of soldering parts. Generally, we can state a decrease of the features with increasing magnetic fields. For more quantitative measurements, we will use the raw-data, directly recorded of SQUID 1, δI_{sq1}.

In Fig. 6.6, we ramp the magnetic field up to $360\,Gauss$. The central peak in the δI_{sq1}-traces is due to the Josephson-effect J_{0a}. We observe a decrease with increasing magnetic field with minimum in the SQUID-response at around $100\,Gauss$. Afterwards, a maximum, similar to $60\,Gauss$ re-appears, which disappears gradually, towards $360\,Gauss$.

---

8. this plot has just been measured down to $V_b \approx -10\,\mu V$

(a) $I_{J5}^{ac} 1\,\mu A$; B=0 Gauss

(b) $I_{J5}^{ac} 1\,\mu A$; B=55 Gauss

(c) $I_{J1}^{ac} 1\,\mu A$; B=0 Gauss

(d) $I_{J1}^{ac} 1\,\mu A$; B=55 Gauss
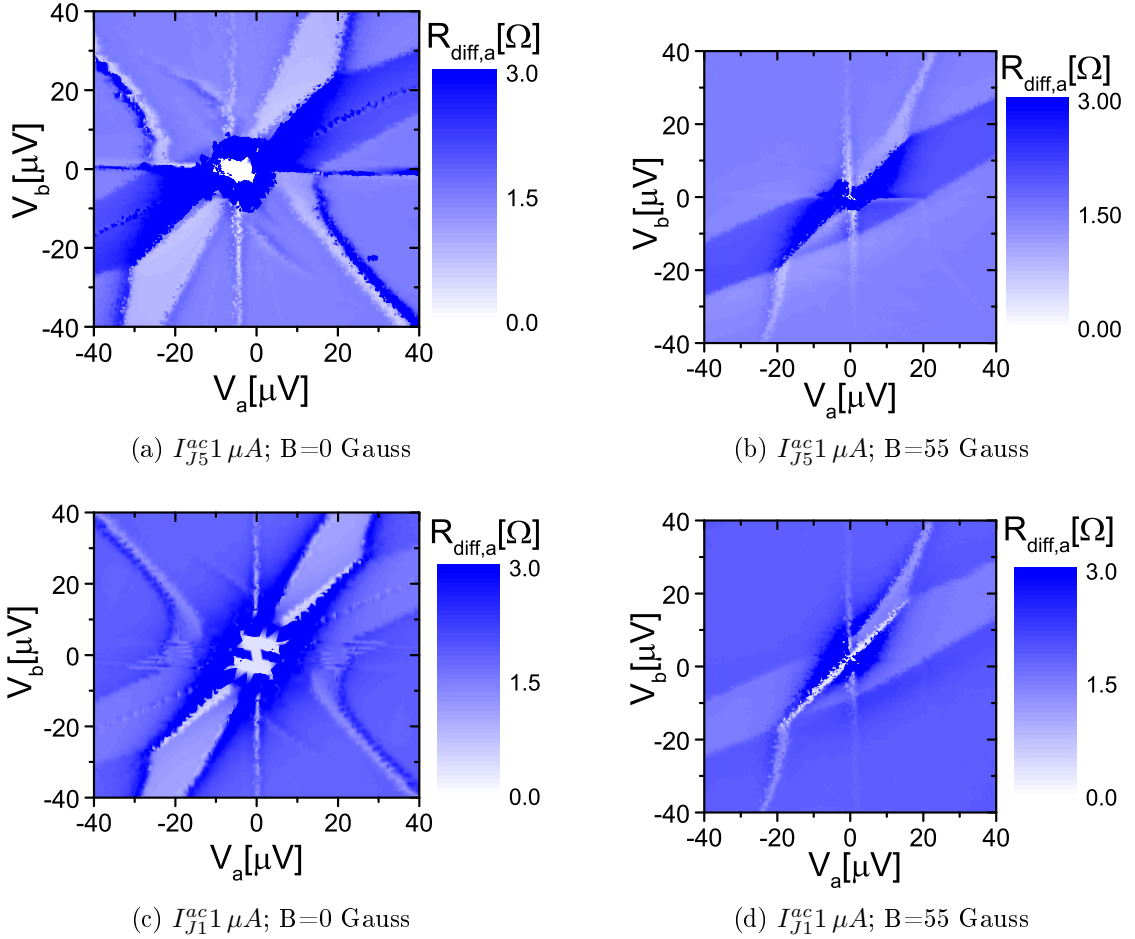
Figure 6.34: T-shape No.2: differential resistance $R_{diff,a}$ as a function of (V_a, V_b) for an ac-excitation, situated at connection J5 respectively J1; for both configurations, the feature at $V_a = -V_b$ has clearly disappeared for $B = 55\,Gauss$; furthermore, the feature Q_a has strongly lost is width and amplitude. The Q_b-feature stays rather the same in width, but the central maxima for ac-excitation at J5, respectively minima for ac-excitation at J1 has disappeared.
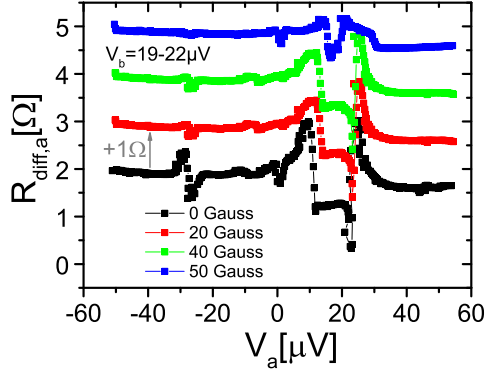
(a) $I^{ac}_{J1}1\,\mu A$; $V_b = 19 - 22\,\mu V$
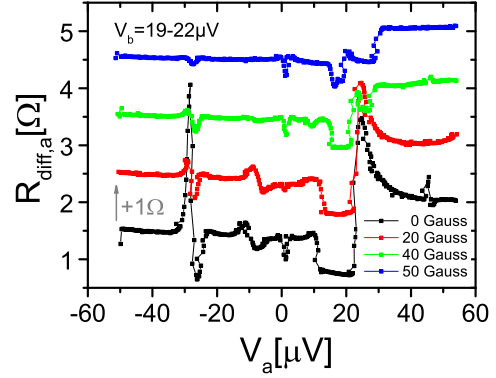
(b) $I^{ac}_{J5}1\,\mu A$; $V_b = 19 - 22\,\mu V$

(c) $I^{ac}_{J1}1\,\mu A$; $V_b = 26 - 33\,\mu V$

(d) $I^{ac}_{J5}1\,\mu A$; $V_b = 26 - 33\,\mu V$

(e) $I^{ac}_{J1}1\,\mu A$; $V_b = 33 - 38\,\mu V$
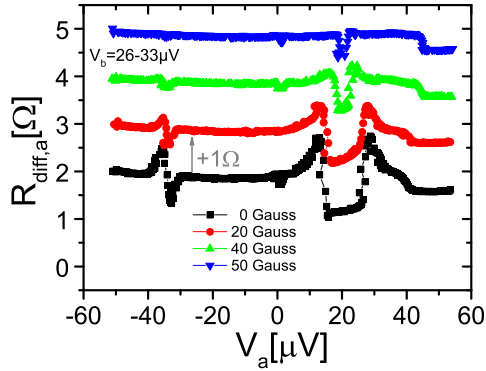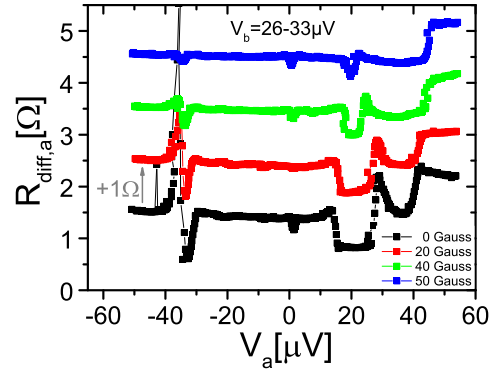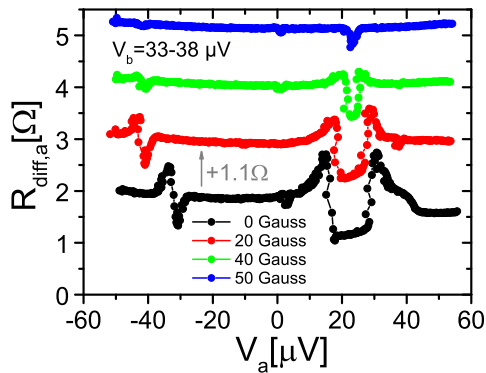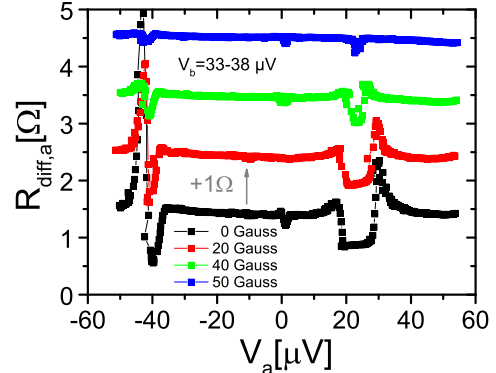
(f) $I^{ac}_{J5}1\,\mu A$; $V_b = 33 - 38\,\mu V$

Figure 6.35: T-shape No.2: line-traces for different magnetic fields; left: ac-excitation at J1; right: ac-excitation, situated at J5-connection
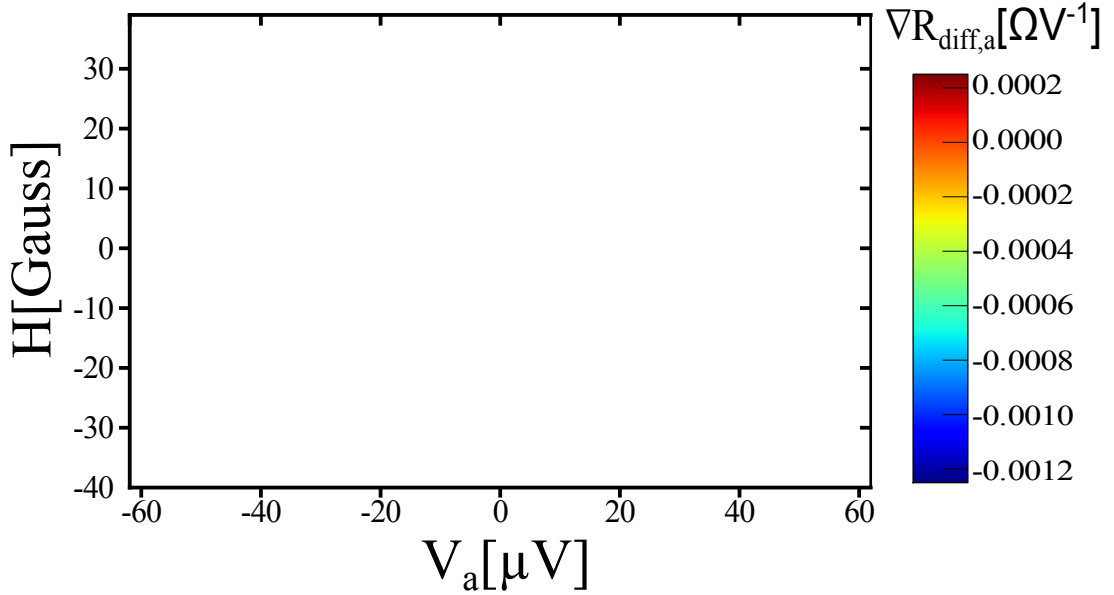
Figure 6.36: T-shape No.4: Line-trace (ac-excitation on J1) at $V_b = 20\,\mu V$; the magnetic field is varied between $\pm 40\,Gauss$. Gradient of $R_{diff,a}$, without background in order to increase the visibility.
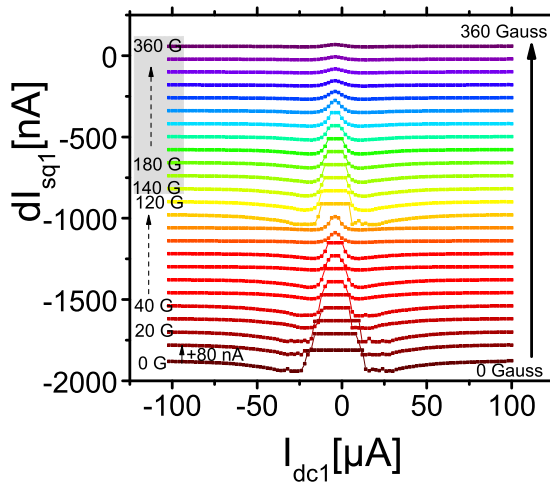
Figure 6.37: Studies for high magnetic fields of an exemplary line-trace δI_{sq1}; the feature J_{0a} is situated in the centre; it shows a decrease od the central maximum down to $100\,Gauss$ and re-establishes for higher magnetic fields. At $360\,Gauss$ the Josephson effect is completely suppressed.

Chapter 7

Preliminary results

In this chapter, we will present some of the obtained preliminary results. We tried measurements in the incoherent regime of our 3-terminal Josephson junctions, in order to study the Three-terminal (I)-MARs, predicted by Houzet and Samuelsson [24].

Furthermore, different approaches for sample fabrication have been tried, as well as the use of new materials, such as boron-doped Silicium. Here, we will just present some data concerning measurements in the incoherent regime of our 3-terminal Josephson junctions. The idea was to study the Three-terminal (I)-MARs, predicted by Houzet and Samuelsson [24].

7.1   3-Terminal Multiple Andreev reflections: incoherent regime

At much higher voltage, dependent on temperature, a big peak appears between110 and $120\,\mu V$, which can be attributed to the transition of the aluminium electrodes. This rather low transition compared to the superconducting gap ($170\,\mu V$) can be explained by the restricted small size of the electrodes and hence a relatively important de-pairing current, which leads also to the general increase of resistance at higher voltage.

In the incoherent regime, features due to IMAR are expected. In our samples, we locate the appropriate region between $70\,\mu V$ and $170\,\mu V$. They are expected to appear as peak or dips in the conductance. However, in our measurement no clear distinct other feature can be seen on the presented data (see Fig. 6.4). The MAR-features are hidden by the strong de-pairing current. In order to reveal possible underlying features, we try to numerically differentiate the data. Before this step, we make a 10 pt-average (this should reduce eventual perturbations due to noise in the voltage-measurement).

The resulting curve is presented in Fig. 7.1. Then, due to this data treatment, further peaks appear, their position can be found in Fig. 7.2. Also, these peaks can be hardly related to MAR-features, and among them, several appear which do not scale with the gap of Aluminium but more with reduced ($310\,\mu V$) or higher gap ($375\,\mu V$) values. In a final attempt, we tried to analyze the data after a similar treatment as before, with a peak location software, which localizes peaks, by removing the experimental background (Fig. 7.3). In these curves, clearly pronounced peaks appear, but now the software localizes that much peaks, that also no reasonable conclusion concerning MAR can be offered, see

Fig. 7.4. We conclude that with the present sample design, de-pairing current at high voltage is to important for a proper analysis in this range. For studies of MAR, we will need to change sample geometry, in order to improve the critical current of the electrodes.
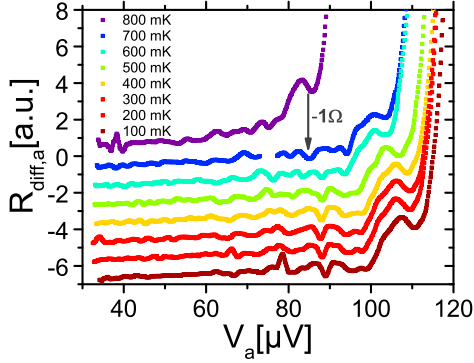
Figure 7.1: Derived differential resistance $R_{diff,a}$ as a function of V_a for different temperatures
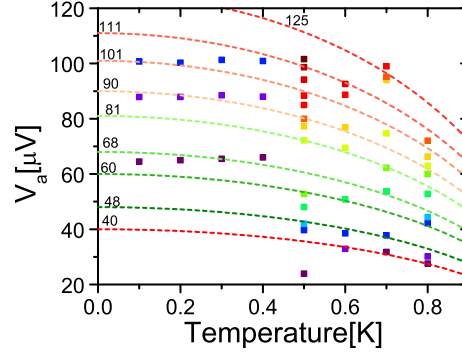
Figure 7.2: Location of peaks in Fig. 7.1; the dashed lines correspond to attempts to obtain the best BCS-fit

Figure 7.3: Derived differential resistance $R_{diff,a}$ (with removed background) as a function of V_a for different temperatures
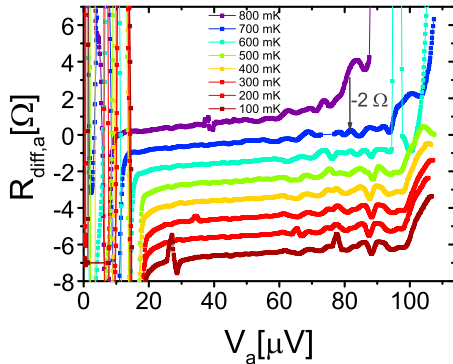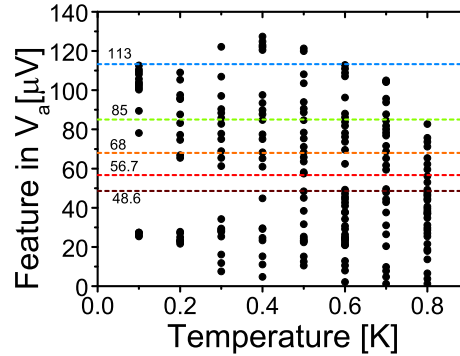

Figure 7.4: Location of peaks in Fig. 7.3, extracted with an implemented ORIGIN-Lab routine; the dashed lines correspond to expected the voltage, where MAR-features would be expected for a typical Al-gap of $\Delta = 170\,\mu eV$

Chapter 8

Conclusion and Perspectives

In the presented PhD work, we have studied diffusive three-terminal superconducting nanostructures. In samples of T-shape geometry, we found features in the conductance, for specific voltage ratio between the two junctions, a and b which persists over a large range of voltage (for $eV > 10\,E_{Th}$). Appearing for $V_a = -V_b$, $V_a = 2V_b$ and $V_a = 1/2V_b$, these features have been reproduced for all measured devices in T-shape geometry, arising from three different fabrication cycles. We have performed studies as a function of temperature and magnetic field. The features have shown a strong decrease with increasing magnetic field, which is much more important than that for the dc-Josephson effect.

We have shown, that in general two theories exist, which can explain in principle the obtained results: First, the predictions of quartet-modes [25], [26], which are expected to be a rather robust mechanism over a large range of voltage. Second, the so-called Voltage-locking or down-mixing mechanism. Generally, we expect, that the ac-Josephson effect decreases above the Thouless energy E_{Th}. This means as a consequence, that for voltage-locking, where the ac-Josephson effect is responsible for the occurrence of the features a significant reduction should be visible within the measurement range. Despite of extensive bibliographic studies, no experiments have been reported, where this fact has been studied quantitatively.

Unfortunately, also no complete mesoscopic model exists yet which can help to differ between the two proposed theories. For that reason, during this work, a cooperation with Denis Feinberg and Régis Mélin from the Institut Néel has been initiated to develop such a model. As a first step, we have achieved, to worked out an extended RSJ-model, where both theories, quartet-mode as well as down-mixing can be implemented. Several geometrical parameters have been added, which can be used to simulate various sample geometries: for instance, γ tunes the asymmetry in the resistive branch of the model, β is added to vary the superconducting coupling between S_a and S_b, q adds to tune the amplitude of the quartet-mode, and β' takes into account its eventual asymmetry for the three junctions. Indeed, voltage-locking reveals the features, situated at the same relation, $pV_a + qV_b = 0$ like the quartets. The amplitudes of the effects can however be seen to increase by adding the quartet-contribution.

In a second step, we adapted our model, that it takes into account the fact, that the experimental set-up is just voltage-biased for $R_n >> R_{ref}$. Now, it can be easily tuned into current-bias by an additional parameter ρ, which allows to study the two experimental limits. Experiments in current-bias configuration have been tried as well, but no features

showed up. For the moment, we cannot state, if this is a hint, that the device must be voltage-bias in order to observe the features or it is just due to the worse quality of more recent samples. Theory shows, that the features should be visible within the experimental conditions in current- and voltage-bias configuration.

We have shown, that the features disappear in the experiment, when we explore the limit $\gamma = 0$, where the device corresponds to two spatially separated Josephson junctions. This means, that the features are not due to any external synchronization via the experimental set-up. Nevertheless, a final proof cannot be given, since neither experimental data nor our simple model give reliable parameters to differ within the two models.

Furthermore, unfortunate circumstances in the sample fabrication limited the possibility for quantitative measurements: since the maximum for our features is given by the maximum amplitude of the critical current, a sufficiently high critical current is crucial in order to get sizable features.

Unfortunately, just one chip delivered samples with sufficiently high critical currents ($I_c > 15\,\mu A$), for quantitative measurements. The reason for the low critical current has been probably caused by two main issues; first, the contact surface was not as big as in the first chip. This means, that the same amount of current passes through a smaller surface. For that reason, the joule heating at the interface is more important and, since the critical current density is the same, the measured critical current is reduced. Furthermore, the size of the normal part is longer for those samples. Since the critical current is inversely proportional to L^3, this gives a further decrease of the critical current. Additionally, residual resist can be seen at the interface of several devices. Finally, the measured junctions have aged with time; the results show, that it is crucial to use junctions fast as possible after their fabrication. Also the first chip showed increased sample resistance and reduced critical current 6 months after the first measurement and several cooling down cycles.

Summarizing, for future experiments, we know, that our junctions have to be shorter than a length $L \leqq 1\,\mu m$ and should be measured quite soon after fabrication. During the thesis, we have developed several promising sample designs, which have not been measured yet: Unfortunately, the PhD-time is strictly limited and this PhD-work has been performed during the move of the Nano-department of the N'eel Institute which restricted the opportunities for new devices. This, however, opens a bunch of possible experiments for the coming years:

- A first one would imply to realize a fully symmetric device. The idea is to design all junctions with the same length, which should give three identical junctions concerning their coupling ($\beta = \beta' = \gamma = 1$). This so-called "fork"-structure (see Fig. 8.1c) should allow to study in more detail the real form of the features. Eventual artefacts due to different de-phasing in the various branches could be ruled out: In the presented data (Fig. 6.8), especially the quartet-modes Q_a and Q_b show a general form, which is rather surprising, with a wide uniform background and an appearing central peak/dip.
- Another interesting experiment would be to replace the highly transparent S_0-contact by a tunnel-barrier (Fig. 8.1b). Then, we could compare our results directly to the predictions by Cuevas and Pothier [114]. Variation of the junction length can be also interesting, since they present precise relations between sample length and feature-amplitude.

– Up to now, Quartet-modes have been only measured in our experimental set-up, on highly transparent diffusive nanostructures. However, there exist an easy way to produce tunnel-junctions in which the Quartet-modes should appear as well: With the help of shadow mask evaporation, using three different angles, we can produce a three-terminal structure, where a big contact interface can be designed. In this way, even the resistance can be tuned relatively easy. We start at angle 1, evaporating 30 nm of aluminium. Then, we oxidize the surface by putting some oxygen in the UHV chamber. Afterwards, in angle 2, a second layer of aluminium gets evaporated, this time 50 nm. After a further controlled oxidation of the surface, a final aluminium layer can be evaporated, using angle 3. This gives a vertical structure, where the thickness of the central superconductor has to be smaller compared to the superconducting coherence length ξ_s, in order to allow transport between the outer electrodes, S_a and S_b. The resulting structure corresponds to that, proposed by Freyn et al. [25] in the initial quartet-article. For a schematic illustration of the described device structure, see Fig. 8.1a.

– Measurements of a device in separated geometry should be done, where the central superconductor has a size less than the superconducting coherence length ξ_s (see Fig. 8.1d). Our previous devices in separated geometry where too long (length $L_{a-b} \approx 2\,\mu m$ between left and right reservoir, S_a and S_b). This gives such a strongly weak coupling between the two electrodes S_a and S_b, that eventual features due to three-terminal mechanisms are extremely weak. In a structure, where the length L_{a-b} is in the order of $1 - 1.5\,\mu m$, possible coupling should be revealed more easily. In this structure, also the high-voltage regime could be interesting: if the coupling between the two junction is indeed mediated by excited quasi-particles, this coupling should be improved for high voltage, since charge-imbalance comes into play. In another point of view, this can be also explained in the sense, that at high voltage, the central superconductor gets more and more normal properties and it should resemble more a T-shape type symmetry at high voltage.

– Another possibility would be to take our present symmetry of two separated junctions and to shunt it by some normal part (see Fig. 8.1e). This device would correspond to the theoretical model by Nerenberg et al. [111]. If the shunt is long enough, the coupling then is only mediated by quasi-particles. This could help to exclude the charge-imbalance as origin of our observed features.

– Experiments using Aluminium micro-bridges (geometry of Jillie et al. [108]) could be done, in order to compare our observed features with those, appearing in micro-bridges.

– Finally, measurements of Shapiro-steps can be done in our present structures: If we achieve to quantify the microwave amplitude, which is necessary to reveal Shapiro-steps for a given voltage, we can see, if the necessary microwave power can be produced as well on-chip. As upper limit, we know from tunnel junctions, that a microwave power of around $10^{-7}W$ can be emitted by a Josephson junction. In general, as explained before, Shapiro-steps are expected to decrease with applied voltage and applied microwave amplitude (see eq. 3.28). By measuring Shapiro-steps within our structure where we record the emitted microwave amplitude, we can extract the necessary microwave power, which must be delivered by one of our junctions, in order to produce Shapiro-steps due to mode-locking at a given

voltage. If the necessary microwave power to induce the observed features at high voltage exceeds the experimental limits, given by the impedance of experimental environment and critical current, we can exclude voltage-locking as origin of the experimental features; However, this implies a lot of experimental development of the set-up: we need to add microwave-cable, assure the thermalization of these cables and add bias-tees, in order to filter the signal, which enters in the SQUID-amplifiers.
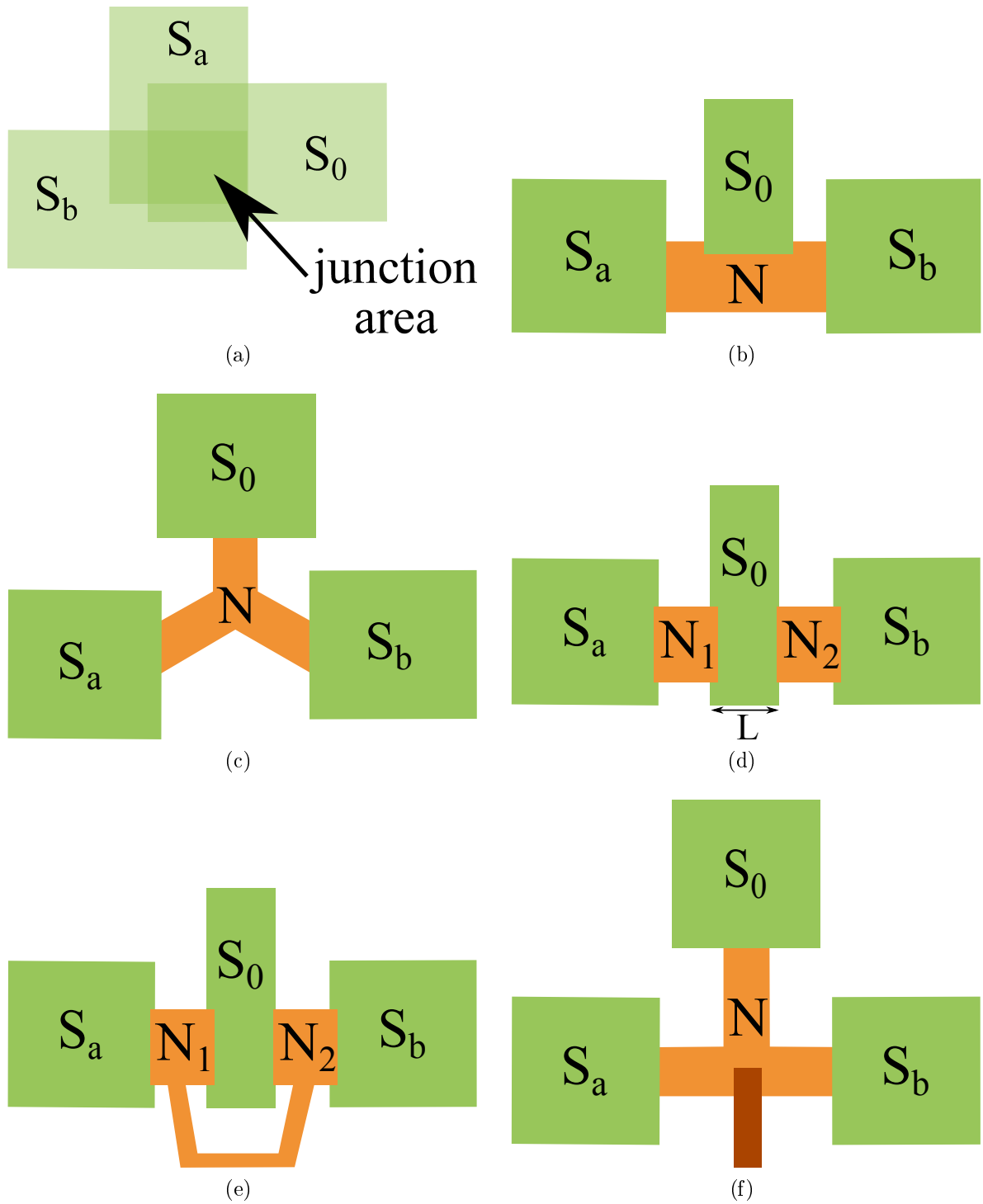
Figure 8.1: Proposals for device-geometries and measurements

Appendix

Appendix A

S-shape transition of the critical current

As mentioned already in chapter 5, our set-up allows voltage-biasing when the sample is in a resistive state. Here, we discuss the transition from the zero-resistance state to the normal state. We know from previous work on diffusive SNS junctions that the IV-characteristics are always hysteretic at very low temperature, even though the RSJ-model predicts no hysteresis. Courtois et al. [124] have proposed that this difference between observed and predicted behaviour is due to heating effects. Independently of the origin of this hysteresis, a voltage-bias configuration should reveal a S-shape IV-characteristics. Fig. A.1 shows the low voltage part of the IV-characteristics with a T-shape sample by sending a dc-current at the J5-connection only. The voltage corresponds to V_a and the current has been obtained by measuring the voltage-drop across the R_{ref}-resistor. Therefore, the curves the sample taken as a whole and do not detail whether the current flows into branch a or b. The reason why the current was measured this way is because the SQUID-response becomes unstable when entering the region of negative differential resistance.

Between $200\,mK$ and $300\,mK$, the expected S-shape transition is measured. The IV-characteristics shows a decrease of the current as a finite voltage develops across the device. At lower temperature (below $200\,mK$) a clear jump appears, still with a decrease of the current together with a small hysteresis. We believe that the origin of this jump is due to the reference resistor R_{ref} whose resistance is not low enough. Indeed, to properly measure an S-shape response, the biasing resistor must have a resistance value that is lower than the absolute value of the negative differential resistance.

From these curves, we can measure the "true" critical current down to $200\,mK$ whereas only the switching current is measured at lower temperature. Because a switching current is very sensitive to external perturbations, it may differ from the critical current. That is why the fit of the critical current as a function of temperature is no longer valid below $200\,mK$ (see Fig. 6.3).
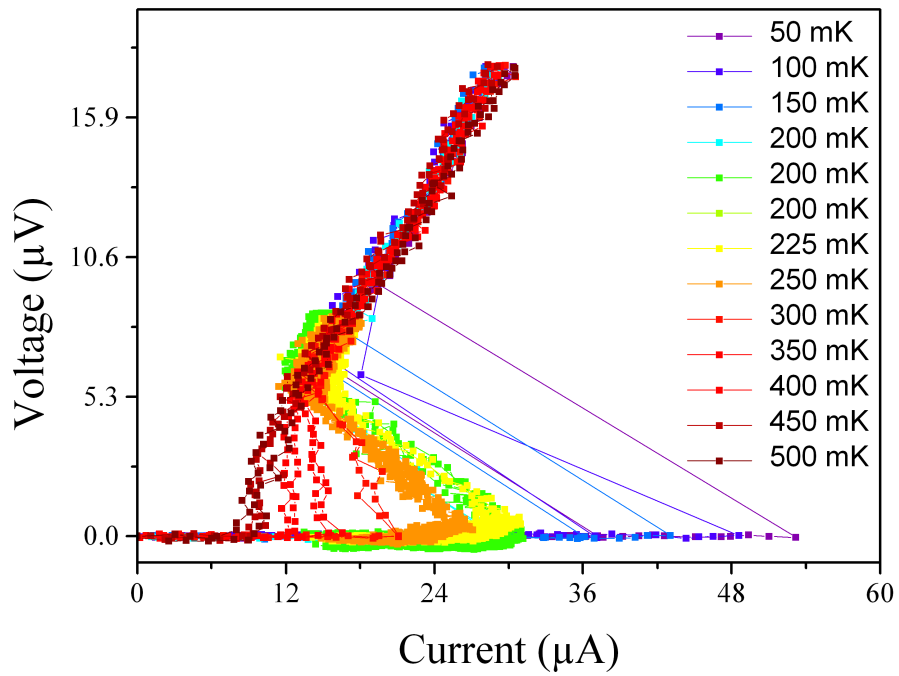
Figure A.1: IV-characteristics of T-shape sample No.1

Appendix B

Overview about measured samples during the thesis

Full Sample Name	short name	length	E_{th}	I_c[100mK]	BIAS	Date
D-SNS#9A C4 R7	T-shape No. 1	$1\mu m$	$5.35\mu eV$	$25\,(50)\,\mu A$	Voltage	08-12/2011
D-SNS#9A C4 R9	T-shape No. 2	$1\mu m$		$18\,\mu A$	Voltage bias	10-12/2012
D-SNS#11 C5 R6	T-shape No. 3	$1.2\mu m$	$4.75\mu eV$	$8.6\mu A$	Current	02-04/2013
D-SNS#11 C6 R5	T-shape No. 4	$1.2\mu m$			Voltage	04-06/2013
D-SNS#11 C2 R5	T-shape No. 5	$1.2\mu m$			Current	01-02/2013
D-SNS#10 C3 R15	T-shape No. 6	$1.2\mu m$			Voltage	04-06/2012
D-SNS#9A C6 R10	separated No. 1	$1\mu m$			Voltage	01-03/2012
D-SNS#9B C3 R4	separated No. 2	$1\mu m$			Voltage	06-07/2013

Appendix C

Publications

C.1 Superconducting Quantum Interference Devices based set-up for probing current-noise and correlations in three-terminal devices

Superconducting quantum interference devices based set-up for probing current noise and correlations in three-terminal devices

A. H. Pfeffer, B. Kaviraj,[a)] O. Coupiac, and F. Lefloch[b)]
SPSMS/LaTEQS, UMR-E 9001, CEA-INAC, and Université Joseph Fourier, Grenoble, France

We have implemented a new experimental set-up for precise measurements of current fluctuations in three-terminal devices. The system operates at very low temperatures (30 mK) and is equipped with three superconducting quantum interference devices (SQUIDs) as low noise current amplifiers. A SQUID input coil is connected to each terminal of a sample allowing the acquisition of time-dependent current everywhere in the circuit. From these traces, we can measure the current mean value, the noise, and cross-correlations between different branches of a device. In this paper, we present calibration results of noise and cross-correlations obtained using low impedance macroscopic resistors. From these results, we can extract the noise level of the set-up and show that there are no intrinsic correlations due to the measurement scheme. We also studied noise and correlations as a function of a dc current and estimated the electronic temperature of various macroscopic resistors. © 2012 American Institute of Physics. [http://dx.doi.org/10.1063/1.4766334]

I. INTRODUCTION

In disordered electrical macroscopic conductors, the amplitude of current flowing in response to an applied voltage is governed by various microscopic mechanisms such as elastic scattering on impurities and inelastic collisions within electrons or between electrons and phonons. The conductance, given by the ratio between the mean value of the current and the applied voltage, averages out all the contributions and is usually well described by the Drude formula. At finite temperature and zero applied voltage, the current fluctuates in time around its mean value because of thermal fluctuations of the electronic state occupation number. The amplitude of fluctuations is given by the fluctuation-dissipation theorem and corresponds to the second moment of current distribution. Through that relation, the spectral density of current-noise is proportional to both the temperature and mean value of conductance. In that sense, thermal noise measurement does not provide any additional information than the conductance. At finite applied voltage, scattering events randomize the flow of electrons and induce, together with the granularity of charge, an additional noise contribution known as "shot noise." However, this contribution vanishes in macroscopic disordered conductors when the events are uncorrelated. It is only when the size of the conductor becomes of the order of phase coherence length of the electronic wave function that shot noise becomes sizable.[3] This cross-over corresponds to entering the mesoscopic world, where quantum effects become important. Since past twenty years, shot noise measurements have contributed to the understanding of electronic transport properties at nanoscale. One of the most emblematic results obtained was the experimental demonstration of existence of fractional charges in two-dimensional elec-

trons gas in fractional quantum Hall regime.[12,14] Another very interesting situation was obtained in hybrid superconducting (S)/normal metal (N) nanostructures, where the shot noise was found to be doubled (SN junctions) or very much enhanced (SNS junctions) due to the conversion of Cooper pairs into normal electrons at the S/N interface.[6,7,9,10]

But the interest of fluctuation measurements is not limited to noise. For example, the third moment of current distribution reveals its (non-)Gaussian character, whereas noise correlations can probe statistics (fermionic or bosonic) of current carriers such as in a Hanbury-Brown Twiss type of experiment.[5] Cross-correlations can also be investigated to reveal the splitting of copper pairs in hybrid normal-superconducting nanostructures.[1,11]

However, in order to address experimentally these quantities, new instruments need to be developed. The pioneer work on the third moment of a simple tunnel junction has revealed a major importance of the environment showing that these quantities need to be investigated with great care.[2,13] The same is true for cross-correlations, where the signal is much smaller than the noise and where all spurious contributions need to be clearly identified.[4,15]

II. INSTRUMENTAL SET-UP

In our set-up, the mean value and fluctuations of currents in each branch of a sample are directly measured using three SQUIDs as current amplifiers (see Figure 1). The measurements are done at very low temperatures, using a dilution fridge with a base temperature of 30 mK. The SQUID electronics operate in the standard flux lock loop mode, which reduces almost completely the spurious feed-back of read-out towards the sample. As current fluctuations are measured, the sample needs to be voltage-biased. This is achieved by placing, in parallel to the sample, a macroscopic "surface mount resistor" R_{ref} whose resistance is much lower than the device resistance and that is mounted at low temperature to reduce

---

its noise contribution (see Fig. 1). Then, a low noise current source I_{DC1} is used to bias the system. Two additional resistors r_1 and r_2 are placed in series with two other branches of the three-terminal device. With a second low noise current source I_{DC2}, it is then possible to control the two voltage drops V_1 and V_2 independently. Additionally, each individual voltage drop can be measured using room temperature low noise differential voltage amplifiers. If needed, the differential resistance can also be measured by sending a small ac-current together with the dc-current.

As current noise is generally inversely proportional to the sample resistance, our set-up is well adapted to low impedance samples, typically around 1 Ω. This statement is exact for thermal noise and can be somewhat generalized to shot noise for hybrid superconducting nanostructures. Indeed, when superconductivity is involved, it exists a typical voltage scale given by the superconducting gap and the current needed to reach this gap is inversely proportional to the sub-gap impedance of the device. In practice, the spectral density of noise can be measured with a set-up noise of $2 \sim 3 \, 10^{-24}$ A^2/Hz = $2 \sim 3$ pA^2/Hz. This noise floor does not strictly correspond to current fluctuations at the input coil of the SQUIDs, but mostly comes from the noise of the room temperature electronics and translates into these values using the overall gain of the amplification/conversion chain. The bandwidth is given by the resistance of the overall device (sample in parallel with the reference resistor, R_{ref}) coupled to the input coil inductance. Using a 0.1 Ω reference resistor and given the SQUIDs input coil inductances ($L \sim 1 \, \mu$H), we obtain a cut-off frequency $f = R_{ref}/(2\pi L) \sim 15$ kHz that limits the bandwidth. Another important advantage of using SQUIDs is the very low 1/f noise that is sizable only below 1 Hz. With these values and considering a reasonable acquisition time of few minutes, we obtain a sensitivity of order of 0.1 pA^2/Hz.

Figure 1 shows the schematic of the experimental set-up together with the microscope image of a typical three-
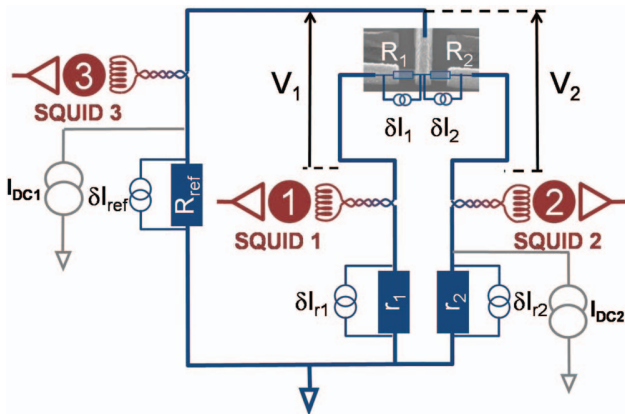

FIG. 1. Schematic description of the experimental set-up. The schematic shows a typical three-terminal nanodevice to be studied with this new instrument. The red circuit's elements are at 4.2 K and the blue ones are thermalized with the mixing chamber of the dilution fridge. For calibration measurements, the sample has been replaced by two macroscopic resistors of ~1 Ω resistance, whereas the others macroscopic resistors in the circuit have a resistance of ~0.1 Ω. All the wiring is made from superconducting leads.

terminal device.[8] For this sample, a central superconducting electrode emits Cooper pairs towards two spatially separated superconducting collectors through two normal metal nanobridges of 1.5 μm length. The sample can be modeled by two nonlinear resistors R_1 and R_2. All the wires connecting different parts of the set-up are superconducting and therefore do not add any additional resistance in the circuit. The three SQUIDs sensors are located at the 4.2 K flange of the dilution refrigerator in the helium liquid bath. All other elements are thermalized with the mixing chamber temperature.

Any resistive part of the circuit is associated with a current source δI in parallel, in accordance with the Nyquist representation. In this model, the current flowing in each SQUID is given by

$$\delta I_{sq}^i = \left(\frac{\widehat{R_i}}{\widehat{R_i} + \widehat{R_{jk}}} \right) \widehat{\delta I_i} - \left(\frac{\widehat{R_{jk}}}{\widehat{R_i} + \widehat{R_{jk}}} \right) \left(\widehat{\delta I_j} + \widehat{\delta I_k} \right), \quad (1)$$

where $\widehat{R_i}$ is the sum of the resistances in branch i, $\widehat{\delta I_i}$ the weighted current contribution of all the elements in branch i, and $\widehat{R_{jk}}$ the equivalent resistance of $\widehat{R_j}$ in parallel with $\widehat{R_k}$. For instance,

$$\widehat{R_1} = R_1 + r_1, \qquad \widehat{R_3} = R_{ref},$$
$$\widehat{\delta I_1} = \frac{R_1}{\widehat{R_1}} \delta I_1 + \frac{r_1}{\widehat{R_1}} \delta I_{r1}, \qquad \widehat{\delta I_3} = \delta I_{ref}. \qquad (2)$$

From the three fluctuating SQUID currents δI_{sq}^i, we can perform three auto-correlations $AC_i \equiv \delta I_{sq}^i \delta I_{sq}^i$ and three cross-correlations $XC_{ij} \equiv \delta I_{sq}^i \delta I_{sq}^j$ non-independent measurements given by

$$AC_i = \langle FFT^*(\delta I_{sq}^i) FFT(\delta I_{sq}^i) \rangle,$$
$$XC_{ij} = \langle FFT^*(\delta I_{sq}^i) FFT(\delta I_{sq}^j) \rangle, \qquad (3)$$

where *FFT* stands for the *Fast Fourier Transform*, *FFT** its complex conjugate, and $\langle \ldots \rangle$ the rms average at the spectrum analyzer. At this stage, the importance of voltage biasing can be seen. Indeed, in the case of a current biasing scheme, the resistance value of the reference resistor would be much larger than all the other resistances. Applying this condition to the set of equations, it becomes obvious that the correlations are always negative as the result of current conservation applied to current fluctuations: $(\delta I_{sq}^1 + \delta I_{sq}^2)^2 = 0$.

In principle, the six measurements are related to the noise and cross-correlations of each element of the circuit through a 6×15 matrix! This can be very much simplified by considering that any cross-correlated noise involving at least one macroscopic resistor is zero. Therefore, the system of equations reduces to

$$\begin{bmatrix} AC_1 \\ AC_2 \\ AC_3 \\ XC_{12} \\ XC_{13} \\ XC_{23} \end{bmatrix} = M_{tot} \begin{bmatrix} S_1 \\ S_2 \\ S_{12} \end{bmatrix} + N_{tot} \begin{bmatrix} S_{r1} \\ S_{r2} \\ S_{ref} \end{bmatrix}, \qquad (4)$$

where S_{ref}, S_{r1}, and S_{r2} are the thermal noises of the three macroscopic resistors R_{ref}, r_1, and r_2. The three quantities

of interest are the noise in each branch of the device, i.e., $S_1 \equiv \delta I_1 \delta I_1$ and $S_2 \equiv \delta I_2 \delta I_2$ and the cross-correlated noise $S_{12} \equiv \delta I_1 \delta I_2$. Therefore, only three measurements are necessary and we usually choose AC_1, AC_2, and XC_{12} that are related to the physical quantities in the following way:

$$\begin{bmatrix} AC_1 \\ AC_2 \\ XC_{12} \end{bmatrix} = M \begin{bmatrix} S_1 \\ S_2 \\ S_{12} \end{bmatrix} + N \begin{bmatrix} S_{r1} \\ S_{r2} \\ S_{ref} \end{bmatrix}. \tag{5}$$

Following Eq. (1), the matrix elements are just given by the values of various resistances. Note that in the case of a sample with nonlinear response, R_1 and R_2 are differential resistances. As an example, the two 3×3 matrices M and N, for $R_1 = R_2 = 1.0\,\Omega$ and $R_{ref} = r_1 = r_2 = 0.1\,\Omega$, are

$$M = \begin{bmatrix} 0.7072 & 0.0049 & -0.1179 \\ 0.0049 & 0.7072 & -0.1179 \\ -0.0589 & -0.0589 & 0.7105 \end{bmatrix},$$

$$N = \begin{bmatrix} 0.007072 & 0.000049 & 0.0059 \\ 0.000049 & 0.007072 & 0.0059 \\ -0.000589 & -0.000589 & 0.0059 \end{bmatrix}. \tag{6}$$

From this example, we see that the AC_1 (AC_2) is mostly due to the noise S_1 (S_2). Focusing on XC_{12}, it reads

$$XC_{12} = -|M_{31}|S_1 - |M_{32}|S_2 + |M_{33}|S_{12}$$
$$\quad - |N_{31}|S_{r1} - |N_{32}|S_{r2} + |N_{33}|S_{ref}, \tag{7}$$

where $|M_{ij}|$ refers to the absolute value of the matrix element M_{ij}. This notation shows that the sign of XC_{12} is not necessary that of the crossed correlated noise S_{12} and that the contribution S_{ref} is always positive. There are different ways to extract S_{12} from XC_{12}. First, if all the contributions other than S_{12} are known, the crossed correlated noise of a sample is known simply by removing those contributions from XC_{12} and divide by M_{33}. Usually, S_1 and S_2 are not known. In that case, the matrix M in Eq. (5) can be inverted and both the spectral densities of noise S_1 and S_2, and the cross-correlations S_{12} can be obtained from measurements.

III. CALIBRATION

In order to test the performance of our instrument, we have measured noise and correlations of a test sample made from two macroscopic resistors of $1\,\Omega$ resistance at room temperature. For this test, these two macroscopic resistors are placed on the sample holder whereas the biasing resistors R_{ref}, r_1, and r_2 are anchored to the mixing chamber. We then expect the current noise in each branch to be given by the thermal noise contribution of each resistive element of the circuit assuming no intrinsic cross-correlated noise between them as they are all macroscopic. The overall results of the six measurements are shown in Figure 2 as a function of the temperature. In this plot, the "SUM" is $(\Sigma \delta I_{sq}^i)^2 = \Sigma AC_i + 2\Sigma XC_{ij}$ accounting for the current conservation law. The precise measurement of the resistances at low temperature gives: $R_1 = R_2 = 0.88\,\Omega$ and $r_1 = r_2 = R_{ref} = 0.088\,\Omega$.
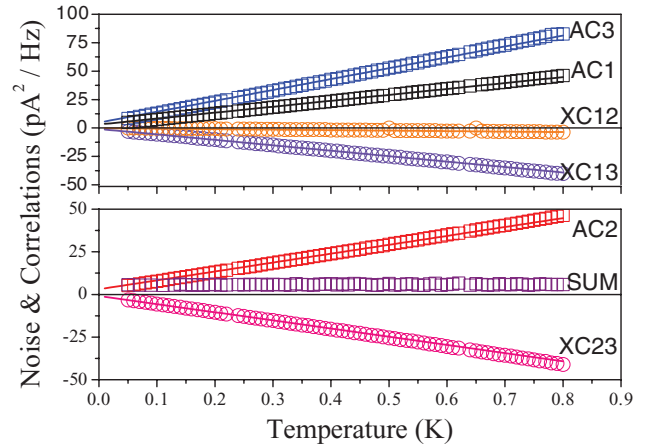

FIG. 2. Noise AC_i and correlations XC_{ij} of the three SQUIDs in response to the circuit depicted in Figure 1 as a function of the mixing chamber temperature with zero dc current. The "SUM" accounts for the current conservation law and the solid lines are adjustments of the data using Eq. (4) and the appropriate offsets (see text).

The solid line in Figure 2 shows the noise and correlations estimates given by Eq. (4) considering only thermal noise and setting $S_{12} = 0$. The only adjusting parameter is then the set-up noise contribution that can be read extrapolating the data at zero temperature. We obtain a set-up noise level of the order of $2-3$ pA^2/Hz for the three auto-correlation AC_i measurements. The set-up noise level correspond to a flux noise of few $\mu\Phi_0/\sqrt{\text{Hz}}$ in a SQUID, which is close to the best noise level given by the manufacturer considering the overall experimental set-up and its connections to room temperature instruments. Note that these measurements have been performed with one dc-current source connected to the circuit but with zero current at its output. Therefore, our results include any additional noise coming from this external source. Regarding the cross-correlation between the SQUID currents XC_{ij}, there are no fitting parameters as we have fixed the intrinsic correlations S_{ij} to be zero. The agreement with the data is very good so we conclude that there is no measurable intrinsic correlations between the three SQUID output signals.

In a second test, we have measured the noise and correlations as a function of a dc-current at fixed temperature. We used I_{DC1} for this measurement and ramped the current up to 1.5 mA at fixed temperatures of 100 mK, 300 mK, and 500 mK. The overall measurements are shown in Figure 3 for a base temperature of 100 mK. As all the resistive elements in the circuits are macroscopic resistors with temperature independent resistances, the shot noise is zero and the noise response should stay constant and given by the thermal noise. However, we clearly see an increase of the noise and correlation responses. This increase corresponds to an elevation of the electronic temperature of the resistors due to Joule heating, whereas the temperature of the mixing chamber was kept regulated at 100 mK. From these results, we can estimate the effective temperature of the resistors. However, at a given value of the dc current, the effective temperatures of the various resistors are not equal. There are two reasons for that. First, because the biasing resistors r_1, r_2,
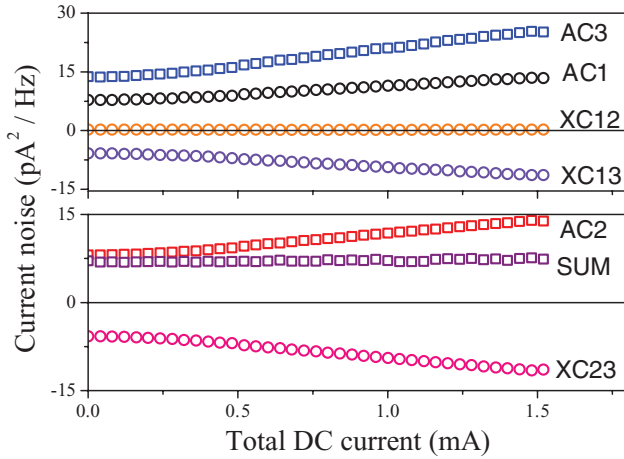
FIG. 3. Noise AC_i and correlations XC_{ij} of the three SQUIDs as a function of the total dc current I_{DC1} applied on the reference resistor side at 100 mK.

FIG. 4. Electronic temperature of the reference resistor R_{ref} and of the sample resistors R_1 and R_2 as a function of the dc current flowing through each of them for three different regulated temperatures. The inset shows the effective temperatures at a base temperature of 100 mK as a function of the dissipated power.

and R_{ref} are anchored to the mixing chamber, their coupling to the cold bath is better than for the R_1 and R_2 resistors that are placed and connected similarly to what a real sample will be, i.e., on a sample holder. Second, for a given dc current I_{DC1}, the current flowing through R_{ref} is different from the current though the other resistors. Thanks to the symmetry of the circuitry, we can consider that $T_{R1} = T_{R2} \equiv T_R$ and $T_{r1} = T_{r2} \equiv T_r$, both sets being different from T_{ref}, where T_R is the effective temperature of a resistor R.

In order to estimate the effective temperatures in the simplest way, we shall be using only the AC_1 and AC_3 measurements (Eq. (4)). Considering only thermal noise, the two equations become

$$AC_1 = \alpha_1 T_R + \alpha_2 T_r + \alpha_3 T_{ref} + AC_1^0,$$
$$AC_3 = \beta_1 T_R + \beta_2 T_r + \beta_3 T_{ref} + AC_3^0,$$
(8)

where $\alpha_1 = 4k_B \times (M_{tot11}/R_1 + M_{tot12}/R_2)$ for instance and AC_1^0 and AC_3^0 the set-up noise of the SQUIDs 1 and 3 obtained from the measurements as a function of the temperature. We can simplify these equations by neglecting the noise contribution of the resistances r_1 and r_2. This assumption is justified, first because $\alpha_2(\beta_2)$ is ten times smaller than $\alpha_1(\beta_1)$ and second because the current through r_1 and r_2 is much smaller than though R_{ref}.[16] The effective temperatures T_R and T_{ref} are then extracted from Eq. (8). The results are shown in Figure 4 for various base temperatures. We do see that the temperature increase is weaker as the base temperature is raised and is almost absent above 500 mK. This behavior is due to the strengthening of the electron-phonon coupling as the temperature is raised. The temperature increase is clearly more pronounced at the reference resistor than for the sample resistors and reaches $\Delta T_{ref} \sim 250$ mK and $\Delta T_R \sim 100$ mK at the lowest temperature investigated (i.e., 100 mK). In the inset, we have plotted the effective temperatures as a function of the power $R I^2$ that is dissipated in each resistor. The different traces for T_R and T_{ref} reflect the fact that the coupling to the mixing chamber of the biasing resistors or the sample resistors is different.
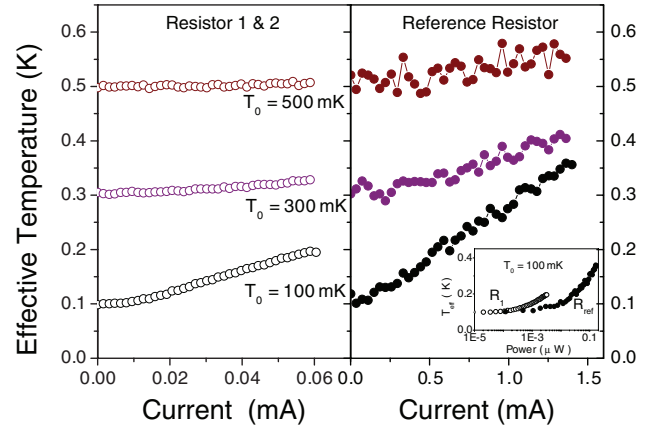
The increase of effective temperature in the biasing resistors translates directly into an increase of their noise contribution in the measured quantities (see Eq. (5)) and may affect the estimate of the quantities of interest. However, because the corresponding matrix elements are small, this additional contribution stays very moderate, but needs to be considered in real samples especially for the XC_{12} measurement.

IV. CONCLUSION

In conclusion, we have described the performances of an experimental instrument implemented to measure current noise and correlations of three terminal nanostructures. This set-up is particularly well adapted to low impedance samples and uses three SQUIDs as current amplifiers. We have calibrated the overall response of the system using macroscopic resistors in place of a real sample. We have shown that despite the complexity of the instrument, we can reach very low intrinsic noise floor and that there is no significant intrinsic noise correlations between the SQUIDs outputs. Finally, the increase of the effective temperature of the various resistive elements of the circuit has been measured as a function of a dc-current.

[1]M. P. Anantram and S. Datta, "Current fluctuations in mesoscopic systems with Andreev scattering," Phys. Rev. B **53**(24), 16390–16402 (1996).
[2]C. W. J. Beenakker, M. Kindermann, and Yu. V. Nazarov, "Temperature-dependent third cumulant of tunneling noise," Phys. Rev. Lett. **90**(17), 176802 (2003).

[3] Ya. M. Blanter and M. Büttiker, "Shot noise in mesoscopic conductors," Phys. Rep. **336**(1–2), 1 (2000).

[4] A. Das, Y. Ronen, and M. Heiblum, "Entangling electrons by splitting cooper pairs: Two-particle conductance resonance and time coincidence measurements," Nature Comm. **3**, 1165 (2012).

[5] R. Hanbury-Brown and R. Q. Twiss, "Correlation between photons in two coherent beams of light," Nature (London) **177**, 27–29 (1956).

[6] C. Hoffmann, F. Lefloch, M. Sanquer, and B. Pannetier, "Mesoscopic transition in the shot noise of diffusive superconductor/normal-metal/superconductor junctions," Phys. Rev. B **70**(18), 180503 (2004).

[7] X. Jehl, M. Sanquer, R. Calemczuk, and D. Mailly, "Detection of doubled shot noise in short normal-metal/superconductor junctions," Nature (London) **405**, 50 (2000).

[8] B. Kaviraj, O. Coupiac, H. Courtois, and F. Lefloch, "Noise correlations in three-terminal diffusive superconductor/normal-metal/superconductor nanostructures," Phys. Rev. Lett. **107**(7), 077005 (2011).

[9] F. Lefloch, C. Hoffmann, M. Sanquer, and D. Quirion, "Doubled full shot noise in quantum coherent superconductor-semiconductor junctions," Phys. Rev. Lett. **90**(6), 067002 (2003).

[10] E. Lhotel, O. Coupiac, F. Lefloch, H. Courtois, and M. Sanquer, "Divergence at low bias and down-mixing of the current noise in a diffusive superconductor/normal-metal/superconductor junction," Phys. Rev. Lett. **99**(11), 117002 (2007).

[11] T. Martin, "Wave packet approach to noise in n–s junctions," Phys. Lett. A **220**(1–3), 137–142 (1996).

[12] R. De Picciotto, M. Reznikov, M. Heiblum, V. Umansky, G. Bunin, and D. Mahalu, "Direct observation of fractional charge," Nature (London) **389**, 162 (1997).

[13] B. Reulet, A. A. Kozhevnikov, D. E. Prober, W. Belzig, and Yu. V. Nazarov, "Phase sensitive shot noise in an Andreev interferometer," Phys. Rev. Lett. **90**(6), 066601 (2003).

[14] L. Saminadayar, D. C. Clattli, Y. Jin, and B. Etienne, "Observation of the e/3 fractionally charge Laughlin quasiparticle," Phys. Rev. Lett. **79**, 2526 (1997).

[15] J. Wei and V. Chandrasekhar, "Positive noise cross-correlation in hybrid superconducting and normal-metal three-terminal devices," Nat. Phys. **6**(7), 494–498 (2010).

[16] We have checked that more elaborated procedures, taking into account the noise of the resistors r_1 and r_2, give the same result.

C.2 Transport in a Three-Terminal Josephson Bijunction: Sub-Gap Structure and Correlated Pair Motion

Subgap structure in the conductance of a three-terminal Josephson junction

A. H. Pfeffer,[1,2] J. E. Duvauchelle,[1,2] H. Courtois,[3,4] R. Mélin,[3,4] D. Feinberg,[3,4] and F. Lefloch[1,2,*]

[1]*Université Grenoble Alpes, INAC-SPSMS, F-38000 Grenoble, France*
[2]*CEA, INAC-SPSMS, F-38000 Grenoble, France*
[3]*Université Grenoble-Alpes, Institut Néel, F-38042 Grenoble, France*
[4]*CNRS, Institut Néel, F-38042 Grenoble, France*

Three-terminal superconductor (S)-normal metal (N)-superconductor (S) Josephson junctions are investigated. In a geometry where a T-shape normal metal is connected to three superconducting reservoirs, new subgap structures appear in the differential resistance for specific combinations of the superconductor chemical potentials. Those correspond to a correlated motion of Cooper pairs within the device that persist well above the Thouless energy and is consistent with the prediction of quartets formed by two entangled Cooper pairs. A simplified nonequilibrium Keldysh-Green's function calculation is presented that supports this interpretation.

I. INTRODUCTION

Josephson effects appear in superconductor-normal metal-superconductor (SNS) junctions where two superconductors (S) are electrically coupled through a nonsuperconducting material (N) [1]. The underlying mechanism is the Andreev reflection that converts a Cooper pair in S into two phase-correlated electrons in N [2].

At zero voltage, the appearance of coherent Andreev bound states leads to a nondissipative supercurrent through the junction and a minigap in the density of states (DOS) of the normal metal. In the case of diffusive junctions and when the length of the normal part L is longer than the superconducting phase-coherence length, both the supercurrent and the minigap scale with the Thouless energy given by $E_{Th} = \hbar D/L^2$, where D is the diffusive constant of the normal metal.

At finite voltages, the nonequilibrium subgap current is governed by multiple Andreev reflections (MARs). In this regime, MARs successively raise a quasiparticle's energy until it reaches the superconducting gap Δ. Due to the superconductor density of states singularity at the gap edge, MARs lead to a subgap structure in the junction differential conductance for $eV = 2\Delta/n$ [3,4], n being an integer. This structure can be observed in diffusive SNS junctions where the diffusion time through the junction is much smaller than the inelastic-scattering time.

In addition to this dc subgap quasiparticle transport, ac Josephson currents also appear in a diffusive SNS junction. However, during the diffusion of an Andreev pair through the junction, phase coherence is maintained only if the energy of the electron or the hole compared to the superconductor chemical potential is smaller than the Thouless energy E_{Th} [5]. The ac Josephson current can be indirectly revealed under microwave irradiation. Shapiro steps [1] in the dc current-voltage characteristics show up when the superconducting phase difference oscillation frequency $2eV/\hbar$ matches the microwave frequency or some multiple of it. The mere existence of Shapiro steps and therefore the ac Josephson currents essentially require a quasistatic superconducting

phase difference, i.e., a diffusion time smaller than the inverse of the Josephson frequency $2eV/\hbar$, or equivalently $eV < E_{Th}$.

More recently, multiterminal junctions started to be investigated and brought a wealth of new properties, among which several remain to be experimentally uncovered. When two normal conductors are closely connected to a superconducting reservoir, crossed Andreev reflections (CARs) can inject two phase-correlated particles, one in each conductor, which amounts to split a Cooper pair into two entangled electrons [6–15]. This only occurs when the distance between the two normal conductors is smaller than the superconducting coherence length.

Another situation is met in mesoscopic three-terminal Josephson junctions in which a single normal conductor is connected to three superconducting contacts [16–20]. The transport properties then depend on two independent (phase or voltage) variables. Therefore, in addition to usual Josephson processes coupling two terminals, new mechanisms are expected that connect all three reservoirs. Several theoretical predictions have been made for such systems [16,17,21–23]. Nonlocal MARs should show up in the so-called incoherent MAR regime where the dwell time exceeds the coherence time [17,24]. On the other hand, the coherent regime where several MARs can occur within the coherence time is also very interesting. Shapiro-like resonances in the absence of external microwaves have been predicted whenever two ac Josephson frequencies match [21]. On similar grounds, the production of nonlocal quartets, as pairs of correlated Cooper pairs, has been proposed as a new dissipationless dc transport mechanism, which is phase coherent, despite the nonequilibrium conditions [22,23]. This present paper reports on an experimental study of such phenomena.

In this article, we report about electronic subgap transport in three-terminal Josephson junctions performed upon a piece of diffusive normal metal connected to three superconducting reservoirs. The junctions are all phase coherent as their length is smaller than the single-particle phase-coherence length L_Φ and in the long junction regime, e.g., the Thouless energy is much smaller than the superconducting gap. They are also rather symmetric and with a high transparency at every SN interface leading to a large subgap Andreev current. Compared

---

*Corresponding author: francois.lefloch@cea.fr

to a pair of two-terminal junctions, additional subgap structures are observed over a wide voltage range, well above the Thouless energy in a regime where one does not expect the presence of strong ac Josephson currents.

In the following, Sec. II contains the experimental details and reports the subgap anomalies. Section III is devoted to a physical discussion of the possible interpretations. Section IV concludes with perspectives.

II. THE EXPERIMENT

A. Samples and measurement process

The samples we have studied have been fabricated by a shadow mask evaporation technique [see scanning electron microscope (SEM) images in Figs. 1 and 2]. Copper and aluminum were evaporated at different angles through a polymethylmethacrylate/methacrylic acid bilayer mask in an ultrahigh vacuum chamber. The evaporation of a thin Cu layer of 50-nm thickness was followed immediately by the evaporation of thick Al electrodes of thickness 500 nm without breaking the vacuum, leading to highly transparent and uniform SN interfaces. The width of the normal metal is about 0.6 μm, and its length L is around 1 μm. Using a diffusion constant for copper $D = 100$ cm^2/s, we get a Thouless energy $E_{\mathrm{Th}} = \hbar D/L^2 \simeq 6$ μeV. This value is confirmed by fitting the temperature dependence of the critical current between two of the superconducting contacts [25]. The superconducting aluminum energy gap is $\Delta = 170$ μeV [26]. The diffusion time $\tau_D = L^2/D \simeq 0.1$ ns is much smaller than the inelastic time $\tau_{\mathrm{in}} \simeq 1$ ns at 100 mK.

Three-terminal differential resistances were measured using an experimental setup specially designed to perform highly sensitive measurements of current average and fluctuations in low-impedance nanodevices at very low temperatures [27], see Fig. 1. The experiment operates down to 30 mK and is equipped with three commercial superconducting quantum interference devices (SQUIDs) as current amplifiers. Each

device terminal is connected to the input coil of a SQUID in series with a macroscopic resistor with a low resistance $R_{\mathrm{ref}} \simeq r_1 \simeq r_2 \simeq 0.09$ Ω.

The measurement scheme consists of sending an ac current modulation $\delta I_{\mathrm{ac}} = 1$ μA on the reference side and recording the current in each branch of the circuit. The differential resistance $R_{\mathrm{diff},a(b)}$ then reads

$$R_{\mathrm{diff},a(b)} = R_{\mathrm{ref}}(\delta I_{\mathrm{ac}} - \delta I_0)/\delta I_{a(b)} - r_{1(2)}, \qquad (1)$$

where δI_i is the ac current measured in the SQUID and $i = 0$, a, or b. For all the samples studied here, $R_{\mathrm{diff},a}$ and $R_{\mathrm{diff},b}$ give the same behavior. In order to explore the nonlinear response in the (V_a, V_b) plane, two dc current sources were used, and the voltage differences V_a and V_b were measured with two room-temperature differential voltage amplifiers. In practice, I_{DC2} is first set to a fixed value, and I_{DC1} is ramped with current steps of 1 or 2 μA. When the ramp is finished, I_{DC2} is increased by a larger current step (typically 20 μA), and I_{DC1} is ramped again. The density of the measurement points is therefore not uniform, which explains the dotted features observed in the contour plots.

B. Results

Figure 2 shows the experimental data measured at $T = 100$ mK in a sample with separated junctions (see SEM image in Fig. 2). For this sample geometry, the separation holds as the Cu underneath the central electrode, although being continuous, is thin enough that the locally induced gap is that of the superconducting gap Δ of aluminum. Only two anomalies corresponding to dc Josephson effects at $V_a = 0$ and $V_b = 0$ are detected. This confirms the absence of multiterminal effects in the presence of a central electrode with a width ($\sim$900 nm) larger than the superconducting coherence length ξ_s as already reported [18]. Such a device therefore behaves like two independent SNS junctions in parallel.

Here and in the following, the voltage range was limited to ± 40 μV because going beyond would require a dc current close to the superconducting electrodes depairing current [18]. As the investigated voltage range remains well below the
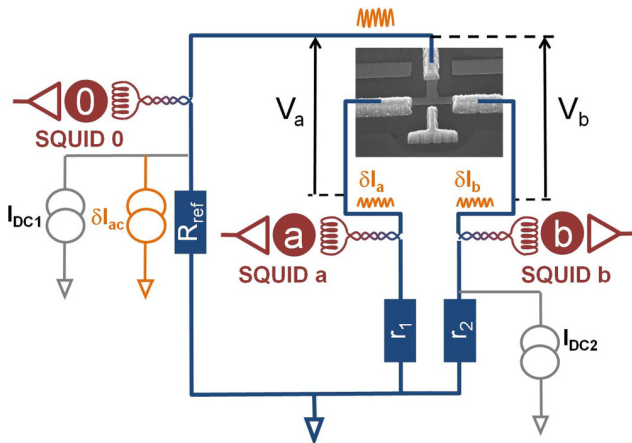

FIG. 1. (Color online) Experimental setup for differential resistance measurements [27]. The three macroscopic resistors have low-resistance values ($\simeq$0.1 Ω) allowing voltage biasing the samples. The SEM image shows a three-terminal junction sample with a T-shape geometry.
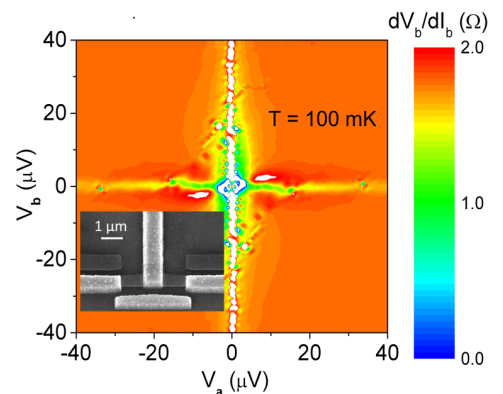

FIG. 2. (Color online) Differential resistance $R_{\mathrm{diff},b}$ of a three-terminal device with separated normal metal parts in the (V_a, V_b) plane at $T = 100$ mK. The SEM image represents a sample with such a typical geometry. In this case, only the upper half with $V_b > 0$ has been measured, and the graph has been symmetrized.
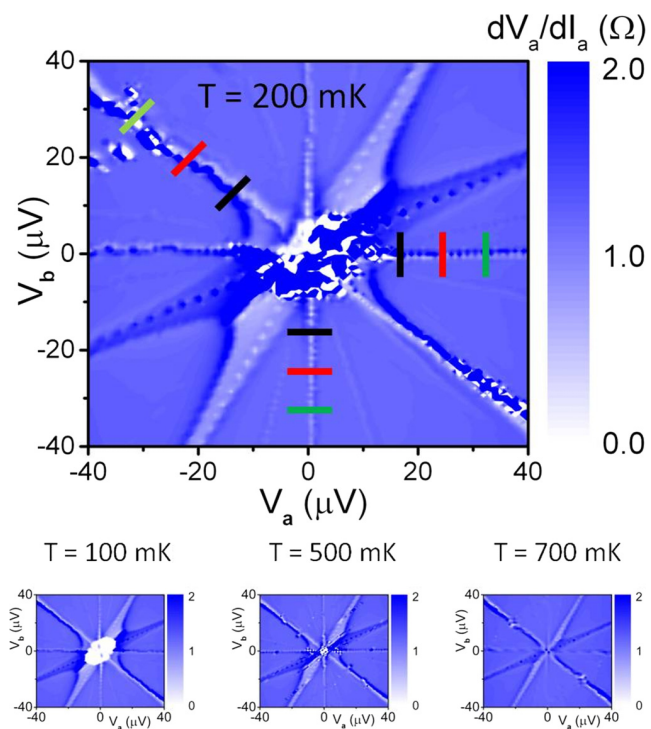
FIG. 3. (Color online) Differential resistance $R_{\mathrm{diff},a}$ of a T-shape junction in the (V_a,V_b) plane for various temperatures. At $T = 200$ mK, the data have been measured for the entire voltage range. For the other temperatures, only the upper half with $V_b > 0$ has been measured, and the graph has been symmetrized for clarity.

superconductor energy gap, the number of multiple Andreev reflections ($\sim 2\Delta/eV$) necessary for a quasiparticle to reach the superconducting gap is more than 8, which would correspond to a total diffusion time much larger than the inelastic-scattering time. This defines a strong interaction regime in which MAR cycles are interrupted by inelastic events. In such a bath of thermalized hot quasiparticles carrying an elevated effective temperature, the MAR-induced steps in the energy distribution function are completely washed out [26,28], and hence the subgap structures related to the singularity of the DOS at the S/N interface cannot be observed.

We have investigated another type of three-terminal junction with a T-shape normal conductor connecting three superconducting electrodes S_0, S_a, and S_b whose SEM image is shown in Fig. 1. Here, S_0 corresponds to the upper central superconducting electrode, and S_a and S_b correspond to the left and right superconducting electrodes, respectively. The differential resistance $R_{\mathrm{diff},a}$ is shown in Fig. 3 at $T = 200$ mK. For this geometry, we expect three Josephson couplings J_{0a}, J_{0b}, and J_{ab} where the two indices label the two involved superconducting terminals. In Fig. 3, the couplings J_{0a} and J_{0b} are clearly observed at $V_a = 0$ and $V_b = 0$, respectively. As expected from the definition of the differential resistance [Eq. (1)], the Josephson coupling J_{0a} appears as a dip in the differential resistance $R_{\mathrm{diff},a}$, whereas J_{0b} shows up as a peak. We have checked that the opposite behavior is observed when plotting $R_{\mathrm{diff},b}$.

We can see in Fig. 3 that the coupling J_{ab} does not show up at $V_b - V_a = 0$. In the actual experiment, the ac modulation was sent to the central electrode S_0 so that the separation of this current into the two branches S_a and S_b is not sensitive to the coupling J_{ab}. We have verified in a similar sample that the latter coupling is indeed revealed when sending the ac modulation through S_a or S_b.

In addition to the two dc Josephson features discussed above, three other lines are clearly visible at $V_b = -V_a$, $V_b = 2V_a$, and $V_b = 1/2V_a$. Notice that in a T-shape geometry, the three superconducting reservoirs are equivalent, meaning that the voltages V_a, V_b, and $V_a - V_b$ are also equivalent. We can thus state that these three lines all originate from the same type of mechanism involving the three superconducting contacts. The observation of this subgap structure in the low-bias differential conductance of a three-terminal superconducting hybrid device is the main experimental finding of the present paper.

In a second step, we have studied the temperature dependence of the differential resistance of the T-shape device. The results are plotted at the bottom of Fig. 3. Apart from the central part that is related to the dc Josephson effect at very low bias, the subgap structure does not evolve much with temperature. All lines are found to be clearly visible up to 700 mK and 40 μV. This confirms that, in the voltage range under investigation, the electronic temperature is well above the bath temperature [29].

To further investigate these new features, we have plotted some line traces perpendicular to the $V_b = -V_a$ line [Fig. 4(a)], to the $V_a = 0$ line [Fig. 4(b)], and to the $V_b = 0$ line [Fig. 4(c)] for various levels of the applied voltages as indicated by the colored lines in Fig. 3. As expected, the differential resistance $R_{\mathrm{diff},a}$ appears as a dc Josephson resonance around $V_a = 0$ for any value of V_b [Fig. 4(b)]. The same type of response is observed when plotting $R_{\mathrm{diff},b}$ around $V_b = 0$
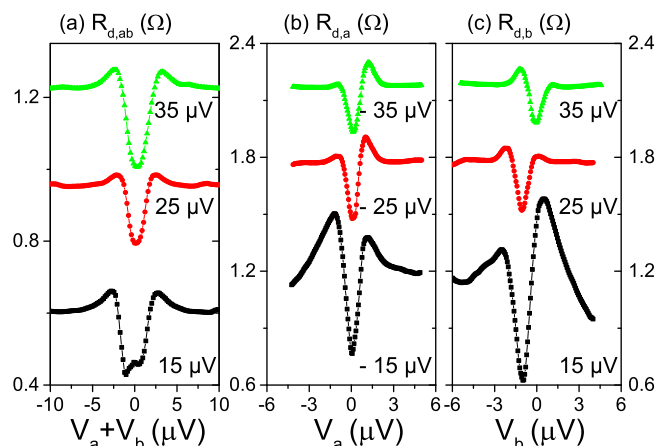
FIG. 4. (Color online) Line traces at various values of the applied voltage of (a) the differential resistance of the full sample considering the two branches a,b as being in parallel as a function of the voltage $V_a + V_b$ for several values of $(V_a - V_b)/2$, (b) the differential resistance of branch a vs V_a for various values of V_b, and (c) the differential resistance of branch b vs V_b for various values of V_a. The color code follows that of the lines in Fig. 3. The data are shifted for clarity except for the lower ones.

for any value of V_a [Fig. 4(c)]. It turns out that when plotting the overall sample differential resistance recalculated by considering the two branches a and b as being in parallel [$R_{\text{diff},ab} = R_{\text{diff},a}R_{\text{diff},b}/(R_{\text{diff},a} + R_{\text{diff},b})$] as a function of the voltage $V_a + V_b$, the observed profile of the subgap structure across the $V_b = -V_a$ line is also in striking resemblance to a Josephson resonance. This observation suggests that the additional anomalies are due to coherent effects involving the three terminals.

Moreover, it is important to notice that the features discussed here are rather robust and constant with respect to the applied voltage. More precisely, as seen in Fig. 4, those persist at energies well above the Thouless energy. Therefore, the scheme to explain the additional features seen at nonzero V_a and V_b and that involve the three terminals must also be robust against voltage-induced dephasing towards all the branches of the device.

III. INTERPRETATION

A. Synchronization of ac Josephson effects

Subgap structures similar to the ones observed here were predicted and observed in the conductance of coupled but separated junctions [30,31]. In this case, two ac Josephson currents coexist with frequencies $\nu_a = 2eV_a/h$ and $\nu_b = 2eV_b/h$. When the two frequencies match, e.g., $V_a = \pm V_b$, down-mixing through the nonlinear response of the device can generate dc subgap structures similar to Shapiro steps. In our experimental scheme with a low-resistive environment ($R_{\text{ref}}, r_1, r_2 \ll R_n$), this coupling could be obtained through the external circuit. Yet, no anomalies are observed in the sample with separate junctions, despite the fact that both samples have exactly the same circuit environment. In fact, due to the SQUID inductances and the wiring, the external impedances at the Josephson frequency are much larger than the resistances of the bias resistors, preventing any ac Josephson current to circulate in the external circuit. Therefore, the relevant coupling can only be within the sample itself.

An extended resistively shunted junction (RSJ) model generalizing that of Ref. [30] could provide a phenomenological description. It involves a triangular Josephson array, shunted by the corresponding normal-state resistances, that account for the quasiparticle processes within the N region. With such a model, the observation of strong resonances requires sizable ac Josephson currents, whereas they are known to decrease when the voltages $eV_{a,b}$ exceed the Thouless energy E_{Th} [32]. Thus, even if the voltage decrease in ac Josephson currents is expected to be progressive, it should definitively lead to a reduction in the resonance for such a variation in $V_{a(b)}$. This is very much in contrast to what is observed in Fig. 4.

In addition to be quantitatively inconsistent, such an RSJ model is only phenomenological. Due to the long coherence time, transport in the present experimental conditions is truly mesoscopic, and the explanation of the observations requires a phase-coherent microscopic mechanism taking place in the normal region.

One might consider a more microscopic approach and seek how the possible ac Josephson oscillations can synchronize together to yield a constant dc component. Such a problem

indeed is similar to the one considered in Refs. [25,33,34]. In a clean SNS junction polarized with a voltage V, oscillations with a frequency double of the basic Josephson frequency $\omega = \frac{2eV}{\hbar}$ are generated and show up under microwave irradiation as half-integer Shapiro steps. This was explained by Argaman [33] within a semiphenomenological description in which the both the Andreev levels and their steady-state distributions oscillate at the Josephson frequency. The argument applies in the adiabatic regime in which the Thouless energy is much larger than the applied voltage.

The same argument could be applied to our three-terminal Josephson junctions for which the oscillating ac Josephson current at a frequency ν_a between two of the three terminals could be modulated by oscillation of the distribution function due to the Josephson coupling between two other terminals at a frequency ν_b. In that case, the second-harmonic response obtained by Argaman [33] in the case of a two-terminal SNS junction transposes into a response at a frequency $\nu_a + \nu_b$ giving rise to dc features when $\nu_a = -\nu_b$.

Again, the conditions for such a scenario to apply are the same as in Refs. [25,33,34], e.g., that the voltage is small enough to allow an adiabatic approximation both in the current components and in the Andreev state distribution. The first one requires that $eV \ll E_{\text{Th}}$, the minigap scale, and the second is even more restrictive, $eV \ll \sqrt{E_{\text{Th}}\frac{\hbar}{\tau_{\text{in}}}}$. For instance, in the experiment of Lehnert *et al.* [34], the frequency doubling is observed for $eV < 40$ μeV, an order of magnitude below the Thouless energy $E_{\text{Th}} = 350$ μeV. But in the experiment reported in our paper, it is the other way around! The subgap anomalies are observed for eV *above* E_{Th}, up to $8E_{\text{Th}}$, only limited by experimental constraints and without any sign of decay. Thus, although qualitatively appealing, the above mechanism does not provide a good explanation for our experimental results.

B. The quartet scenario

1. Qualitative description

The limitation of the synchronization scenario is the voltage-induced dephasing suffered by the two electrons of each of the Cooper pairs transferred between two superconducting terminals. Let us instead show that the quartet mechanism, proposed for clean bijunctions [22,23], can be generalized to a diffusive system and is fully robust against dephasing at voltages much higher than E_{Th}.

The main idea is that two Cooper pairs are transferred in a single and fully energy-conserving quantum process in which the two pairs cross in an entangled way by exchanging an electron between them.

To describe this mechanism, let us consider a piece of diffusive normal metal N connected to three superconducting reservoirs (S_0, S_a, and S_b) whose potentials are set to $V_0 = 0$, $V_a = +V$, and $V_b = -V$ respectively, as depicted in Fig. 5. Two Cooper pairs from S_0 can be simultaneously split in N, each of them in two electrons with opposite energies (with respect to the Fermi energy) that we define, without losing generality, as $\pm(eV + \varepsilon)$ and $\pm(eV - \varepsilon)$. When these energies are larger than the Thouless energy E_{Th}, the two electrons of each pair do not follow the same trajectory. Nevertheless, if the energy ε
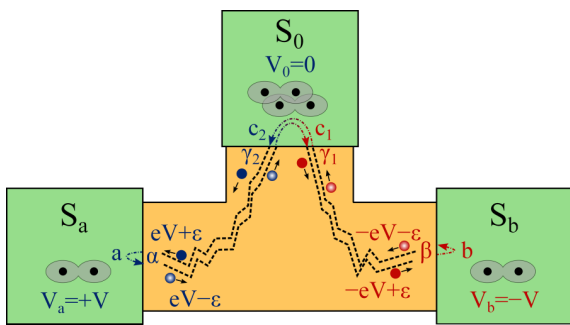
FIG. 5. (Color online) Schematic for Q_0 quartet production from S_0 to S_a and S_b. Two Cooper pairs are split simultaneously at S_0 with one electron of each pair propagating towards S_a and S_b where, under the appropriate energy condition ($V_a = -V_b$), they recombine to create two separated Cooper pairs.

is small compared to E_{Th}, the electron *of the first pair* at $eV + \varepsilon$ can follow the same phase-coherent trajectory as the electron *of the second pair* at $eV - \varepsilon$ and, for instance, reach S_a. Since $V_a = +V$, the two particles have relative opposite energies $\pm\varepsilon$ and can recombine as a Cooper pair in S_a. The same mechanism holds for the two other particles at S_b. In the whole process, two Cooper pairs from S_0 are split altogether to create two spatially separated Cooper pairs in S_a and S_b, a so-called quartet, named hereafter Q_0 as it originates from S_0.

The key point favoring the quartet mechanism is that the coherence of each Andreev pair reaching S_a or S_b can be satisfied at any voltage $V_a = -V_b$, even when $|eV_{a(b)}| > E_{\text{Th}}$. Considering again the four electrons emitted from the two split pairs, two of them have energies $eV \pm \varepsilon$ [pair (a),] and the two others have energies $eV \pm \varepsilon$ [pair (b)] (see Fig. 5). As the quartet mechanism is a quantum process, the sum of all the possible diffusion probabilities has to be considered altogether. Among those, the situation where pair (a) propagates towards S_a and pair (b) towards S_b is phase coherent and independent of the applied voltage V. Indeed, the phase difference accumulated by pair (a) [pair (b)] scales as $\varepsilon\tau_{Da(b)}/\hbar$ where $\tau_{Da(b)}$ is the diffusion time from S_0 to $S_a(S_b)$. The quartet mode is therefore a fully coherent dc process taking place in the mesoscopic N region and involving four Andreev reflections.

This is very different from the scheme where two electrons of a single Cooper pair propagate towards S_a or S_b. In that case, the two electrons of a single pair have energies $\pm(eV + \varepsilon)$ or $\pm(eV - \varepsilon)$, and the accumulated phase difference scales with eV/E_{Th}. The effect of such trajectories has, therefore, a vanishing contribution to the electronic transport when $eV \gg E_{\text{Th}}$.

Let us note that the quartet response bears some resemblance to MARs [17] with two important differences. First, the total energy balance of the process is zero, and second, it does not lead to quasiparticle transport above the superconducting gap.

In this quartet description, the line at $V_b = -V_a$ corresponds to the production of quartets Q_0, whereas the line at $V_b = 2V_a$ ($V_b = 1/2V_a$) originates from quartets Q_a (Q_b) produced in S_a (S_b) towards S_0 and S_b (S_0 and S_a). At lowest order, the quartet mechanism requires only four Andreev

reflections, much less than needed in the same voltage range for a quasiparticle to reach the gap edge in a usual MAR process, which makes the quartet mechanism much more robust to inelastic collisions.

2. Sketch of the microscopic calculation

The above arguments can be substantiated by a microscopic calculation (the Appendix), valid under the separation of energy scales $E_{\text{Th}} < eV < \Delta$. One uses nonequilibrium Keldysh-Green's functions and performs a lowest-order calculation in tunnel amplitudes at the different SN interfaces, inspired by Ref. [35]. The quartet current is calculated using a Hamiltonian formalism, and an essential step is averaging over disorder.

The current appears as a sum of contributions, each being a product of six propagating amplitudes associated with the diagrammatic lines in Fig. 5 [Eqs. (A7)–(A9)]. As a classical procedure in the treatment of diffusion in metals and in an SNS junction [36], disorder averaging takes advantage of the energy separation of these lines. In fact, two lines are correlated by disorder provided their energies are closer than E_{Th}. It results that the averaged product of six amplitudes can be decoupled into three factors. One corresponds to the diffusion of an Andreev pair from S_0 to S_a at energies $eV \pm \varepsilon$ with $\varepsilon < E_{\text{Th}} < eV$, another one corresponds to the diffusion of an Andreev pair from S_0 to S_b at energies $-eV \pm \varepsilon$, and the third corresponds to the anomalous diffusion within S_0 that achieves Andreev reflection at energies eV and $-eV$ [37].

The principle of the above calculation can be benchmarked on the simpler case of an SNS junction at equilibrium for which the coherent *pair* current is proportional to the *single-particle* conductance G_N times the coherent energy window given by the Thouless energy. This leads to the known scaling for the critical current $eI_c \propto G_N E_{\text{Th}}$ [25].

The main result of our calculation detailed in the Appendix is to show that the coherent *quartet* current has a similar form and is given by the *two-particle* CAR conductance times the same energy window E_{Th}. It follows a scaling given by

$$eI_Q \sim -G_{\text{CAR}}E_{\text{Th}}. \tag{2}$$

The minus sign comes from the exchange and recombination process [23]. The conductance G_{CAR} is the crossed Andreev conductance of a $N_a S_0 N N_b$ structure in which the electrodes S_a and S_b are in the normal state and at voltages $\pm V$.

The CAR conductance can then be evaluated (see the Appendix) and recast as

$$G_{\text{CAR}} \sim \frac{G_{N_a} G_{N_b}}{G_0(\xi_s)}, \tag{3}$$

where $G_{N_{a,b}}$ is the conductance within each normal branch of the bijunction and $G_0(\xi_s)$ is the normal-state conductance of a region of size ξ of the superconductor S_0. This calculation shows that the ratio between the quartet maximum current at a bias V and the single junction critical current at zero bias is $I_Q/I_c(0) \sim G_{\text{CAR}}/G_N \sim G_N/G_0(\xi_s)$, which is not necessarily small. Based on measured sample parameters, we estimate this ratio to ~ 0.1–0.5, in fair agreement with the experiment. Notice that if $eV \ll \Delta$, G_{CAR} thus $I_{Q,\text{max}}$ does not decrease with V, in agreement with the present experiment.

IV. CONCLUSION

In conclusion, we reported about new subgap structures in the differential conductance of a metallic nanostructure with three superconducting reservoirs, a so-called bijunction. The existence of such anomalies well above the Thouless energy points towards a new and fully coherent mechanism, different from the synchronization of separated Josephson junctions, or any mesoscopic generalization of such a process. Our results are consistent with the production of nonlocal quartets as a resonant pair of Cooper pairs splitting and recombining within the N region. Therefore, our results provide convincing experimental evidence for (double) crossed Andreev reflections in metallic superconducting/normal metal hybrid three-terminal nanostructures with a signature in the electronic response at low temperatures much larger than in metallic Cooper pair splitters using only one superconducting reservoir.

The quartet mechanism carries intrinsic four-particle entanglement, generalizing two-fermion entanglement from CAR's [10] that could be exploited if adding more degrees of freedom, such as in quantum dots [22]. More refined probes are necessary to quantitatively study the correlated pair transport involving quartets as well as possible other regimes not evidenced in the present experiments, such as the low-voltage adiabatic transport. A useful tool is to couple the bijunction to microwaves and to study the Shapiro steps coming from deviations from the resonant situation $V_a = -V_b = V$.

APPENDIX: ANALYTICAL CALCULATION OF THE QUARTET CURRENT

The superconductors $S_{0,a,b}$ are described by the mean-field BCS Hamiltonian with identical gaps Δ and phases $\varphi_0 = 0, \varphi_a, \varphi_b$. To simplify, all materials S_i, N are taken with the same bandwidth w, and they are connected by a hopping parameter τ, related to the interface transparency T by $T = \frac{4\tau^2/w^2}{(1+\tau^2/w^2)^2}$. In Nambu notations, the hopping amplitudes take the form ($i = 0$, a, b, and α denoting the position on the interface)

$$\hat{\Sigma}_{i,\alpha}(t) = \tau \begin{pmatrix} e^{ieV_i t} & 0 \\ 0 & -e^{-ieV_i t} \end{pmatrix}. \quad (A1)$$

The local advanced Green's functions in the superconductors are as follows in the frequency domain ($\omega_\eta = \omega - i\eta$):

$$\hat{g}_{i,i}^A(\omega) = \frac{1}{w\sqrt{\Delta^2 - \omega_\eta^2}} \begin{pmatrix} -\omega_\eta & \Delta e^{i\varphi_i} \\ \Delta e^{-i\varphi_i} & -\omega_\eta \end{pmatrix}, \quad (A2)$$

The retarded Green's functions are obtained by changing η into $-\eta$ in the above expression. The choice of the gauge is such that the time dependence of the phases $2eV_{a(b)}t/\hbar$ are included in the Nambu hopping amplitudes $\hat{\Sigma}_{a(b)}$ (with

$\hbar = 1$). The phases $\varphi_{a(b)}$ at the origin of time are included in the off-diagonal components of the Nambu-Green's functions. The local advanced Green's functions are $\hat{g}^A(\omega) \sim i\pi\rho_N$ in the normal metal, where ρ_N is the local density of states of the normal metal.

The current at some point a of the interface of the superconductor S_a is given by

$$I_a(t) = \frac{2e}{h}\mathcal{R}e\left[\hat{\Sigma}_{a,\alpha}(t)\hat{G}_{\alpha,a}^{(\pm),11}(t,t) - \hat{\Sigma}_{a,\alpha}(t)\hat{G}_{\alpha,a}^{(\pm),22}(t,t)\right], \quad (A3)$$

where $\hat{G}_{\alpha,a}^{(\pm),11}(t,t)$ [respectively, $\hat{G}_{\alpha,a}^{(\pm),22}(t,t)$] is the electron (respectively, hole) Keldysh-Green's function at point a.

Together with $\hat{G}^{(R,A)}$, $\hat{G}_{\alpha,a}^{(\pm)}(t,t)$ obeys a Dyson equation which allows calculating the current as a product of Green's functions propagating electrons (holes) in the normal or superconducting regions and hopping self-energies $\hat{\Sigma}$ at the interfaces. Stationarity allows Fourier transforming the time quantities and calculating the current contributions as a sum over the Fourier components $\hat{G}(\omega_n)$ with $\omega_n = \omega + neV$. Specifying to the voltages $V_a = V$, $V_b = -V$, the self-energies $\hat{\Sigma}(\omega)$ connect Green's functions with indices n differing by ± 1.

The quartet diagram on Fig. 5 takes a typical chain form, starting at the $S_0 - N$ interface (with the frequency arguments omitted),

$$(\mathcal{A})_Q = \Sigma_{c_1,\gamma_1}^{11/00} g_{\gamma_1,\beta}^{11/00} \Sigma_{\beta,b}^{11/01} g_{bb}^{12/11} \Sigma_{b,\beta}^{22/12} g_{\beta,\gamma_1}^{22/22}$$
$$\times \Sigma_{\gamma_1,c_1}^{22/22} g_{c_1,c_2}^{21/22} \Sigma_{c_2,\gamma_2}^{11/22} g_{\gamma_2,\alpha}^{11/22} \Sigma_{\alpha,a}^{11/21} g_{aa}^{12/11}$$
$$\times \Sigma_{a,\alpha}^{22/10} g_{\alpha,\gamma_2}^{22/00} \Sigma_{\gamma_2,c_2}^{22/00} g_{0,c_1}^{21/00}. \quad (A4)$$

The first two upper labels correspond to Nambu matrix notation, and the second two correspond to the harmonics (n,n') of half the Josephson frequency $\omega_0 = \frac{2eV}{\hbar}$. The advanced, retarded, and Keldysh labels have to be inserted in this expression, resulting in eight different terms. Next, each of the eight terms is evaluated. The final expression for $(\mathcal{A})_Q$ is as follows:

$$(\mathcal{A})_Q = n_F(\omega - eV)\tau^8$$
$$\times \left\{ g_{aa}^A g_{\alpha,\gamma_2}^A g_{\gamma_2,\gamma_1}^A g_{\gamma_1,\beta}^A g_{bb}^A g_{\beta,\gamma_1}^A g_{\gamma_1,\gamma_2}^A g_{\gamma_2,\alpha}^A - A \leftrightarrow R \right\}, \quad (A5)$$

where $A \leftrightarrow R$ means that advanced and retarded have been interchanged. The unperturbed Green's functions g_{ij}^A represent the amplitudes for electron and hole propagation, and they are evaluated at the appropriate energies $\pm eV \pm \varepsilon$ shown in Fig. 5. Those energies correspond to the transitions between n and n' indices [see Eq. (A4)] induced by the hopping matrix elements. A summation over the labels α (β) and γ at the interfaces has to be carried out. This procedure is justified to describe extended contacts at lowest order in the tunnel amplitudes. As far as the applied voltages are small enough compared to the gap, the energy dependence of the Green's functions can be discarded.

The next step is to perform disorder averaging. A contribution, such as $(\mathcal{A})_Q$ should be replaced by its average $\langle\langle(\mathcal{A})_Q\rangle\rangle$ over disorder in the N region and in the superconductors. Expression (A5) contains several amplitudes, matrices in S_i and numbers in N. First, g_{aa}^A, g_{bb}^A, which yields density of

states factors in S_a and S_b. Second, the product $(g_{\gamma_2,\gamma_1}^A g_{\gamma_1,\gamma_2}^A)$ of amplitudes in S_0 at energies close to eV (electrons) and $-eV$ (holes) that can be averaged separately. It describes the anomalous diffusion of a quasiparticle within S_0, yielding Andreev reflection at the NS_0 interface [37], and third, the product $(g_{\alpha,\gamma_2}^A g_{\gamma_2,\alpha}^A g_{\gamma_1,\beta}^A g_{\beta,\gamma_1}^A)$ of amplitudes in N. The two first amplitudes contribute at energies $eV \pm \varepsilon$, and the two others contribute at energies $-eV \pm \varepsilon$. We assume that $eV > E_{\text{Th}} > \varepsilon$ and use the fact that the coherence between electron and hole trajectories is limited by the Thouless energy. Then it is justified to decouple $\langle\langle g_{\alpha,\gamma_2}^A g_{\gamma_1,\beta}^A g_{\beta,\gamma_1}^A g_{\gamma_2,\alpha}^A \rangle\rangle \simeq \langle\langle g_{\alpha,\gamma_2}^A g_{\gamma_2,\alpha}^A \rangle\rangle \langle\langle g_{\gamma_1,\beta}^A g_{\beta,\gamma_1}^A \rangle\rangle$. This amounts to separately averaging the diffusive trajectories connecting S_a to S_0, and S_b to S_0, relying on energy rather than spatial separation. Then one obtains

$$\langle\langle (\mathcal{A})_Q \rangle\rangle = 2 n_F(\varepsilon - eV)(\pi \rho_N)^2 \tau^8$$
$$\times \left\{ P_{\beta,\gamma_1} \tilde{P}_{c_1,c_2} P_{\gamma_2,\alpha} \right\} \sin(\varphi_a + \varphi_b). \quad (A6)$$

with

$$P_{\beta,\gamma_1} \equiv \langle\langle g_{\gamma_1,\beta}^{11}(\varepsilon - eV) g_{\beta,\gamma_1}^{22}(\varepsilon + eV) \rangle\rangle, \quad (A7)$$

$$P_{\gamma_2,\alpha} \equiv \langle\langle g_{\gamma_2,\alpha}^{11}(\varepsilon + eV) g_{\alpha,\gamma_2}^{22}(\varepsilon - eV) \rangle\rangle, \quad (A8)$$

$$\tilde{P}_{c_1,c_2} \equiv \langle\langle g_{c_1,c_2}^{12}(\varepsilon - eV) g_{c_2,c_1}^{21}(\varepsilon + eV) \rangle\rangle, \quad (A9)$$

and where the characteristic phase dependence of the quartet mode stems from the four involved Andreev reflections, one at S_a, one at S_b, and two at S_0. A product of three probabilities appear: $P_{\gamma_2,\alpha}$ for electron-hole (Andreev pair) diffusion from S_a to S_0, $\tilde{P}_{c_1,c_2}$ for the anomalous diffusion inside S_0, and P_{β,γ_1} for the Andreev pair diffusion from S_0 to S_b. $\tilde{P}_{c_1,c_2}$ tracks the probability of two Andreev reflections at S_0. The Andreev pair diffusion modes $P_{ij} = P(R_{ij},\omega)$ showing out in Eq. (A6) are obtained by a summation of the ladder diagrams [36], standard in the diffusion problem.

The diffusion probability on a distance R is $P_0(R,\omega,V) = \langle\langle g^{11,A}(R,\omega - eV) g^{22,A}(R,\omega + eV) \rangle\rangle$, and its space Fourier transform is proportional to

$$P_0(\mathbf{q},\omega,V) \sim \frac{1}{w(i\omega + Dq^2)}. \quad (A10)$$

Importantly, $P_0(\mathbf{q},\omega,V)$ has no dependence on V in the $V \ll \Delta$ limit. Most importantly, the quartet current appears even if the voltage is larger than the Thouless energy.

The above principle for the quartet current calculation can be benchmarked on the simpler case of an SNS junction at equilibrium. One considers the dc Josephson current in a $S_a I N I S_b$ junction and evaluates it on the same line as above by a expansion of the current to fourth order in the transparencies.

Then the Fourier transform of the diffusion probability associated with the Andreev pair modes $\langle\langle g_{\gamma_1,\beta}^{11,A}(\omega - eV) g_{\beta,\gamma_1}^{22,A}(\omega + eV) \rangle\rangle$ in N is also given by $P_0(\mathbf{q},\omega,V)$. For comparison, in a $N_a I N I N_b$ junction with mode $\langle\langle g_{\gamma_1,\beta}^{11,A}(\omega - eV) g_{\beta,\gamma_1}^{11,R}(\omega + eV) \rangle\rangle$, the diffusion probability is $P_0(\mathbf{q},0,V)$, thus without the $i\omega$ factor in the denominator of Eq. (A10).

Depending on the diffusion taking place in N or S, this results after integration over q,

$$P_{0N}(R,\varepsilon) \sim 2\pi \rho_N \frac{1}{2DR} \exp\left(-\sqrt{\frac{\varepsilon}{E_{\text{Th}}}}\right) \cos\left(\sqrt{\frac{\varepsilon}{E_{\text{Th}}}}\right),$$

$$\tilde{P}_{0S}(R,\varepsilon) \sim 2\pi \rho_N \frac{1}{2DR} \exp\left(-\frac{R}{\xi}\right), \quad (A11)$$

where the Thouless energy for a junction of length R is $E_{\text{Th}} = \frac{\hbar D}{R^2}$. Notice that $\tilde{P}_{0S}$ decays on the effective coherence length in S_0 (taking into account disorder) [37].

The quartet current calculation follows from Eqs. (A3)–(A6):

$$I_{\text{tot}} \sim \frac{2e}{h} \mathcal{N} \frac{\tau^8}{w^2} \int d\omega \, P_{\beta,\gamma_1}(\omega) P_{\gamma_2,\alpha}(\omega)$$
$$\times \int_{\mathcal{S}_c} \frac{d^2 r}{\xi^2} \tilde{P}_{c_1,c_2}(\omega) (\delta\mathcal{V})^3 \sin(\varphi_a + \varphi_b), \quad (A12)$$

where $\mathcal{N}$ is the average number of channels due to integration on one of the interfaces of $S_{a,b}$. The integration volume $\delta\mathcal{V} \sim \lambda_F l_e^2$ accounts for the absorbing boundary conditions for diffusion in the reservoirs [36] (λ_F is the Fermi wavelength). Integration over the surface of S_0 accounts for the range ξ of the Andreev reflection and yields a total factor $\frac{\xi}{w l_e}$ for the integrated Andreev probability in S_0. Integration over frequency yields the factor E_{Th}, and each diffusion probability contributes by a factor $\frac{l_e}{wL}$. One finally obtains

$$e I_Q \sim -G_{\text{CAR}} E_{\text{Th}} \sin(\varphi_a + \varphi_b). \quad (A13)$$

A yet unknown prefactor has to be added in Eq. (2), which is expected to be of the same order as that involved in the case of a SNS junction.

The conductance G_{CAR} refers to the CAR in a $N_a N S_0 N N_b$ hybrid structure. The maximum quartet current is thus naturally obtained by multiplying the CAR conductance by the Thouless energy that sets the coherence of Andreev pairs on both branches a,b of the bijunction.

The CAR conductance is evaluated from above,

$$G_{\text{CAR}} \sim \frac{2e^2}{h} \mathcal{N} \left(\frac{\tau}{w}\right)^8 \left(\frac{l_e}{L}\right)^2 \frac{\xi}{l_e}, \quad (A14)$$

where the ratio $\frac{\tau}{w}$ is taken from the rather good experimental conductance $T \sim 0.3$.

[1] K. Likharev, *Dynamics of Josephson Junctions and Circuits* (Gordon and Breach, New York, 1986).

[2] A. F. Andreev, Sov. Phys. JETP **19**, 1228 (1964).

[3] T. M. Klapwijk, G. E. Blonder, and M. Tinkham, Physica B+C **109–110**, 1657 (1982).

[4] M. Octavio, M. Tinkham, G. E. Blonder, and T. M. Klapwijk, Phys. Rev. B **27**, 6739 (1983).

[5] H. Courtois, P. Gandit, B. Pannetier, and D. Mailly, Superlattices Microstruct. **25**, 721 (1999).

[6] J. M. Byers and M. E. Flatté, Phys. Rev. Lett. **74**, 306 (1995).

[7] M. P. Anantram and S. Datta, Phys. Rev. B **53**, 16390 (1996).

[8] J. Torrès and T. Martin, Eur. Phys. J. B **12**, 319 (1999).

[9] G. Deutscher and D. Feinberg, Appl. Phys. Lett. **76**, 487 (2000).

[10] P. Recher, E. V. Sukhorukov, and D. Loss, Phys. Rev. B **63**, 165314 (2001).

[11] D. Beckmann, H. B. Weber, and H. v. Löhneysen, Phys. Rev. Lett. **93**, 197003 (2004).

[12] P. Cadden-Zimansky and V. Chandrasekhar, Phys. Rev. Lett. **97**, 237003 (2006).

[13] L. Hofstetter, J. Csonka, S. Nygård, and C. Schönenberger, Nature (London) **461**, 960 (2009).

[14] L. G. Herrmann, F. Portier, P. Roche, A. L. Yeyati, T. Kontos, and C. Strunk, Phys. Rev. Lett. **104**, 026801 (2010).

[15] A. Das, Y. Ronen, M. Heiblum, D. Mahalu, A. V. Kretinin, and H. Shtrikman, Nat. Commun. **3**, 1165 (2012).

[16] S. Duhot, F. Lefloch, and M. Houzet, Phys. Rev. Lett. **102**, 086804 (2009).

[17] M. Houzet and P. Samuelsson, Phys. Rev. B **82**, 060517 (2010).

[18] B. Kaviraj, O. Coupiac, H. Courtois, and F. Lefloch, Phys. Rev. Lett. **107**, 077005 (2011).

[19] F. Giazotto and F. Taddei, Phys. Rev. B **84**, 214502 (2011).

[20] A. V. Galaktionov, A. D. Zaikin, and L. S. Kuzmin, Phys. Rev. B **85**, 224523 (2012).

[21] J. C. Cuevas and H. Pothier, Phys. Rev. B **75**, 174513 (2007).

[22] A. Freyn, B. Douçot, D. Feinberg, and R. Mélin, Phys. Rev. Lett. **106**, 257005 (2011).

[23] T. Jonckheere, J. Rech, T. Martin, B. Douçot, D. Feinberg, and R. Mélin, Phys. Rev. B **87**, 214501 (2013).

[24] N. M. Chtchelkatchev, T. I. Baturina, A. Glatz, and V. M. Vinokur, Phys. Rev. B **82**, 024526 (2010).

[25] P. Dubos, H. Courtois, O. Buisson, and B. Pannetier, Phys. Rev. Lett. **87**, 206801 (2001).

[26] C. Hoffmann, F. Lefloch, M. Sanquer, and B. Pannetier, Phys. Rev. B **70**, 180503 (2004).

[27] A. H. Pfeffer, B. Kaviraj, O. Coupiac, and F. Lefloch, Rev. Sci. Instrum. **83**, 115107 (2012).

[28] F. Pierre, A. Anthore, H. Pothier, C. Urbina, and D. Esteve, Phys. Rev. Lett. **86**, 1078 (2001).

[29] H. Courtois, M. Meschke, J. T. Peltonen, and J. P. Pekola, Phys. Rev. Lett. **101**, 067002 (2008).

[30] M. A. H. Nerenberg, J. A. Blackburn, and D. W. Jillie, Phys. Rev. B **21**, 118 (1980).

[31] D. W. Jillie, M. A. H. Nerenberg, and J. A. Blackburn, Phys. Rev. B **21**, 125 (1980).

[32] A. F. Volkov and H. Takayanagi, Phys. Rev. Lett. **76**, 4026 (1996).

[33] N. Argaman, Superlattices Microstruct. **25**, 861 (1999).

[34] K. W. Lehnert, N. Argaman, H.-R. Blank, K. C. Wong, S. J. Allen, E. L. Hu, and H. Kroemer, Phys. Rev. Lett. **82**, 1265 (1999).

[35] J. C. Cuevas, A. Martín-Rodero, and A. Levy Yeyati, Phys. Rev. B **54**, 7366 (1996).

[36] E. Akkermans and G. Montambaux, *Mesoscopics Physics of Electrons and Photons* (Cambridge University Press, Cambridge, UK, 2007).

[37] D. Feinberg, Eur. Phys. J. B **36**, 419 (2003).

Appendix D

Acknowlegment

introducing me into french language and culture. Without you, my time in France would have been much less exciting. All the best for your future!

Thanks to Marie-José Blanchard, Frédéric Gustavo, Michel (mechanics), Pierre and Fred Poletti (electronics/ IT) for their support during my PhD and all the other members of GT, LaTEQS and IMAPEC for the pleasant time in Grenoble.

Thanks to Yves Rassendren and his vocal ensemble Stravaganza for three years of wonderful music and concerts together, which were a perfect recreation for me. All the best!

I would like to thank all my friends in Grenoble, especially Aremi & Thierry, Ika, Russo, Claire, Fréd & Stéphanie, Franck & Rudeeshan for the common time in Grenoble. I hope we'll stay in contact and hope to see you soon in Regensburg. Thanks to my family for their interest in my work and their understanding of my temporal constraints during my PhD. Last but not least, I would like to thank my wonderful wife, admitting to our adventure in Grenoble. Without your advice, encouragement and patience, this would have been impossible. My darling, this is for you.

Bibliography

[1] A. Einstein, B. Podolsky, and N. Rosen. Can quantum-mechanical description of physical reality be considered complete? *Phys. Rev.*, 47:777–780, May 1935.

[2] J. S. Bell. On the problem of hidden variables in quantum mechanics. *Rev. Mod. Phys.*, 38(3):447–452, 1966.

[3] P. W. Anderson and J. M. Rowell. Probable observation of the Josephson superconducting tunneling effect. *Phys. Rev. Lett.*, 10(6):230–232, March 1963.

[4] J. M. Rowell. Magnetic field dependence of the Josephson tunnel current. *Phys. Rev. Lett.*, 11(5):200–202, September 1963.

[5] S. Shapiro. Josephson currents in superconducting tunneling: The effect of microwaves and other observations. *Phys. Rev. Lett.*, 11(2):80–82, July 1963.

[6] M. D. Fiske. Temperature and magnetic field dependences of the Josephson tunneling current. *Rev. Mod. Phys.*, 36:221–222, January 1964.

[7] I. K. Yanson, V. M. Svistunov, and I. M. Dmitrenko. Experimental observation of the tunnel effect for Cooper pairs with the emission of photons. *Sov. Phys. JETP*, 21:650, 1965.

[8] P. G. de Gennes. *Superconductivity of metals and alloys*. Addison Wesley, 1966.

[9] A. A. Golubov, M. Yu. Kupriyanov, and E. Il'ichev. The current-phase relation in Josephson junctions. *Rev. Mod. Phys.*, 76:411–469, April 2004.

[10] P. E. Lindelof. Superconducting microbridges exhibiting Josephson properties. *Reports on Progress in Physics*, 44(9):949, 1981.

[11] J. Bindslev Hansen and P. E. Lindelof. Static and dynamic interactions between Josephson junctions. *Rev. Mod. Phys.*, 56(3):431–459, July 1984.

[12] J. J. A. Baselmans, A. F. Morpurgo, B. J. van Wees, and T. M. Klapwijk. Reversing the direction of the supercurrent in a controllable Josephson junction. *Nature*, 397:43–45, 1999.

[13] J. Edrich, B. Sullivan, and D.G. McDonald. Results, potentials, and limitations of Josephson-mixer receivers at millimeter and long submillimeter wavelengths. *Microwave Theory and Techniques, IEEE Transactions on*, 25(6):476–479, 1977.

[14] N. Bergeal, F. Schackert, M. Metcalfe, R. Vijay, V. E. Manucharyan, L. Frunzio, D. E. Prober, R. J. Schoelkopf, S. M. Girvin, and M. H. Devoret. Phase-preserving amplification near the quantum limit with a Josephson ring modulator. *Nature*, 465(7294):64–68, 2010.

[15] J. M. Byers and M. E. Flatté. Probing spatial correlations with nanoscale two-contact tunneling. *Phys. Rev. Lett.*, 74(2):306–309, January 1995.

[16] G. Deutscher and D. Feinberg. Coupling superconducting-ferromagnetic point contacts by Andreev reflections. *Applied Physics Letters*, 76(4):487, 2000.

[17] D. Beckmann, H. B. Weber, and H. v. Löhneysen. Evidence for crossed Andreev reflection in Superconductor-Ferromagnet hybrid structures. *Phys. Rev. Lett.*, 93:197003, November 2004.

[18] S. Russo, M. Kroug, T. M. Klapwijk, and A. F. Morpurgo. Experimental observation of bias-dependent nonlocal Andreev reflection. *Phys. Rev. Lett.*, 95:027002, July 2005.

[19] J. Brauer, F. Hübler, M. Smetanin, D. Beckmann, and H. v. Löhneysen. Nonlocal transport in Normal-metal/Superconductor hybrid structures: Role of interference and interaction. *Phys. Rev. B*, 81:024515, January 2010.

[20] L. Hofstetter, J. Csonka, S. Nygård, and C. Schönenberger. Cooper pair splitter realized in a two-quantum-dot y-junction. *Nature*, 461:960–963, 2009.

[21] L. G. Herrmann, F. Portier, P. Roche, A. Levy Yeyati, T. Kontos, and C. Strunk. Carbon nanotubes as Cooper-pair beam splitters. *Phys. Rev. Lett.*, 104:026801, January 2010.

[22] J. Wei and V. Chandrasekhar. Positive noise cross-correlation in hybrid superconducting and normal-metal three-terminal devices. *Nature Physics*, 6(7):494–498, July 2010.

[23] J. Schindele, A. Baumgartner, and C. Schönenberger. Near-unity Cooper pair splitting efficiency. *Phys. Rev. Lett.*, 109(15):157002–, October 2012.

[24] M. Houzet and P. Samuelsson. Multiple Andreev reflections in hybrid multiterminal junctions. *Phys. Rev. B*, 82(6):060517–, August 2010.

[25] A. Freyn, B. Douçot, D. Feinberg, and R. Mélin. Production of nonlocal quartets and phase-sensitive entanglement in a superconducting beam splitter. *Phys. Rev. Lett.*, 106:257005, June 2011.

[26] T. Jonckheere, J. Rech, T. Martin, B. Douçot, D. Feinberg, and R. Mélin. Multipair dc Josephson resonances in a biased all-superconducting bijunction. *Phys. Rev. B*, 87(21):214501–, June 2013.

[27] G. Deutscher and P. G. De Gennes. Proximity effects. In R. D. Parks, editor, *Superconductivity*, volume 2, pages 1005–34. Marcel Dekker, New York, 1969.

[28] K. K. Likharev. Superconducting weak links. *Rev. Mod. Phys.*, 51(1):101–159, January 1979.

[29] D. Beckmann and H. v. Löhneysen. Negative four-terminal resistance as a probe of crossed Andreev reflection. *Applied Physics A: Materials Science & Processing*, 89:603–607, 2007. 10.1007/s00339-007-4193-4.

[30] P. Dubos. *Transport électronique dans des nanojonctions supraconducteur - métal normal - supraconducteur*. PhD thesis, Université Joseph Fourier, Grenoble I, 2000.

[31] B. Pannetier and H. Courtois. Andreev reflection and proximity effect. *J. Low Temp. Phys.*, 118(5-6):599, 2000.

[32] A. F. Andreev. The thermal conductivity of the intermediate state in superconductors. *Sov. Phys. JETP*, 19:1228, 1964.

[33] A. F. Andreev. Electron spectrum of the intermediate state of superconductors. *Sov. Phys. JETP*, 22:455, 1966.

[34] C. Hoffmann, F. Lefloch, M. Sanquer, and B. Pannetier. Mesoscopic transition in the shot noise of diffusive Superconductor/Normal metal/Superconductor junctions. *Phys. Rev. B*, 70(18):180503–, November 2004.

[35] H. Courtois, P. Gandit, B. Pannetier, and D. Mailly. Long-range coherence and mesoscopic transport in N/S metallic structures. *Superlattices and Microstructures*, 25(5-6):721–732, May 1999.

[36] H. Pothier, S. Guéron, N. O. Birge, D. Esteve, and M. H. Devoret. Energy distribution function of quasiparticles in mesoscopic wires. *Phys. Rev. Lett.*, 79(18):3490, 1997.

[37] A. B. Gougam, F. Pierre, H. Pothier, D. Esteve, and Norman O. Birge. Comparison of energy and phase relaxation in metallic wires. *Journal of Low Temperature Physics*, 118(5-6):447–456, 2000.

[38] F. Hübler, M. J. Wolf, D. Beckmann, and H. v. Löhneysen. Long-range spin-polarized quasiparticle transport in mesoscopic Al superconductors with a Zeeman splitting. *Phys. Rev. Lett.*, 109:207001, November 2012.

[39] P. G. De Gennes. Boundary effects in superconductors. *Rev. Mod. Phys.*, 36(1):225–237, January 1964.

[40] T. Schäpers. *Superconductor/Semiconductor Junctions*, volume 174. Springer Berlin / Heidelberg, 2001.

[41] A. Bauer. *Spontaneous Magnetic Flux Induced by Ferromagnetic pi-Junctions*. PhD thesis, Universität Regensburg, 2005.

[42] H. Sellier. *Courant supraconducteur au travers d'un métal ferromagnétique - étude de la jonction π*. PhD thesis, Université Joseph Fourier - Grenoble I, 2002.

[43] G. E. Blonder, M. Tinkham, and T. M. Klapwijk. Transition from metallic to tunneling regimes in superconducting microconstrictions: Excess current, Charge Imbalance, and supercurrent conversion. *Phys. Rev. B*, 25(7):4515, 1982.

[44] D Daghero and R S Gonnelli. Probing multiband superconductivity by point-contact spectroscopy. *Superconductor Science and Technology*, 23(4):043001–, 2010.

[45] W. Escoffier. *Etude de la cohérence quantique dans les systèmes supraconducteur-métal normal par microscopie à effet tunnel*. PhD thesis, Université Joseph Fourier, Grenoble I, 2004.

[46] X. Jehl, M. Sanquer, R. Calemczuk, and D. Mailly. Detection of doubled shot noise in short normal-metal/superconductor junctions. *Nature*, 405:50, 2000.

[47] F. Lefloch, C. Hoffmann, M. Sanquer, and D. Quirion. Doubled full shot noise in quantum coherent Superconductor-Semiconductor junctions. *Phys. Rev. Lett.*, 90(6):067002, 2003.

[48] T. Dubouchet. *Spectroscopie locale à basse température dans des supraconducteurs désordonnés*. PhD thesis, Université Joseph Fourier, Grenoble I, 2010.

[49] T. M. Klapwijk, G. E. Blonder, and M. Tinkham. Explanation of subharmonic energy gap structure in superconducting contacts. *Physica B+C*, 109–110, Part 3(0):1657–1664, July 1982.

[50] M. Octavio, M. Tinkham, G. E. Blonder, and T. M. Klapwijk. Subharmonic energy-gap structure in superconducting constrictions. *Phys. Rev. B*, 27(11):6739, 1983.

[51] P. C. van Son, H. van Kempen, and P. Wyder. Andreev reflection and geometrical resonance effects for a gradual variation of the pair potential near the Normal metal/Superconductor interface. *Phys. Rev. B*, 37(10):5015, 1988.

[52] N. A. Mortensen, K. Flensberg, and A.-P. Jauho. Angle dependence of Andreev scattering at Semiconductor/Superconductor interfaces. *Phys. Rev. B*, 59(15):10176, 1999.

[53] B. D. Josephson. Possible new effects in superconductive tunneling. *Phys. Lett.*, 1(7):251, 1962.

[54] L. D. Landau and V. L. Ginzburg. On the theory of superconductivity. *Journal of Experimental and Theoretical Physics (USSR)*, 20:1064, 1950.

[55] T. Van Duzer and C. W. Turner. *Princples of Superconducting devices and circuits*. Prentice Hall PTR, 2 edition, 1981.

[56] R. P. Feynman, R. B. Leighton, and M. Sands. *Lectures on Physics, vol. III*, volume III. Addison-Wesley Reading, Mass., 1965.

[57] A. F. Morpurgo, J. J. A. Baselmans, B. J. van Wees, and T. M. Klapwijk. Energy spectroscopy of Josephson supercurrent. *Journal of Low Temperature Physics*, 118(5-6):637–651–, 2000.

[58] H. Sellier, C. Baraduc, F. Lefloch, and R. Calemczuk. Temperature-induced crossover between 0 and π states in S/F/S junctions. *Phys. Rev. B*, 68(5):054531–, August 2003.

[59] J. Bentner. *Zur Strom-Phasen-Relation diffusiver Supraleiter/Normalleiter/-Supraleiter Josephson-Kontakte*. PhD thesis, Universität Regensburg, 2004.

[60] N. Argaman. Nonequilibrium Josephson-like effects in wide mesoscopic SNS junctions. *Superlattices and Microstructures*, 25(5/6):861 – 875, 1999.

[61] J-D. Pillet, C. H. L. Quay, P. Morfin, C. Bena, A. Levy Yeyati, and P. Joyez. Andreev bound states in supercurrent-carrying carbon nanotubes revealed. *Nature Physics*, 6(12):965–969, December 2010.

[62] L. Bretheau, C. O. Girit, H. Pothier, D. Esteve, and C. Urbina. Exciting Andreev pairs in a superconducting atomic contact. *Nature*, 499(7458):312–315, July 2013.

[63] J.-D. Pillet, P. Joyez, R. Zitko, and M. F. Goffman. Tunneling spectroscopy of a single quantum dot coupled to a superconductor: From Kondo ridge to Andreev bound states. *Phys. Rev. B*, 88(4):045101–, July 2013.

[64] E. J. H. Lee, X. Jiang, M. Houzet, C. M. Lieber R. Aguado, and S. De Franceschi. Spin-resolved andreev levels and parity crossings in hybrid superconductor-semiconductor nanostructures. *Nature Nanotechnology*, pages 79–84, 2014.

[65] F. Chiodi. *Dynamical effects in Superconductor/ Normal Metal/ Superconductor long Josephson Junctions*. PhD thesis, University Paris-Sud, 2010.

[66] I. Giaever. Detection of the ac Josephson effect. *Phys. Rev. Lett.*, 14(22):904–906, May 1965.

[67] D. N. Langenberg, D. J. Scalapino, B. N. Taylor, and R. E. Eck. Investigation of microwave radiation emitted by Josephson junctions. *Phys. Rev. Lett.*, 15(7):294–297, August 1965.

[68] D. N. Langenberg, D. J. Scalapino, B. N. Taylor, and R. E. Eck. Investigation of microwave radiation emitted by Josephson junctions. *Phys. Rev. Lett.*, 15(21):842–842, November 1965.

[69] S. Shapiro, A. R. Janus, and S. Holly. Effect of microwaves on Josephson currents in superconducting tunneling. *Rev. Mod. Phys.*, 36(1):223–225, January 1964.

[70] P. Dubos, H. Courtois, B. Pannetier, F. K. Wilhelm, A. D. Zaikin, and G. Schön. Josephson critical current in a long mesoscopic S-N-S junction. *Phys. Rev. B*, 63:064502, 2001.

[71] O. Vávra, W. Pfaff, and C. Strunk. Planar S-(S/F)-S Josephson junctions induced by the inverse proximity effect. *Applied Physics Letters*, 95(6):062501, 2009.

[72] L. P. Rokhinson, X. Liu, and J. K. Furdyna. The fractional a.c. Josephson effect in a Semiconductor-Superconductor nanowire as a signature of Majorana particles. *Nature Physics*, 8(11):795–799, November 2012.

[73] M. Chauvin. *The Josephson effect in Atomic Contacts*. PhD thesis, Université Paris 6, 2005.

[74] P. E. Gregers-Hansen, E. Hendricks, M. T. Levinsen, and G. R. Pickett. Subharmonic energy-gap structure and a Josephson-radiation-enhanced gap in Dayem bridges. *Phys. Rev. Lett.*, 31(8):524–527, August 1973.

[75] E. Scheer, P. Joyez, D. Esteve, C. Urbina, and M. H. Devoret. Conduction channel transmissions of atomic-size aluminum contacts. *Phys. Rev. Lett.*, 78(18):3535–3538, May 1997.

[76] J. Kutchinsky, R. Taboryski, O. Kuhn, C. B. Sørensen, P. E. Lindelof, A. Kristensen, J. Bindslev Hansen, C. Schelde Jacobsen, and J. L. Skov. Coherent diffusive transport mediated by Andreev reflections at $V = \Delta/e$ in a mesoscopic Superconductor/Semiconductor/Superconductor junction. *Phys. Rev. B*, 56(6):R2932–R2935, August 1997.

[77] R. Taboryski, J. Kutchinsky, J. B. Hansen, M. Wildt, C. B. Sørensen, and P. E. Lindelof. Multiple Andreev reflections in diffusive SNS structures. *Superlattices and Microstructures*, 25(5/6):829, 1999.

[78] T. Hoss, C. Strunk, T. Nussbaumer, R. Huber, U. Staufer, and C. Schönenberger. Multiple Andreev reflection and giant excess noise in diffusive Superconductor/Normal metal/Superconductor junctions. *Phys. Rev. B*, 62:4079–4085, August 2000.

[79] M. Fuechsle, J. Bentner, D. A. Ryndyk, M. Reinwald, W. Wegscheider, and C. Strunk. Effect of microwaves on the current-phase relation of Superconductor-Normal metal-Superconductor Josephson junctions. *Phys. Rev. Lett.*, 102(12):127001–, March 2009.

[80] P. Dubos, H. Courtois, O. Buisson, and B. Pannetier. Coherent low-energy charge transport in a diffusive S-N-S junction. *Phys. Rev. Lett.*, 87:206801, October 2001.

[81] J. C. Cuevas, J. Heurich, A. Martin-Rodero, A. Levy Yeyati, and G. Schön. Subharmonic Shapiro steps and assisted tunneling in superconducting point contacts. *Phys. Rev. Lett.*, 88(15):157001–, March 2002.

[82] R. Duprat and A. Levy Yeyati. Phase diffusion and fractional Shapiro steps in superconducting quantum point contacts. *Phys. Rev. B*, 71(5):054510–, February 2005.

[83] F. K. Wilhelm. *Ladungstransport in supraleitenden Nanostrukturen*. PhD thesis, Universität Karlsruhe, 1999.

[84] F. Chiodi, M. Ferrier, S. Guéron, J. C. Cuevas, G. Montambaux, F. Fortuna, A. Kasumov, and H. Bouchiat. Geometry-related magnetic interference patterns in long SNS Josephson junctions. *Phys. Rev. B*, 86(6):064510–, August 2012.

[85] C. Hoffmann. *Etude du transport électronique dans les jonctions hybrides supraconducteur / métal normal par des mesures de bruit en courant*. PhD thesis, Université Joseph Fourier, 2003.

[86] S. Rajauria. *Electronic refrigeration using superconducting tunnel junctions*. PhD thesis, Université Joseph-Fourier - Grenoble I, 2008.

[87] A. Barone and G. Paterno. *Physics and applications of the Josephson effect*. John Wiley & Sons, Inc, 1982.

[88] J. F. Clauser and A. Shimony. Bell's theorem. experimental tests and implications. *Reports on Progress in Physics*, 41(12):1881, 1978.

[89] A. Aspect, P. Grangier, and G. Roger. Experimental tests of realistic local theories via Bell's theorem. *Phys. Rev. Lett.*, 47:460–463, August 1981.

[90] R. Ursin, F. Tiefenbacher, T. Schmitt-Manderbach, H. Weier, T. Scheidl, M. Lindenthal, B. Blauensteiner, T. Jennewein, J. Perdigues, P. Trojek, B. Omer, M. Furst, M. Meyenburg, J. Rarity, Z. Sodnik, C. Barbieri, H. Weinfurter, and A. Zeilinger. Entanglement-based quantum communication over 144 km. *Nature Physics*, 3(7):481–486, July 2007.

[91] X.-S. Ma, S. Zotter, J. Kofler, R. Ursin, T. Jennewein, C. Brukner, and A. Zeilinger. Experimental delayed-choice entanglement swapping. *Nature Physics*, 8(6):480–485, June 2012.

[92] C. Strunk. Quantum devices: Towards entangled electrons. *Nature Nanotechnology*, 5(1):11–12, January 2010.

[93] A. Kleine, A. Baumgartner, J. Trbovic, and C. Schönenberger. Contact resistance dependence of crossed Andreev reflection. *EPL (Europhysics Letters)*, 87(2):27011, 2009.

[94] G. Falci, D. Feinberg, and F. W. J. Hekking. Correlated tunneling into a superconductor in a multiprobe hybrid structure. *EPL (Europhysics Letters)*, 54(2):255, 2001.

[95] Mikhail S. Kalenkov and Andrei D. Zaikin. Nonlocal Andreev reflection at high transmissions. *Phys. Rev. B*, 75:172503, May 2007.

[96] M. S. Kalenkov and Andrei D. Zaikin. Crossed Andreev reflection at spin-active interfaces. *Phys. Rev. B*, 76:224506, December 2007.

[97] R. Mélin and D. Feinberg. Sign of the crossed conductances at a Ferromagnet/Superconductor/Ferromagnet double interface. *Phys. Rev. B*, 70:174509, November 2004.

[98] P. Cadden-Zimansky and V. Chandrasekhar. Nonlocal correlations in normal-metal superconducting systems. *Phys. Rev. Lett.*, 97:237003, December 2006.

[99] A. Levy Yeyati, F. S. Bergeret, A. Martin-Rodero, and T. M. Klapwijk. Entangled Andreev pairs and collective excitations in nanoscale superconductors. *Nature*, 3(7):455–459, July 2007.

[100] J. Cadden-Zimansky, P. Wei and V. Chandrasekhar. Cooper-pair-mediated coherence between two normal metals. *Nature Physics*, 5:393 – 397, 2009.

[101] A. Das, Y. Ronen, M. Heiblum, D. Mahalu, A. V. Kretinin, and H. Shtrikman. High-efficiency Cooper pair splitting demonstrated by two-particle conductance resonance and positive noise cross-correlation. *Nature Communications*, 3:1165–, November 2012.

[102] L. G. Herrmann. *Carbon nanotubes as Cooper pair beam splitters.* PhD thesis, Université Paris 6, 2010.

[103] T. D. Clark. Experiments on coupled Josephson junctions. *Physics Letters A*, 27(9):585 – 586, 1968.

[104] K. K. Likharev, L. S. Kuzmin, and G. A. Ovsyannikov. Mutual phase locking in multijunction Josephson arrays. *IEEE Transactions on Magnetics*, 17(1):111 – 114, 1981.

[105] S. Duhot, F. Lefloch, and M. Houzet. Cross correlation of incoherent multiple Andreev reflections. *Phys. Rev. Lett.*, 102:086804, 2009.

[106] B. Kaviraj, O. Coupiac, H. Courtois, and F. Lefloch. Noise correlations in three-terminal diffusive Superconductor/Normal metal/Superconductor nanostructures. *Phys. Rev. Lett.*, 107:077005, August 2011.

[107] A. Freyn, M. Flöser, and R. Mélin. Positive current cross-correlations in a highly transparent normal-superconducting beam splitter due to synchronized Andreev and inverse Andreev reflections. *Phys. Rev. B*, 82:014510, July 2010.

[108] D. W. Jillie, M. A. H. Nerenberg, and James A. Blackburn. Voltage locking and other interactions in coupled superconducting weak links. II. Experiment. *Phys. Rev. B*, 21(1):125–131, January 1980.

[109] P. E. Lindelof and J. Bindslev Hansen. Coherent behavior of two interacting Dayem bridges. *Journal of Low Temperature Physics*, 29(5-6):369–396, 1977.

[110] C. Varmazis, R. D. Sandell, A. K. Jain, and J. E. Lukens. Generation of coherent tunable Josephson radiation at microwave frequencies with narrowed linewidth. *Applied Physics Letters*, 33(4):357–359, 1978.

[111] M. A. H. Nerenberg, James A. Blackburn, and D. W. Jillie. Voltage locking and other interactions in coupled superconducting weak links. I. Theory. *Phys. Rev. B*, 21(1):118–124, January 1980.

[112] D. W. Jillie, J. E. Lukens, and Y. H. Kao. Observation of interactions between two superconducting phase-slip centers. *Phys. Rev. Lett.*, 38(16):915–918, April 1977.

[113] F. Pierre, A. Anthore, H. Pothier, C. Urbina, and D. Esteve. Multiple Andreev reflections revealed by the energy distribution of quasiparticles. *Phys. Rev. Lett.*, 86:1078–1081, February 2001.

[114] J. C. Cuevas and H. Pothier. Voltage-induced Shapiro steps in a superconducting multiterminal structure. *Physical Review B: Condensed Matter and Materials Physics*, 75:174513, 2007.

[115] A. H. Pfeffer, B. Kaviraj, O. Coupiac, and F. Lefloch. Superconducting quantum interference devices based set-up for probing current noise and correlations in three-terminal devices. *Review of Scientific Instruments*, 83(11):115107–115107–5, 2012.

[116] O. Coupiac. *Réalisation d'un dispositif à trois SQUIDs pour la mésure de correlations de bruit de grenaille*. PhD thesis, Université Joseph Fourier, 2006.

[117] R. L. Fagaly. Superconducting quantum interference device instruments and applications. *Review of Scientific Instruments*, 77(10):101101–101101–45, 2006.

[118] W. Schottky. Über spontane Stromschwankungen in verschiedenen Elektrizitätsleitern. *Annalen der Physik*, 57:541, 1918.

[119] Ya. M. Blanter and M. Büttiker. Shot noise in mesoscopic conductors. *Phys. Rep.*, 336(1-2):1, 2000.

[120] G. Bignon, M. Houzet, F. Pistolesi, and F. W. J. Hekking. Current-current correlations in hybrid superconducting and normal-metal multiterminal structures. *Europhysics Letters*, 67(1):110–116, 2004.

[121] R. Mélin, C. Benjamin, and T. Martin. Positive cross correlations of noise in superconducting hybrid structures: Roles of interfaces and interactions. *Phys. Rev. B*, 77:094512, March 2008.

[122] A. Bednorz, J. Tworzydlo, J. Wrobel, and T. Dietl. Maximal positive cross-correlation of current noise from Andreev reflection. *Phys. Rev. B*, 79:245408, June 2009.

[123] D. Chevallier, J. Rech, T. Jonckheere, and T. Martin. Current and noise correlations in a double-dot Cooper-pair beam splitter. *Phys. Rev. B*, 83:125421, March 2011.

[124] H. Courtois, M. Meschke, J. T. Peltonen, and J. P. Pekola. Origin of Hysteresis in a proximity Josephson junction. *Phys. Rev. Lett.*, 101:067002, August 2008.

Electronic properties of diffusive three-terminal Josephson junctions and non-local quartet mechanism

Andreas H. Pfeffer

Multi-terminal superconducting hybride nanostructures are a highly active field of current research, driven by the goal to realize entangled electronic states in mesoscopic systems.

In this context, we have studied the electronic transport properties of three terminal superconductor (S) - normal metal (N) - superconductor (S) nano-devices using a new SQUID-based experimental set-up working at very low temperature (30 mK) and dedicated for high sensitive conductance and current noise correlations measurements. In a geometry where a T-shaped normal metal (Cu) is connected to three superconducting reservoirs (Al), new subgap anomalies appear in the differential conductance for specific values of the chemical potential applied to the superconductors. The most emphasized line appears when two superconductors (collectors) are biased at opposite voltage with respect to the third superconducting electrode (injector).

This anomaly is consistent with the prediction of non-local quartets as the result of double crossed Andreev reflections (dCAR). In this particular process, a Cooper pair originating from the injector is split in two quasi-particles that recombine into Cooper pairs in each of the two collectors.

Nevertheless, also other mechanism, such as synchronization of ac-currents or down-mixing [3] could reveal the observed features.

Additional features appear for other integer voltage ratios and could be attributed to higher order processes of dCAR. The mechanism of non-local quartet opens perspectives toward a new generation of entanglers.